Experimental Investigation on Selective Withdrawal from Two-Layer Reservoirs Using a Temperature Control Curtain

by

Yaser Shammaa ©

A thesis submitted to the
Faculty of Graduate Studies and Research
in partial fulfillment of the requirements for the degree of
Doctor of Philosophy

In

Water Resources Engineering
Department of Civil and Environmental Engineering

Edmonton, Alberta

Fall 2007

Your file Votre référence
ISBN: 978-0-494-33061-6
Our file Notre référence
ISBN: 978-0-494-33061-6

ABSTRACT

Withdrawal from reservoirs using curtain-control technique has been studied experimentally. The flow into the reservoir occurred under a curtain and the outflow was withdrawn through a round intake. Several outlet elevations (b) and different flow densities were used. The research has resulted in five main contributions, which are presented in this paper-format thesis.

The first contribution presents analytical solution for point/line intake flows. Potential flow solutions were extended to study the velocity field upstream of a finite-size orifice and sluice gate. It was found that in the "near field" zones (approximately $3\sqrt{A}$, where A is the cross sectional area of the intake), the iso-velocity surfaces appeared to be semi-ellipsoidal; while in the "far field" zones they became hemispheres. The shape and size of the orifice/sluice gate were found to have no effect on the flow field beyond a certain distance.

The second contribution investigates experimentally the flow field in a confined reservoir with jet inflow and circular outflow. Three flow zones were distinguished: a jet zone with strong recirculation, an outlet zone with particular flow pattern and secondary recirculation, and a separation zone. The jet spreading and the entrainment rate were found to exceed those of a classical wall jet and to reach their maximal where $b \approx H/2$, H being the total water depth. The trajectory of the maximum horizontal velocity in the separation zone was found to fit a quadratic curve. A particular 3-D flow pattern was observed upstream of the outlet. The extent of that outlet zone increased with b and with the distance between the outlet and the location of the velocities causing the secondary recirculation. Thus, the extent of that zone was observed to be maximal where $b=H/2$. Potential flow theory seemed to agree with the experimental data up to a distance of approximately $3d$ from the outlet (d being the outlet diameter).

The third contribution investigates experimentally the selective withdrawal in a two-layer confined reservoir using a temperature-control curtain where the inflow was under the curtain.

The flow evolution was found to pass through two time-stages: one sub-critical (one layer is withdrawn) and one super-critical (both layers are withdrawn). Three flow zones were distinguished: a jet zone with large recirculation, an intake zone, and a middle "separation" zone. A considerable mixing was observed in the recirculation zone. In spite of that mixing, it was found that the supercritical withdrawal compared well with the theory of semi-infinite reservoirs. The interface has dipped directly above the center of the recirculation zone. The dip moved one-third of the reservoir length from the curtain area by the end of each experiment. A withdrawal time scale (t_w) was introduced such that it described the withdrawal process practically and efficiently.

The fourth contribution presents further experiments and discussion on selective withdrawal from two-layer reservoir with emphasis on the relation between the internal seiches and interfacial waves and the process of selective withdrawal. It was found that significant interfacial waves affected the overall withdrawal. That effect was reflected in the continuous rising of the interface beyond the theoretical h_c (critical height) and thus the withdrawal continued to be from both layers. The interface rising was found possible to exceed $1.5h_c$ above the intake level. Waves' characteristics were also investigated and revealed that internal seiches had a significant effect on the instantaneous horizontal velocity. The instantaneous vertical velocity was more affected by shear waves.

The fifth contribution expanded on the previous two-layer case to report experimentally the flow generated by a horizontal plane buoyant jet discharging into a shallow enclosure (reservoir). The stability (i.e. clear layer separations) of the flow was transient and appeared only for short periods. The longer stability periods were associated with lower initial Froude number. Using a withdrawal time scale t_w, the rate of the withdrawal from the inflow was found to considerably precede that of a two-layer case up to $\approx 0.68\ t_w$. At that time, *2/3 of* Q_o (total withdrawal) was from the inflow fluid in the buoyant jet experiments whereas it was *½ of* Q_o for the two-layer experiments.

ACKNOWLEDGEMENTS

I am truly grateful to the Almighty God who pours me with His mercy everyday.

I would like to express my thanks to my supervisor, Dr. David Zhu, who throughout the research has been resourceful in providing valued suggestions and initiatives. My thanks are also to Dr. N. Rajaratnam and Dr. P. Steffler for their valuable comments in the initial stage of this research.

Special gratitude is to my ex-colleagues Muhamad El-Gamal and Hesham Fouli and my current colleague Aqeel Jalil for their tremendous support along the course of this research.

Thanks are also extended to Mr. Perry Fedun for his proactive technical support. I wish also to extend my gratitude to my colleagues at the University of Alberta, especially Iran Neto, for his encouragement and inspire.

Warm thanks go to my neighbor Hussien Jime and his family who shared their feeling, help, and encouragement during my study.

I am highly indebted to my wife for her support, understanding, and patience.

Finally, all the debt is to my father's soul, who built my thought and shaped my personality. I am also truly grateful to my mother, my sister, and my five brothers for their encouragement, concern and love which are the secrets that have driven me on all these years.

Table of Content

List of Tables

List of Figures

Notations

A	area of the opening (orifice, sluice gate, or jet)
A_h	horizontal cross section area of the inner reservoir
B	width of the reservoir (enclosure)
F_c	critical Froude number
I	gray scale value of any pixel
I_{max}	maximum grey scale value at a certain x-location
H	total water depth
L	length of the inner reservoir
L_b	distance from the outlet wall to the center of the separation zone
L_c	Length of the recirculation zone
L_d	dip's length from the curtain
N	buoyancy frequency
Q	volumetric discharge at time t
Q_1	volumetric flow from the upper later
Q_2	volumetric flow from the lower later
Q_c	volumetric critical withdrawal
Q_{ed}	recirculation's backward discharge
Q_o	total volumetric withdrawal ($=Q_1+Q_2$)
R_e	Reynolds number
T	wave period
U_o	uniform velocity at an opening
V	jet-front velocity
V_1	instantaneous volume of the upper layer
V_c	withdrawal layer volume defined between two lines, $2h_c$ apart
V_{ers}	upper layer volume erosion
V_r	radial velocity
a	curtain opening
b	intake level with respect to the bed;
b'	vertical distance to the point where $u^*=0.5u^*_{max}$
b_o	depth of the vena contrata
c	two-layers interfacial long wave celerity
d	orifice (intake) diameter
e_s	recirculation's strength $=u_{e\,max}/u_b$
f	wave frequency

g	gravity acceleration
g'	reduced gravity ($=(\Delta\rho/\rho).g$)
h	interface height with respect to the intake level; water depth above an opening centerline
h_1	upper layer depth
h_2	lower layer depth
h_c	critical height with respect to the intake level
h_d	dip's height above the bed
$h_{i\,avg}$	average interface level with respect to the bed
m	sink strength
n, m	modes oscillation (=0, 0.5, 1, 1.5, etc) in the length and width directions, respectively
q_1	specific discharge in the upper layer at a certain x-section
q_o	specific discharge at the inlet
r	radial coordinate
r_o	radial coordinate of the centroid of an infinitesimal sink area
s	jet spreading (where $u \approx 0$)
t	time passed since the experiment started
t_1	sub-critical flow period
t_2	super-critical flow period
t_c	time the critical withdrawal (Q_c) reached
t_i	time the average interface level reached the intake level
t_{int}	time that interface level reached a certain point
t_o	time the designed steady withdrawal (Q_o) reached
t_w	withdrawal time scale
t'	time passed since t_o reached ($= t - t_o$)
t'_c	time the critical withdrawal (Q_c) reached since t_o reached($= t_c - t_o$).
t'_i	time the average interface level reached the intake level since t_o reached($= t_i - t_o$).
u	horizontal velocity component at any grid point
u^*	$u - u_{min}$
u_b	average velocity in the bottom layer at a certain time ($u_b=Q_o/h_i$)
u_d	depth-average horizontal velocity component at a certain x location
$u_{e\,max}$	maximum horizontal velocity in the recirculation's returning flow
u_m, u_{max}	maximum horizontal velocity
u_{min}	minimum horizontal velocity
u^*_{max}	$=u_{max} - u_{min}$
u_∞	uniform velocity far upstream of a sluice gate ($u_\infty=q/h$)
v	vertical velocity component at any grid point

v_e	jet entrainment velocity
v_i	vertical velocity component along the interface line
v_r	radial velocity
v_{ins}	instantaneous horizontal velocity at a point
v_{imax}	maximum vertical velocity component along the interface line
z_b	base interface level (pixels)
z_e	estimated equivalent excess level in the interface due to mixing (pixels)
z_f	level of the free surface (pixels)
z_m	level where u_{max} is located
z_t	estimated true interface (pixels)
x	horizontal co-ordinate
x'	distance from the curtain (x'=150-x)
z	vertical co-ordinate
Y	transversal co-ordinate
α	jet entrainment factor
β	experimental to theoretical u_m ratio upstream a round intake
ϕ	velocity potential function
θ	polar angle with respect to z-axis; horizontal dip's angle $\theta = arc\ tan\ (h_d/L_d)$
θ_o	polar angle of an infinitesimal sink area with respect to z-axis
ω	polar angle with respect to X-Z plane
ω_o	polar angle of an infinitesimal sink area with respect to X-Z plane
ψ	streamline function
ρ	reference density
ρ_i	density of layer i
ρ_{12}	ρ_1/ρ_2
$\Delta\rho$	density difference between two layers

Chapter 1

General Introduction

There is a wide diversity of density stratification in lakes and reservoirs, which are caused by a variety of reasons. These reasons could be classified primarily as the temperature variation including heating and cooling, and secondarily by variable concentration of solvents, suspended solids, and inflows and outflows.

The depth of the lake or reservoir, however, plays the major role in the thermal density stratification where almost all lakes and reservoirs having depths greater than about 6 m are exposed to the thermal stratification phenomenon. This thermal stratification is mainly due to the heat flux at the surface water and the wind stress effect. The resulting stratification however, is a function of the weather and it often causes serious environmental concerns. This usually creates the needs to selectively withdraw the water from different depths.

In fish habitat, for example, Vermeyen (2001) showed the important relation of water withdrawn from Lake Natoma on the natural spawning and egg fertilization of Chinook salmon downstream Shasta Dam in California. In agricultural aspect, warmer water is needed in order to irrigate paddy fields and water of lowest salinity is desired if the withdrawal is done in an estuary stratified with salinity (Kataoka *et al.* 2001). In solar ponds, energy is extracted by withdrawing water from the hot saline layer and the withdrawal and inflow is controlled to maintain the most efficient density gradient for the collection and storage of energy in the pond (Hocking 1991). In cooling ponds, withdrawal of coolest possible water would considerably reduce the fuel consumption (Wood 1978).

Selective withdrawal structures however, can take several forms such as: inclined intakes tower on a sloping embankment, freestanding intake tower, usually incorporated into the flood control outlet facilities of embankment dams, face-of-dam intake tower, constructed as an integral part of a concrete dam, and a canal with a skimmer wall (Wood and Lai 1972; Jirka 1979; Holland 1984). The appropriate structure type, however, depends on the project

purposes, water quality objectives, and construction materials.

Even though many reservoirs were designed with the consideration of selective withdrawal use, many others were not built with that regard in mind. This fact has lead to consider retrofitting structures. Typically, retrofitting consists of rigid structure extensions of existing intakes. Options might include: bulk heading of the trash rack structure to allow high level withdrawal, use of the diversion tunnel as a deep penstock intake, use of the low level outlets as deep penstock intakes, excavating a new deep level penstock through the dam, and attaching a rigid steel multi-level intake to the dam face (Johnson, 1991; Jirka 1979). Even though rigid retrofits are often not designed to withstand full hydrostatic pressure (dewatering) they tend to be substantial and expensive (Johnson, 1991).

A recent low-cost retrofitting solution was proposed by Vermeyen (2000) to use a temporary vertical barrier control (a curtain) to control the depth from which water is drawn, see Fig 1.1. The curtain creates an inner reservoir within a reservoir. The curtain can be designed to underdraw the cold water at its bottom and/or to skim the warm surface water atop of it. In addition, the curtain creates a modified stratification between the curtain and the dam, a wall jet inflow, and a confined space. Thus, a complicated flow pattern is produced depending on the operation; and obviously this needs more than one research to explore. Furthermore, as simplifications are essential to approach this type of flow only two-layer stratification flow will be focused on in the present study.

1.1. Background

There are two common engineering problems coupled with selective withdrawal. The first is where an outlet valve can be approximated to a point sink in a dam. This is commonly used in selective withdrawal from a deep reservoir. The second case is where we have a gated outlet of significant horizontal dimension and this can be approximated to a line sink (Wood, 2001). The flow in these two cases can be approximated to three- and two-dimensional flow, respectively.

Physically, when water is drawn from a stratified fluid, a withdrawal zone is created from which the bulk of the water flows out through the intake. Water above and below the boundaries of this zone can't act against buoyancy and gravity, respectively, to reach the outlet. The stratification thus inhibits the vertical motion, but not the horizontal motion. This layered horizontal flow could be stretched up to 30 km upstream of a dam (Imberger, 1980).

The nature and value of the critical parameters that affect the selective withdrawal are still subjected to some conjecture, both in the case of two-dimensional flows (line sink) or three-dimensional flows (point sink) (Hocking and Forbes, 2001). In discrete stratification however, extensive effort has been expanded to examine this issue both analytically and experimentally. Eventually, the qualitative behavior of the flow when withdrawal occurs is well understood. Quantitative results, however, are still ambiguous (Hocking and Forbes, 2001). On the other hand, when the stratification is linear and the withdrawal is steady, the flow is well understood (Hocking and Forbes, 2001).

Modeling a complex stratification is usually difficult, and also of limited use (Clarke and Imberger, 1996). Therefore research in this field has concentrated on two alternative models of the fluid dynamics. In one case the reservoir is modeled as a linear stratification fluid and in the alternative case, as a two-layer (or discrete stratification) fluid. The later case is the main focus of this study, and thus a general related review will be provided.

Discrete Stratification

When withdrawing from a fluid consisting of two or more discrete layers of different density, most of the analytical and numerical work has been undertaken considering thin/sharp interfaces and using a model of the flow as steady and irrotational and the fluid as invicid and incompressible. It is interesting that if one assumes that the flow in the upper layer is stagnant, the equations describing the flow of a single layer of fluid beneath a free surface are identical to those describing the flow in the lower layer of a two-layer fluid beneath an interface, except that the gravity g is replaced by the reduced gravity (g') (see e.g. Jirka 1979). Tuck and

Vanden-Broeck (1984) have shown numerically, with the previous described assumptions however, that only two types of flow are possible if only a single layer is to be flow out through a sink: 'stagnation point type' and 'cusp type' flow. Both names have come from the shape of the interface that could outcome due to withdrawal. The first type involves a stagnation point on the interface directly above the sink. The second type is characterized by a downward cusp forms in the interface directly above the sink, as the interface is drawn down to enter the sink vertically.

The fundamental works in selective withdrawal for a discrete two-layer fluid could be that of Craya (1949). Neglecting viscous effect at the interface, assuming hydrostatic conditions, and using Boussinesq approximation, Craya (1949) presented an exact 'cusp' type solution of the flow by solving the Bernoulli equation for the intakes in the form of horizontal line and point sink flows where the vertical extent of both upper and lower layers is unlimited (see Fig 1.2). He presented the following two relations for the critical Froude number at which water is withdrawn from the upper layer

$$F_c = \frac{q_c}{\sqrt{g' h^3}} = C_1 \qquad \text{(for line sink) ..... (1)}$$

$$F_c = \frac{Q_c}{\sqrt{g' h^5}} = C_2 \qquad \text{(for point sink) ..... (2)}$$

where q_c, Q_c are the specific and volumetric critical discharge respectively, h is the vertical distance between the sink and the upstream interface level, $g'=(\Delta\rho/\rho)g$ is the reduced gravity, where g is the acceleration due to gravity, $\Delta\rho$ is the density difference between the two layers, and ρ is a reference density. Craya (1949) found that C_1=1.52 for a small slot ($<h/8$) and C_2=2.55 for a small orifice. Gariel (1949) verified experimentally Craya's result. These equations became the basis for use or be modified by many later researchers. In this research we will only focus on the point sink (orifice) case.

Point Sink (Orifice) Intake

Following Craya (1949), Bryant and Wood (1976) and Wood (1978) have treated the flow of multiple layers into a sector and generalized Eq. 2 to flows into a sector of a sphere. Wood (1978) has also investigated the supercritical flow of two layers and derived an expression $\lambda=q_1/q_2$ as a function of the Froude number defined in Eq. 2, where q_1, q_2 is the flow from the upper layer and the bottom later respectively. Lawrence and Imberger (1979) carried out experiments for a point sink in the centre of a reservoir with a density interface. They measured the density profile, the withdrawal discharge Q, and the ratio of the discharges from upper and lower layers and plot this ratio as a function of Q/Q_c where Q_c is the critical withdrawal discharge.

Jirka and Katavola (1979) have examined experimentally the effect of the intake dimensions and interface thickness on the critical withdrawal conditions and found that the critical Froude number is smaller by one or two orders of magnitude compared to value defined by Craya (1949) and Gariel (1949) for a point sink flow. They have related the discrepancy to the effects of the intake diameter and the pycnocline thickness that are not considered in the former studies. They also demonstrated that the withdrawal characteristics in the supercritical range, with simultaneous withdrawal from both layers, can be represented by a unique empirical curve independent of geometric effects. Imberger (1980) presented a very good review of the state-of-the-art in selective withdrawal for both discrete and continuous stratified withdrawal. He also related the previous discrepancy to the experimental difficulties in keeping the steady flow due to changing in the upstream boundary conditions. Wood (2001) extended the theory of selective withdrawal for both 2-D and 3-D flows and determined the maximum withdrawal discharges when two layers flowing below and/or above a stationary layer.

All earlier studies however, were based on the assumption of a quiescent environment where the velocity field is induced by the withdrawal (outflow) only, and the supply is tranquil and far enough from the outlet. In the case of using a temperature curtain however,

the inflow is confined by the curtain opening, and its impact on the flow velocity field and the mixing needs to be evaluated. There is in fact little understanding of how the three processes of inflow, internal waves and selective withdrawal processes interact. Thus, the knowledge about jet inflow into a stratified medium and the parameters that control the mixing and entrainment at an interface as well as the interfacial waves' characteristics are necessary. Some other complications come from different other sources like reservoir operations or the stratification itself. For example, the end case of a two-layer withdrawal is that the withdrawal become from only single-density water (homogeneous flow). Other examples might come from assuming that the upper or the bottom layer is small such that the inflow is presented as a buoyant (denser or lighter) inflow. With these diverse complications other literatures beyond that related to selective withdrawal were involved. Two major categories were concerned: the jet studies and the interfacial mixing. The most relevant studies were briefly reviewed in the following.

In jet studies, Iamandi and Rouse (1969) have shown that the flow structure of a non-buoyant jet consists of alternative circulation cells (primary circulation followed by an opposite-direction secondary circulation and so on). Anwar (1969) has conducted round buoyant jet experiments in deep calm liquids for several densimetric Froude number and plotted their trajectories. Jirka and Harleman (1979) and Andreopoulos *et al.* (1986) have studied buoyant jets in shallow depths and discussed the effect of downstream on the flow stability. Baddour and Abbink (1983) have experimented with buoyant plane underflows (jump) in shallow-short channel. Rajaratnam and Subramanyan (1986) have studied the growth rate of the plane turbulent denser wall jets. Kuang *et al.* (2001) have investigated vertical turbulent plane jets in water of finite depth. Ead and Rajaratnam (2002) have presented a theoretical and laboratory study of plane turbulent wall jets discharged into large ambients at rest. Lee and Chu (2003) and Law *et al.* (2003) have compared numerically their results on buoyant round jets to those of Anwar (1969). Kuang and Lee (2006) reported a numerical study on a vertical round buoyant jet in confined depth.

Mixing phenomenon at the interface has a considerable attention in literature as well. Fernando (1991) presented a review of the stratified entrainment literature and described several interfacial mixing regimes. Larson and Jonsson (1996) have studied the mixing caused by a vertical turbulent jet in a two-layer stratified fluid in a confined system. Stevens and Lawrence (1997) have described the appropriate parameterization of wind-forced temperature dynamics in stratified domains. Saggio and Imberger (1998) provided a 3-D numerical model on the evolution of the basin-scale waves responded to wind forcing. Tory and Koseff (2005) have showed experimentally that the nature of internal wave instability and breaking is not universal in character. Farrow and Hocking (2006) studied numerically the effect of interfacial waves on selective withdrawal from a line sink. Anohin *et al.* (2006) have investigated the interaction of long internal waves to the selective withdrawal in a linear stratification.

1.2. Scope and Approaches of the Study

Due to the flow complexity resulting when a curtain is used, the research will focuse on two-layer stratification. The possible cases that could result from this stratification are: homogeneous or no stratification (or end of stratification) in the inner reservoir; two-layer stratification; and two different densities between the outside and the inside reservoir. The main objective of this study, though, is to examine the effect the curtain on the flow behavior in the inner reservoir and on the withdrawal quality. Three sub-objectives can be summarizes as follows:

- Study the homogeneous flow patterns in confined reservoirs.
- Examine the withdrawal quality from a two-layer reservoir when a curtain control is used with a specific concern on the interfacial waves effect.
- Study the plane buoyant jet flow behavior in a confined reservoir with emphasis on the withdrawal quality.

The over all knowledge will have practical application for control of water quality in lakes and reservoirs when a curtain is used. The knowledge however could expand to many similar

flow patterns like for example those found in ventilation (Kuznik et at. 2006) or smoke confinement (Cheung *et al.*, 2006). On the other hand, the results will be essential for validating future numerical modeling of such flows.

The research starts in Chapter 2 by introducing a theoretical approach for the flow upstream of intakes. Round and flat (sluice gate) intakes were considered as infinite number of point and line sinks, respectively. The development of velocity profile away from the orifice and sluice gate was then examined, and the effects of water depth are studied. The study provides a general understanding of the flow field upstream of orifices and sluice gates.

Non-buoyant jet flow in a confined reservoir with round intake was then investigated in Chapter 3 through a set of particle image velocimetry (PIV) experiments. The general flow regimes were distinguished and examined. Velocity field and streamlines were presented. Jets' spreading, velocity, as well as its entrainment rate were studied. Flow in the third dimension was also explored. Turbulence intensities were also investigated.

In Chapter 4, selective withdrawal in a two-layer confined reservoir using a temperature-control curtain was investigated through a set of laser induced fluorescent (LIF) and PIV experiments. Jet inflow, round intake, as well as different intake and stratifications levels were considered. LIF experiments have clearly illustrated the over all flow evolution and interface progression, whereas the PIV measurements have devise the velocity characteristics in the reservoir. Different flow zones were distinguished and studied in details. The change of withdrawal quality with time was studied and compared to the theory in un-confined environments.

In Chapter 5, processes of inflow, internal waves and selective withdrawal interact in the two-layer confined reservoir used in Chapter 4 was further investigated experimentally. The mechanism of waves affects the withdrawal was explored. Waves' characteristics were also investigated and its dominant frequencies were isolated. Instantaneous horizontal and vertical velocities were studied in details and connected to the interfacial waves in different parts of the reservoir.

Chapter 6 presented the LIF and PIV experiments on flow generated by a horizontal plane buoyant jet into the reservoir used before. Lighter and denser inflow was considered. The progresses of mixing and withdrawal quality with time were explored. The effect of the initial inflow Froude numbers was also examined. Instantaneous velocities and mean velocity fields were also presented and discussed. Comparison to the two-layer case was also made.

A summury of the work in this research is provided in Chapter 7 along with some discussion and suggestions for further studies.

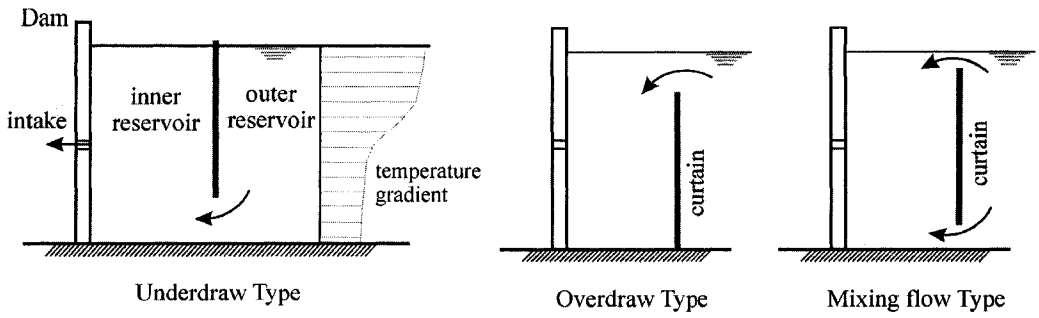

Fig 1. 1 Schematics of selective withdrawal according to flow type using a temperature control curtain.

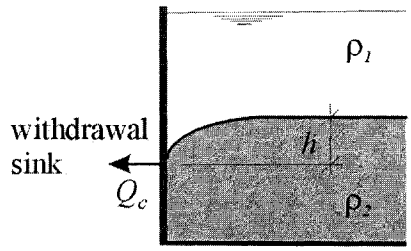

Fig 1. 2 Schematics of critical withdrawal from two-layer stratification.

References

Andreopoulos, J., Praturi, A., and Rodi, W., 1986. "Experiments on vertical plane buoyant jets in shallow water", *J. Fluid Mech.*, 168, 305–336.

Anohin, V.V., Imberger, J., Romero, J.R., and Ivey, G.N, 2006. "Effect of Long Internal Waves on the Quality of Water Withdrawn from a Stratified Reservoir" *J. Hydr. Engrg.*, 132(11), 1134-1145.

Anwar, H.O., 1969. "Behavior of a buoyant jet in a calm fluid", *Proc. Am. Soc. Civ. Eng.*, 95(4), 1289-1303.

Baddour, R.E., and Abbink, H., 1983. "Turbulent underflow in a short channel of limited depth", *J. Hydr. Engrg., ASCE*, 109, 722-740.

Bryant, P.J., and Wood, I.R., 1976. "Selective withdrawal from a layered fluid", *J. Fluid Mech.*, 77(3), 581-591.

Clarke, S.R., and Imberger, J., 1996. "Nonlinear effects in the unsteady, critical withdrawal of a stratified fluid", *DYNAMICS OF ATMOSPHERES AND OCEANS* 24(1-4), 163-171.

Craya, A., 1949. "Theoretical research on the flow of nonhomogeneous fluids", *La Houille Blanche,* 4, 44–55.

Cheung, S.C.P., Lo, S.M., Yeoh, G.H., and Yuen, R.K.K., 2006. "The influence of gaps of fire-resisting doors on the smoke spread in a building fire", *Fire Safety J.*, 41, 539-546.

Ead, S.A., and Rajaratnam, N., 2002. "Plane turbulent wall jets in shallow tailwater", *J. Eng. Mech.,* 128(2), 143–155.

Farrow, D.E., and Hocking, G.C., 2006. "A numerical model for withdrawal from a two-layer fluid", *J. Fluid Mech.,* 549, 141–157.

Fernando, H., 1991. "Turbulent mixing in stratified fluids", *Ann. Rev. of Fluid Mech.*, 23, 455-493.

Gariel, P., 1949. "Experimental research on the flow of non-homogeneous fluids", *La Houille Blanche,* 4, 56–65.

Hocking, G.C., 1991. "Critical withdrawal from a two-layer fluid through a line sink", *J.*

Engng. Maths., 25, 1-11.

Hocking, G.C., and Forbes, L.K. 2001. "Super-critical withdrawal from a two-layer fluid through a line sink if the lower layer is of finite depth", *J. Fluid Mech.*, 428, 333-348.

Holland, A.M., 1984. "Design of selective withdrawal intake structures", *Water for Resources Development, ASCE Annual Conference*, 319-324.

Iamandi, C., and Rouse, H., 1969. "Jet induced circulation and diffusion", *J. Hydraul. Div., Proc. ASCE*, 95(HY2), 589-601.

Imberger, J., 1980. "Selective withdrawal: a review", *the 2nd Intl. Symposium on Stratified Flows*, 381-400.

Jirka, G.H., 1979. "Supercritical withdrawal from two-layered fluid systems – Part 1: Two-dimensional skimmer wall", *J. Hydraul. Res.*, 17, 43–51.

Jirka, G.H., and Harleman, D.R.F., 1979. "Stability and mixing of a vertical plane buoyant jet in confined depth", *J. Fluid Mech.*, 94, 275–304.

Jirka, G.H., and Katavola, D.S., 1979. "Supercritical withdrawal from two-layered fluid systems, Part 2. Three dimensional flow into a round intake", *J. Hydraul. Res.*, 17, 53-62.

Johnson, P.L., 1991. "Hydraulic features of flexible curtains used for selective withdrawal". *Proceeding of the 1991 national conference on Hydraulic Engineering, ASCE*, 184-189.

Kataoka, T., Tsutahara, M., and Mizutani, S., 2001. "Selective withdrawal through a line sink of non-rotating and rotating stratified fluid in a reservoir of finite depth", *Eur. J. Mech. B – Fluids*, 20(2), 167–186.

Kuang, C.P., and Lee, J.H.W., 2006. "Stability and mixing of a vertical axisymmetric buoyant jet in shallow water", *Environ. Fluid Mech.*, 6, 153–180.

Kuang, J., Hsu, C.T., and Qiu, H., 2001. "Experiments on vertical turbulent plane jets in water of finite depth", *J. Eng. Mech.*, 127, 18-26.

Kuznik, F., Rusaouen, G., and Hohota, R., 2006. "Experimental and numerical study of a mechanically ventilated enclosure with thermal effects", *Energy and Buildings*, 38, 931-938.

Larson, M., and Jonsson, L., 1996. "Efficiency of mixing by a turbulent jet in a stably stratified fluid", *Dynamics of Atmospheres and Oceans*, 24, 63-74.

Law, A.W.-K., Wang, H., and Herlina, 2003. "Combined particle image velocimetry/planer laser induced fluorescence for integral modeling of buoyant jets", *J. Eng. Mech.,* 129(10), 1189-1196.

Lawrence, G.A., and Imberger, J., 1979. "Selective withdrawal through a point sink in a continuously stratified fluid with a pycnocline", *Tech. Rep. ED-79-002*, Dept. of Civil Engineering, University of Western Australia, Australia.

Lee, J.H.W., and Chu, V.H., 2003. *Turbulent Jets and Plumes, A Lagrangian Approach*, Kluwer Academic Publishers, USA.

Rajaratnam, N., and Subramanya, S., 1986. "Plane denser wall jets and jumps", *J. Hydraul. Res.,* 24(4), 281-296.

Saggio, A., and Imberger, J., 1998. "Internal wave weather in a stratified lake", *Limnology Oceanography*, 43, 1780–1795.

Stevens, C., and Lawrence, G.A., 1997. "Estimation of wind-forced internal seiche amplitudes in lakes and reservoirs, with data from British Columbia, Canada" *Aquat. Sci.*, 59, 115–134.

Tory, C.D., and Koseff, J.R, 2005. "The generation and qualitative visualization of breaking internal waves", *Experiments in Fluids,* 38, 549-562.

Tuck, E.O., and Vanden-Broeck, J.M., 1984. "A cusp-like free-surface flow due to a submerged source or sink", *J. Austral. Math Soc. B,* 25, 443-450.

Vermeyen, T.B., 2000. "Application of flexible curtains to control mixing and enable selective withdrawal in reservoirs", *Proceeding of the 5th Intl. Symposium on Stratified Flows*, 457-462.

Vermeyen, T.B., 2001. "Lake Natoma temperature curtains pilot project", *The Water Forum, Sacramento, CA, Tech. rep.,* 24p.

Wood, I.R., 1978. "Selective withdrawal from two-layer fluid", *J. Hydraul. Div.,* HY12, 104, 1647-1659.

Wood, I.R., 2001. "Extensions to the theory of selective withdrawal", *J. Fluid Mech.,* 448, 315-333.

Wood, I.R., and Lai, K.K., 1972. "Selective withdrawal from a two layered fluid", *J. Hydraul. Res., 10*(4), 475-496.

Chapter 2

Flow Upstream Of Orifices and Sluice Gates*

2.1. Introduction

Orifices and sluice gates are commonly used flow control and metering devices. Predicting the flow velocity field upstream of these devices is important. For example, it is vital to understand the velocity field in the vicinity of penstocks/intakes for various reasons like fish diversion and pumping operations. For fish habitat it is important that an appropriate screen placement be chosen so that fish will not be trapped in a high velocity zone. In ventilation, it is important to know how the velocity field varies as a function of the shape of the suction aperture and the distance from the aperture.

In their studies on the orifice-induced velocity field, Rodriguez *et al.* (1992), Anayiotos *et al.* (1995), and Myers *et al.* (1997) showed that close to the orifice isovel surfaces are not hemispherical throughout the flow field; rather they become semi-elliptical. These results were verified by numerical simulations of Myers *et al.* (1997) using CFD codes. Recently, Chanson *et al.* (2002) also measured the velocity field upstream of an orifice for an unsteady flow. Several studies have been conducted to investigate the flow field upstream of a sluice gate. Rajaratnam and Humphries (1982) and Finnie and Jeppson (1991) reported their laboratory measurements of the horizontal velocity upstream of a sluice gate. The effect of viscosity is found to be negligibly small for flow upstream of sluice gates (Hager and Roth 1999), thus numerical analysis of sluice gate flows has commonly used potential flow assumption, i.e., irrotational flow motion of an inviscid fluid. Monies (1997), for example, developed a numerical technique to solve the inviscid flow equations using conformal

---

* *A version of this chapter has been published. Shammaa, Y., Zhu, D.Z., and Rajaratnam N. (2005)." Flow upstream of orifices and sluice gates", Journal of Hydraulic Engineering, 131(2), 127-133.*

transformation method. Masliyah *et al.* (1985) applied the boundary-fitted coordinates method to sluice gate flows. Finnie and Jeppson (1991) applied a finite element code using a modified *k-e* turbulence model.

In this paper the velocity field upstream of an orifice and a sluice gate is constructed by using a distribution of point/line sinks over the surface of an orifice/sluice gate opening. After a detailed comparison with previous experimental results, the developed potential flow solutions will then be used to study the characteristics of the flow field. The effect of orifice shapes is studied. In sluice gate flows, the variation of the velocity profiles with distance from a sluice gate is studied, and the effect of water depth is also examined.

2.2. Potential Flow Solutions

Assuming that the fluid is inviscid and incompressible, and the flow is steady and irrotational, the potential flow solutions can be used to study the flow velocity field upstream of finite size orifices or sluice gates. Assuming a uniform velocity at the opening of the orifices or sluice gates, the velocity field can be obtained by distributing point/line sinks with equal strength over the surface of the opening. In the following, flows in infinite water depth will be studied first, followed by the flow in finite water depth. The channel width, however, will be considered infinite throughout this study, which is justified for two-dimensional (2D) sluice gate flows, but not for orifice flows.

Orifice Flow

For an orifice flow, the flow is three dimensional and we can define a velocity potential function ϕ which satisfies Laplace equation ($\Delta^2\phi=0$). For computational convenience, a polar coordinate system (ρ, θ, ω) is adopted to study the velocity field up-stream of an orifice (see Fig 2.1-a). Here we will focus on the velocity field in the *x-z* plane ($\omega=0$).

If the orifice is infinitely small, the velocity potential ϕ is given by the point sink

solution

$$\phi = m/r \qquad \text{with} \qquad m = -Q/2\pi \qquad \ldots\ldots\ldots (1)$$

where r=radial coordinate; m=sink strength; and Q= volumetric flow rate of the sink. Notice Q is divided by $2\pi r$ rather than $4\pi r$ as the withdrawal is from the upstream half space.

For a finite-sized circular orifice centered at the origin (see Fig 2.1-a), we can distribute the above sink solution across the orifice opening. Considering an infinitesimal sink area dA on the orifice opening, and using r_o and θ_o as the coordinates, $dA = r_o\, dr_o\, d\theta_o$. and $dm = -U_o dA/2\pi = -2QdA/(\pi d^2)$, where $U_o = Q/(\pi d^2/4)$ is the uniform velocity across the orifice, and d is the diameter of the orifice. The velocity potential due to such a sink at a point N on the x-z plane, $N(\rho, \theta, 0)$ is given

$$d\phi = \left(-\frac{2 \cdot Q}{\pi^2 \cdot d^2}\right) \cdot \frac{r_o \cdot dr_o \cdot d\theta_o}{L} \qquad \ldots\ldots\ldots (2)$$

where $L = (r_o^2 + r^2 - 2rr_o \,.\, cos\ \theta \,.\, cos\ \theta_o)^{1/2}$ = distance from the sink at (r_o, θ_o) to the point $N(\rho, \theta, 0)$. Integrating over the orifice surface the velocity potential at the point N becomes

$$\phi = \left(-\frac{2 \cdot Q}{\pi^2 \cdot d^2}\right) \cdot \int_0^{2\pi} \int_0^{d/2} \frac{r_o \cdot dr_o \cdot d\theta_o}{(r^2 + r_o^2 - 2 \cdot r \cdot r_o \cdot \cos\theta \cdot \cos\theta_o)^{1/2}} \qquad \ldots\ldots\ldots (3)$$

Eq. (3) is for the orifice flow where the orifice is placed far from both the free surface and the reservoir bed with $h >> d$, where h = depth of the orifice center. The flow of finite depth will be discussed later in this section. Eq. (3) was solved numerically using *Matlab* to find the velocity field in the x-z plane. However, we can obtain the flow velocity along the x axis (u_{max}) by differentiating Eq. (3) with respect to r and let $\theta = \pi/2$

$$\frac{u_{max}}{U_o} = 1 - \left(1 + \frac{d^2}{4x^2}\right)^{-1/2} \qquad \ldots\ldots\ldots (4)$$

where x=distance along the orifice centerline from the orifice. This result will be discussed later. Notice that for $x=0$, Eq. (4) gives $u_{max} = U_o$, unlike a point sink where the velocity becomes singular.

For a rectangular orifice of a vertical and transverse dimension of a and c, the velocity potential at the point $N(x, 0, z)$ can be obtained using the Cartesian coordinates (y_o and z_o for the transverse and vertical direction, respectively)

$$\phi = -\frac{Q}{2\cdot\pi\cdot a\cdot c}\cdot\int_{-\frac{a}{2}}^{+\frac{a}{2}}\int_{-\frac{c}{2}}^{+\frac{c}{2}}\frac{dy_o\cdot dz_o}{\left[x^2+y_o^2+(z-z_o)^2\right]^{1/2}} \qquad \text{..... (5)}$$

Flow towards a Sluice Gate

In studying the flow under a sluice gate, the flow is considered as half of the "double" sluice gate with two boundaries at $z=h$ and $z=-h$, where h is the depth of the water above the bed (see Fig 2.1-b). The size of the double sluice gate opening is then $2a$, where a is the size of the sluice gate opening. Notice that the horizontal velocity is maximal at the centerline of the double sluice gate (i.e. the bed), and decreases away from the centerline. In real flows, however, the maximal velocity will be slightly above the bed due to the presence of the floor and the no-slip condition there. Here, the flow where the sluice gate is far from the water surface $(h>>a)$ will be considered. The effect of the depth is discussed below.

For 2D sluice gate flows, it is convenient to deal with the stream function ψ. Similarly ψ can be obtained by distributing line sinks along $z=-a$ to $z=+a$. Assume a uniform velocity distribution across the gate $U_o=q/a$, where q is the unit width discharge of the sluice gate. For an infinite thickness (dz_o) of the opening located at $z=z_o$, the strength of the sink $dm = q\,dz_o/(a\pi)$, and its contribution to ψ at a point $N(x, 0, z)$ is

$$d\psi = dm\cdot\theta = -\frac{q}{a\cdot\pi}\cdot\arctan\left(\frac{z-z_o}{x}\right)\cdot dz_o \text{ ..... (6)}$$

Integrating Eq. (6) with respect to z_o from $-a$ to a, and after some algebraic manipulations

$$\psi = -\frac{q}{a\cdot\pi}\cdot\left\{(z+a)\cdot\arctan\left(\frac{z+a}{x}\right)-(z-a)\cdot\arctan\left(\frac{z-a}{x}\right)+\frac{x}{2}\cdot\ln\left[\frac{x^2+(z+a)^2}{x^2+(z-a)^2}\right]\right\} \text{ .(7)}$$

Horizontal and vertical velocities *(u,w)* can be obtained by differentiating Eq. (7) with respect to *z* and *x*, respectively

$$u = -\frac{q}{a \cdot \pi} \cdot \left\{ \arctan\left(\frac{z-a}{x}\right) - \arctan\left(\frac{z+a}{x}\right) \right\} \qquad \ldots\ldots\ldots (8)$$

$$v = -\frac{q}{2 \cdot a \cdot \pi} \cdot \ln\left[\frac{x^2 + (z+a)^2}{x^2 + (z-a)^2}\right]$$

Notice that u is proportional to the angle between the two lines from the point N to the top and bottom of the double sluice gate opening. For a given x, when z goes to infinity this angle goes to zero and u=0; and when z=0 this angle is maximum and $u=u_{max}$. Normalizing u_{max} with respect to U_o gives

$$\frac{u_{\max}}{U_o} = \frac{2}{\pi} \cdot \arctan\left(\frac{a}{x}\right) \qquad \ldots\ldots\ldots\ldots (9)$$

Notice that at x=0, Eq. 9 gives $u_{max}=U_o$, unlike a line sink where the velocity becomes singular.

Effect of Finite Depth

If the water depth is finite, the boundary conditions at $z=-h$ and $z=h$ (Fig 2.1) require that image sinks with same strengths to those in the original opening be added. For the flow shown in Fig 2.1, the imaginary openings should be centered at $\pm 2h, \pm 4h, \ldots \pm 2kh, \ldots \pm \infty$. These openings have the same size and shapes as the original opening. For a circular orifice, the potential function at N becomes

$$\phi = \left(-\frac{2 \cdot Q}{\pi^2 \cdot d^2}\right) \cdot \sum_{k=-\infty}^{\infty} \int_0^{2\pi} \int_0^{\frac{d}{2}} \frac{r_o \cdot dr_o \cdot d\theta_o}{(r_k^2 + r_o^2 - 2 \cdot r_k \cdot r_o \cdot \cos\theta_k \cdot \cos\theta_o)^{1/2}} \qquad \ldots\ldots (10)$$

where r_k and θ_k are the radial coordinate and its angle with the Z-axis related to the k^{th} orifice, given respectively, as

$$r_k = \left[r^2 + (2kh)^2 - 2 \cdot r \cdot (2kh) \cdot \cos\theta\right]^{1/2} \quad \text{..... (11)}$$

$$\theta_k = \arccos\left(\frac{r \cdot \cos\theta - 2kh}{r_k}\right)$$

Notice that when $h=\infty$ the contribution of the imaginary openings (i.e., $k \neq 0$) in ϕ disappears as $r_k = \infty$, $\theta_k = \pi$, and Eq. (10) reduces to Eq. (3).

Similarly, the stream function at N for a sluice gate in a flow of finite depth is

$$\psi = -\frac{q}{a \cdot \pi} \cdot \sum_{k=-\infty}^{\infty} \left\{ \begin{array}{l} (z - 2kh + a) \cdot \arctan\left[\frac{z - 2kh + a}{x}\right] - \\ -(z - 2kh - a) \cdot \arctan\left[\frac{z - 2kh - a}{x}\right] + \frac{x}{2} \cdot \ln\left[\frac{x^2 + (z - 2kh + a)^2}{x^2 + (z - 2kh - a)^2}\right] \end{array} \right\} \text{.(12)}$$

2.3. Results and Comparison to Experimental Measurements

Flow Upstream of Orifice

The above potential flow solutions will now be used to study the flow field upstream of an orifice. The change of the centerline velocity u_{max}, with x for a circular orifice as predicted from Eq. (4) is shown in Fig 2.2. Results from the finite-difference numerical work of Rodriguez *et al.* (1992) and finite-element numerical work of Myers *et al.* (1997) as well as their experimental data are included in Fig 2.2. It is clear from Fig 2.2 that the results of the present study agree well with the computational and experimental results. The velocity u_{max} decreases rapidly away from the orifice and is about 10% of U_o at $x=d$. The point sink solution predicts a uniform velocity across the hemispherical surface (for the infinite depth considered here), which gives radial velocity $V_r = Q/(2\pi x^2)$, thus $u_{max}/U_o = d^2/(8x^2)$. The point sink solution becomes singular at $x=0$. However, for $x \geq 1.5d$, the point sink solution models the velocity variation well, indicating that the velocity is becoming uniform across the semicircle surface, and that the size of the orifice has no effect on the flow behavior beyond a distance of

x= 1.5d.

The radial velocity V_r upstream of an orifice can be obtained by differentiating ϕ with respect to r. Contours of V_r upstream of a circular orifice are compared with those obtained from the numerical and experimental work of Anayiotos *et al.* (1995) in Fig 2.3. The contours of V_r /U_o=0.2 and 0.3 cross the x axis at distances of *0.5d* and 0.66d, respectively. These results are the same as those obtained in Fig 2.2. Notice that these contours have elliptical shapes with the short to long axis ratio of 0.67 and 0.78 for the two cases. The elliptical shapes found in Fig 2.3 indicate that the 3D radial velocity contours upstream of a circular orifice are approximately semiellpsoids. The results from this study are in good agreement with both numerical and experimental results. Notice that the potential flow solution fails to predict the velocity correctly at the wall (at *x=0)* due to the inviscid assumption.

Isovels of the radial velocity V_r upstream of rectangular orifices (with the same discharge Q and surface area *A)* are shown in Fig 2.4. Here the length scale is chosen to be the square root of the orifice area $\sqrt{A}$. Fig 2.4 showed that the isovels for circular and square orifices coincides in the x-z plane. This implies that the velocity distortion due to the corners of the square orifice is limited to the vicinity of the orifice edges. For a rectangular orifice with an aspect ratio of *c/a*=0.25 (i.e. its height is four times its width), the isovel surfaces near the orifice have a shape close to semiellipsoids. For example, at V_r/U_0=0.1, the x axis of the semiellipsoid equals 1.07 (Fig 2.4), and its y and z axes are 1.1 and 1.6, respectively, with the value 1.6 shown on the z axis in Fig 2.4. For the rectangular orifice of *c/a=4,* on the other hand, the semiellipsoid of the isovel at V_r/U_0=0.1 has y and z axes of 1.6 and 1.1, respectively. The value 1.1 can be seen on the z axis. Notice that the shortest semiellipsoids axis is perpendicular to the orifice (i.e. x axis). The y and z axes of the semiellipsoids are such that the longer axis is along the longer dimension of the orifice.

Fig 2.4 also shows far from the orifices that these semiellipsoids turn into hemispheres. Thus the shape of the orifice has no effect on the flow behavior beyond a certain distance: while this distance is related to the shape of the orifice, it does not exceed

2-3 times $\sqrt{A}$ for typical cases. This is consistent with the results for a circular orifice, where this distance is about $1.5d$ ($=1.7\sqrt{A}$).

The effect of finite water depth on the flow behavior upstream of a circular orifice was studied for the case of $h=2d$. The velocity of finite depth flow is slightly larger than that of the infinite depth flow. For instance, at $x=\sqrt{A}$, $V_r/U_o=0.15$ in the finite depth flow, while $V_r/U_o=0.13$ for the infinite depth flow. This is because the flow field is more restricted in the finite depth flow, which results in a larger velocity. When x is larger than about $3\sqrt{A}$, the velocity becomes almost uniform across the depth.

Flow Upstream of Sluice Gate

A typical flow velocity field upstream of a sluice gate is obtained using the potential flow solution and is shown in Fig 2.5. Horizontal velocity profiles at different x sections from $x=a$ to $x=40a$ are plotted for the flow with the gate opening a=0.10m, depth $h=20a$, and the uniform velocity at the gate (x=0) $U_o=1.0$ m/s. Notice that the maximum horizontal velocity u_{max} occurs at the bed, which is the centerline of the double sluice gates (see Fig 2.1-b). As expected, u_{max} decreases quickly away from the gate. At $x=a$ and $x=2a$, for example, u_{max} was about 0.5 and 0.3 U_o, respectively. The withdrawal layer also expands from a narrow thickness close to the bed to the whole depth when the x is large. At $x=h=20a$, the flow becomes almost uniform. In the following, features of the flow upstream of a sluice gate will be examined.

The predictions of the present study are compared with the experimental data and numerical results. Figs 2.6-a and b show a comparison with Finnie and Jeppson (1991) experimental and numerical results (using finite element analysis) and Montes (1997) results (using conformal transformation method) for a small depth h/a=1.9 with a=0.15 m. The actual horizontal velocity at the gate is close to uniform over about 60% of the opening (x=0) in the experiments of Finnie and Jeppson (1991). Given the velocity

variation at the opening, one would expect that line sinks of varying strength need to be distributed on the opening. In this study, however, constant strength sinks (i.e., constant horizontal velocity) will be used to simplify the analysis. Despite this assumption, Figs 2.6-a and b show that the predicted horizontal and vertical velocity compares well with the measurements of Finnie and Jeppson (1991) and other numerical results. Finnie and Jeppson (1991) have reported that accurate measurement of the vertical velocity is difficult due to its large fluctuations at the gate.

Further comparisons are also made between the predictions of this study and the study of Rajaratnam and Humphries (1982) and Masliyah *et al.* (1985). In the following, the minimum velocity u_{min} which occurs at the water surface (see Fig 2.5), will be removed from the profiles of the horizontal velocity. Thus $u^*=u-u_{min}$ increases from zero at the surface to a maximum of $u^*_{max} = u_{max} - u_{min}$ at the bed. Following the study in jets, a vertical length scale b for the velocity profiles is also defined, where b is the vertical distance from the bed to the location where $u^*/u^*_{max}=0.5$ (see Fig 2.5). The predicted u^*/u^*_{max}-z/b relations at $x=a$ for h/a=4.1 and at $x=2a$ for h/a =8.5 are shown in Fig 2.6-c, and compare very well with the data of Rajaratnam and Humphries (1982) and Masliyah *et al.* (1985). Notice that the shape of the velocity profiles is also well predicted. These shapes will be further discussed later.

The above comparisons confirm that our potential flow solutions are able to predict the details of the flow upstream of a sluice gate. The characteristics of the flow will then be studied. The variations of u_{max} with x for different h/a ratios are plotted in Fig 2.7. For the flow of infinite depth, initially u_{max} decreases rapidly with x, and at $x=3a$, $u_{max}/U_o=0.2$. This result can be compared with the line sink solution for an infinitely deep flow, which is also shown in Fig 2.7. Notice that the line sink solution has uniform velocity across the quarter of a circle surface, which gives $V_r=u_{max}=2q/(\pi x)$, thus $u_{max}/U_o=2a/(\pi x)$. Obviously the line sink solution becomes singular at $x=0$. However, after x is about 3a, the line sink solution predicts the velocity very well as the velocity is becoming uniform across the quarter circle surface.

For flows of finite depth, the velocity profile eventually becomes uniform far from the gate $(u_\infty / U_o = a/h)$ and u_{max}/U_o becomes constant (Fig 2.7). At $x=1.5h$ the relative difference between u_{max} and u_∞ was found to be less than 2% for a wide range of h/a from 2 to ∞. Thus, the flow can be considered uniform across the depth beyond a distance of $1.5h$. For $h/a=2$, 4, 10, for example, the flow can be considered uniform when x is larger than $3a$, $6a$, and $15a$, respectively, as it is shown in Fig 2.7.

The development of velocity profiles away from the sluice gate will now be examined. The velocity profiles at different sections for infinitely deep flow $(h>>a)$ are plotted in Fig 2.8. At x=0 (the gate), the velocity is uniform. As x increases, a Mexican hat-shape velocity profile develops and smoothes toward z/b axis, see, for example, velocity curves at $x=0.2a$ and $x=a$. After $x=2a$, however, the difference in the velocity profiles becomes negligibly small, and these profiles approach asymptotically to that of a line sink flow. This is expected as it has been shown that the effect of the gate opening is limited to a distance of about $3a$ from the gate, and the flow approaches to that induced by a line sink (see Fig 2.8).

The velocity profile of a line sink flow can be obtained as follows: $u=m\,x/(x^2+z^2)$ for a line sink. Notice that $u_{max}=m/x$, which is obtained at z=0, and the flow velocity is zero at the free surface for infinitely deep flow. Let u/u_{max}=0.5, we obtain $b=z=x$, i.e., for a line sink flow, the thickness b increases linearly with the distance x. Substituting x with b, we obtain

$$u/u_{\max} = \left[1+(z/b)^2\right]^{-1} \qquad \text{..... (13)}$$

Thus the non-dimensionalized velocity profile for a line sink does not vary with location. A Gauss function (normal distribution) is also plotted in Fig 2.8 for comparison. Here the Gauss function takes the form of

$$u/u_{\max} = \exp\left[-0.963(z/b)^2\right] \qquad \text{..... (14)}$$

The coefficient 0.693 is obtained from the requirement that $u/u_{\max} = 0.5$ when $b=z$.

The effect of finite water depth on the velocity profiles at $x=a$, $0.5h$, and $2h$ is studied in Fig 2.9 for different h/a ratios (with the same specific discharge q and gate opening a). Notice

that at $x=2h$, the velocity profiles for all h/a ratios become a cosine function

$$u^* / u^*_{\max} = 0.5(1+\cos(0.5\pi z / b)) \qquad \text{..... (15)}$$

Recall that the flow can be approximated by that of a line sink flow when $x>3a$, which is satisfied at $x>2h$. Yih (1965) showed that the ψ function in a line sink flow of finite depth is composed of infinite numbers of sine functions. For large x, the contribution of higher order sine functions decreases exponentially, and only the first-order term becomes important. In fact when $x>1.5h$, the velocity profile can be very well approximated by the cosine function in Eq. (15). Notice that u^*/u^*_{max} increases from 0 at the free surface ($z=h$) to 1 at z=0. Eq. (15) also gives $u^*/u^*_{max}= 0.5$ at $b=z=h/2$.

The velocity profiles at $x=a$ shows less a similarity due to its proximity to the gate. For shallower flow, i.e., smaller h/a, the profiles are closer to Eq. (15) indicating that the flow transits to its final state (equal velocity distribution along the whole depth) much faster. For $h/a=2$, the velocity profile at $x=a$ is already very close to Eq. (15). It appears that the Gauss function [Eq. (14)] approximates reasonably well the velocities at $x=0.5h$ for a large range of h/a (from 4 to 20).

The variation of b with x is shown in Fig 2.10 for different h/a ratios. Notice that for a line sink in infinite deep flow, $b=x$, as is shown earlier. For sluice gate flow of infinite depth, the velocity profile is given by Eq. (8). Let u/u_{max}=0.5, and after some simplification, we obtain

$$b^2 - x^2 = a^2 \qquad \text{..... (16)}$$

Thus b increases from $b=a$ at the gate asymptotically to the line $b=x$ when x increases. This is expected as the flow approaches a line sink flow after x=3a. For flow of finite depth, the b value starts from $b=a$, but is restricted by the depth h. The growth of b with x is slower for smaller h/a (i.e., shallower flows). After a distance of x=1.5h, the flow approaches uniformity, and the b value approaches asymptotically to $b=h/2$ while the velocity profile becomes a cosine function [Eq. (15)] (see Fig 2.10). Notice that for a plane turbulent jet, the growth of b with x is about 0.1 (Rajaratnam, 1976), which is about 1 order of magnitude

smaller. It should be mentioned that for small h/a (=2 for example), the flows are likely to produce vortices which represents a limitation for the potential solution discussed in previous figures (Figs. 2.7 to 2.10).

2.4. Summary and Conclusions

Potential flow solutions have been used to study the velocity field upstream of an orifice and sluice gate by distributing point/line sinks of equal strength (uniform velocity U_0) over the opening of the orifice/sluice gate. For flow of a finite depth, image sinks are added to the solution to satisfy the free surface and bottom boundary conditions. Despite the fact that the actual velocity might not be uniform, our potential flow solutions are in excellent agreement with the results of earlier studies in orifice and sluice gate flows. Thus our solutions can be used to study the detailed flow field upstream of an orifice and sluice gate.

Studies of orifice flows showed that the near-field radial isovel V_r appears to have the shape of a semiellipsoid, while the far-field velocity has a hemispherical shape. For a circular orifice in infinite water depth, contours of the radial velocity near the orifice have approximately an elliptical shape with the short axis in the horizontal direction (x axis). However, for $x>1.5d$, the velocity can be very well modeled by a point sink solution, indicating that the effect of a finite-size orifice is limited within that distance. For orifices of different geometries, this distance typically does not exceed 2-3 times of $\sqrt{A}$, where A is the area of the opening.

For flow upstream of a sluice gate, it can be treated as a simple line sink flow at $x \geq 3a$. Thus the local effect of a gate opening is restricted to a distance of about 3a. For flows of infinite depth, the velocity profile approaches asymptotically that of a line sink flow when $x \geq 2a$. This is consistent with the fact that the flow approaches a line sink flow after $x=3a$. For flows of finite depth, the velocity profile eventually becomes uniform far from the gate. After $x=1.5h$; u_{max} is already within 2% of the depth averaged velocity, and the flow can be considered uniform across the depth. In addition, the normalized velocity profiles can be approximated by a simple cosine function. The Gauss function approximates reasonably well the normalized

velocity profiles at $x=0.5h$ for a large range *of* h/a. The vertical length scale b value starts from $h=a$ at the gate and approaches asymptotically $b=h/2$ after a distance of $x=1.5h$, where the velocity profile is described by a cosine function.

The results of this study can be used in several applications; mainly the reservoirs and the power plants. In fish habitat for example, knowing the 'high' velocity zone upstream an intake can help the designer to put a mesh or screen at the edge of that zone so that the fish will not be trapped in the high velocity and sucked towards the turbines.

Acknowledgment

The writers are grateful to Yanming Zhang for doing some preliminary work on the use of distributed line sinks for the sluice gate flow in a class project report some years ago.

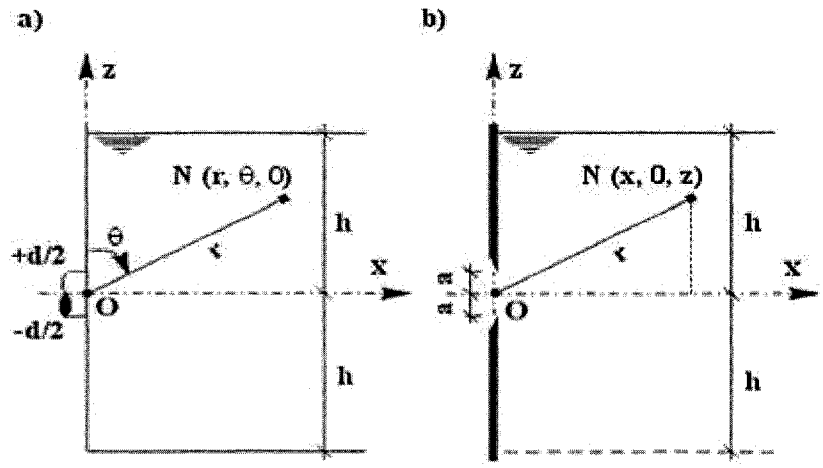

Fig 2. 1 Schematic diagram of withdrawal through: a) a circular orifice; b) a "double" sluice gate. Polar coordinates (ρ, θ, ω) are used for the orifice and Cartesian coordinates (x, y, z) are used for the sluice gate. N is a point of interest in the X-Z plane.

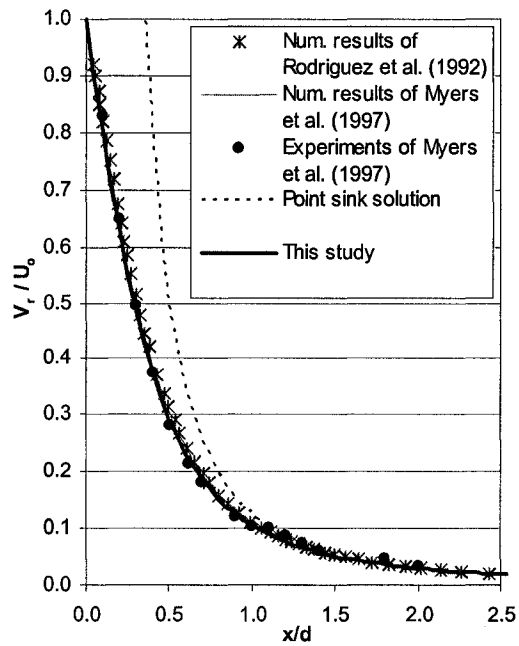

Fig 2. 2 Changes of velocity along x axis for a deep circular orifice (h>>d), U_o = uniform velocity at the orifice.

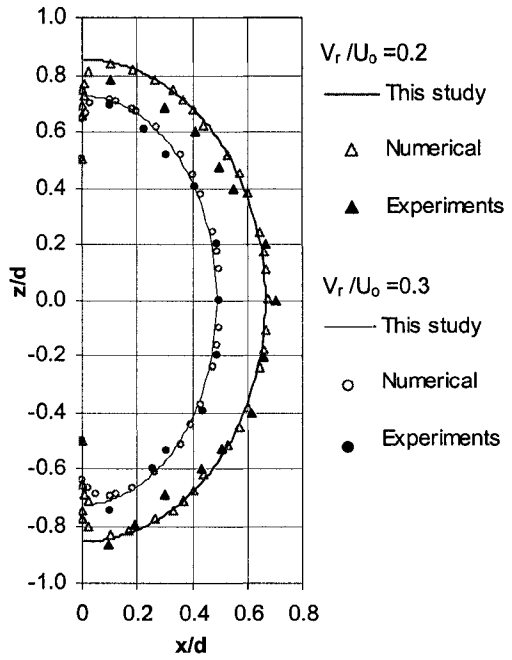

Fig 2. 3 Velocity contours for a deep circular orifice ($h>>d$). The numerical and experimental results are from Anayiotos *et al.* (1995).

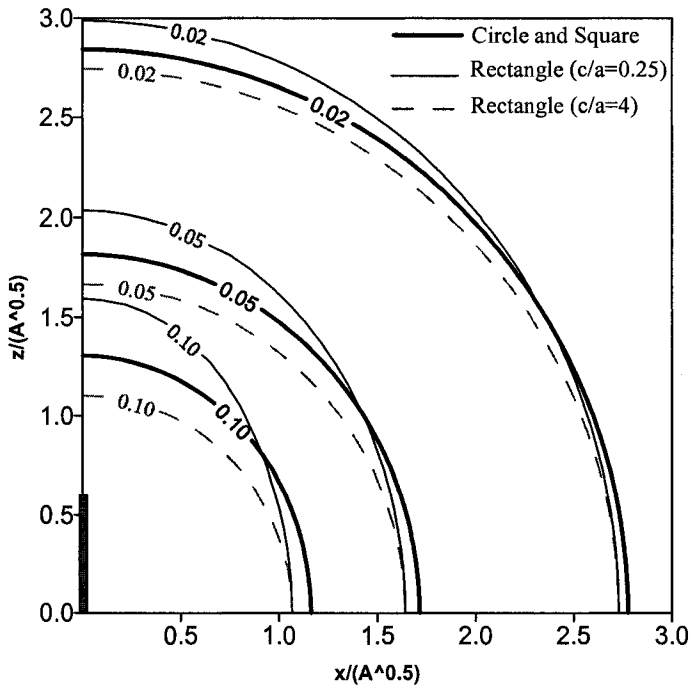

Fig 2. 4 Isovelocity V_r/U_o upstream of orifices of different shapes ($h >> d$).

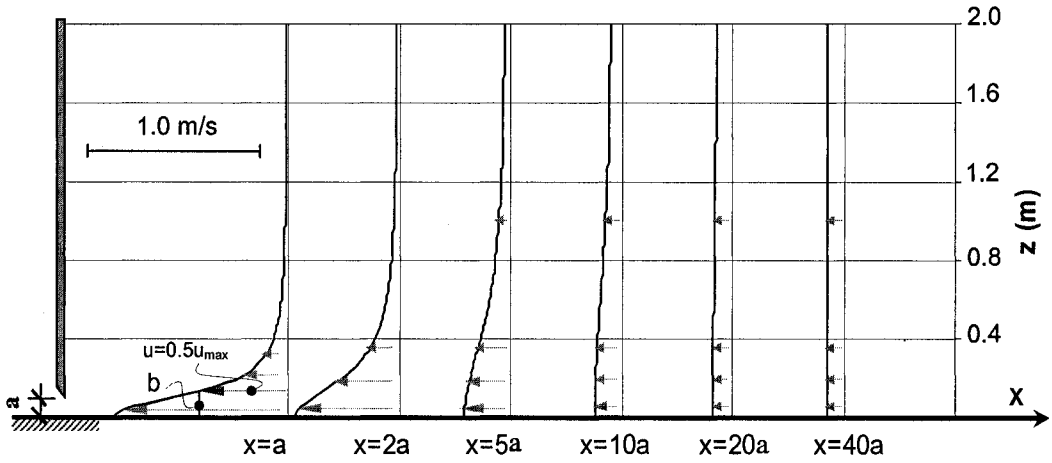

Fig 2. 5 Predicted horizontal velocity profiles upstream of a sluice gate. (h/a=20; a=0.05 m; U_o=1 m/s). Vertical length scale b is defined at u=0.5 u_{max}.

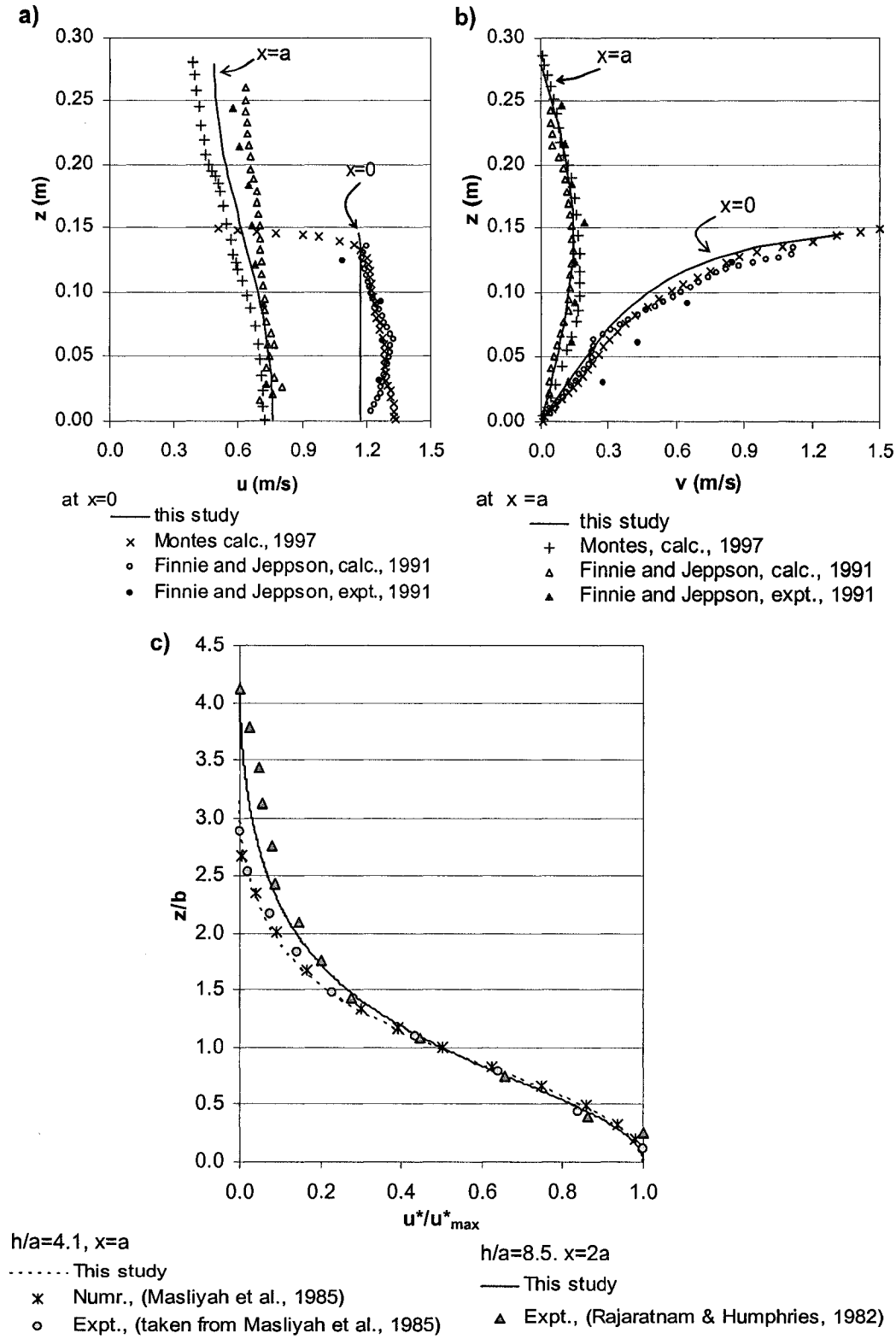

Fig 2. 6 Comparison of velocity predictions upstream of sluice gate: (a) and (b) horizontal and vertical profiles for *h/a*=1.9; and (c) normalized horizontal profiles for *h/a* =8.5 and *hla =4.1.*

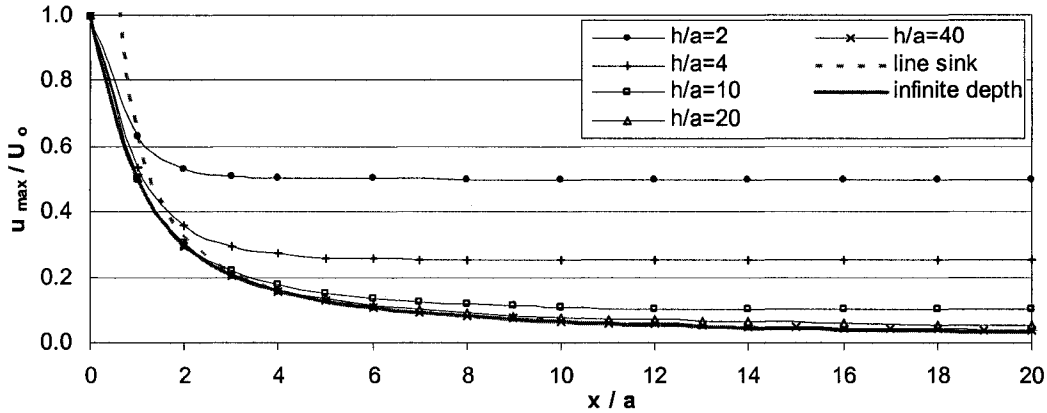

Fig 2. 7 Normalized maximum horizontal velocity upstream of a sluice gate for different water depths

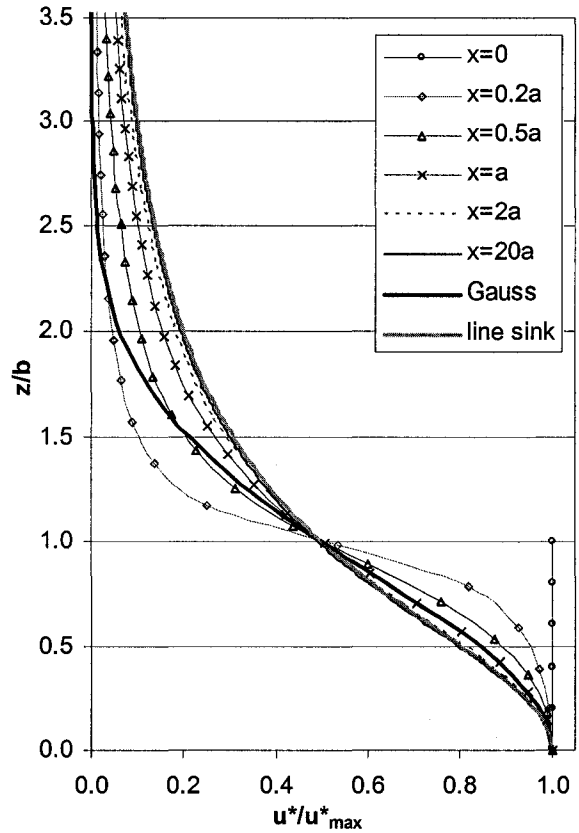

Fig 2. 8 Normalized horizontal velocity profiles for infinite depth ($h>>a$)

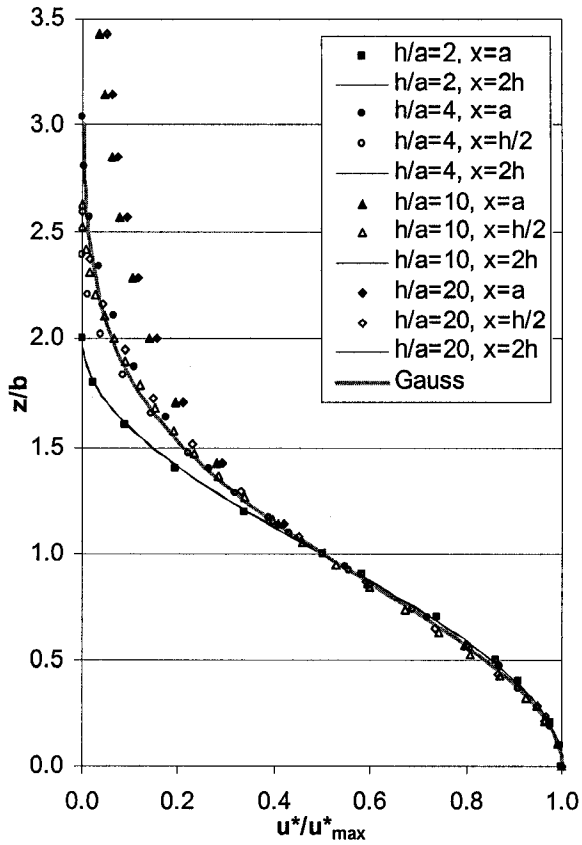

Fig 2. 9 Normalized horizontal velocity profiles for finite depths

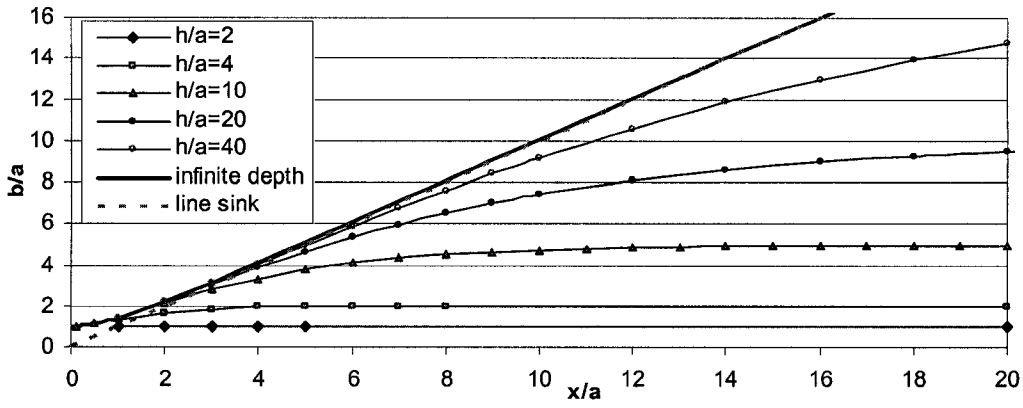

Fig 2. 10 Growth of vertical length scale *b* along *x* axis for different *h/a* ratios

References

Anayiotos, A.S., Perry, G.J., Myers, J.G., Green, D.W., Fan, P.H., and Nanda, N.C. 1995. "A numerical and experimental investigation of the flow acceleration region proximal to an orifice", *Ultrasound Med. Biol.*, 21(4), 501-516.

Chanson, M.H., Aoki, S., and Maruyama, M., 2002. "Unsteady two-dimensional orifice flow: a large size experimental investigation", *J. Hydraul. Res.*, 40(1), 63-71.

Finnie, J.I., and Jeppson, W., 1991. "Solving turbulent flows using finite elements", *J. Hydr. Engrg.*, 117(11), 1513-1530.

Hager, W.H., and Roth, A., 1999. "Underflow of standard sluice gate", *Experiments in Fluids*, 27, 339-350.

Masliyah, J.H., Nandakumar, K., Hemphill, F., and Fung, L., 1985. "Body-fitted coordinates for flow under sluice gates", *J. Hydr. Engrg.*, 111(6), 922-933.

Montes, J.S., 1997. "Irrotational flow and real fluid effects under planar sluice gates", *J. Hydr. Engrg.*, 123(3), 219-232.

Myers, J. G., Fox, J.F., Elmahdi, A.M., Perry, G.J., and Anayiotos, A.S., 1997. "Evaluation of the proximal flow field to circular and noncircular orifices of different aspect ratios", *J. Biochemical Engrg.*, 119, 349-356.

Rajaratnam, N., 1976. *Turbulent Jets*, Elsevier Publishing Co., Amsterdam, the Netherlands.

Rajaratnam, N., and Humphries, J.A., 1982. "Free flow upstream of vertical sluice gates", *J. Hydraul.. Res.*, 20(5), 427-437.

Rodriguez, L., Anconina, J., Flanshchskampf, F.A., Weyman, A.E., Levine, R.A., and Thomas, J.D., 1992. "Impact of finite orifice size on proximal flow convergence: implications for Doppler quantification of valvular regurgitation", *Circ. Res.*, 70, 923-930.

Yih, C., 1965. *Dynamics of Non-homogenous Fluids*, Macmillan.

Chapter 3

Flow Field in a Reservoir with a Wall-Jet Inlet and Orifice Outlet

3.1. Introduction

Jets have been studied extensively for several decades because of their wide engineering use. Among many examples are the sewage discharges into riverine (Raymundo and Preston, 1992), ocean dumping of sludge (Wood *et al.*, 1993), and thermal effluents from power stations (Harleman and Stolzenbach, 1972). However, they were usually studied on the assumption that the flow can be extended freely along the channel (unconfined). Hence, if this extension is blocked by any means, the mechanics of flow in this situation is not well explored. A particular example is a wall jet and an orifice used in a confined space as inlet and outlet, respectively. Such a flow condition is of interest for selective withdrawal in reservoirs (Vermeyen, 2000), in ventilations of confined spaces (Nielsen, 2000), and in smoke propagation in tunnels (Chen, 2000). In all these cases, understanding the flow behavior as well as the inter-effect of the inlet and outlet are important.

The development of a free jet in an unconfined ambient is generally characterized by two zones: the zone of flow establishment (ZFE) near the jet orifice, and the zone of established flow (ZEF) further away. The flow characteristics in these two zones have well been established in literature (see e.g. Albertson (1950)). In ZEF it was established that the mean longitudinal velocity profiles become self-similar at about $30a$ from the jet opening and they fit well to Gaussian distribution (see e.g. Rajaratnam (1976), Kotsovinos and List (1977), and List (1982)).

Wall jets released in deep ambient were also studied extensively (e.g. Goldschmidt and Eskinazi (1966), Rajaratnam (1976), Schlichting (1979)). However, less attention were given to the shallow environments. Ead and Rajaratnam (2002) however, have presented a

theoretical and laboratory study of plane turbulent wall jets discharged into large ambients at rest with shallow tailwater depth. They showed some deviations from the normal wall jet results; mainly, that the momentum flux of the forward flow in the wall jet decays appreciably with the distance from the nozzle due to the entrainment of the return flow. They also demonstrated that the jet discharge increases with distance at the same rate as that of the wall jet with large tailwater up to a certain section and then deviates from it.

In confined spaces where the jet can't spread freely, a re-circulation will be created. In vertical confined jets, for example, Iamandi and Rouse (1969) have shown experimentally that the flow structure of such jets consists of circulation cells (along the channel) of alternate rotations with a primary cell length scale of 2-2.5H (H is the total water depth). Jirka and Harleman (1979) have explained this primary cell length with respect to the momentum conserved after impingement. This argument was later supported by Andreopoulos *et al.* (1986) who carried out experiments on non-buoyant and buoyant jets in a relatively short channel L=2.2 m ($L/H \approx 3$) and have also noticed a secondary circulation cell. Fannelop *et al.* (1991), however, showed experimentally longer lengths of the primary cell (4-5H). They argued that the shorter length found by the previous studies was related to the relatively short-length channels used in those studies and thus to the effect of endwall. Kuang *et al.* (2001) have reported that the spreading of the confined vertical jets in finite depths is larger than that of a free jet and the decay of jet centerline velocity is faster than that of a free jet.

Flow upstream of orifices, on the other hand, has also been explored by many researchers (e.g. Rodriguez *et al.* (1992), Anayiotos *et al.* (1995), and Myers *et al.* (1997)). They generally concluded that potential flow theory can well predict the flow structure upstream an orifice. All their studies however, were for extended environments. Shammaa *et al.* (2005) however, have discussed the effect of finite depth, based on a theoretical approach, and demonstrated that the velocity of finite depth flow is slightly larger than that of the infinite depth flow up to about $3\sqrt{A}$ distance from the orifice (A is the orifice area).

A recent withdrawal control technique in reservoirs is investigated in this study. The technique is simply based on inserting a curtain (barrier) in the reservoir so that a smaller "inner" separate reservoir is created (Vermeyen, 2000) and the inflow towards this "inner" reservoir will be similar to a jet flow. Depending on the initial stratification in the reservoir, several flow cases will result using this technique. In this study, we are interested in the case of no-stratification. A set of Particle Image Velocimetry (PIV) experiments has been conducted to investigate the flow behavior in a confined shallow-depth rectangular space with a "wall jet" inlet and a "circular orifice" outlet. Steady discharge and four outlet levels were considered. Flow evolution, velocity vectors, and streamlines in the symmetric plane were studied. Velocity profiles in the jet and in the outlet areas were also investigated. 3-D flow was also explored. Instantaneous velocity and turbulence characteristics were also provided.

3.2. Experimental Design and Methodology

A set of experiments were conducted in a rectangular horizontal tank of 6.0m length x 0.5m width x 0.51 m height (see Fig 3.1). An outlet of 3/4 inch (1.9 cm) diameter was positioned at various depths on one end panel of the tank. The outlet was connected to a centrifugal pump which withdraws water at a set discharge (Q_o). The outflow is measured using a magnetic flowmeter. Another panel (1.2 cm thickness) was placed 1.5 m from the outlet leaving 2 cm opening "a" permitting a jet-like flow regime with a vena contracta depth ($b_o \approx 0.6a$=1.2 cm) at a distance $1a$=2cm from the outer edge of the panel (Rajaratnam and Subramanaya, 1967). The water level in the reservoir is controlled by a weir at the far end of the main reservoir where the overflow water returns to a small tank that used as a 'feeding tank'.

Four experiments (Exps. 1 to 4) were conducted with a different outlet level b= 30, 20, 10, and 2 cm, see Fig 3.1. In all experiments, the total water depth H=41.2 cm, the length of the inner reservoir L=150 cm ($L/H \approx 3.5$), and the discharge Q_o=600 cm3/s (36 l/min). For this Q_o, average velocity, Froude number ($F_o=(Q_o/Bb_o)/\sqrt{gb_o}$), and Reynolds number

(R_e=(Q_o/Bb_o)b_o/ν) at the vena contracta are U_o=10 cm/s, F_o=0.3, and R_e=1178, respectively. According to Pearce (1966) and Rajaratnam and Flint-Petersen (1989), for this R_e the turbulent wall jet will have only a small length of laminar region at the beginning.

In all experiments, both the tank and the feeding tank were first filled with fresh water. Tracer particles (silver-coated spherical glass particles with mean diameter of 15 μm and specific gravity of 1.65, Potters Industries) were added. Water was then pumped from the feeding tank to the main tank using a submersible pump. The water was then circulated (with a steady discharge Q_o) between the main and the feeding tanks so that to ensure complete mixing. The flow was then left about 2-3 minutes in order to avoid the initial effects of pump-start. A flow period of 3 minutes was then recorded.

Experimental measurements were made using PIV. A laser sheet was produced through a 5W argon-ion laser operating at 488 nm (Stabilite 2017, Spectra-Physics Lasers). A fibre optical cable (OZ Optics Ltd.) transmitted the light to a top-located lens that produced a thin laser sheet at the center plane of the channel where measurements were made.

Velocity measurements were taken separately with a field of view of about 80 cm: first, close to the curtain and second, close to the outlet side. A high resolution 16-bit JAI-Pulnix CCD camera (1392 x 1040 pixels) was used to capture the PIV images with sampling frequency 10 Hz.

The velocity fields were computed using an iterative multi-grid cross-correlation PIV algorithm (Scarano and Riethmuller, 1999). By 3 iterations, the final search and interrogation windows were 16 and 8 pixels, respectively, with a grid velocity measurement each 8 pixels. The average error in the instantaneous velocity measurements was estimated at 4.0%.

Velocity measurements, however, in a band of 2-2.5 cm close to both sides (curtain and outlet walls) and bed were not possible due to the high illumination reflection at edges and due to the high velocity under the curtain and at the outlet which exceeds the possible grapping by the softwares used. In addition, results close to the water surface (within 1 cm) were not reliable as well.

For Exp. 1 (b=30 cm), Rhodamine 6G dye was homogeneously mixed with the water and then, while the experiment was running, Rhodamine WT dye was added continuously about 30 cm upstream of the jet in order to visualize the flow evolution in the inner reservoir. Digital Sony Hi-8 video camera (30 Hz) was used to capture this evolution. Also, Rhodamine WT dye was used for Exp. 3 (b=10 cm) to visualize the 3-D flow close to the outlet. Further experimental details and error analysis are available in Appendix A.

3.3. Experiment Results and Analysis

Flow Observation

Time-sequence images of the flow advancement in Exp. 1 (b=30 cm) were presented in Fig 3.2 considering t=0 s when the dye first entered the reservoir. In the initial stage of the dye entering, frequent small eddies at the jet boundary could be observed in Fig 3.2-a. The dye-front was enlarging with distance at this stage and a change in its flow direction could also be observed in Fig 3.2-a. In the later stage, two dye-front branches were developed around the middle length: the first continued with main flow direction and the second returned up backward as could be seen in Fig 3.2-b at t=22 s. Flow departed from the bed in a later stage around one-third distance from the outlet as could be seen in Fig 3.2-c. At t=62 s, flow arrived at the outlet for the first time as could be seen in Fig 3.2-d. Major flow separation establishment in the upper half of the water could also be observed in Fig 3.2-d. At later stages, no significant changes could be observed except that two areas remained almost stagnant: upper right and lower left of the reservoir (see Fig 3.2-e at t=92 s).

Dye-front advancement with time for Exp. 1 was plotted in Fig 3.3 along with its velocity V (calculated approximately as $\Delta x'/\Delta t$) where x' is the distance from the curtain (barrier) measured from the recorded images. Fig 3.3 showed that the dye-front advanced on an approximately quadratic curve (proportional to t^2). Also, as expected, V has generally decreased with distance especially in the initial distance. The average velocity along the first

70 cm, however, was about 3.8 cm/s.

Further detailed observations were available in Figs 3.4 and 3.5 where time-average velocity vectors and streamlines at the center plane of the inner reservoir were plotted, respectively. For all experiments, Figs 3.4 and 3.5 showed general three main flow regimes (see those regimes in Fig 3.5 for the case b=10 cm): I) a jet zone with strong recirculation; II) a separation zone in front of the previous zone; III) an outlet zone with a special 3-D flow shape. The mean flow field in these three regimes will be explored in details in the following.

Mean Flow Field

Jet Zone (Zone I)

Owing to the shallowness of the reservoir, not all of the fluid that the jet needs to entrain could be supplied by the undisturbed ambient; rather the jet turned backward after a certain distance and a large part of its fluid was re-entrained forming a "circulation" as could be seen in Figs 3.4 and 3.5. The horizontal length of this recirculation in this zone was about L_c=100-115 cm (~2.5H) in all experiments (see for example L_c in Fig 3.4 for the case b=20 cm). It was interesting to notice that this length was similar in principle to that observed by Iamandi and Rouse (1969), Jirka and Harleman (1979) and Andreopoulos *et al.* (1986); however for vertical jets. Jirka and Harleman (1979) have explained this length with respect to the jet spreading s (where horizontal velocity $u \approx 0$) and the returned flow that should happen at a height $H/2$. If we adapt the same principle here, the recirculation length would be about $L_c=((H/2)/s+H/2)$. For a wall jet, s=0.2 (Rajaratnam, 1976) and thus $L_c \approx 3H$. Jet spreading, however, was plotted for all experiments in Fig 3.6 as well as that of the wall jet. Fig 3.6 showed that $s \approx 0.25$ for the cases b=2 and b=30 cm, $s \approx 0.27$ for b=10cm, and $s \approx 0.29$ for b=20 cm. For these slopes, assuming the jet will turn backward at about a height $H/2$, the calculated L_c would be about 92-105 cm (i.e. ~2.5H) which is the same observed in Figs 3.4 and 3.5. It should be mentioned however, following Fannelop et at. (1991), that the limited reservoir

length and thus the endwall effect might be the main reason of this 2.5H length.

Fig 3.6, however, showed that all jet slopes were larger than that of a classical wall jet which was probably due to the additional entrainment caused by the strong recirculation. Similar larger spreading observations were reported by Kuang *et al.* (2001) for vertical turbulent plane jets in water of finite depth and by Jirka and Harleman (1979) for a vertical plane buoyant jet in confined depths. Another noticeable result, however, was that the jet spreading was increasing when the outlet moved towards the middle of the reservoir while it decreased when it was close to the bed or relatively close to the surface (b=2 and b=30 cm). In fact, these changes were related to the type of flow created around the outlet as will be seen in zone III.

Typical horizontal velocity "u" profiles in the jet forward flow were plotted for Exp. 1 in Fig 3.7-a at four x' distances from the vena contracta: x'=50, 60, 70, and 76 cm which corresponded to x'/b_o= 41, 50, 58, and 63, respectively (as the distance between the vena contracta and the wall of the reservoir is about 0.8 cm, x' was simply considered to start from the wall itself (i.e. x'=150-x)). Profiles for x'<50 cm were not used due to the error expected in the PIV results at locations where the maximum velocity u_m are located (refer to experimental setup). On the other hand, profiles beyond x'=76 cm didn't show any trend as the flow was quickly climbing up. Fig 3.7-a showed that the maximum u (u_m) was decreased from about 4.0 into 3.0 cm/s between x'=50 and 76 cm. Also, the average velocities in the lower part of the profiles (say lower 5 cm) were generally in consistent with the jet-front velocity V found in Fig 3.3 previously (refer to Fig. 3.3).

To test for the similarity of velocity profiles, however, the maximum velocity u_m at any x'-section was chosen as the velocity scale, and the length scale b' is equal to z where u=0.5u_m and the results were plotted in Fig 3.7-b for all experiments. Similarity curve for plane wall jet has also been added to the figure. Fig 3.7-b showed similarity in the velocity distributions. However, the location of maximum u was clearly located further away from the bed beyond that of the classical wall jet.

Since the velocity profiles were similar, the decay of u_m/U_o along the distance from the jet opening x' in the jet forward flow was studied and plotted in Fig 3.8 for all experiments along with that of the classical wall jet ($u_m/U_o=3.5/\sqrt{(x'/b_o)}$) (Rajaratnam 1976). Fig 3. 8 showed that u_m was less than that of the wall jet for the whole experiments. This result was expected as the water shallowness caused more jet expansion and thus more flattened velocity profile (i.e. longer profiles) (and thus less u_m). However, the highest u_m values were for b=20 cm case while the lowest values were for b=30 cm case. This means that the recirculation was strongest when the withdrawal was close to the middle of the height.

Assuming 2-D flow (up to the middle of the reservoir), the jet's forward flow rate q per width was calculated by integrating the velocity distribution profiles. The average increment of q/q_o along the distance x' is shown in Fig 3.9. The relation of a classical wall jet: $q/q_o = 0.35\sqrt{(x'/b_o)}$ was used to fit the data of the four experiments by varying the numerical factor (0.35). Hence, for b=30, 20, 10, and 2 cm, the numerical factor was 0.35, 0.51, 0.42, and 0.37, respectively. As can be seen in Fig 3.9, all experiments have shown larger increment than that of a classical wall jet. However, in consistence with the results of Fig 3.6, the largest discharge increment was for b=20 cm while the lowest was for b=30 cm and b=2 cm whereas intermediate value was for b=10cm. At x'/b_o=50, for example, q/q_o was about 2.7, 3.0, 3.7, and 2.5 for b= 2, 10, 20, and 30 cm, respectively.

Having studied the forward flow rate q, the jet entrainment velocity v_e was then calculated by taking the derivative of q with respect to the distance ($v_e=dq/dx$). It is usual in studying wall jets to consider this velocity as a percentage of u_m at any x-section ($v_e=\alpha u_m$, where α is the entrainment factor). Thus, α related to each experiment was determined by dividing v_e by u_m. The variation of α with b/H was plotted in Fig 3.10. Fig 3.10 showed that α reached its maximum value 0.08 at b/H =0.49 whereas it decreased when b moved above or below the middle height of the reservoir. It was also noticeable that the entrainment factor reached about 1.6, and 1.4 times its value for a classical wall jet (α=0.05; Rajaratnam 1976) when the withdrawal was in the middle and in the quarter of the water depth, respectively.

A small triangular-shape stagnant zone in the upper right corner of the reservoir, on the other hand, could be noticed in the jet zone (see Figs 3.4 and 3.5; some error however made this zone not very clear for the case b=30 cm in Fig 3.5). This zone was created by the main recirculation through momentum transfer process.

Separation Zone (Zone II)

This zone existed beyond the recirculation area of the previous jet zone. The jet seemed to depart the bed around x=40-55 cm in all experiments while the center of this zone, except for the case (b=30 cm), was around L_p=40 cm from the outlet wall (see Figs 3.3 and 3.4). The reason of this flow separation is believed to be a result of the jet impingement on the outlet wall. This impingement causes the pressure to rise on the bed close to the wall which in turns affects backward and decelerate the jet which eventually detached from the bed at a certain distance. For b=30 cm, separation zone extended to reach the surface around L_p=25 cm. This shorter distance indicated that the jet boundary approached the water surface close to the outlet wall when b moved towards the surface (or, obviously, when L become longer; i.e. the downstream effect disappears), and thus the jet behavior will be as close as to a regular wall jet. A critical b, however, occurred between b=20 and b=30 cm where L_p started to decrease.

The trajectory of u_m in the separation zone in all experiments was plotted in Fig 3.11. Except for the case b=10 cm, Fig 3.11 showed that the trajectory of all other cases has followed a single quadratic curve which was shown in a thick solid line (see Fig 3.11). For b=10 cm, however, another quadratic curve was also fitted the data (shown in dashed line, see Fig 3.11). As these curves are close to each other, one could conclude that some similarity behavior in the separation zone existed regardless of the outlet level. These curves, on the other hand, were parallel to the streamlines in the separation zone as shown for example on the case b=20 cm in Figs 3.4 and 3.5 (i.e. they were the same trajectories of the maximum plane velocity).

Outlet Zone (Zone III)

Another interesting phenomenon observed in this study was the special 3-D shape flow in the vicinity of the outlet where the flow didn't go directly towards the outlet; instead, it curved almost in a circle before it went through the outlet. This "globe" flow could be seen clearly in Figs 3.5-b, c, and d. The globe flow, however, was less apparent in Fig 3.5-a. The bottom part of the globe flow, however, indicated that the flow was supplied from out of plane (3-D flow).

To investigate this 3-D flow, a dye was injected at several locations close to the outlet. Fig 3.12-a, for example, showed a sequence of images of the dye injected a little below the upper corner of the reservoir for the case b=10 cm. Arrows were added to the images to show the main direction of the flow observed in the recorded film (see Fig 3.12-a). A schematic representation of this flow was plotted in Fig 3.12-b. Figs 3.12-a and b showed that the main flow curved down away from the corner towards the middle symmetric plane where, before reaching the symmetric plane, it curved upward further away from the outlet wall following a globe-like path where it then curved downstream towards the outlet (see Figs 3.12-a and b).

The reason of this flow behavior could be related to the momentum transfer at the boundary of the recirculation in the jet zone which causes an opposite "weaker" circulation cell downstream the primary one presenting the other end of the separation zone (see Fig 3.5). However, as this second circulation are affected by a 'presumably' 2-D flow from the jet side and a 3-D flow close to the outlet, the resultant circulation will thus have a 3-D "globe" shape (widens away from the outlet). Fig 3.5 showed, however, that the globe size has varied with b. For b=2, 10, and 20 cm, the vertical globe distance was about 10, 23, and 25 cm, respectively; while its horizontal distance was about 30-35 cm ($\approx$15-18d) for the same b cases. Thus when the 'space' above and below the outlet was available, the vertical dimension of the globe was enlarged; whereas when it was only available above the outlet (like the case b=2cm), the vertical dimension decreased (see Figs 3.5-b, c, and d). Another important effect on the globe dimensions, however, appears to be the distance between the main velocity that cause the circulation and the outlet (i.e. approximately: the length of the perpendicular line drawn from

the outlet on the trajectory of the maximum velocity found before in zone II). Since this line was very short in the case of b=30 cm, the globe flow was weakly noticed in this experiment (see Fig 3.5-a). It is noticeable on the other hand, that the larger the dimensions of the globe found, the larger the jet slope found in the recirculation zone and vice versa. In other words, the flow adjusts itself to compromise the required recirculation in zone I and the required 'globe' around the outlet.

In the outlet close-vicinity, potential u profiles at several x-sections adopted from Shammaa *et al.* (2005) were compared to the current experimental u profiles in Fig 3.13. Three x-sections were presented in the figure: x=6, 13, and 20 cm which were about 3, 6.5, and 10d distances from the outlet, respectively. For all experiments, Fig 3.13 showed that very close to the orifice (at x=6cm), potential theory modeled the major part of the flow, however, with less fitting the data as b decreased. Moreover, u_m at this section was very close to b level (within 1.5 cm from the center of the outlet). Due to the bottom "reverse" flow (globe-flow), however, velocity in the other two x-sections was significantly mismatched the theory. Since this reversed flow is from both sides of the reservoir (refer to Fig 3.12-a), the upper forward flow in the plane of symmetry was significantly higher than the potential one as could be seen in Fig 3.13 (i.e. this increment is due to continuity conservation at each x-section). Fig 3.13 also showed that u profiles did not change significantly from x=6.5d to x=10d. In addition, studying u profiles for x<6.5d (not shown) has revealed that the profiles' shapes started to change significantly around x=6d.

Experimental to theoretical u_m ratio "β" showed in Fig 3.13 at x= 3d was about 1.05, 0.96, 0.85, and 0.86 for b= 30, 20, 10, and 2 cm, respectively. Variation of β along x (up to x=6d) where plotted in Fig 3.14 for all experiments. For b=10 cm, however, only 2 points data were used in the figure as u_m for the other distances was far away from the outlet level. For each b case, Fig 3.14 showed a clear linear increment of β with x. The increment of β was about 0.14, 0.24, 0.12, and 0.08 for b=30, 20, 10, and 2 cm, respectively, indicating that the highest increment was for the case b=20 cm.

3-D Flow Investigation

In order to further investigate on the 3-D flow structure, extra experimental runs were done at two vertical *Y-Z* planes (x=10 and x=20 cm) and at two horizontal *X-Y* planes (z=30 and z=15 cm) for the case of Exp. 1 (b=30 cm) and the results (time-average velocity vectors) were plotted in Figs 3.15-a, b, c, and d, respectively. Due to some experimental difficulties, however, bands close to walls were in lack of measurements, especially in Figs 3.15-c and d were measurements were only available up to about x=130cm. Fig 3.15-a showed that the flow was descending at the sides and climbing in the middle creating two opposite circles with maximum upward velocity close to the symmetric plane. The deviation of the vectors from being symmetrical was probably due to short period of measurements (3 min). In the core of each circle, however, it could be said that the flow is almost perpendicular to the section; which explained the general upstream path of the dye observed in Fig 3.12 previously for the case b=10cm. The two circles were expected to vanish with x as could be seen in Fig 3.15-b at x=20 cm where most of the flow was upward. This vanishing, however, was expected to take longer x-distance for other b cases as was seen in Fig 3.12 for the case b=10 cm (say up to about the middle of zone II, i.e. x=30-50 cm).

Fig 3.15-c, on the other hand, showed a general agreement in zone I with Fig 3.4-a where a reasonable 2-D flow could be seen up to about the middle of the reservoir length. Horizontal velocity u didn't change significantly in this part and its average value was about 2 cm/s. Less 2-D appearance, however, could be seen afterwards in zone II (from x=70 to x=30 cm) and somehow 'potential' flow could be finally noticed in zone III (see Fig 3.15-c).

Fig 3.15-d showed some different behavior from that in Fig 3.3-a. The descending circulated flow between x=100 and x=130 as well as the forward jet flow between x=100 an x=70 cm were not symmetric. The reason seemed to be related to the intense small eddies generation watched in this area in Fig 3.2 before. These eddies are not necessarily 2-D and thus when they block the main 2-D flow (forward and backward ones), they tend to scatter its original 2-D flow. The main jet flow after the middle of the reservoir (x<70 cm), on the other

hand, showed a deviation towards one side wall and a horizontal eddy seemed to be generated. The reason of this eddy was not clear. However, the effect of the small eddies observed in the previous area (in the jet zone) might have extended beyond the middle length. If that's true, an averaging of longer recording period might cancel out this effect. Another possible reason for this horizontal eddy might be related to the possible small error in the physical dimensions of the experiments (like a non-rectangular jet opening or a bend in a sidewall, etc). Low velocities upstream flow, on the other hand, could be observed in zone III at this level (see Fig 3.15-d close to the outlet).

Velocity in the closed-vicinity of the outlet was also studied in the plane of the outlet level. Radial velocity (v_r) contour at plane z=30 cm for the case b=30 cm were plotted in Fig 3.16. Data beyond x=12 cm ($x \approx 6d$) was not plotted as it didn't show any pattern. For clarity, only v_r =1, 1.5, 2, and 2.72 cm/s were plotted in Fig 3.15. Potential solution reported in Shammaa *et al.* (2005) for finite water depths was added into Fig 3.16-a for the comparison. At x=6 cm ($3d$), Fig 3.16-a showed a good agreement between data and theory. However, beyond x=6 cm, v_r values were faster than the potential ones close to the middle width and gradually, as approaching the side walls, they became slower. This result was in consistent with the velocity vectors found previously in Fig 3.15-a.

Experimental data of the radial velocity v_r were able to be fitted by ellipses with their long axes along x-axis as shown in Fig 3.16-b. Short-to-long axes ratio of these ellipses was about 0.85 except at x=6 cm where it was about 0.9. This interesting result recalls the elliptical shape of the radial velocity near the orifice (x<1.5d) reported experimentally by Anayiotos *et al.* (1995) and theoretically by Shammaa *et al.* (2005), however with the short axis along the x-axis.

Instantaneous Velocities and Turbulence Characteristics

Instantaneous velocities were mainly studied in the jet zone. Typical instantaneous u and v in the forward jet direction was plotted in Figs 3.17-a and b at (x=110 cm, z=6 cm). Time

average values were drawn in dash-dot lines. Figs 3.17-a and b showed large velocity changes. While the time average u was about 4.2 cm/s, for example, the positive and negative fluctuations (above and below u average) have reached about 4.6 and 4 cm/s, respectively (see Fig 3.17-a) (i.e. the total fluctuation has reached double of u average). Another noticeable remark was in Fig 3.17-b where v had large positive and negative values (upward and downward directions) that reached about 3 cm/s. Its time average value, however, was close to zero ($\approx$0.4 cm/s) (notice that this point was relatively close to the location of u_{max} at that x-section).

Spectra of u and v were also studied at several grid points in the recirculation zone using Fast Fourier Transform (FFT). A typical u spectra of at z=8.3 cm at several equal-spaced points between x=90 and 120 cm were plotted in Fig 3.17-c. While Fig 3.17-c showed a dominant frequency and time period of (f=0.077Hz; T=1/f=13 s), no specific frequency was detected in other areas. In fact, Fig 3.17-c represented the u spectra in the region relatively close to the recirculation core and close to the jet boundary. Thus, the time period found might be related to the eddies existed at the jet boundary within the recirculation zone (refer to Fig 3.2-a). Another imbedded factor might be related to the turbulence structure itself.

Turbulence structure was studied for all experiments in the whole vertical plane of symmetry. Contours of streamwise turbulent intensities $\sqrt{\overline{u'^2}}/U_o$, vertical turbulence intensities $\sqrt{\overline{w'^2}}/U_o$, and Reynolds shear stress $-\overline{u'w'}/U_o^2$ for the case (b=30 cm) were plotted in Figs 3.18-a, b, and c, respectively. For easier visualization, jet slope ($u\approx 0$) was added in dash line to the figure. Fig 3.18 showed that the maximum values of the three turbulence intensities were located in the streamwise jet path area and were growing away from the bed with distance increasing (see Fig 3.18). Similar phenomena were also found for the other b cases. Another $\sqrt{\overline{u'^2}}/U_o$ intensity concentration however, was found in the lower part of the separation zone (between x=30-40 cm) (see Fig 3.18-a). This was reasonable as the mean flow has separated before this location upward (low u components). Fig 3.18, on the

other hand, pointed clearly to the stagnation area in the upper right corner where the three turbulence intensities were very low. Higher intensity values could also be seen around the outlet as expected.

General comparison to similar studies on turbulence intensities in jets showed that the intensities found in Fig 3.18 were in the same range reported in literature (see e.g., Nasr and Lai, 1998; Kuang *et al.*, 2001; Giger *et al.* 1991, and Fitzgerald and Garimella, 1998). The maximum values for $\sqrt{\overline{u'^2}}/U_o$ reported in those studies, for examples, were about 0.2-0.3 whereas they found here around 0.3. However, the turbulence might be a bit higher close to the jet where we didn't have data in this study. Also, the maximum $\sqrt{\overline{w'^2}}/U_o$ and $-\overline{u'w'}/U_o^2$ were about 0.2 and 0.012, respectively. Similar maximum turbulence intensities were found for the other b cases, however with a relatively higher $\sqrt{\overline{u'^2}}/U_o$ value in the middle of the reservoir for the case b=2 cm where it was about 0.4 (not shown).

Normalized $\sqrt{\overline{u'^2}}$ and $\sqrt{\overline{w'^2}}$ by their maximum values at three locations along the jet path (x/b_o=50, 58, and 63) for the case (b=30 cm) were plotted in Figs 3.19-a and b, respectively. Profiles of $\sqrt{\overline{u'^2}}$ were found to be self-similar with maximum value around z/b_o=5 where it decreased afterwards as z increased as could be seen in Fig 3.19-a. The trend of $\sqrt{\overline{w'^2}}$, on the other hand, seemed to swing around z/b_o=9 with no specific location for its maximum value as could be seen in Fig 3.19-b.

3.4. Summary and Conclusions

Flow in a confined shallow-depth rectangular reservoir with a wall jet inlet and a circular outlet has been investigated in this study by means of a set of PIV experiments. Steady flow discharges and four outlet levels (b) were used. The results showed three general flow regimes: jet zone with strong recirculation, outlet zone with a globe-like flow shape, and separation zone between the previous two zones.

A strong recirculation was found in the jet zone with approximate length 2.5*H*. The shallow water depth as well as the relatively short reservoir length has caused this circulation. This strong recirculation caused the jet to spread larger than the spreading of the classical wall jet. The highest spreading rate, however, was corresponding to the case $b=H/2$. The decay of u_m/U_o along the jet was lower than that of the classical wall jet as well. Jet entrainment was also found to be larger than that of a wall jet and that it reached about 1.6 times the latter's entrainment when $b=H/2$.

In the separation zone, flow was found to detach the bed close to a third reservoir length from the outlet wall. Pressure increment due to the jet impingement on the outlet wall was believed to cause this flow detachment. The flow was then continued in a 3-D flow shape close to the outlet where the flow was rounded spatially around a 'globe' before it went through the outlet. The momentum transfer process at the boundary of the recirculation zone were suggested to be the reasons of this flow phenomenon. The dimensions of the 'globe' however were increased by b and by the perpendicular distance between the main velocity causing the circulation and the outlet.

Potential theory, on the other hand, seemed to model the experimental data up to about $x=3d$ from the outlet (d is the outlet diameter). However, due to the bottom reverse flow (globe-flow), data beyond $x=3d$ was significantly mismatched the theory.

Flow in the third dimension was also explored. Radial velocity v_r contours upstream the outlet, on the other hand, in the plane $z=b$ were found to draw ellipses with their long axes along x-axis.

Instantaneous u and v have shown large changes along the jet flow. Spectral analysis didn't detect any dominant frequency except along the forward jet flow. Turbulence intensities were also investigated and profiles of jet's $\sqrt{\overline{u'^2}}$ were found to be self-similar.

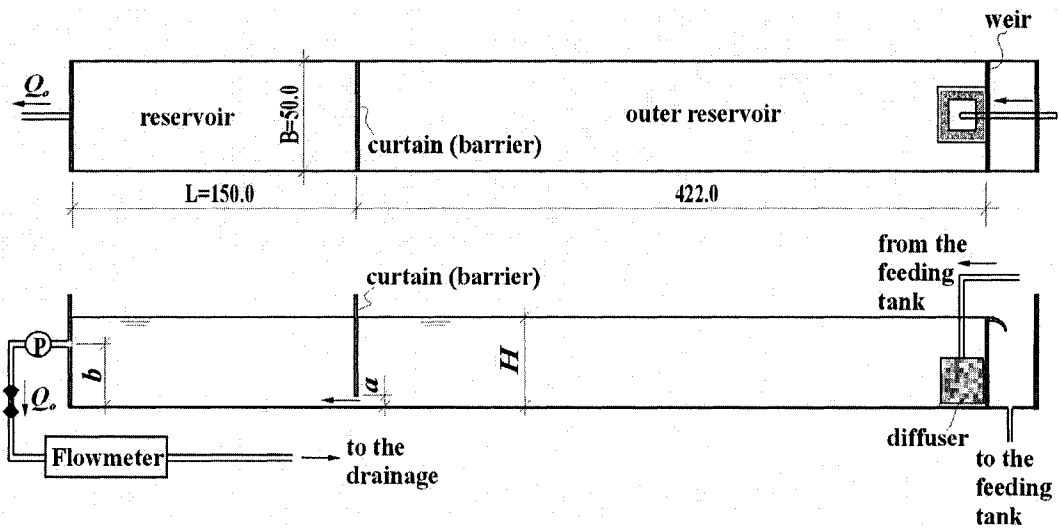

Fig 3. 1 Schematic of Experimental setup (Dimensions are in centimeters). (not to scale).

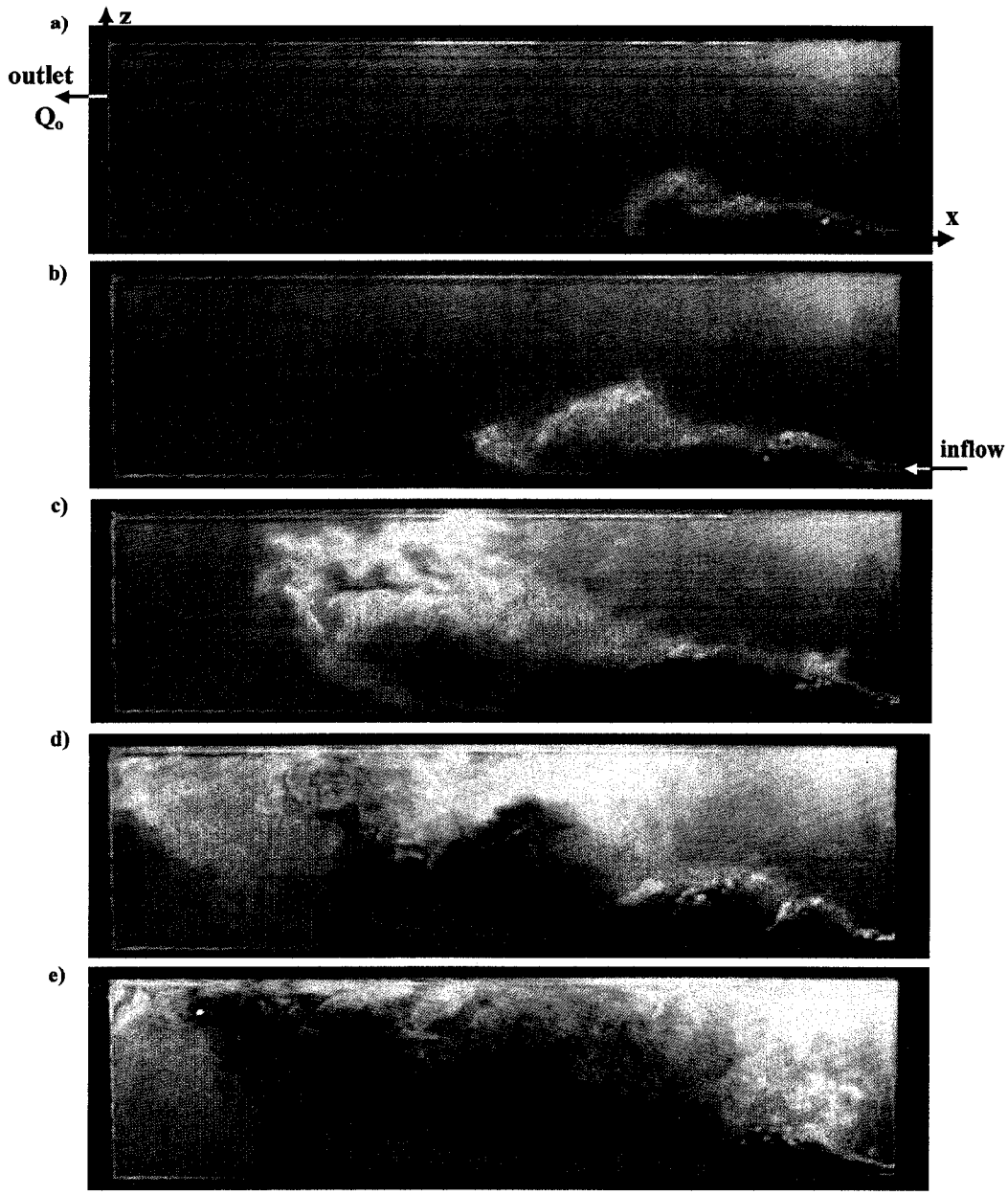

Fig 3. 2 Flow evolution in Exp. 1 (b=30 cm): a) initial stage at t=13 s from the time of dye entering; b) two dye-front branches developed around the middle length (t=22 s); c) dye separated from the bed around one-third distance from the outlet (t=41 s); d) flow arrived the outlet for the first time at t=62 s and major flow separation established; e) late stage (t=92 s)

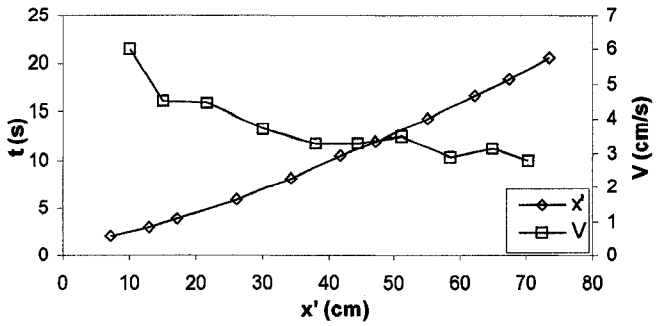

Fig 3. 3 Changes of dye-front advancement with time and its velocity *V*.

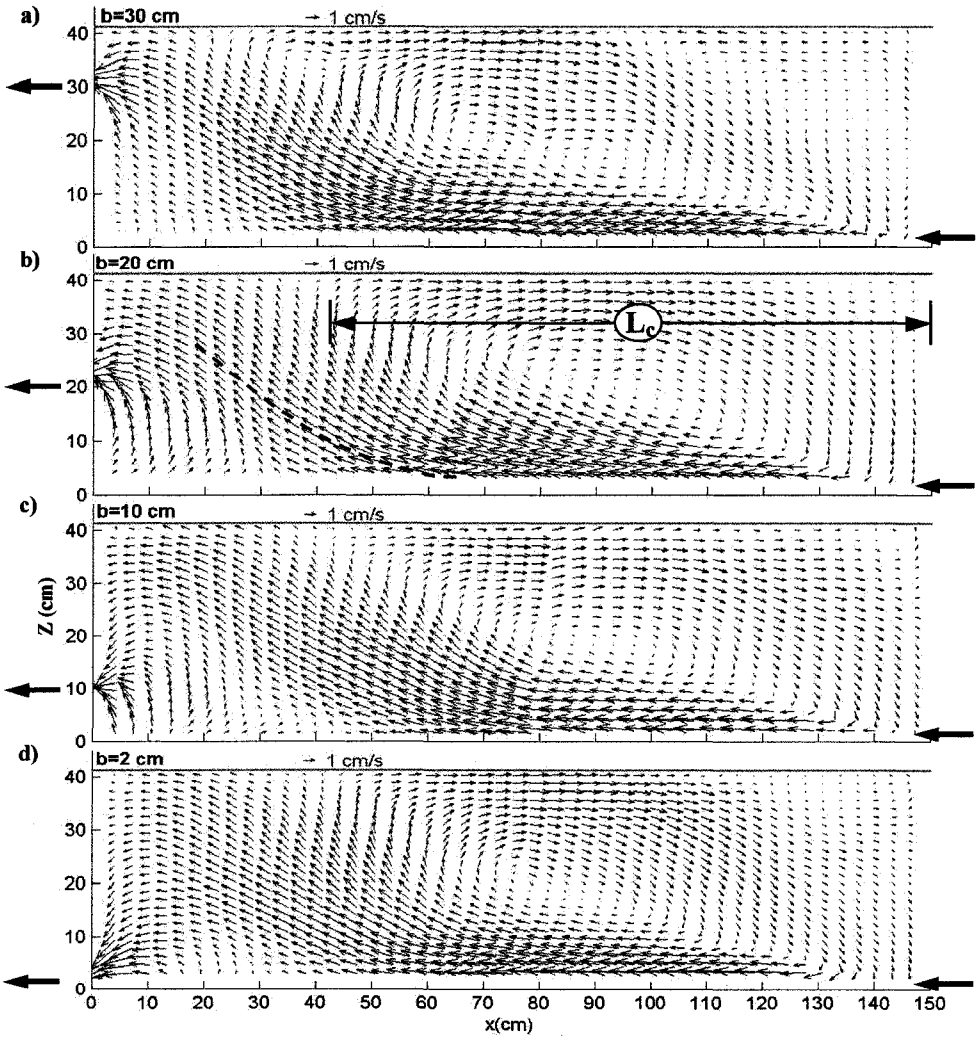

Fig 3. 4 Velocity vectors for different withdrawal height *b*: a) *b*=30 cm, b) *b*=20 cm, c) *b*=10 cm, and d) *b*=2 cm. The dash line showed the trajectory of u_{max} for the case *b*=20 cm. Thick arrows indicate the locations of the inflow and outflow.

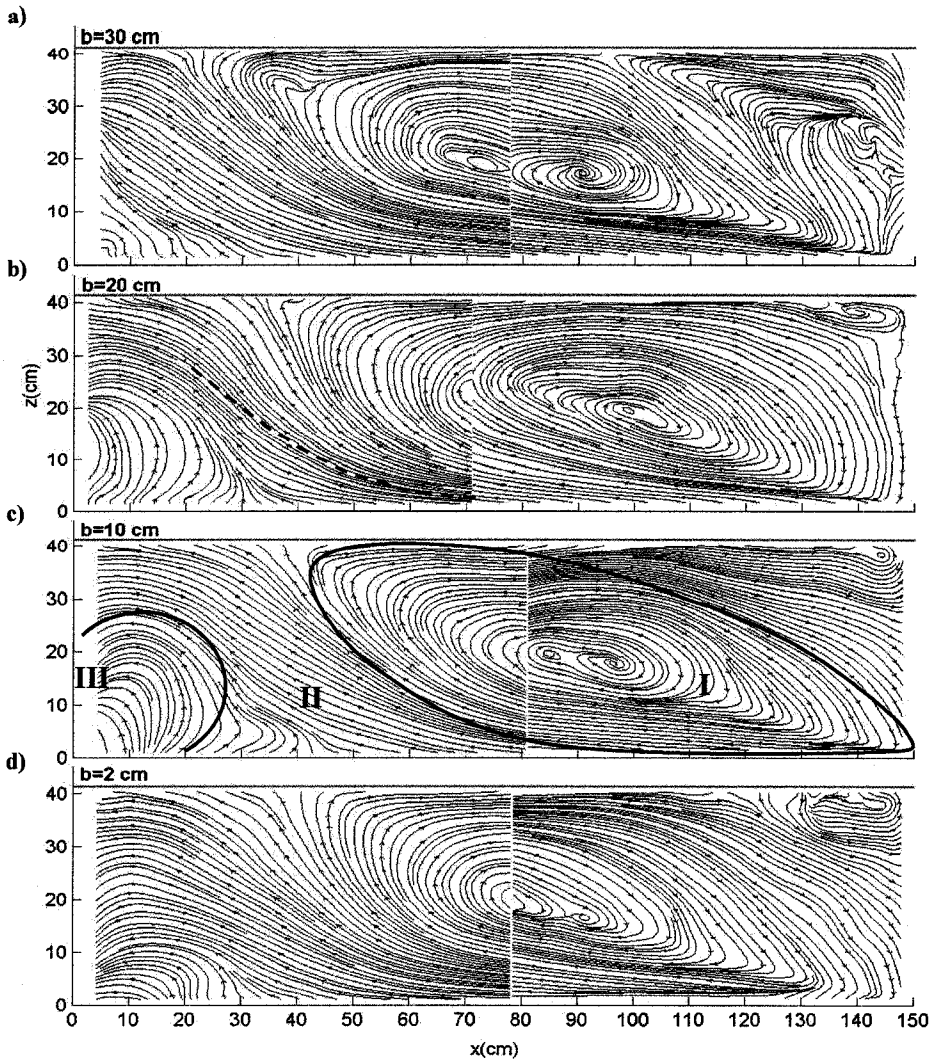

Fig 3. 5 Streamlines for different withdrawal height b: a) b=30 cm, b) b=20 cm, c) b=10 cm, and d) b=2 cm. Four main flow regimes were shown on the case b=10 cm. The dash line showed the trajectory of u_{max} in zone II for the case b=20 cm.

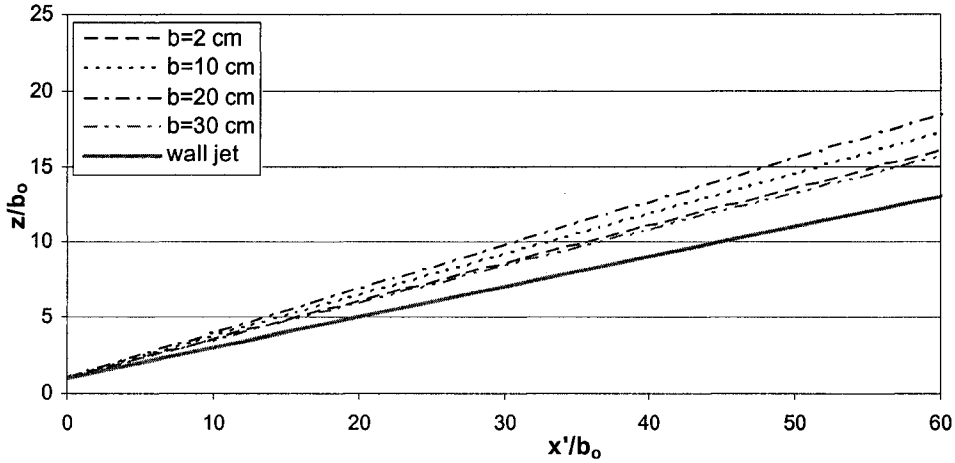

Fig 3. 6 Jet spreading for different withdrawal level "*b*"

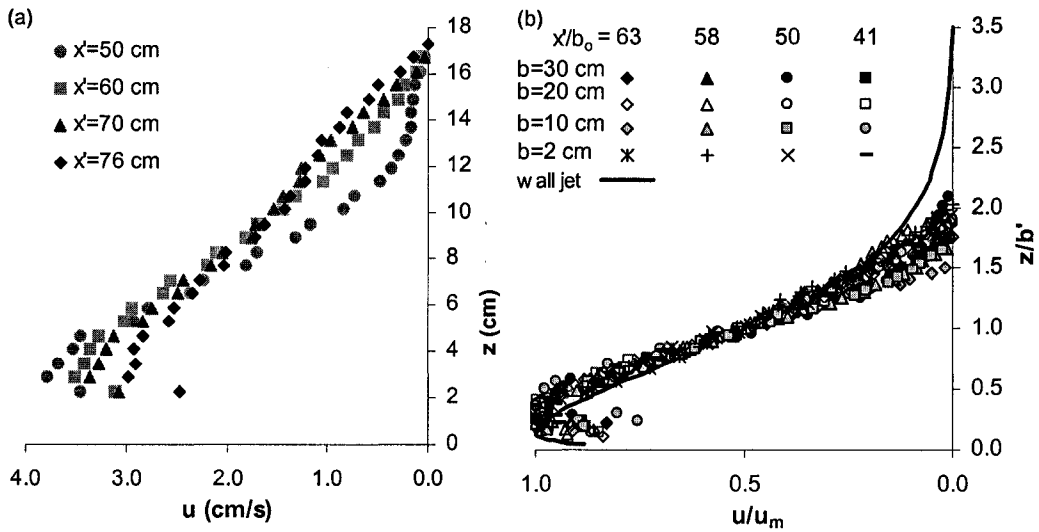

Fig 3. 7 Velocity distribution in the jet: (a) Typical velocity profiles at several *x*-sections in Exp. 1; (b) similarity profiles for all experiments.

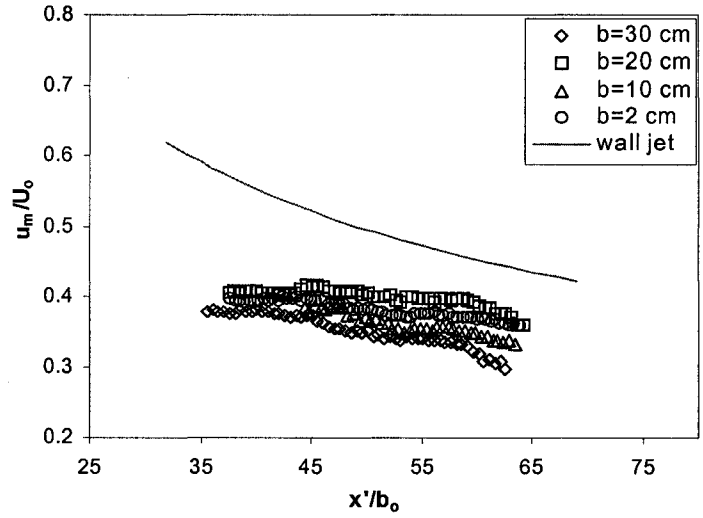

Fig 3. 8 Decay of u_m with distance.

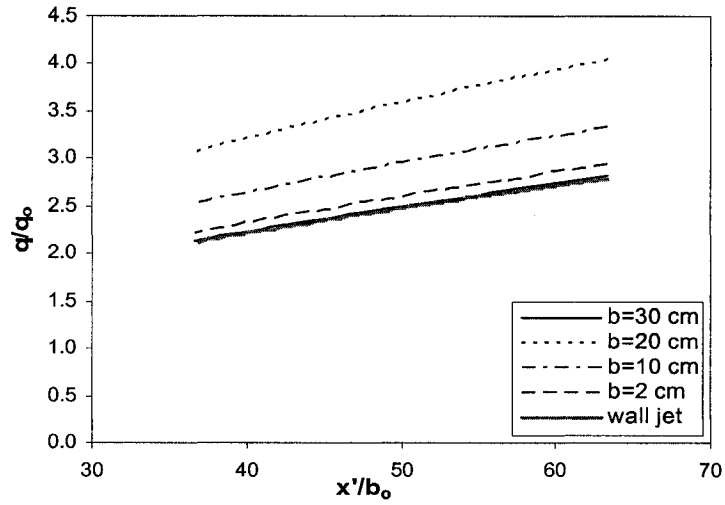

Fig 3. 9 Variation of average jet discharge with distance.

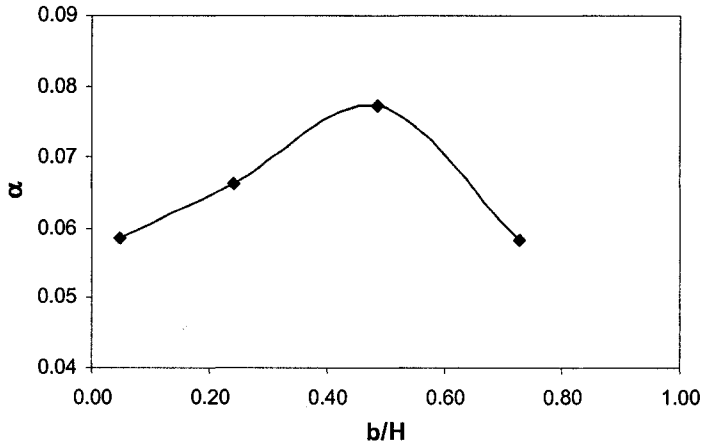

Fig 3. 10 Variation of jet entrainment coefficient with withdrawal level.

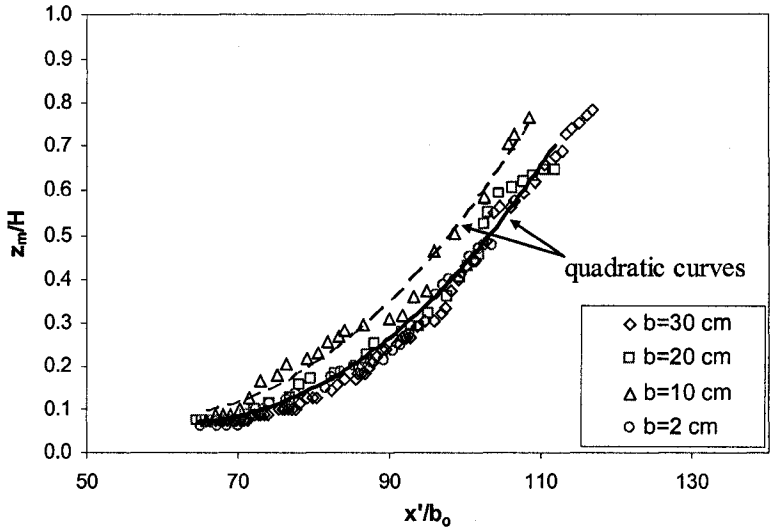

Fig 3. 11 Trajectory of u_{max} in the separation zone

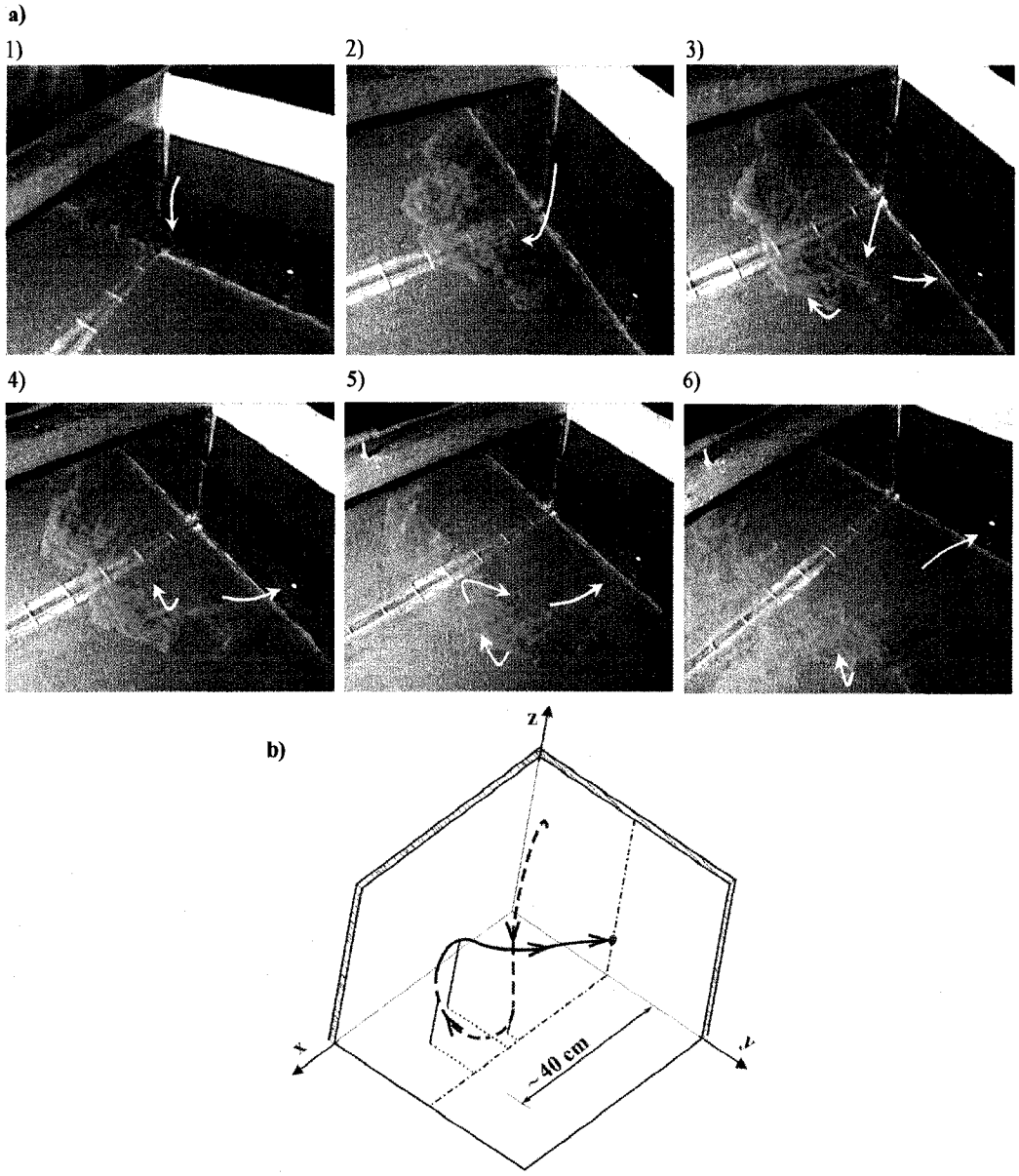

Fig 3. 12 A globe-like flow for the case b=10cm: a) A series of images of the dye injected in the upper corner of the reservoir (arrows show the direction of the flow; Note: image reflections of the flow at the wall should be disregarded), b) A schematic representation of this flow (dashed curves show the upstream flow, solid curves show the downstream flow, solid lines parallel to z-axis show the relative distance from the bed, and dotted lines parallel to y-axis show the relative distance from the symmetric plane).

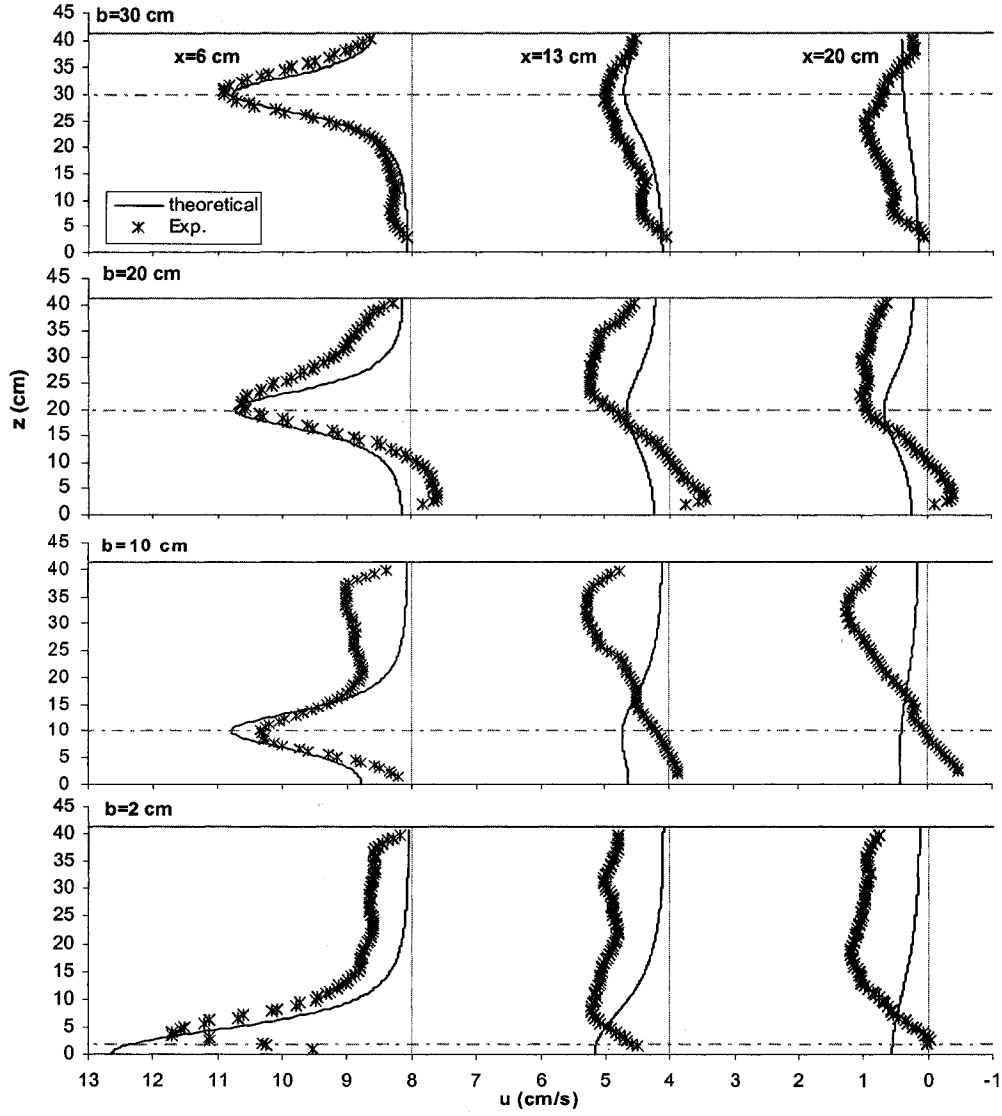

Fig 3. 13 Comparison of experimental to theoretical u upstream a circular outlet at different x-sections.

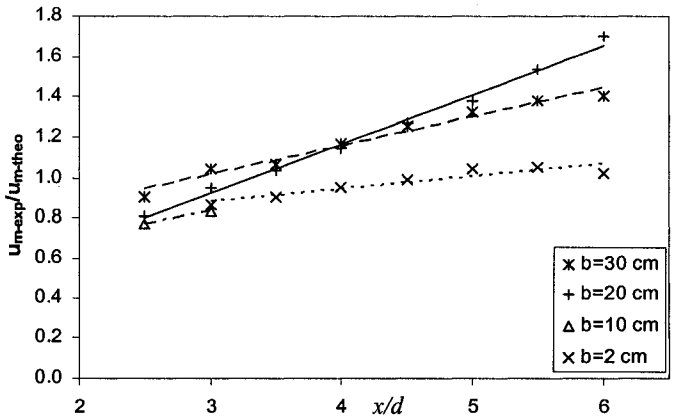

Fig 3. 14 Variation of axial $u_{m\text{-}exp}/u_{m\text{-}theo}$ upstream the outlet with x/d for different withdrawal height b.

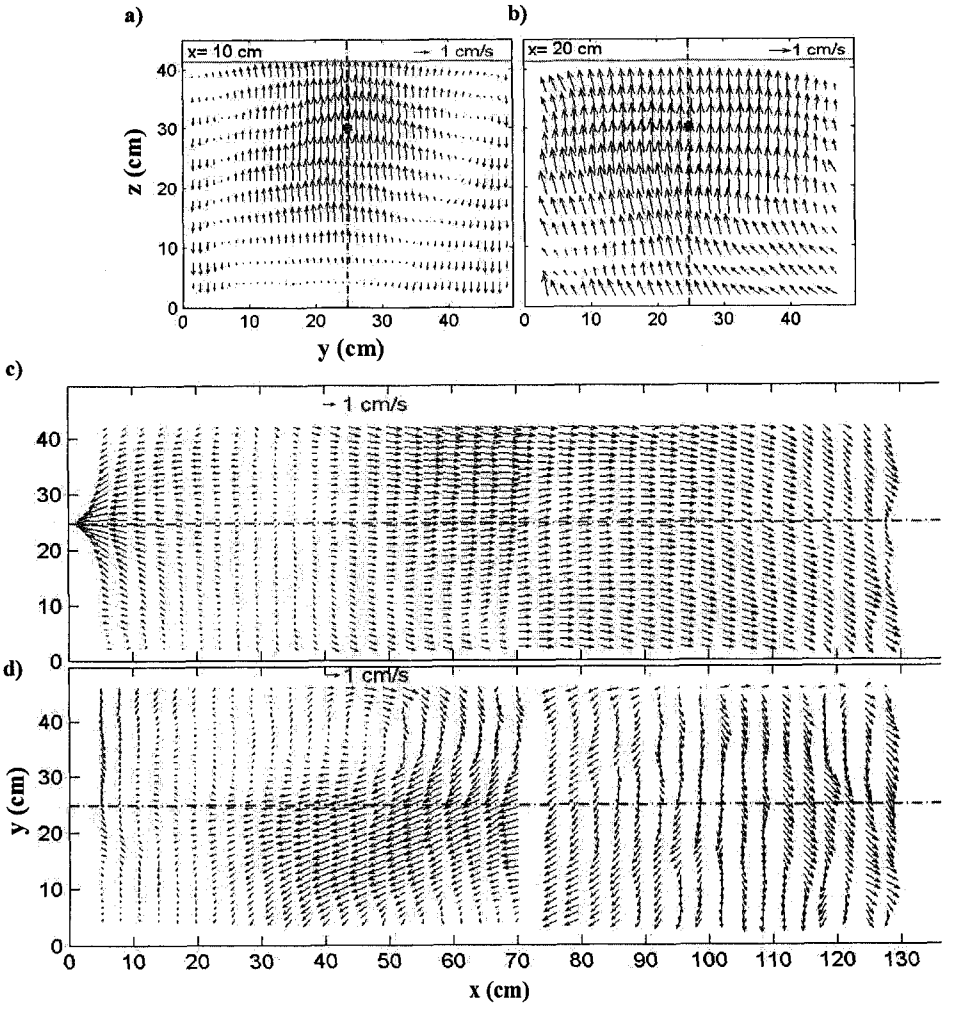

Fig 3. 15 Velocity vectors for the case b=30 cm: a and b) in y-z plane at x=10 and x=20 cm, respectively (outlet was drawn in solid circle; looking downstream); b and c) in x-y plane at z=30 and z=15 cm, respectively.

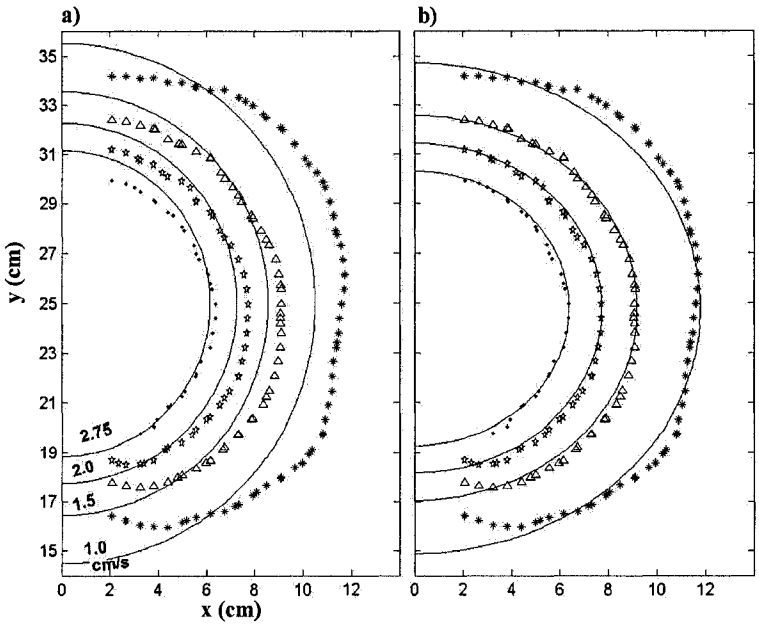

Fig 3. 16 Radial velocity contour (symbols) upstream the outlet at z=30 cm for Exp. 1: a) comparison to potential (circles), and b) ellipses fitting the data.

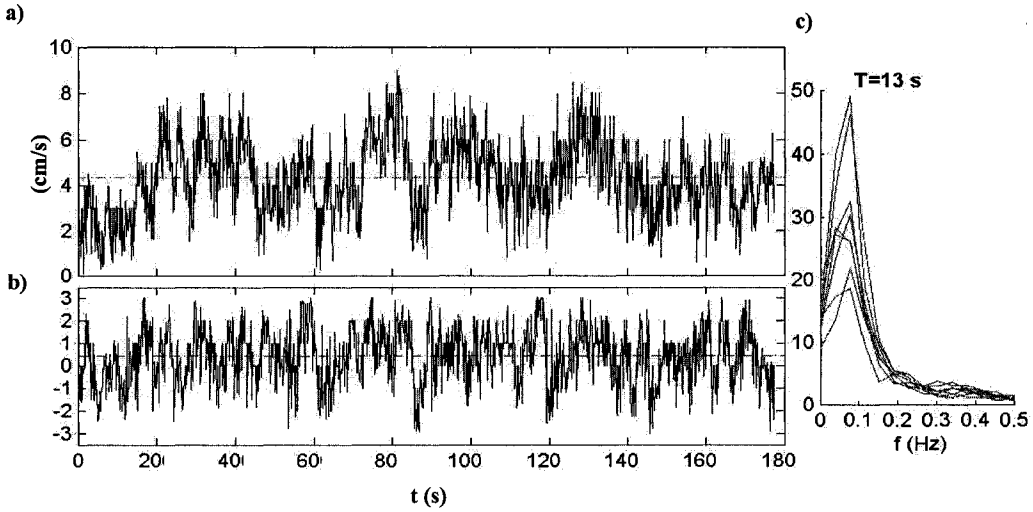

Fig 3. 17 Instantaneous velocity in Exp. 1 (b=30 cm) at x=110 cm and z=6 cm: a) u, b) v, and c) spectra of u at z=8.3 cm at several equal-spaced points between x=90 and 120 cm.

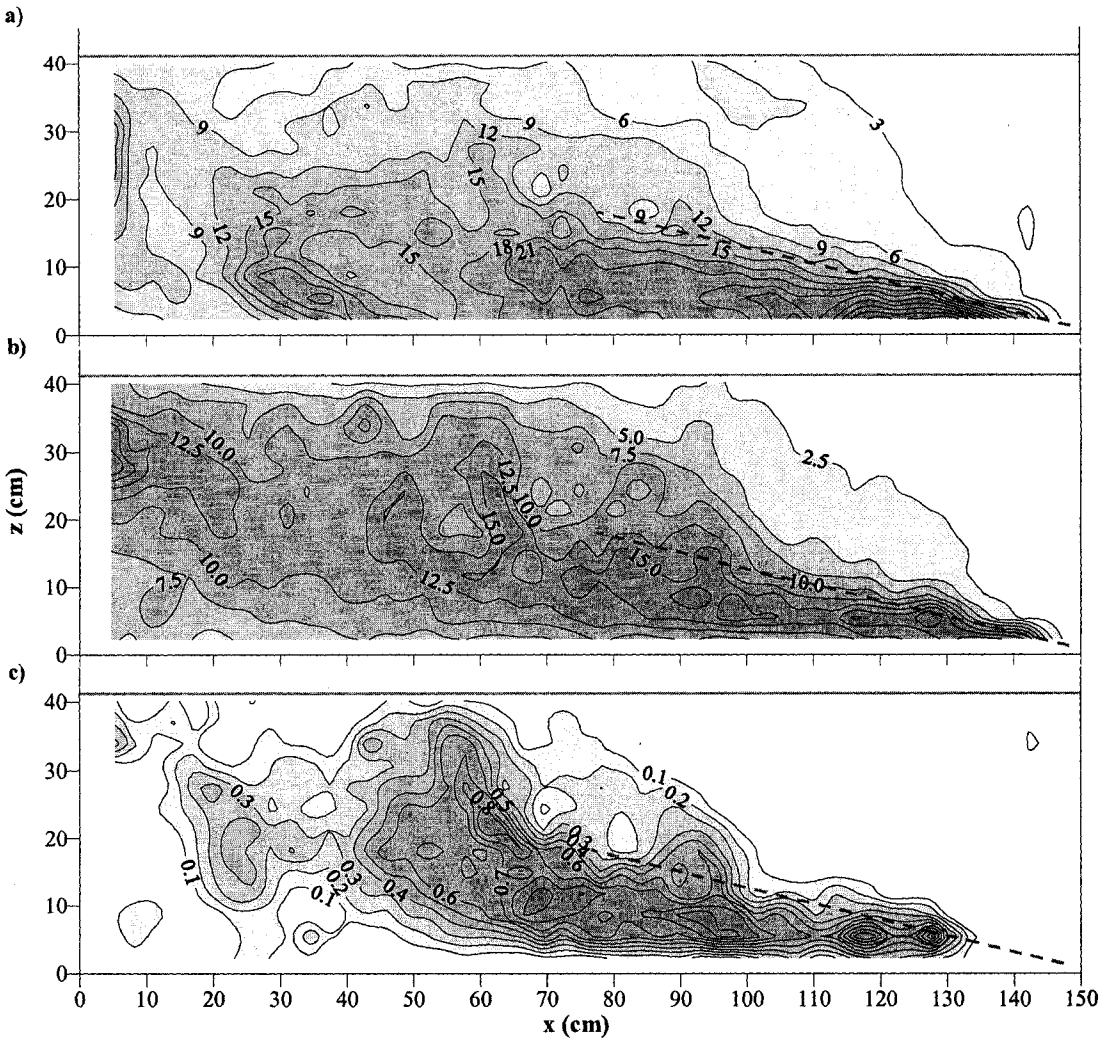

Fig 3. 18 Contours of turbulence intensities for the case (b=30 cm): a) $\sqrt{\overline{u'^2}} / U_o$ *100%, b) $\sqrt{\overline{w'^2}} / U_o$ *100%, c) $-\overline{u'w'} / U_o^2$ *100%. Slope of the jet ($u \approx 0$) is added in dash line.

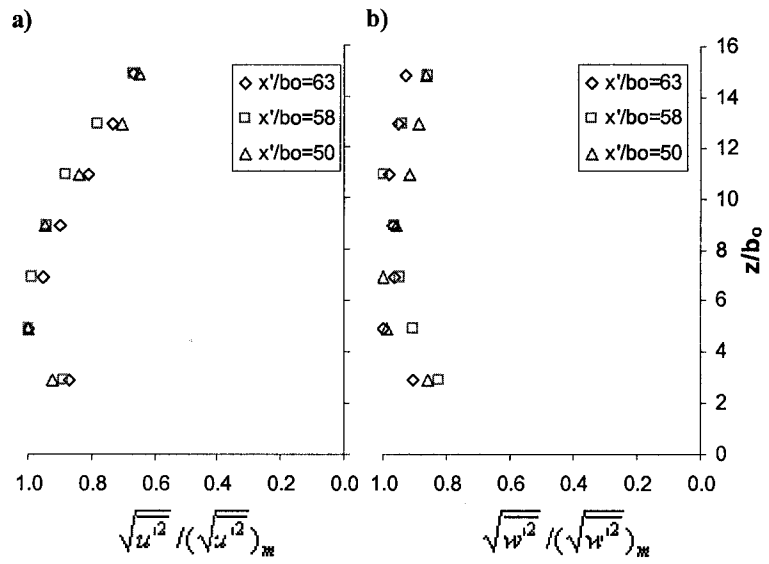

Fig 3. 19 Turbulent intensity distribution at several x-sections along the jet in Exp. 1: a) longitudinal, b) vertical.

References

Albertson, M.L., Dai, Y.B., Jensen, R.A., and Rouse, H., 1950. "Diffusion of submerged jets", *Trans., ASCE*, 115, 639–664.

Anayiotos, A.S., Perry, G.J., Myers, J.G., Green, D.W., Fan, P.H., and Nanda, N.C., 1995. "A numerical and experimental investigation of the flow acceleration region proximal to an orifice", *Ultrasound Med. Biol.*, 21(4), 501-516.

Andreopoulos, J., Praturi, A., and Rodi, W., 1986. "Experiments on vertical plane buoyant jets in shallow water", *J. Fluid Mech.*, 168, 305–336.

Chen F., 2000. "Smoke propagation in road tunnels", *Appl. Mech. Rev.*, 53(8), 207-218.

Ead, S.A., and Rajaratnam, N., 2002. "Plane turbulent wall jets in shallow tailwater", *J. Eng. Mech.*, 128(2), 143–155.

Fannelop, T.K., Hirchberg, S., and Kuffer, J., 1991. "Surface current and recirculating cells generated by bubble curtains and jets", *J. Fluid Mech.*, 229, 629-657.

Fitzgerald, J.A., and Garimella, S.V., 1998. "A study of the flow field of a confined and submerged impinging jet", *J. Heat Mass Transfer.*, 41, 1025-1034.

Giger, M., Jirka, G.H., and Dracos, T., 1991. "Entrainment and mixing in plane turbulent jets in shallow water", *J. Hydraul. Res.*, 29(5), 615-642.

Goldschmidt, V., and Eskinazi, S., 1966. "Two phase turbulent flow in a plane jet", *Trans. ASME, Series E, J. Appl. Mech.*, 33(4), 735–747.

Harleman, D.R.F., and Stolzenbach, K.D., 1972, "Fluid mechanics of heat disposal from power generation", *Ann. Rev. Fluid Mech.*, 4, 7-32.

Iamandi, C., and Rouse, H., 1969. "Jet induced circulation and diffusion", *J. Hydraul. Div., Proc. ASCE*, 95(HY2), 589-601.

Jirka, G.H., and Harleman, D.R.F., 1979. "Stability and mixing of a vertical plane buoyant jet in confined depths", *J. Fluid Mech.*, 94, 275–304.

Kotsovinos, N.E., and List, E.J., 1977. "Plane turbulent buoyant jets: I: Integral properties", *J. Fluid Mech.*, 81, 25-44.

Kuang J., Hsu C., and Qiu H., 2001. "Experiments on vertical turbulent plane jets in water of finite depth" *J. Eng. Mech.,* 127(1), 18-26.

List, E.J., 1982. "Turbulent jets and plumes", *Ann. Rev. Fluid Mech.,* 14, 189-212.

Myers, J. G., Fox, J.F., Elmahdi, A.M., Perry, G.J., and Anayiotos, A.S., 1997. "Evaluation of the proximal flow field to circular and noncircular orifices of different aspect ratios." *J. Biochemical Engrg.*, 119, 349-356.

Nasr, A., and Lai, C.S., 1998. "A turbulent plane offset jet with small offset ratio" *Experiments in Fluids,* 24, 47-57.

Nielsen P.V., 2000. "Velocity distribution in a room ventilated by displacement ventilation and wall-mounted air terminal devices", *Energy and Buildings,* 31, 179–187.

Pearce, A.F., 1966. "Critical Reynolds number for fully-developed turbulence in circular submerged water jets", *National Mech. Eng. Research Institute, Report 475*, Pretoria, South Africa.

Rajaratnam, N., 1976. *Turbulent Jets*, Elsevier, Amsterdam, the Netherlands.

Rajaratnam, N., and Subramanya, K., 1967. "Flow immediately below submerged sluice gate," *J. Hydr. Div.,* HY4, 93, 57-77.

Rajaratnam, N., and Flint-Petersen, L., 1989. "Low Reynolds number circular turbulent jets", *Proc. Instn Civ. Engrs, Part 2*, 87, 299-305.

Raymundo, C.C., and Preston, M.R., 1992, "The distribution of linear alkylbenzenes in coastal and estuarine sediments of the western North Sea", *Marine Pollution Bulletin*, 24(3), 138-146.

Rodriguez, L., Anconina, J., Flanshchskampf, F.A., Weyman, A.E., Levine, R.A., and Thomas, J.D., 1992. "Impact of finite orifice size on proximal flow convergence: implications for Doppler quantification of valvular regurgitation." *Circ. Res.*, 70, 923-930.

Scarano, F. and Riethmuller, M.L., 1999. "Iterative multigrid approach in PIV image processing with discrete window offset", *Experiments in Fluids,* 26, 513-523.

Schlichting, H., 1979. *Boundary layer theory*, 4th Ed., McGraw-Hill, New York.

Shammaa, Y., Zhu, D.Z., and Rajaratnam N., 2005. "Flow upstream of orifices and sluice gates", *J. Hydr. Engrg.*, ASCE, 131(2), 127-133.

Vermeyen, T.B., 2000. "Application of flexible curtains to control mixing and enable selective withdrawal in reservoirs", *Proceeding of the 5th Int. Symposium on Stratified Flows*, 457-462.

Wood, I.R., Bell, R.G., and Wilkinson, D.L., 1993, *Ocean disposal of waste water*, World Scientific Publishing C. Ltd., Singapore.

Chapter 4

Experimental Study on Selective Withdrawal in Two-Layer Fluids Using a Control Curtain

4.1. Introduction

Most lakes and reservoirs with a depth greater than 6 m are temperature stratified from late spring to early fall as a result of surface heating and wind mixing. Given that later spring and early summer are usually critical months for fish spawning in rivers downstream of dams, temperature of the reservoir outflow is usually regulated; thus there is a need to release water from different depth (i.e. temperature) – the concept of selective withdrawal (Imberger, 1980). Even though many recent dams were designed with the capability of selective withdrawal, earlier dams were often built without that capability. Unfortunately, retrofitting structures can be expensive; for example, the temperature-control device (TCD) used in the Shasta Dam in California cost over $75 million dollars (Bureau of Reclamation, 1997).

Recently, Vermeyen (2000) proposed the use of a temporary barrier (temperature-control curtain) to control the depth from which water is drawn, see Fig 4.1. The curtain creates an inner reservoir within the reservoir. The stratification in the inner reservoir can be controlled/modified by the curtain. With the curtain in a floating position as shown in Fig 4.1, only cooler water at the bottom can flow into the inner reservoir, thus it allows the withdrawal of cool water from the reservoir.

The confinement of the reservoir created by the curtain creates a modified stratification between the curtain and the dam, thus a complicated flow pattern is produced depending on the operation. Field measurements confirmed that significant mixing caused in the operation of a curtain could limit the curtain effectiveness on water temperature control (Vermeyen,

---

* *Part of this Chapter has been published as a paper in the Proceedings of the 17th Hydrotechnical Conference, Hydrotechnical Engineering, CSCE, Edmonton, Alberta, Canada, 2005. (CD Rom).*

2000). The curtain also creates a wall jet inflow in a confined space which adds a flow restriction that is different from the traditional wall jets in unconfined reservoirs.

All earlier studies have assumed that the velocity field is induced by the withdrawal (outflow) only, and the supply is tranquil and far enough from the outlet. In the case of using a temperature curtain, the inflow velocity is created by the curtain, and its impact on the flow velocity field and the mixing needs to be evaluated. The effect of the inflow dynamics on the flow stratification and on the outlet flow, thus the knowledge about jet inflow into a stratified medium and the parameters that control the mixing and entrainment at an interface are necessary.

This paper presents results of an experimental study on withdrawal from two-layer stratification reservoir controlled by a temperature curtain. The major goal of this study is to examine the effect of the curtain on the withdrawal quality.

The results of this study could have wide applications in many hydraulic and environmental flows. Examples include the case of fish habitat like the one in Lake Natoma where Vermeyen (2001) has showed the important relation of water withdrawn from the lake on the natural spawning and egg fertilization; the case of withdrawal from estuary stratified in salinity where warmer water is needed in order to irrigate paddy fields and water of lowest salinity is desired (Kataoka *et al.*, 2001); the case of cooling ponds where controlling the temperature of the withdrawn water would considerably reduce the fuel consumption (Imberger and Hamblin, 1982); and the case of solar ponds where the energy is extracted by withdrawing water from the hot saline layer and the withdrawal and inflow is controlled to maintain the most efficient density gradient for the collection and storage of energy in the pond (Imberger and Hamblin, 1982). Applications could also be expanded to ventilations from confined spaces whether it is natural (Heiselberg *et al.*, 2001), mechanical (Kuznik et at. 2006), or passive (Drori *et al.*, 2005).

4.2. Literature Review

When water is withdrawn from a basin containing two-layer density stratification, water flows from the layer adjacent to the outlet until some 'critical flow' rate is exceeded, after which water flows from both layers (Fig 4.2). The fundamental works in two-layer flow goes back to Craya (1949). Neglecting viscous effect at the interface, assuming hydrostatic conditions, and using Boussinesq approximation, Craya presented an exact solution of the flow by solving the Bernoulli equation for the intakes in the case of unlimited vertical extent of both upper and lower layers. He defined the critical Froude number, beyond which water in the lower layer will also be withdrawn, see Fig 4.2,

$$F_c = Q_c / \sqrt{g' h_c^5} \qquad \text{(for point sink)} \ \ldots\ldots\ldots\ldots\ldots\ldots\ldots\ldots\ (1)$$

where Q_c is the volumetric critical discharge, h_c is the critical height (vertical distance between the sink's center and the upstream interface level at critical discharge), $g'=(\Delta\rho/\rho_2)\, g$ is the reduced gravity, where g is the acceleration due to gravity, $\Delta\rho = \rho_2 - \rho_1$ is the density difference between the lower and the upper layers, respectively. He found that F_c=2.55 for a small orifice. Gariel (1949) verified experimentally Craya's result.

Wood (1978) assumed that flow into the point sink is spherically symmetric and generalized Eq. 1 to flow into a sector of a sphere. Lawrence & Imberger (1979) carried out experiments for a point source in the centre of a reservoir for the case $F > F_c$ and measured the ratio of the discharges from upper and lower layers. Jirka and Katavola (1979) examined experimentally the effect of the intake dimensions and interface thickness on the critical withdrawal conditions.

Wood (2001) have extended the theory of selective withdrawal for both 2-D and 3-D flows and determined the maximum withdrawal discharges from a two layers flowing below and/or above a stationary layer without affecting the stationary layer. For a withdrawal from a two-layer flow when both layers are withdrawn, he obtained the following 2 equations

$$\frac{\rho_1 Q_1^2}{\rho_2 Q_c^2} = \frac{(1-\sin\phi)^3(2+\sin\phi)}{2^3(\sin\phi)^5} \quad , \quad \frac{Q_2^2}{Q_c^2} = \frac{(1+\sin\phi)^3(2-\sin\phi)}{2^3(\sin\phi)^5} \quad \ldots (2)$$

where Q_c is the rate of the critical withdrawal, Q_1, Q_2 is the flow from upper and bottom later, respectively, and $\sin\phi$ is a dummy variable that represents the 'virtual' point of control where the calculations are made.

Jet behavior in stratified mediums is also studied in literature. Denser wall jet behavior, for example, was studied experimentally by Rajaratnam and Subramanyan (1986) where they provided diagrams for predicting its growth rates. Roberts and Matthews (1984) have studied the dynamics of jets in a stratification that is characterized by a homogeneous upper layer and a linearly stratified lower layer. They demonstrated that the jet behaves initially in a manner similar to that in unstratified fluid, but at some distance from the nozzle, the jet collapses vertically and spread rapidly sideways and then the inflow proceeds as a density current. Roland *et al.* (2003) have studied experimentally the horizontal buoyant jets flow into a denser sludge in final settling tanks. They presented excellent basic information about the physics of the flow regime and showed that the filter effect of the fluidized flow regime is mainly dependent on the jet velocity and on the sludge depth such that: the higher the jet velocity and the lower the sludge depth (bottom layer), the more suspended solids particles reach the clear water zone (upper layer).

Entrainment and stability of jets in stratifications had also quite interests in literature. Cotel *et al.* (1997) conducted laboratory experiments of vertical and inclined round jets impinging on a stratified interface and studied the jet entrainment with respect to the Richardson number. Kuang and Lee (2006) presented a comprehensive numerical study on the stability of turbulent buoyant round jets discharging in shallow stagnant water. General entrainments in stratified medium, however, was tremendously reviewed by Fernando (1991) where he described several interfacial mixing regimes that depend on the relative influence of the buoyancy and turbulence at the interface.

The flow pattern in the case of temperature curtain could also be simulated to that in room

temperature's flow as well as in ventilation. Heiselberg *et al* (2001) performed a series of laboratory measurements on two different window types to determine the characteristics of the air flow in rooms and shown that the air flow can be described by traditional theory for jets and stratified flow. Calay *et al.* (2000) have investigated experimentally the influence of exhaust location on the overall ventilation in large enclosures. Dubovsky *et al.* (2001), Ziskind *et al.* (2002) and Drori *et al.* (2005) have performed laboratory and real-sized experimental and numerical studies on the feasibility of the passive ventilation of one-story detached building (with one entrance and one exit). They concluded that the method may be effective in removing toxic gases, like radon, from the ground floor of the building.

4.3. Experimental Design and Methodology

Experiments were conducted in a rectangular tank of 6.0 m long, 0.5 m wide, and 0.5 m high (see Fig 4.3). An intake of 3/4 inch (1.9 cm) diameter was positioned on one end panel of the tank. The intake was connected to a centrifugal pump which withdraws water at a set discharge (Q_o). The outflow was measured using a magnetic flowmeter. A curtain was placed 1.5 m from the intake with a 2-cm opening at the bottom permitting under-withdrawal. The water level in the reservoir is controlled by a weir at the far end of the main reservoir. Salt water with a density of ρ_2 is fed from a feeding tank using a submersible pump to compensate the withdrawal water which was drained. A diffuser is used to dissipate the momentum of the feed water, and the overflow water returns back to the feeding tank.

Three experiments were conducted with a different intake level (b) and initial height of the two-layer density interface (h_2), see Fig 4.2, and Table 4.1 lists the conditions of the experiments. Different combination of h_2 and b were chosen such that to represent real-case intake position: in the upper part of the upper layer (Exp.1), in the middle depth of the upper layer (Exp. 2), and at the initial interface level (Exp. 3). In all the experiments, the total water depth H=41.2 cm, the length of the inner reservoir L=150 cm, the discharge Q_o=583 cm^3/s (35 l/min), and $g' \approx 1.5$ cm/s^2. The value of g' was chosen such that the density difference between

the upper and the lower layer represents a typical temperature difference between epilimnion and hypolymnion in reservoirs in summer (in the range of 10 °C). The curtain opening a=2 cm. This size was chosen solely to create a turbulent jet under the curtain. The calculated Reynolds number at the vena contracta depth (b_o=0.6a=1.2 cm, Rajaratnam and Subramanaya 1967) gives R_e=1178. According to Rajaratnam and Flint-Petersen (1989) this value creates turbulent wall jet with a small length of laminar region at the beginning. In real operations, a relatively large curtain opening is expected to avoid excessive flow velocity.

In all experiments, both the tank and the feeding tank were first filled with fresh water. Sodium chloride salt (*NaCl*), Rhodamine 6G dye (for interface visualization), and tracer particles (silver-coated spherical glass particles with mean diameter of 15 μm and specific gravity of 1.65, Potters Industries) were added. The water was then circulated between the main and the feeding tanks so that to ensure complete mixing. The initial two-layer stratification in the inner reservoir (between the curtain and the intake panel) was created by adding fresh water into the surface layer using a diffuser, which floated on the top of the 'coloured' salty layer. Considerable attentions were given while creating this layer so that a very thin interface would be created. Tracer particles were added slowly into the diffuser while the upper layer was created.

Before an experiment was started, both layers were left enough time until the temperature difference was within 1 °C (measured using digital thermometer). Salt water was then pumped from the feeding tank to the main tank using a submersible pump (with gradual discharge increase) for about 10 minutes where the over-weir flow return back to the feeding tank in a recycling pattern. This process was to make sure that the initial motions caused by pumping water to the main reservoir were sufficiently damped. Leaving the submersible pump working, the withdrawal pump was then started and its discharge was increased slowly until it reached the intended steady discharge. The volume of the feeding tank allows the steady discharge flow to continue for about 12-15 minutes (when the water in the feeding tank runs out).

Experimental measurements include both particle image velocity (PIV) and laser induced

florescence (LIF). A laser sheet was produced through a 5W argon-ion laser operating at 488 nm (Stabilite 2017, Spectra-Physics Lasers). A fibre optical cable (OZ Optics Ltd.) transmitted the light to a top-located lens that produced a thin laser sheet at the center plane of the channel where measurements were made. A Sony Hi-8 video camera was used to capture the images of the interface position over the whole inner reservoir of a length of 150 cm. Video recording from this camera was then digitized into individual 8-bit greyscale images (640 x 480 pixels) at a rate of 5 frames per second. The density interface position was detected using an algorithm based on the differing gray scale values of the upper and lower layers.

Velocity measurements were taken separately with a field of view of about 65 cm: first, close to the curtain and second, close to the intake side. Two high resolution 16-bit JAI-Pulnix CCD cameras (1392 x 1040 pixels) were used to simultaneously capture the PIV and LIF images. Rhodamine 6G dye has excitation and emission wavelength peaks in water at ≈526 and 550 nm, respectively (Bindhu *et al.*, 1999). A band-pass filter with a rejection range of 525 - 800 nm was used with the PIV camera to filter out the dye and a high-pass filter with a cutoff at 520 nm was used with the LIF camera to filter out the particles. Both cameras were connected to a PC computer which had an image acquisition software and a frame grabber. Two sampling frequencies were used: 10 and 15 Hz.

The velocity fields were computed using an iterative multi-grid cross-correlation PIV algorithm (Scarano and Riethmuller, 1999). For curtain area, with 3 iterations, the final search and interrogation windows were 16 and 8 pixels, respectively, with a grid velocity measurement each 8 pixels. The sampling frequency used for this area was 10 Hz. For intake area, 4 iterations have been used and the final search and interrogation windows were 8 and 4 pixels, respectively, with a grid velocity measurement each 4 pixel. The sampling frequency used for this area was 15 Hz. The velocity measurements are not reliable within about 2-2.5 cm from the sides and the bed due to the relatively large field of view (65 cm in PIV images) and the high illumination reflection at the curtain, intake wall and the tank bed. Measurements close to the water surface (within 1 cm) were not accurate as well.

Estimates of experimental errors are as follows. The flowmeter measurements showed a fluctuation of around ±2% in Q_o. The density of the fresh and salt water was determined using the CRC handbook for sodium chloride solution (Lide, 1998). The weighing scale allowed a precision of 0.1 g while the amount of added salt was more than 3.0 kg in all experiments. Also, the water temperature was measured to 0.1°C using a high precision thermometer. With these parameters, the error estimates for g' was less than 1%. The average error in the instantaneous velocity measurements was estimated at 4%, and the error in time-averaged velocities is expected to be smaller due to the averaging. Errors in detecting the interface position were estimated to about 1-2 pixels (2-4 mm) for the whole inner reservoir view (Sony camera) which corresponds to about 2% or less in the different experiments; and about 2-3 pixels (1-1.5 mm) for both curtain and intake areas (Pulnix cameras) which corresponds to about 1% or less in the different experiments. Further experimental details and error analysis are available in Appendix A.

4.4. Evolution of the Mean Flow

As the inner reservoir is the focus of this study, it will henceforth be referred to as 'reservoir'.

Experiments were started when the withdrawal discharge was slowly increased (in a period t_o) from zero to the steady discharge Q_o. To reduce the disturbances created by initial transient effects, this increase in the discharge was controlled to take a minimum of about 40 s. Observations showed that this period is somehow enough for the flow field to be established everywhere in the reservoir. After that, the discharge remains at Q_o for about 15 min in all experiments. As the replenishing fluid to the reservoir is the heavier fluid to the lower layer, the interface position generally increases during the experiments. The rate of the increase, however, depends on the composition of the outflow: when the entire outflow is from the lower layer, the rise of the interface level goes down to zero. The evolution of the experiments thus allows us to examine the withdrawal under different reservoir conditions (i.e. different

interface levels).

Flow evolution was presented for Exp. 1 in Fig 4.4. In the initial start-up period, interface disturbance was observed close to the curtain caused by the inflow jet disturbance. This phenomena continued (but more actively) later in the experiment as can be seen in Fig 4.4-a at t=82 s. The interface continuously rose with time as the heavier fluid flowed into the reservoir while the lighter fluid was withdrawn. At about t=160 s, the interface reached the critical level ($h=h_c$, refer to Fig 4.2) and the lower layer fluid started to be withdrawn (see Fig 4.4-b). At this critical time t_c, the interface was also noticeably inclined towards the intake as a result of the change of the inflow along the channel.

With the rise of the interface, with $t>t_c$, more fluid from the lower layer was withdrawn and less was withdrawn from the upper layer. Thus the rate of the interface rise decreased. More noticeable interface decrement was noticed after the general interface line reached the intake level as the withdrawn from the lower layer suppress that from the upper layer. The interface position at t = 790 s, for example, was shown in Fig 4.4-c.

Significant wave activity was observed during the experiments. A large dip at the interface accompanied with active Kelvin-Helmholtz (K-H) waves was observed from the early stage of the experiments in the curtain area. Holmboe-types of instabilities are also observed in the middle part of the reservoir especially after t_c. It appears however, that more mixing occurred right behind the curtain, while beyond the dip, the interface was relatively sharp despite the significant interfacial wave activities (see the interface far from the curtain in Figs 4.4-a and b). Due to the eddy enlargement with time, the dip was noticed to move from the area behind the curtain towards the middle part of the reservoir (compare the dip location growth in Fig 4.4-a, -b, and -c). A study of these waves will be presented later.

Several time stages could be distinguished along the experiment. The time to reach Q_o would be defined as the initial unsteady period, after which the reservoir's quasi-steady flow evolution was observed to have three stages: stage 1, the time to reach the critical withdrawal t_c (i.e. sub-critical stage, $t_o<t<t_c$), stage 2, the time the average interface level reached the

intake level t_i (bottom half of the supercritical stage, $t_c<t<t_i$), and stage 3, the time the average interface reached the upper critical level (upper half of the supercritical stage, $t>t_i$).

The previous flow observations were used to quantify the withdrawal quality. This was firstly done by studying the change of the interface with time. The density interface position was obtained by first estimating its base position and then adding the excess level to account for the mixing and the interface wave activities. The base position was detected based on the gray scale value of the lower layer and the gray scale values less than that of the lower layer was computed based on the weighted contribution of the lower layer fluids above the base position.

The interface position (with respect to the bed) away from the intake effects (which was approximately 17 cm) and the high activity waves close to the curtain (which was approximately 50 cm) was averaged (for about 85 cm of the interface length) and plotted with time in Fig 4.5-a for Exp. 1. Stage 1 in this experiment was reached around t_o=59 s as could be seen in Fig 4.5-a. The average interface level $h_{i\,avg}$ increased, as expected, with time where the withdrawn was merely from the upper layer until a critical withdrawal height (h_c) was reached around t_c=158 s with a value of about 7.8 cm (below the intake level, see Fig 4.5-a) and thus F_c = 2.75. These values are very close to the prediction of Eq. 1 (h_c=8.1 cm and F_c = 2.55). $h_{i\,avg}$ reached the intake level (b=30 cm) around t_i=292 s (stage 3).

The withdrawal from the upper layer, Q_1, was then obtained from the change of the volume of the upper layer (V_1) assuming the flow is 2-D (neglecting the changes close to the intake). The change of the upper layer volume V_1 in Exp. 1 was depicted in Fig 4.5-b. The total withdrawal rate increases from zero to a steady Q_o at time t_o. The withdrawal from the lower layer (Q_2) was calculated by subtracting Q_1 from Q_o. The importance of Q_2/Q_o curve is that it represents the quality of the withdrawal water. It can be seen from Fig 4.5-b that the rate of changes of Q_2/Q_o has increased quickly in the beginning whereas it decreased in a later period until it became very small close to the end of experiment. This was consistent with the rate of the interface rising shown in Fig 4.5-a previously.

Considering the steady Q_o period (only stages 2 and 3) and the supercritical withdrawal (where both layers were withdrawn), the change of Q_2/Q_o was plotted against h/h_c for the three experiments in Fig 4.6, along with the theoretical results of Wood (2001) (Eq. 2) and experiments of Lawrence and Imberger (1979). The overall trends of all experiments were in a good agreement with the previous studies. The fluctuation in h, however, has caused h/h_c to be fluctuated as well. The continuous result of the present experiment though, gives a good picture of the overall withdrawal. Fig 4.6 showed that Q_2/Q_o increased from zero (critical discharge) where h/h_c =1 up to 0.5 where h/h_c =0 (i.e. the interface is at the intake level, refer to Fig 4.5-b and a). It is apparent from Fig 4.6 that the critical withdrawal for this reservoir length (L/H=3.5) compares well with the theory developed for the semi-infinite reservoirs even though there was a clear mixing due to the curtain existence. This agreement revealed that at this 'moderate' reservoir length the 'data transfer' between the inlet and the outlet was relatively slower than the speed of change in withdrawal quality. It also supports the general agreement between the theory in semi-infinite reservoirs and those experiments found in literature when the interface thickness is thin and the intake dimensions are small.

It would be useful to predict the composition of the withdrawal at a given time, and the time when the complete withdrawal becomes solely from the lower layer. Simple argument gives this time as a sum of two periods: $t = t_1+t_2$ where t_1 is the period of sub-critical flow (stage 1, only the upper layer is withdrawn), and t_2 is the period of the super-critical flow (stages 2 and 3, withdrawn from both layers). Depending on the designed withdrawal discharge, the height between the intake level and the initial interface level, and the reservoir geometry, t might include both t_1 and t_2 or only t_2. If the initial h (the height between the intake level and the average interface height $h_{i\,avg}$, see Fig 4.2) is larger than h_c, then $t = t_1+t_2$; whereas if $h < h_c$ then $t = t_2$. The sub-critical flow period t_1 can be calculated (for the case of a prism reservoir) as follows:

$$t_1 = LB\,(h - h_c)/Q_o \quad \ldots\ldots\ldots\ldots\ldots\ldots\ldots\ldots\ldots\ldots (5)$$

Notice that t_1 cannot be negative (thus if $h<h_c$ then t_1=0). The second period t_2 can be

described by defining a time scale t_w. If a withdrawal layer (with volume V_c) is defined between two lines, $2h_c$ apart, above and below the intake level (see Fig 4.2), the time required to empty this volume using Q_o discharge would be equal to: $t_w = V_c / Q_o$. Substituting h_c from Eq. 1 gives:

$$t_w = 2\ \left(6.5 / Q_o^3 g'\right)^{1/5} L\ B \quad \ldots\ldots\ldots\ldots\ldots\ldots\ldots\ldots (6)$$

Using this time scale, the change of Q_2/Q_o (in the super-critical period) with time for the three experiments has been plotted in Fig 4.7. We should recall that the super critical flow did not start from zero except in Exp. 1. Theoretical curve extracted from Eq. 2 was added to the figure. Fig 4.7 showed that the flow rate Q_2/Q_o has only reached about 97% when t_2/t_w was about 4.0. Since Q_2/Q_o asymptotically approaches 1.0, a very long time is required to reach 100% of Q_2/Q_o. Here we use $Q_2/Q_o = 97\%$ as a criteria, which gives a corresponding time t_2 of $4t_w$. This time was chosen as the time needed for the complete withdrawal from the lower layer. The relation of Q_2/Q_o with t_2/t_w was found to be well described by the following:

$$Q_2 / Q_o = -0.0081(t_2 / t_w)^4 + 0.0982(t_2 / t_w)^3 - 0.4641(t_2 / t_w)^2 + 1.0575(t_2 / t_w) - 0.0366 \quad .. (7)$$

$$r^2 = 0.9997$$

Using the previous criteria, combining Fig 4.6 with the curve of Q_2/Q_o in Fig 4.7, the change of h/h_c with respect to t_2/t_w was plotted in Fig 4.7. Since the relation Q_2/Q_o - h/h_c is not linear, h/h_c has only reached about 90% at t_2=$4t_w$ in Fig 4.7. It is interesting to observe in Fig 4.7 that the interface rises up to the intake level (stage 3: the bottom half of the withdrawal layer) at t about 0.68 t_w whereas the rise of the interface above the intake (stage 4) was much slower with the upper half takes more than 3 t_w. Fig 4.7 also showed that the interface rising in stage 3 was almost steady and could be approximated by a linear line. Above the intake level, the interface rising could also be approximated to a linear line up to $h/h_c = 50\%$ (see Fig 4.7) whereas the rising decreased with time in the remaining 50%. It is also interesting that the time the interface rises in stage 3 is equal to the time the interface rises half of the height of stage 4 (thus, the interface is rising to about 75% of the total withdrawal layer in about 1.35

t_w). The relation of h/h_c with t_2/t_w was found to be well described by the following equation:

$$h/h_c = -0.0166(t_2/t_w)^4 + 0.197(t_2/t_w)^3 - 0.9005(t_2/t_w)^2 + 1.9876(t_2/t_w) - 0.9953 \quad \ldots(8)$$

$$r^2 = 0.9999$$

4.5. Flow Velocity Field

As discussed earlier, two runs for each experiment were conducted with one focus on the curtain area and the other focus on the intake area. In the following, we will discuss the velocity field in Exp. 1. Velocity measurements in a strip of about 2-2.5 cm close to reservoir's edges (curtain, bed and intake wall) were not possible. Typical velocity vectors were presented in Fig 4.8 at different times t' ($t'=t-t_o$). Velocity vectors were averaged over 1 second. This short time averaging is needed due to the relative fast change of the flow conditions. The position of the density interface was overplotted on the figure. Figs 4.8-a and b showed an image at t'=2 min for the intake and curtain areas, respectively. Fig 4.8-a showed the general potential flow close to the intake whereas Fig 4.8-b showed the strong eddy nature of the flow in the lower layer. Fig 4.8-c at t'=6 min, on the other hand, showed that the main flow contributed to the withdrawal was in the bottom part of the lower layer as could be seen between x=30 and x=60 cm before it turned up towards the intake. Fig 4.8-d at t'=4 min showed the expansion of the large eddy seen before with several small eddies along the main slope of the large eddy in the bottom layer (where $u \approx 0$; see dash-dot line in Fig 4.8-d). Remarkable change in velocity could be generally observed in Fig 4.8-b, c, and d in the lower layer. Whereas, on the other hand, a small and smooth velocity changes could be observed in the upper layer in Fig 4.8-c and d. Velocity vectors, however, were found to change significantly along the experiment.

In order to study the development of the flow structure along the time, streamlines of Exp. 1 were constructed at several $t's$ using its horizontal u and vertical v velocity components and plotted in Fig 4.9 for intake side. The short time averaging discussed before has caused few

streamlines not to be in consistence with their neighbours. Velocity vectors in the curtain side were also shown in Fig 4.9. Surface water lines (continues line) and interface lines (dashed line) were added to the figure. Time stages were found approximately to happen in this experiment at: t_o=38 s, t_c=107 s, and t_i=228 s (Notice that different run for same experiment has different time stages).

The overall view of Fig 4.9 have devised three distinguished zones: the recirculation zone close to the curtain in the lower layer where the flow field is dominated by the momentum of the inflow jet and interfacial buoyancy, the intake flow zone where the flow field is induced by the withdrawal (momentum dominated), and the middle zone separating these two zones. Boundaries, extensions, and velocity fields in these three zones were mainly inter-affected by the interface positions along the experiments. In the following we will discuss the development and characters of each zone separately.

Recirculation Zone

This zone was developed in front of the curtain mainly due to the buoyancy objection to the jet entrainment. The jet was continuously inducing a recirculation zone with several small eddies embedded in the body of this recirculation. Fig 4.9, for example, showed a recirculation zone consisted of two developed eddies at t'=10 s around x=135 cm and around x=126 cm. Withdrawal stages, on the other hand, were found to affect the nature and characters of the recirculation zone. In stage 2, for example, as the withdrawal started from the lower layer, the flow exhibits a shock-like and thus was re-adjusted in the whole reservoir and consequently the recirculation zone has considerably enlarged and a long counter clockwise eddy at the interface in the curtain area was created (see Fig 4.9 at t'=1 min at the curtain side). In fact, it was noticed that eddies phenomena have prevailed most of the flow pattern in the lower layer most of the experimental time especially at the interface.

While $h_{i\ avg}$ was rising, the recirculation zone was enlarging by time. The length of this zone L_e (taken from the curtain wall up to the end of the "returning" velocity vectors in the

zone) at t'=1min, for example, was about L_e=45 cm (see L_e at t'=1 min in Fig 4.9). The circulation continued its enlargement, however, till the end of the experiment where it reached about 100 cm (~2.5 H) (see Fig 4.9 at t'=15 min). The circulation was also changing along the experiment. For example, the upper thickness of the circulation dropped from 10 to 6 cm between x=92.5 and x=104 cm at t'=2 min (see Fig 4.8-b).

Considerable entrainment caused by recirculation developed at the interface could be noticed as well. Around the start of stage 3 (t'=3 min, $h_{i\,avg} \approx b$), for example, a remarkable disturbances in the recirculation zone were observed as the flow was re-establishing itself to respond to the condition $Q_1 \approx Q_2$. Consequently, counter clockwise eddies developed at the interface were noticed to cause, accompanied with the seiches effect, a considerable entrainment from the upper layer as could be seen in at t'=3 min in Fig 4.9. However, since $h_{i\,avg} \approx b$ at this time, the entrainment was quickly transferred to the intake and thus the total withdrawal quality has not remarkably affected.

u profiles along the jet have been studied along the experiment. An example of these profiles could be seen in Fig 4.10 at t'=6 min between x= 56 and x=68 cm. Apparently, u profiles in Fig 4.10 didn't show a sign of similarity (contrary to classical wall jet). This non-similarity, however, is probably due to the quick and transient flow changes.

The relation of the withdrawal to the evolvement of the recirculation zone was searched for by studying the change of the specific discharge (q_1) in the upper layer in this zone. Assuming 2-D flow, q_1 was calculated by integrating u profiles and plotted against x in Fig 4.11 for several t'. A general linear increment away from the curtain could be observed in the figure. However, some deviations was observed around x=110 cm at t'=2 min. This deviation might be related to the interface disturbance observed at that minute (see Fig 4.8-b). In stage 1, however, Fig 4.11 showed that at t'=10 s, most of q_1's were negatives, i.e. the flow was upstream. In the beginning of stage 2, as $h \approx h_c$ (near t'=1 min), q_1 increased almost linearly with distance from the curtain and reached 32 l/m ($\approx 0.91 Q_o$) around x=93 cm (see Fig 4.11 at t'=1 min). In stage 3, Fig 4.11 showed that q_1 dropped considerably due to the flow

adjustment resulted as Q_2 started (see Fig 4.11 at t'=3 min). Linear increment was also observed at this time and in the later times, however with lower values, until it was close to zero around t'=15 min (not shown).

In the lower layer, on the other hand, the maximum horizontal velocity $u_{e\,max}$ in the eddy's upstream flow (back flow) was plotted with time in Fig 4.12. $u_{e\,max}$ increased from about 2.2 cm/s ($0.22u_o$, where u_o=10.0 cm/s is the average velocity in the vena contracta) at t'=10 s into a maximum value 3.2 cm/s ($0.32u_o$) at t'=1 min ($t \approx t_c$). In relating to q_1, this was reasonable as q_1 was maximum at t'=1 min (refer to Fig 4.11). $u_{e\,max}$ was then dropped back till $t=t_i$ where it seemed to stay almost constant for a while (as long as the difference between Q_1 and Q_2 was small); weakening its relation with q_1 however. A little increment was then observed in $u_{e\,max}$ up to about t'=6 min. This increment was a respond to Q_2 increment. $u_{e\,max}$ seemed to decrease slowly afterwards till the end of the experiment.

The strength of the recirculation e_s was measured by non-dimensionalzing $u_{e\,max}$ with respect to the average velocity in the bottom layer u_b ($u_b=Q_o/h_{i\,avg}$) (thus $e_s=u_{e\,max}/u_b$) and was added to Fig 4.12. e_s was found to increase relatively quick up to about t'=1 min where it reached about 2.2. The increment was then decreased up to about t'=4 min. While the increment in $u_{e\,max}$ afterwards was higher than the 'slow increment' in $h_{i\,avg}$, e_s has reached a maximum value 7.3 around t'=6 min (see Fig 4.12). Beyond t'=6 min, both $u_{e\,max}$ and u_b (and thus e_s) was changing in the same rate till the end of the experiment. Thus, Fig 4.12 showed that the recirculation strength has continuously increased until the whole flow phenomena's changes (the withdrawal quality, the interface rising, the recirculation length, and jet slope) became very slow around t'=6 min (i.e. around the time $h_{i\,avg}$ reached half of the upper half of the withdrawal layer).

The slope of the jet S (recirculation centers where $u \approx 0$; refer to Fig 4.8-d) was studied along the experiment. Variation of S along time was plotted in Fig 4.13. The corresponding slope found for the homogeneous layer (same as Exp. 1 however without stratification; S=25%) as well as the slope of a classical wall jet (S=20%) were also added to the figure.

Times of t'_c and t'_i were added to the figure as well. The jet slopes in all intervals were between S=20% and S=25% (see Fig 4.13). Two noticeable changes in S could be seen in Fig 4.13: lowering trend in stage 1 from about 22% at t'=10 s into 20.5% around t'=1 min; and increasing one in stage 2 to about 24% at t'=3 min (see Fig 4.13). This general sloping behavior might be explained as follows: In stage 1 as the flow was increasing in the upper layer in the recirculation zone, the replenishing water caused the circulation's returning flow to be thickened in a rate higher than that of the interface's rising which caused the slope to lower down. In stage 2, however, the interface reached the intake and the specific discharge declined in the upper layer and thus the jet relaxed back where its slope increased. Later on, however, the interface rising slowed down losing gradually its effect on the jet and thus the slope tended (by time) to its final 'one layer' value (25%).

The correlation between the recirculation's length L_c and the average interface height $h_{i\,avg}$ was also investigated. L_c and $h_{i\,avg}$ at a certain time t' normalized by the vena contracta depth (b_o) were plotted in Fig 4.14. The figure showed that L_c growths linearly with $h_{i\,avg}$ with an average slope 28% according to the equation:

$$h_{i\,avg}/b_o = 0.2859\,(L_c/b_o) + 6.4497 \qquad r^2 = 0.9935 \quad \ldots\ldots\ldots \quad (9)$$

It was interesting, on the other hand, to notice that the location of the dip in the interface was directly above the recirculation's center at all times (see for example, Fig 4.9 at t'=10 s, 1 min, and 3 min). The change of the dip location with time was studied by tracing the ratio of its height h_d (above the bed) divided by its length L_d (taken from the curtain). The change of the angle $\theta = arc\ tan\ (h_d/L_d)$ with time was plotted in Fig 4.15 (notice however that the time used here is for different experimental run than that used in Fig 4.9). Two general trends could be observed in Fig 4.15: a steady $\theta \approx 28.4^\circ$ for a certain period followed by a linear decrement towards $\theta \approx 25.0^\circ$ by the end of the experiment. The time separated these two trends appeared to be between t=520-580 s (see Fig 4.15). It is noticeable that this time was about the time the average interface reached half of the upper half of the withdrawal layer. The initial relation of

L_d and h_d, however, in the initial time stages have showed a linear growth relation with about 34% slope as follows:

$$h_d / b_o = 0.3416\ (L_d / b_o) + 5.03 \qquad r^2 = 0.9957 \quad \ldots\ldots\ldots \quad (10)$$

This slope was verified in the next wave characteristics plot presented in Fig 4.16 (see dotted line between t=80 and t=170 s in Fig 4.16).

Series of the interface positions as shown in Fig 4.9 can be obtained and a wave characteristics plot can be generated by converting the measured interfacial height into light intensities as seen in Fig 4.16 for Exp. 1. Here the plot is divided into four periods (each one is about 230 s). The propagation of the waves can be traced by following the wave patterns. Fig 4.16 showed that the origin of the positive and negative wave characteristics moved with time from the curtain area towards the middle of the reservoir by about 50 cm (about 1/3 of the reservoir length). Since this origin is stick to the circulation (mostly around half of its length L_e), its movement will not exceed ½ L_{emax}=½ H/0.2 (S=20% for a classical wall jet) (recall that in our experiments (L<H/0.2) we found that S was larger than 20%).

Wave celerity c for different periods was obtained by tracing the wave characteristics as shown in dashed lines (left direction) and dash-dot lines (right direction) in Fig 4.16. The lines represent the wave propagation with time while the slopes of these lines represent the wave celerity. As shown in the figure, the celerities were ranged between 1.6 to 2.2 and 0.8 to 1.2 cm/s for left and right propagation, respectively (i.e. c's values in the left direction was almost double their values in the right direction). Wave length at a certain time could also be found from Fig 4.16. At t=350 s, for example, the average 'left-propagate' wave's length and the 'right-propagation' waves had a wavelength of about 6 cm, and 12 cm, respectively. A detailed waves study will be presented in a separate work.

Separation Zone

This zone was defined between about 5-10 d distance from the intake and the front end of the recirculation zone and thus its length was moving by time towards the intake. Thus, while it was prevailing most of the reservoir's length in the initial stages, it was reduced to about 30 cm width by the end of the experiment. This zone, however, was not developed until the end of stage 1. For example, at t'=1 min, Fig 4.9 denoted that the flow was detached from the bed around x=70 cm. It should be noticed however, that the streamlines appeared at t'=1 min for x<70 cm should be read as follows: below the interface the flow is pushing the interface upward while above the interface the flow is 'sucked' towards the outlet; and thus the flow doesn't penetrate the interface as one could think from the figure.

The characteristics of this zone could be clearly seen at t'=2 min where the flow in the middle of the reservoir, up to about z=10 cm, was almost parallel to the bed until it detached from the bed around x=60 cm and continued up to about x=50 cm where it was then diverted (separated) into three parts: the first inclined gradually towards the intake (withdrawal), the second went directly upward (to replace the 'eroded' volume from the upper layer), and the third inclined up backward (to feed back the recirculation). This third stream, however, was divided again close to the interface into two sub-parts: one continued to finally join the recirculation zone in the lower layer, and the other was 'returned back' and jointed the main stream in the upper layer (see this phenomena in Fig 4.8-a and similar phenomena, but more clearly, in Fig 4.8-c at t'=6 min). It was suspected, however, that all these three parts flowed as a 3-D flow. The separation distance (x=50 cm) was noticed to be valid in the later time of the experiment (similar distance was found in the homogeneous flow) (see Fig 4.8-c at t'=6 min and Fig 4.9 at t'=15 min).

Velocity field in this zone, especially in the upper layer, was generally uniform, linearly decreased, or linearly increased with x following the withdrawal stages. By the end of stage 1, at t'=1 min for example, velocity has decreased linearly from u_d=0.85 cm/s at x=66 cm into u_d =0.7 cm/s at x=57 cm (not shown). Using 2-D flow assumption, these values would result

$Q_1 > Q_o$ which indicated that the flow was not 2-D in this area (at least at t'=1 min). In stage 3, an opposite-direction shear was extended all over the middle of the reservoir (see Fig 4.10-b between x=56 and x=68 cm). Also, around t'=6 min where $h_{i\,avg}$ was around $b+h_c/2$, velocities were noticed to increase numerously in both layers. At x=60.5 cm for example, u_d in the upper layer was about 0.7 cm/s while u_{max} of the reverse flow in the lower layer was about 2.2 cm/s at z=30 cm (see Fig 4.10-b). u was increased reversely with depth in the same section until it reached u=5.5 cm/s ($\approx u_o$) at z=2.6 cm. Later stages of the experiment where $h_{i\,avg}$ was approaching the upper h_c bound have experienced no significant changes except that u values were decreased in general in this zone.

Intake Zone

The flow in this zone was characterized by the intake sucking (momentum), the buoyancy while the interface was rising, and the jet flow expansion in the lower layer. Thus, when the later two effects were far from the intake (in early stages) more potential-like flow was observed in this zone. See, for example, velocity profiles at t'=10 s in Fig 4.10-a for x<17 cm. While see on the other hand, contrary to potential flow, the strip flow in the lower layer (between z=10 and 20 cm) at t'=6 min between x=11 and x=17 cm in Fig 4.10-b.

u profiles of Exp. 1 are compared with the potential flow solution for a round intake in a homogenous fluid (Shammaa *et al.*, 2005) in Fig 4.17. Three x-sections were presented in the figure: x=6, 13, and 20 cm which were about 3, 6.5, and 10d distances from the intake, respectively.

Close to the intake (x=3d), while momentum dominated, Fig 4.17 showed that the flow was generally in agreement with the potential flow up to the end of stage 2 ($t'=t_i$) (see also Fig 4.9). The best agreement, however, was in the early stage of the experiment (t'=10 s) and at $t'=t_i$ ($Q_1 \approx Q_2$, at t'=3 min) where, in both cases, potential conditions were ultimate (see Fig 4.17 at x=3d at t'=10 s and at t'=3 min). By the end of stage 1, at t'=1 min, and due to cross-sections' flow decrement in the upper layer, an increase in u where realized. The effect of the

buoyancy on u was observed in other time intervals. At t'=2 min for example, u profiles were generally skewed inward below the interface. Close to the end of the experiment ($h \approx h_c$), at t'=15 min, the upper limb of u profiles was skewed inward in a similar manner for that observed at min 2 before. The skewing has started at $h_{i\,avg}$ level as well (see t'=15 min in Fig 4.17).

Beyond x=3d, on the other hand, Fig 4.17 showed that the flow has deviated significantly from potential flow mainly due to jet expansion as well as buoyancy effects. Also, viscosity effect at the side walls appeared to cause an increment in u values at the measurement's plane. At t'=10 s, for example, u value at the intake level was about 1.6 times the potential one at x=10d (see x=10d in Fig 4.17 at t'=10 s). At t'=3 min, velocities were larger than potential values above the interface and lower than potential values below the interface at x=6.5d and x=10d (see Fig 4.17 at t'=3 min). At t'=15 min, the profiles skewed at $h_{i\,avg}$ level and a reverse flow in the upper layer could be observed (see x=6.5d and x=10d at t'=15 min in Fig 4.17).

Maximum velocity u_{max} at x=3d was mostly around the intake level (b=30 cm). At t'=1 min, for instance, u_{max} was around the intake level and was about 3.2 cm/s (=0.016 u_{int} where u_{int}=2.05 m/s is the average velocity at the intake) whereas the potential solution gave about 2.7 cm/s (=0.014 u_{int}). At t'=6 min, however, where $h_{i\,avg} > b$, the location of u_{max} was dropped about 1.5 cm below b (see t'=6 min in Fig 4.10-b at x=4.5 and x=6 cm). This drop was related to that, at this stage, the increment rate of Q_2 withdrawn was larger than the increment rate of the interface rising and thus more horizontal flow in the lower layer has occurred which resulted in lowering the jet slope. At t'=15 min, on the other hand, u_{max} was shifted about 1.5 cm above b. This shifting was due to the recirculation expansion increment discussed before. The flow has therefore hit the interface around x=10d and then 'curved' towards the intake and thus u_{max} locations were shifted outwards the center line of the 'curve' (see u_{max} above the intake level at x=3d, x=6.5d, and x=10d at t'=15 min in Fig 4.17).

4.6. Summary and Conclusions

Experiments were performed to investigate the withdrawal quality out of a confined two-layer stratified environments with a wall jet inflow. This flow condition has wide applications such as those related to selective withdrawal from reservoirs for the purpose of fish habitat, cooling ponds, solar ponds, etc, or those related to ventilation. The main aim, however, was to investigate the case of using a temperature control curtain for reservoir's regulations.

Both PIV and LIF were used to measure the gross flow characteristics for a range of intake's and layers' depths conditions. The LIF images have revealed the general withdrawal quality as they represented the interface features' changes with time; whereas the PIV results have provided the general flow progress as well as the local flow properties.

Despite the clear mixing observed due to the curtain existence, the measurements of critical withdrawal was found to well compare with the theory for the semi-infinite reservoirs. This was due to the thin pycnocline thickness attained before the experiments, the relatively small intake diameter, the little withdrawal discharge fluctuations, and the relatively moderate reservoir length (150 cm) (which made the interaction speed between the inlet and the outlet relatively longer than the speed of change in the withdrawal quality).

The super-critical withdrawal stage was found to be described by a time scale t_w related to a withdrawal layer defined between two lines, $2h_c$ apart, above and below the intake level. Two polynomial equations where found to describe the withdrawal quality changes and the interface changes with t_w, respectively. The interface rising was found to take about 0.68 t_w in stage 2 (bottom half of the withdrawal layer); whereas the rise of the interface in stage 3 (upper half of the withdrawal layer) was much slower where it took more than 3 t_w. The total time needs for the withdrawal to be completely form the lower layer was about $4t_w$.

Three main zones were distinguished inside the reservoir: the recirculation zone close to the curtain in the lower layer where the flow field is dominated by momentum and buoyancy, the intake flow zone where the flow field is induced by the withdrawal (momentum dominated), and the middle "separating" zone. Extensive velocity measurements for the three

zones were provided.

The recirculation zone was found to enlarge with time in both x and z directions. The maximum returning velocity in this zone was noticed around the critical withdrawal time t_c. The interface has dipped directly above the center of the recirculation zone and this dip has moved with time from the curtain area about one-third of the reservoir length by the end of each experiment. Contrary to classical wall jet, on the other hand, horizontal velocity profiles in the jet forward flow didn't show a sign of similarity. The 'separation' zone was found to move towards the intake zone until it finally resided around x=50 cm from the intake wall (~2.5H from the curtain). Close to the intake ~3d (intake diameter), horizontal velocity profiles were found to be in a good agreement with the potential theory up to the end of stage 2 (the stage where the interface reached the intake level). Beyond 3d, however, the profiles were considerably deviated from the theory due to the jet effect.

Interfacial waves' celerity for different periods was obtained through a wave characteristics plot. Waves' origin seemed to 'born' close to the curtain and moves by time towards the middle of the reservoir. Waves were found to propagate in both opposite directions: left and right. The left-propagation waves were double in speed than the right-propagation ones.

The results of this study can be used directly in reservoir management when a curtain is used. If L/H is larger than 3, one could predicts the time the critical withdrawal happens, the time the total withdrawal be from the lower layer, and the withdrawal quality in the transient time in between. Thus, for a certain initial stratification, Q_o can be adjusted according to the desired withdrawal quality downstream. The other knowledge presented in this study could help understanding the flow characteristics inside the reservoir.

Table 4.1. List of experiments

L=150 cm, g'=1.5 cm/s^2, H=41.2 cm, a=2 cm (b_o=1.2 cm), B=50cm, Q_o=35 l/m			
	Initial conditions		
Exp. #	h_1 *cm*	h_2 *cm*	b *cm*
1	31	10	30
2	21	20	30
3	21	20	20

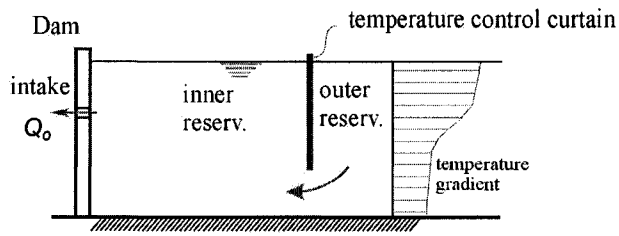

Fig 4. 1 Schematics of selective withdrawal using a temperature control curtain

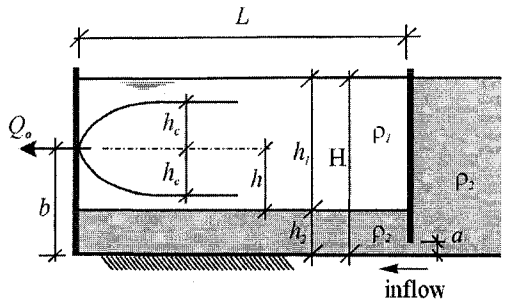

Fig 4. 2 Schematics of 2-layer flow. Curved lines show the critical withdrawal condition

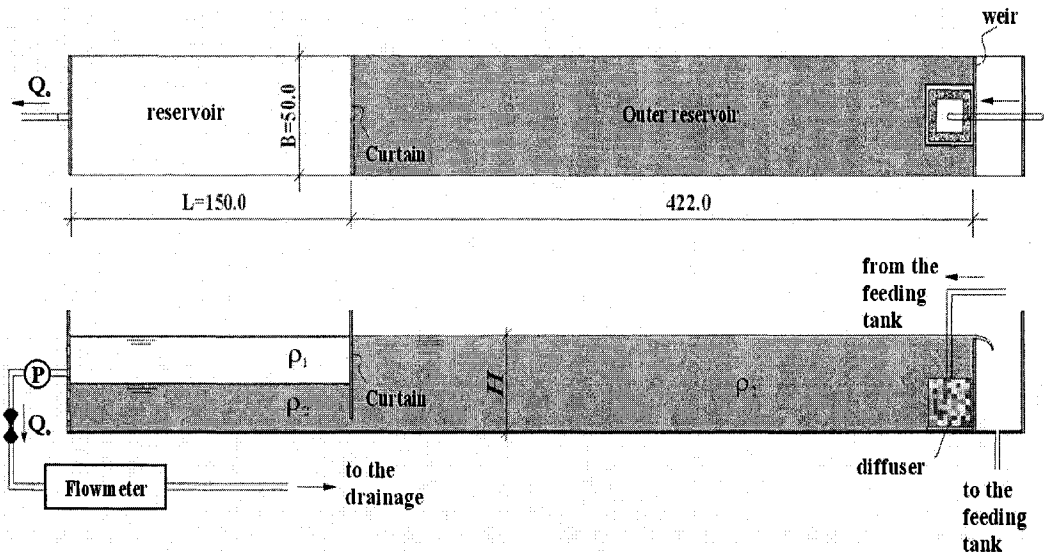

Fig 4. 3 Schematic of experimental setup (Dimensions are in centimeters). (not to scale).

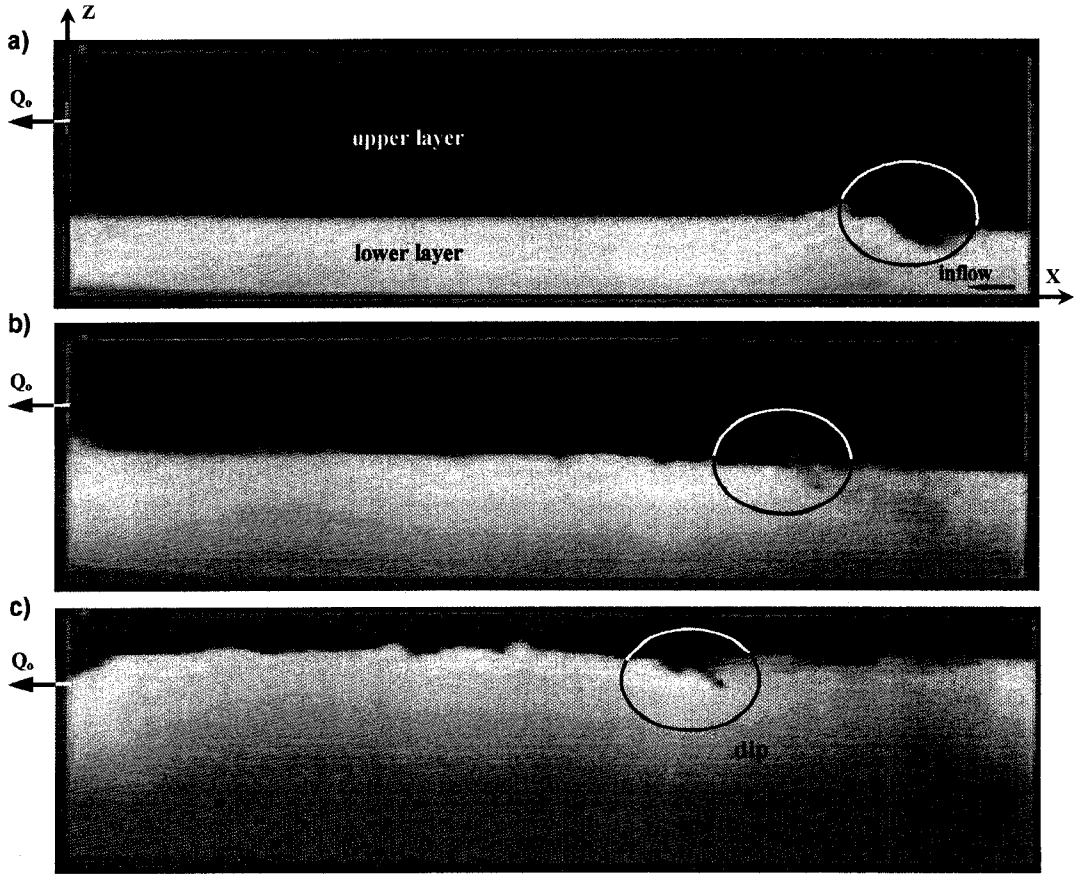

Fig 4. 4 Images showing the evolution of Exp. 1: a) initial stages at t= 82 s after the start of the experiment, b) critical withdrawal at t=162 s, c) late stage of the experiment (t = 790 s).

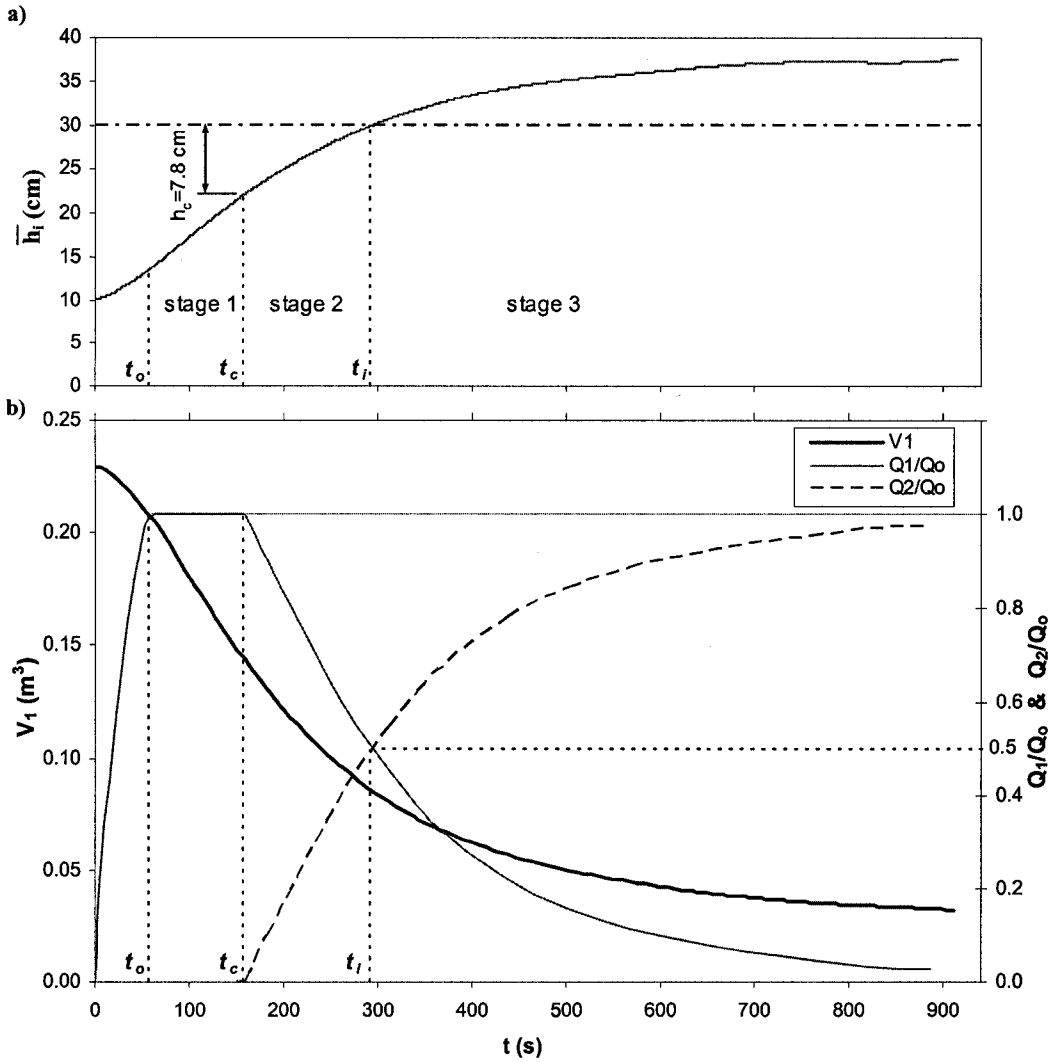

Fig 4. 5 a) Change of the average interface level with time in Exp. 1 and b) Change of the upper layer volume V_1, Q_1/Q_o and Q_2/Q_o with time in Exp. 1. (dash-dot line denoted to the intake level).

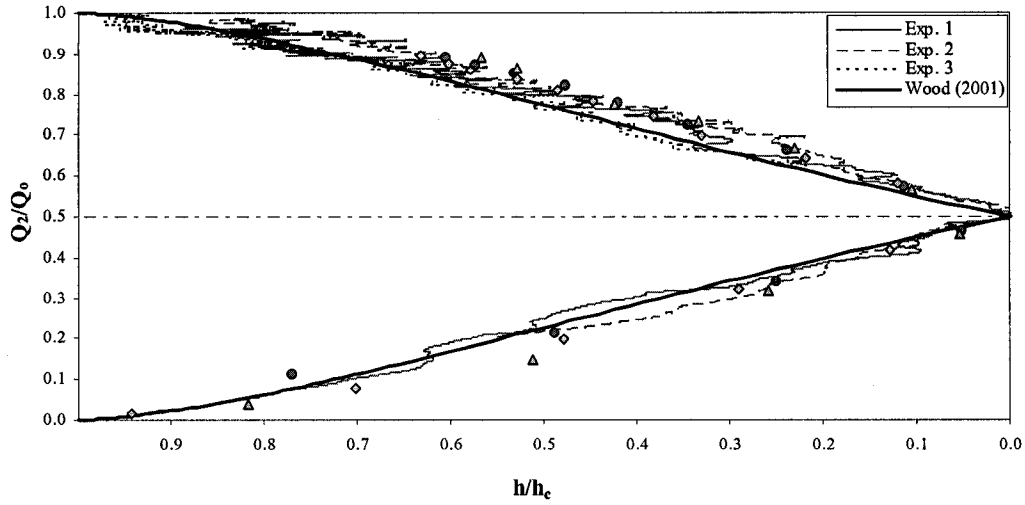

Fig 4. 6 Change of Q_2/Q_o with h/h_c. *A* comparison with experiments of Lawrence & Imberger (1979) (shown in symbols) and theoretical calculations of Wood (2001).

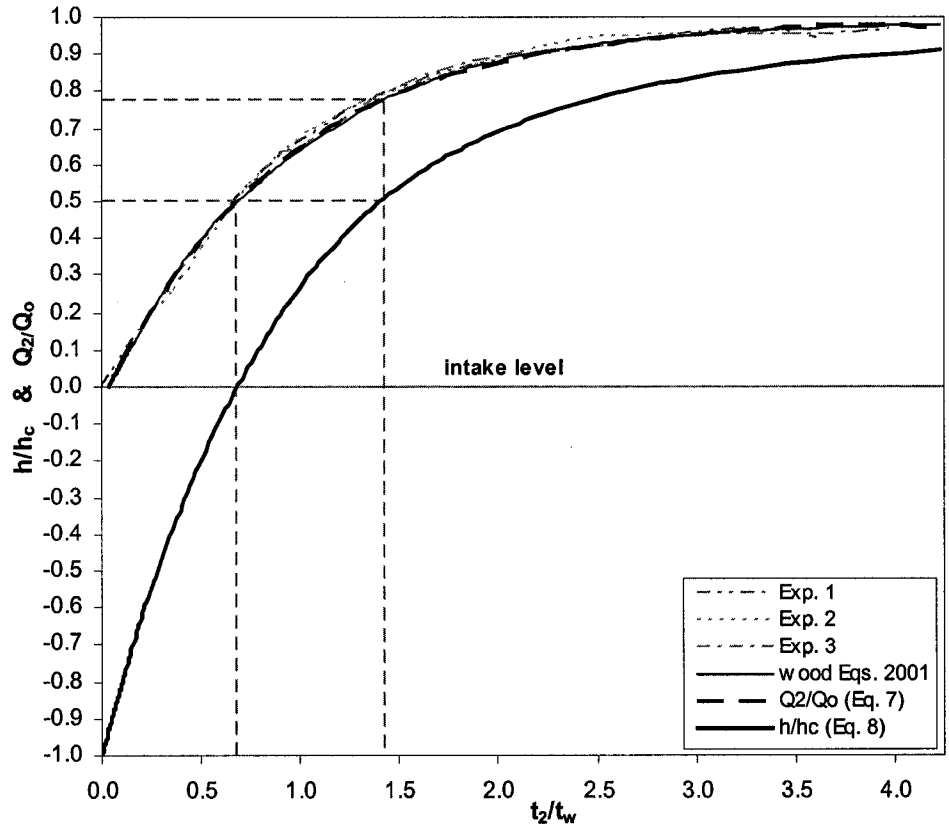

Fig 4. 7 Change of withdrawal quality Q_2/Q_o and the interface height in the super-critical flow period h/h_c with t_2/t_w.

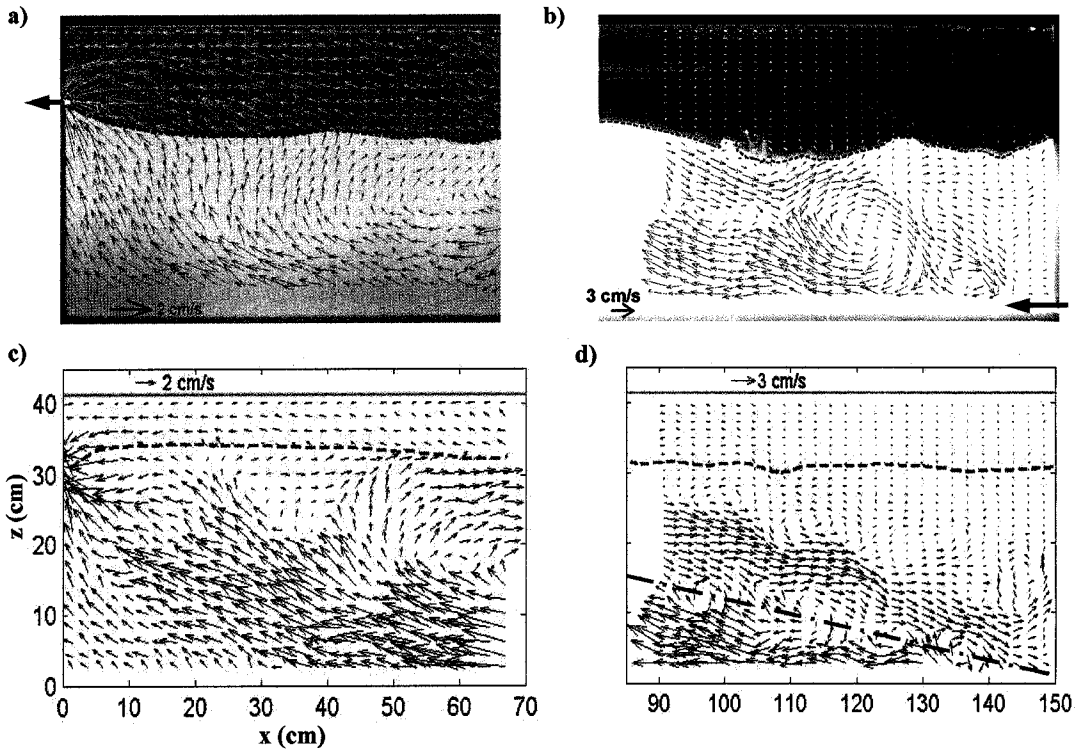

Fig 4. 2 Images and velocity vectors in Exp. 1 at: a) t'=2 min at intake side, b) t'=2 min at curtain side, c) t'=6 min at intake side, and d) t'=4 min at curtain side. Interface position was shown in dash line. Dash-dot line indicated the jet slope S (where $u\approx 0$).

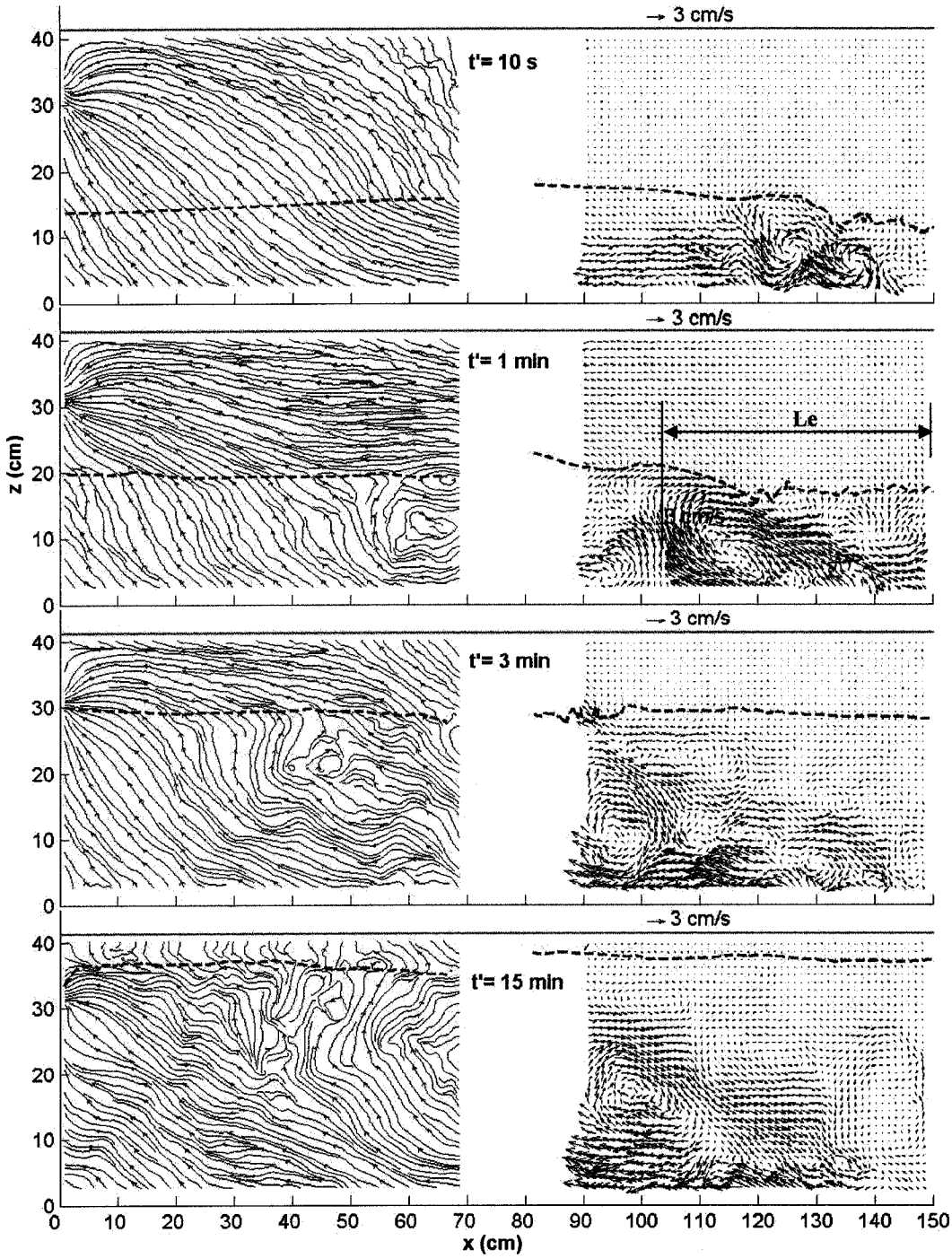

Fig 4. 9 Streamlines and velocity vectors of Exp. 1 at different *t'*.

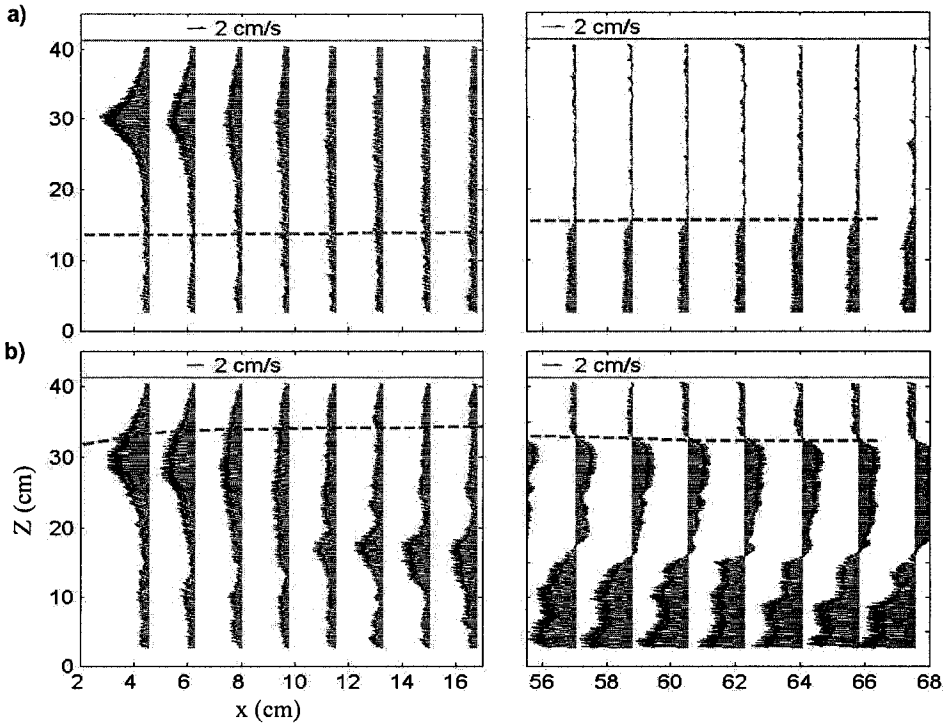

Fig 4. 10 Velocity profiles at: a) t'=10 s, and b) t'=6 min. Interface was shown in dash line.

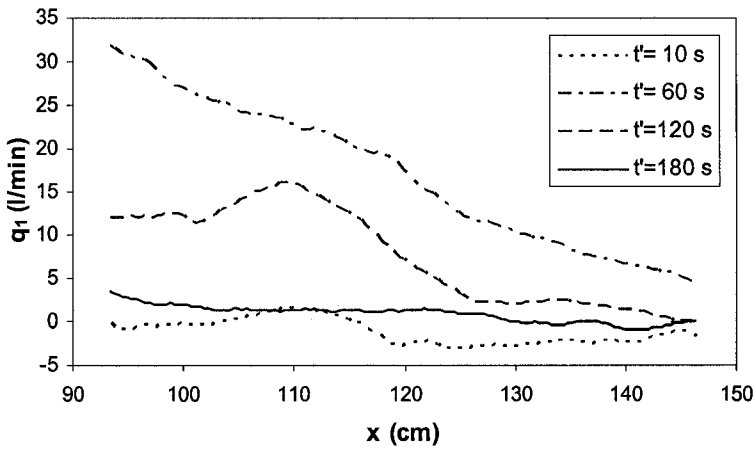

Fig 4. 11 Change of specific discharge in the upper layer with time in Exp. 1.

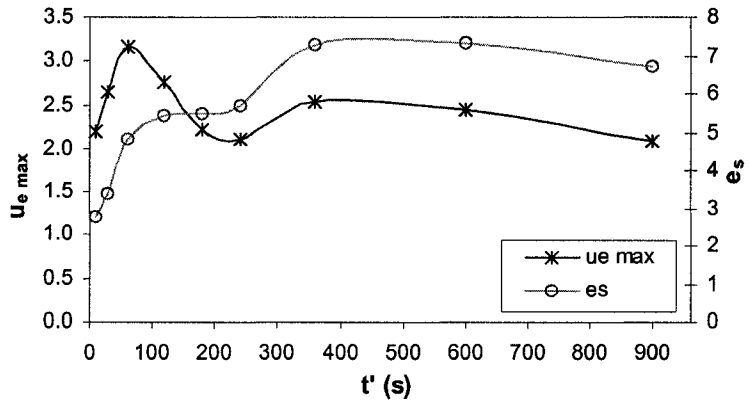

Fig 4. 12 Variations of $u_{e\,max}$ and e_s with time.

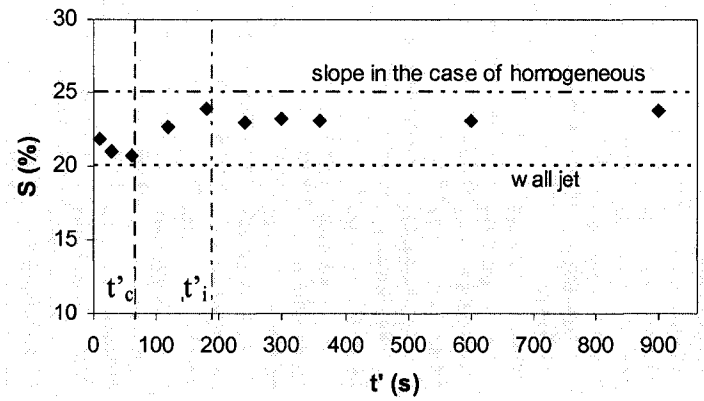

Fig 4. 13 Variation of the slope of the recirculation centers with time in Exp. 1. Slopes of the case of homogeneous layer as well as that of wall jet were added to the figure.

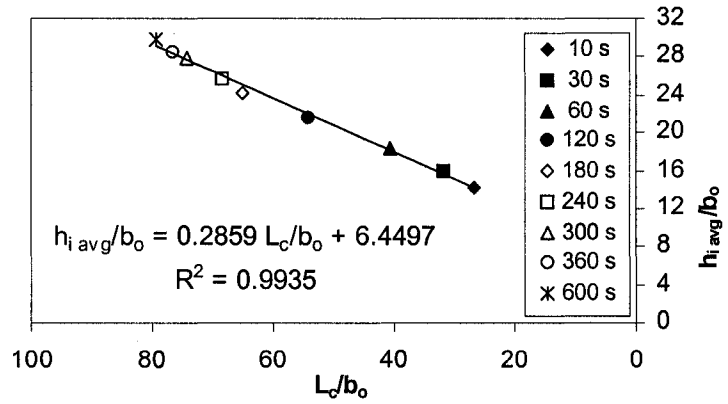

Fig 4. 14 Growth of recirculation length-average interface height in Exp. 1. (time mentioned was after t_o).

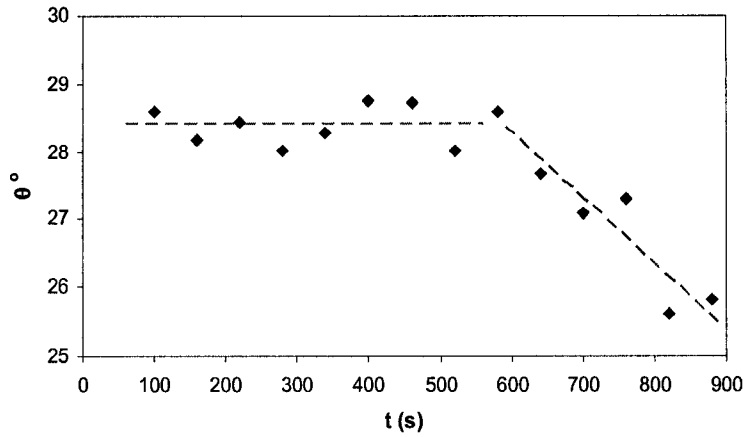

Fig 4. 15 Change of θ with time in Exp. 1. Data fitted in dashed lines.

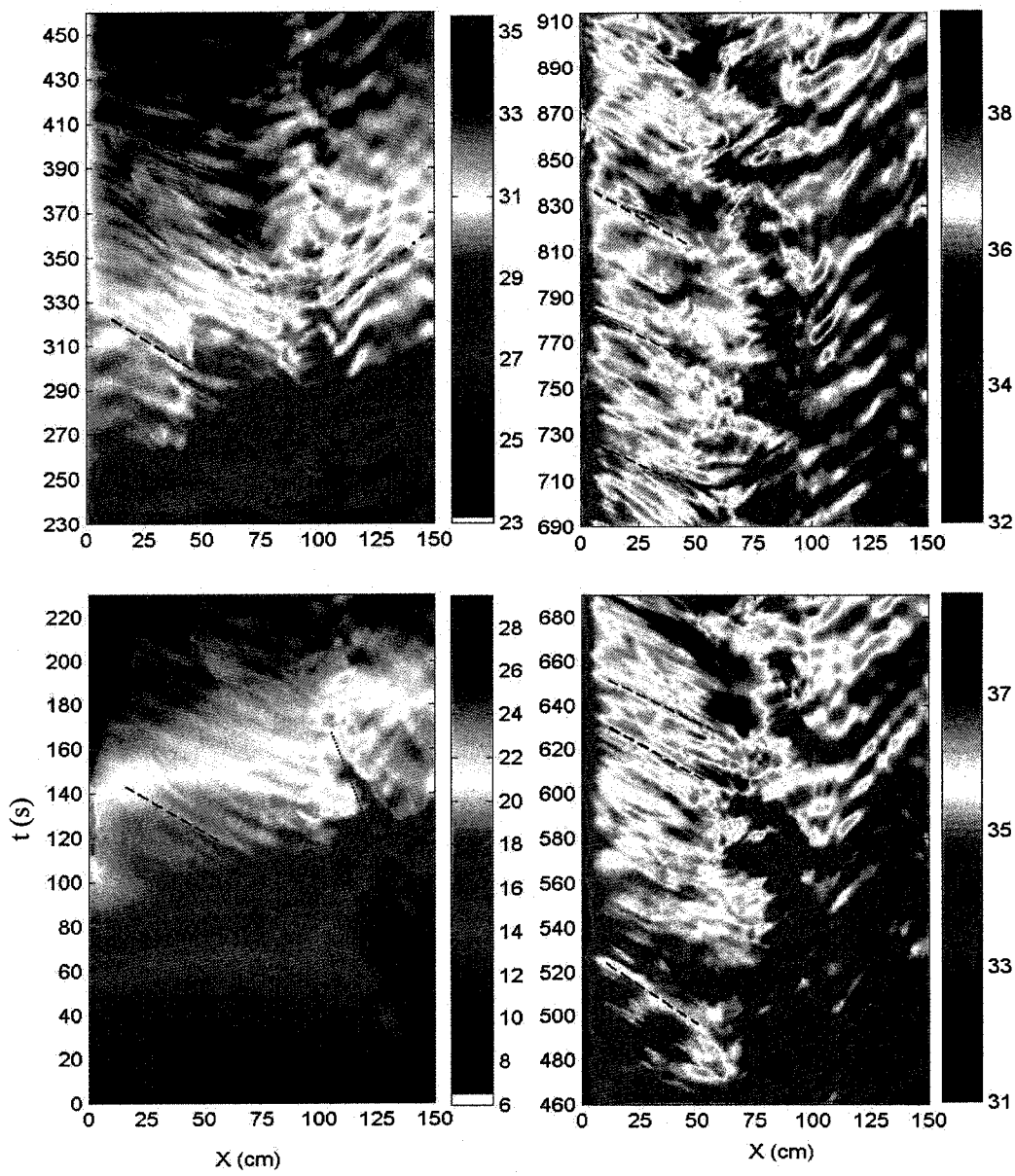

Fig 4. 16 Wave characteristic plot for Exp. 1. The colors represent the depths above the bed. Dotted line denoted the dip growth in stages 1 and 2. Notice the right and left waves' propagation.

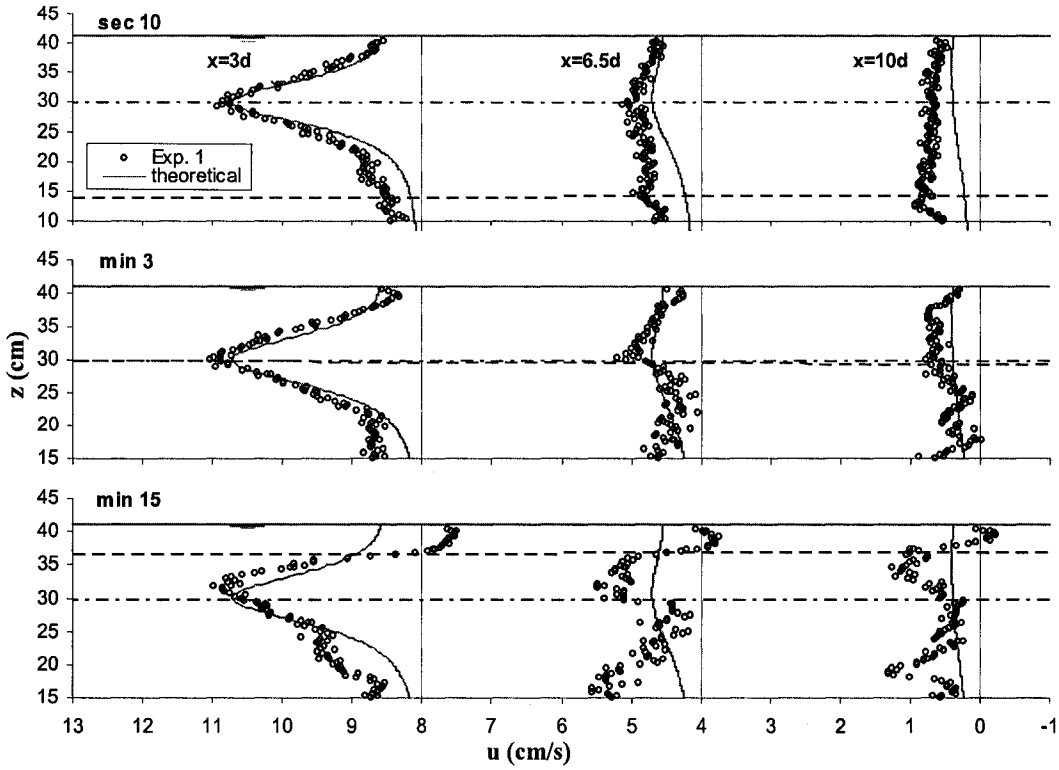

Fig 4. 17 Comparison of experimental u in Exp. 1 to the potential solution for homogenous flows of Shammaa *et al.* (2005) upstream of round intake. Interface at a certain time intervals was shown in dash line. Intake level was shown in dash-dot line.

References

Bindhu, C.V., Harilal, S.S., Nampoori, V.P.N. and Vallabhan, C.P.G., 1999. "Solvent effect on absolute fluorescence quantum yield of Rhodamine 6G determined using transparent thermal lens technique", *Modern Physics Letters B*, 13 (16), 563-576.

Bureau of Reclamation, 1997. http://www.doi.gov/pfm/acct97/bor.html.

Calay, R.K., Borreson, B.A., and Holdø, A.E., 2000. "Selective ventilation in large enclosures", *Energy and Buildings*, 32, 281-289.

Cotel, A.J., Gjestvang, J.A., Ramkhelawan, N.N., and Breidenhal, R.E., 1997. "Laboratory experiments of a jet impinging on a stratified interface", *Experiments in Fluids,* 23, 155-160.

Craya, A., 1949. "Theoretical research on the flow of nonhomogeneous fluids", *La Houille Blanche,* 4, 44–55.

Dubovsky, V., Ziskind, G., Druckman, S., Moshka, E., Weiss, Y., and Letan, R., 2001. "Natural convection inside ventilated enclosure heated by downward-facing plate: experiments and numerical simulations", *Int. J. Heat and Mass Transfer*, 44, 3155-3168.

Drori, U., Dubovsky, V., and Ziskind, G., 2005. "Experimental verification of induced ventilation", *J. Environ. Engrg.*, 131(5), 820–826.

Fernando, H., 1991. "Turbulent mixing in stratified fluids", *Ann. Rev. of Fluid Mech.*, 23, 455-493.

Gariel, P., 1949. "Experimental research on the flow of non-homogeneous fluids", *La Houille Blanche,* 4, 56–65.

Heiselberg, P., Svidt, K., and Neilson, P.V., 2001. "Characteristics of airflow from open windows" *Building and Environment*, 36, 859-869.

Imberger, J., 1980. "Selective withdrawal: a review", *the 2nd Intl. Symposium on Stratified Flows,* 381-400.

Imberger, J., and Hamblin, P.F., 1982. "Dynamics of lakes, reservoirs and cooling ponds", *Ann. Rev. of Fluid Mech.* 14, 153–187.

Jirka, G.H., and Katavola, D.S., 1979. "Supercritical withdrawal from two-layered fluid systems, Part 2. Three dimensional flow into a round intake", *J. Hydraul. Res.*, 17, 53-62.

Kataoka, T., Tsutahara M., and Mizutani S., 2001. "Selective withdrawal through a line sink of non-rotating and rotating stratified fluid in a reservoir of finite depth", *Eur. J. Mech. B-Fluids,* 20, 167–186.

Kuang, C.P. and Lee, J.H.W., 2006, "Stability and mixing of a vertical axisymmetric buoyant jet in shallow water", *Environ. Fluid Mech.*, 6, 153–180.

Kuznik, F., Rusaouen, G., and Hohota, R., 2006. "Experimental and numerical study of a mechanically ventilated enclosure with thermal effects", *Energy and Buildings*, 38, 931-938.

Lawrence, G.A., and Imberger, J., 1979. "Selective withdrawal through a point sink in a continuously stratified fluid with a pycnocline", *Tech. Rep. ED-79-002*, Dept. of Civil Engineering, University of Western Australia, Australia.

Lide, D.R., 1998. *CRC handbook of chemistry and physics*, 79th Ed., CRC, Boca Raton, Fla.

Rajaratnam, N., and Flint-Petersen, L., 1989. "Low Reynolds number circular turbulent jets", *Proc. Instn Civ. Engrs, Part 2*, 87, 299-305.

Rajaratnam, N., and Subramanya, K., 1967. "Flow immediately below submerged sluice gate", *J. Hydraul. Div., HY4*, 93, 57-77.

Rajaratnam, N., and Subramanya, S., 1986. "Plane denser wall jets and jumps", *J. Hydraul. Res.,* 24(4), 281-296.

Roberts, P.J.W., and Matthews, P.R., 1984. "Dynamics of jets in two-layer stratified fluids", *J. Hydr. Engrg., ASCE*, 110(9), 1201-1217.

Roland, H., and Volkart, P., 2003. "Buoyant jets in horizontal-flow final settling tanks", *Swiss Federal Institute of Technology Zurich*, http://www.vaw.ethz.ch/research/2_phase/waste_water_hydr/ wb_influence_inflow_jet, 9p.

Scarano, F. and Riethmuller, M.L., 1999. "Iterative multigrid approach in PIV image processing with discrete window offset", *Experiments in Fluids,* 26, 513-523.

Shammaa, Y., Zhu, D.Z., and Rajaratnam N., 2005. "Flow upstream of orifices and sluice gates", *J. Hydr. Engrg., ASCE*, 131(2), 127-133.

Vermeyen, T.B., 2000. "Application of flexible curtains to control mixing and enable selective withdrawal in reservoirs", *Proceeding of the 5th Intl. Symposium on Stratified Flows*, 457-462.

Vermeyen, T.B., 2001. "Lake Natoma temperature curtains pilot project", *The Water Forum, Sacramento, CA, Tech. rep.,* 24p.

Wood, I.R., 1978. "Selective withdrawal from two-layer fluid", *J. Hydraul. Div., HY12*, 104, 1647-1659.

Wood, I.R., 2001. "Extensions to the theory of selective withdrawal", *J. Fluid Mech.,* 448, 315-333.

Ziskind, G., Dubovsky, V., and Letan, R., 2002. "Ventilation by natural convection of a one-story building", *Energy and Building*, 34, 91-102.

Chapter 5

Waves Effect on Selective Withdrawal from a Two-Layer Curtain-Controlled Reservoir

5.1. Introduction

Selective withdrawal has been widely applied as an effective tool for water quality control from a reservoir. It is well established that this withdrawal is related to the type of stratification, the geometries of both the reservoir (mainly the depth) and the intake, and the discharge (. For two-layer stratification, this relation was first established by Craya (1949) by introducing a Froude number F_c as follows

$$F_c = \frac{Q_c}{\sqrt{g' h_c^5}} \qquad \text{(for point sink)} \quad \ldots\ldots\ldots\ldots\ldots\ldots\ldots\ldots\ldots\ldots \quad (1)$$

where Q_c is the volumetric critical discharge, h_c is the critical height (vertical distance between the sink and the upstream interface level at critical discharge), $g'=(\Delta\rho/\rho)\, g$ is the reduced gravity, where g is the acceleration due to gravity, $\Delta\rho$ is the density difference between the two layers, and ρ is a reference density. Craya (1949) found that F_c=2.55 for a small orifice. The following researchers however, have either limited or generalized the previous relation. Wood (2001) extended the theory of selective withdrawal for both 2-D and 3-D flows and determined the maximum withdrawal discharges from a two layer flowing below and/or above a stationary layer without affecting the stationary layer. All earlier studies however, have assumed that the velocity field is induced by the withdrawal (outflow) only, and the supply is tranquil and far enough from the outlet. Thus, interfacial waves as well as the interaction between the inflow and outflow were generally neglected in the literature.

Interfacial waves (also called 'instabilities') in two-layer stratification are caused by interfacial shear which in turn is a result of velocity gradients present at the interface. These instabilities may produce interfacial turbulence and cause interfacial mixing. Sheared density

interfaces have been studied since the work of Taylor (1931) and Goldstein (1931). Recent relevant studies are that of Fernando (1991) who presented a review of the stratified entrainment literature and described several interfacial mixing regimes. McGrath *et al.* (1997) performed a laboratory study to investigate turbulence, waves, and mixing at a shear-free sharp density interfaces and showed that the dominant mixing mechanism is different for different Richardson number. Tory and Koseff (2005) have showed experimentally that the nature of internal wave instability and breaking is not universal in character but rather dependent on the type of breaking internal wave considered.

The dynamics of internal waves in stratified reservoirs, on the other hand, have been extensively studied in numerous publications (e.g. Fischer *et al.* (1979) Monismith (1985), Imberger and Patterson (1990), Stevens and Lawrence (1997)). However, most of the studies were concerned with the surface wind effect on tilting the internal thermocline. Stevens and Lawrence (1997) for example, have described the appropriate parameterization of wind-forced temperature dynamics and compared their findings to field observations from four lakes in British Columbia (Canada). Saggio and Imberger (1998) have reproduced in 3-D numerical models the evolution of the basin-scale waves responded to wind forcing in Lake Biwa (Japan) and discussed the spectrum of the internal waves as well. Stevens (1999) studied the waves in small reservoirs and determined modes of energy transfer from the turbulent surface layer to the stratified thermocline region. He identified both basin-scale and higher-frequency internal waves using stationary and non-stationary spectral analyses. Using a simple two-layer rectangular model, Horn *et al.* (2001) defined five different small-scale wave regimes of the disintegration of the initial basin-scale internal seiche: damped linear waves, solitons, supercritical flow, Kelvin-Helmholz K-H billows, and bores. The names of regimes were given according to the basic phenomenon which predominates at the beginning of the motion. Their study was later generalized with the emphasis on the generation of billows and shear instabilities by Stashchuk *et al.* (2005).

Few studies on the other hand, were involved in the dynamic effect of basin-scale internal waves on selective withdrawal (Anohin *et al*, 2006). Farrow and Hocking (2006) however, have reported the results of numerical simulations of the withdrawal of a two-layer fluid with a finite-thickness interface through a slot. They paid particular attention to the role of long (basin scale) interfacial waves on the processes of withdrawal and showed that these waves can either delay or accelerate interface's drawdown. In a recent field study conducted in Lake Burragorang (Australia), Anohin *et al.* (2006) investigated the interaction of long internal waves to the selective withdrawal in a linear stratification. They found that the timescale associated with the formation of selective withdrawal is an order of magnitude smaller than the typical period of the internal wave. They also demonstrated that the steady-state theory of selective withdrawal can be used to predict outflow temperature fluctuations in reservoirs where long internal waves are presented. This last findings was confirmed in our previous study on two-layer stratification as well (refer to Chapter 4).

Even though Anohin et at. (2006) have investigated the interaction of the internal waves and the selective withdrawal; however their study has focused on linear stratifications. For a two-layer stratified reservoir, however, it appears that no previous study dealt with how the processes of inflow, internal waves and selective withdrawal interact. The later case is raised as a result of a recent low-cost retrofitting solution for selective withdrawal from reservoirs using a temperature-control curtain which was proposed for the Shasta Dam in California (Bureau of Reclamation, 1997). The solution includes a curtain that creates an inner reservoir within the main reservoir where it controls/modifies the stratification in the inner reservoir (see Fig 5.1). The curtain therefore, creates a wall jet-like inflow that produces a complicated transient flow pattern depending on the operation. One consequence of this complication is the significant waves' activity and its relation to the overall withdrawal. In addition, the transient flow pattern introduces the isolation of different waves' characteristics as a challenge. As was confirmed by field measurements, however, significant mixing (caused by waves) should be avoided for effective temperature control (Vermeyen, 2000).

This paper presents the second part of a laser induced fluorescence (LIF) and particle image velocimetry (PIV) experimental study on withdrawal from two-layer stratification reservoir controlled by a temperature curtain where various reservoir conditions have been investigated. While the first part has examined the overall effect of the curtain on the withdrawal quality in the case when the intake was above the initial interface, the present part deals with the case when the initial interface is higher than the critical withdrawal height where the wave activities plays the primary roles. The study also provides a detailed velocity field for this case and compares it to the homogeneous flow structure upstream an intake. The characters and spectra of the waves in both cases including the instantaneous velocities changes were broadly studied.

The results of this study will specifically contribute to the theory of the withdrawal from two-layer stratification through enlightening the additional roles that the waves play as well as describing their nature and character. However, from practical point of view, many hydraulic and environmental applications could benefit from the results as well. Examples could include: fish habitat (Vermeyen, 2001), withdrawal from salinity-stratified estuary (Kataoka *et al.*, 2001), cooling ponds and solar ponds (Imberger and Hamblin, 1982). Applications could also be expanded to ventilations from confined spaces whether it is natural (Heiselberg *et al.*, 2001), mechanical (Kuznik et at. 2006), or passive (Drori *et al.*, 2005).

5.2. Experimental Procedures

Experimental setup is the same as that described in Chapter 4 where a rectangular tank of 6.0 long, 0.5 wide, and 0.5 m high was used as shown in Fig 5.2. Only one new two-layer experiment (Exp. 4) have been conducted here (repeated several times) with the upper and lower layer depths were h_1=21.2 and h_2=20 cm, respectively, and the intake positioned at b=10 cm above the bed (i.e. in the middle depth of the lower layer). The total water depth was H=41.2 cm, the curtain opening was a=2 cm, the length of the inner reservoir was L=150 cm, the discharge was Q_o=583 cm^3/s (35 l/min), and the reduced gravitational acceleration was

$g' \approx 1.5$ cm/s^2. Table 5.1 summarizes the conditions of the previous 3 experiments as well as Exp. 4. Other experimental details and measurement techniques could be referred to in Chapter 4 and Appendix A.

5.3. Flow evolution and withdrawal quality

As was described previously in Chapter 4, experiments were started when the withdrawal discharge was slowly increased (in a period t_o) from zero to the steady discharge of Q_o. Previous experimental observations showed three main zones along the experiments: the recirculation zone close to the curtain in the lower layer, the intake flow zone, and the middle zone separating these two zones (refer to Chapter 4).

It was shown in the first part of this study that despite the clear mixing observed due to waves activities, the interface rising in Exp. 1, 2, and 3 was limited to (h_c =8.1 cm) obtained from Eq. 1 which related to semi-infinite reservoirs. In Exp. 4, however, the difference between the initial interface level (h_2=20 cm) and the intake level (b=10 cm) was higher than (h_c=8.1 cm). A time sequence of interface profiles at the intake part at various minutes of Exp. 4 takes from the LIF images is plotted in Fig 5.3. Time used in the figure was t' ($t'=t-t_o$).

Fig 5.3 showed a general interface rising all over the experiment. At t'=0, for example, the interface reached its maximum downward slope and a cusp-like curve was formed at the intake wall (see t'=0 in Fig 5.3). This interfacial descending resulted in a withdrawal from the upper layer. At t'=2 min however, the interface was sloped upward reaching about 5.5 cm at the intake wall above the initial interface level (see t'=2 min in Fig 5.3; and see also Fig 5.8 at t'=30 s). This height (5.5 cm), in the trough mode, would result in a vertical distance (10-5.5=4.5 cm) above the intake level; i.e. the interface positions in the vicinity of the intake would be below h_c (=8.1 cm) and thus a withdrawal from the upper layer occurred. Notice that the rate of the withdrawal from the upper layer to the total withdrawal during the trough mode period could be roughly estimated according to Fig 5.6 in Chapter 4 to be about ($Q_1/Q_o \approx 20\%$) which is relatively high. In other word, the seiches have accelerated the

withdrawal from the upper layer. This is in fact consistent with the numerical result of Farrow and Hocking (2006) for withdrawal from a line sink.

In the later time of the experiment, the average interface slope was horizontal with increasing height with time (see t'= 3 and 6 min in Fig 5.3). In these stages of the experiment, however, the interface was noticed to have a complicated structure associated with dominant small active left-going waves with thickened interface in the intake area. These waves shared in upper layer's erosion as well. It can be noticed from the figure, however, that these waves were very active around t'=3 min and became less active by time.

Along with the LIF experimental observations, Fig 5.3 showed that the reason for the interface rising above the theoretical h_c was due to the interfacial waves throug two effects: first, close to the curtain, the K-H waves caused some mixing that was partially transported towards the intake and then released, and second, close to the intake, the interfacial waves and seiches caused the interface to oscillate up and down resulting, in the down mode, in withdrawing from the upper layer. In both effects, the withdrawn water was replaced by the incoming salt water causing the interface to keep rising.

The rate of the average interface $h_{i\,avg}$ rising (with respect to the bed) and thus the upper layer's erosion with time were presented in Fig 5.4. The upper layer erosion was determined assuming that the interface is prolonged along the whole width. The interface position away from the intake effects (leaving about 15 cm from the intake) and away from the high activity waves close to the curtain (about 50 cm) was averaged and plotted in Fig 5.4. The average interface was plotted in this figure after the interface was relatively stabilized (around t'=3 min). The procedure required first to detect the density interface position which was achieved using a special algorithm based on the differing gray scale values of the upper and lower layers. The change of the volume of the upper layer (V_1) was then calculated assuming the flow is 2-D (neglecting the changes close to the intake) and plotted in Fig 5.4 as well.

An average 'power-curve' fitting was found to represent the data in the figure. Fig 5.4 showed that the average interface $h_{i\,avg}$ has risen about 1.3 cm up to t'=3 min and thus the

upper layer volume erosion V_{ers} was about 6% of its initial volume V_1. The majority of this amount, however, had occurred in the first 2 min as discussed above. The rising, later on, decreased with time where in the next 3 minutes (between t'=3 and t'=6 min) $h_{i\,avg}$ rose only about 0.4 cm and thus an increase in V_{ers}/V_1 by 1.5%. The total $h_{i\,avg}$ rising by t'=12 min was about 2 cm (i.e. 4 cm above h_c) and the upper layer erosion was about 10% (notice that the height of the average interface above the intake was about $1.5h_c$). Even though the interface rising was considerably slowing down towards the end of the experiment, however, the experiment (repeated several times) didn't show that the interface rising will stop soon as can be seen in Fig 5.4. It should be mentioned here that even though repeated experiments have shown that seiches effect on withdrawal would probably reduced if t_o was taken long enough, almost the same trend of $h_{i\,avg}$ rising was found.

This important finding revealed that the withdrawal layer depth would expand beyond the theoretical one when the interfacial waves are active. As the interface level was continuously close to the inflow depth in Exp. 4 than in the other 3 experiments and thus the recirculation zone's depth was short and relatively constant, the interfacial waves were active and resulted in a higher withdrawal from the upper layer. The level of the intake b, however, is a major factor in keeping the interface level close to the inflow level: when b increases, the final interface level is further away from the inflow depth and thus the latter's effect on the overall withdrawal process decreases.

5.4. Wave Characteristics

Several interfacial waves were observed throughout the whole experiments. K-H waves were born and slide down along a large dip created at the interface in the recirculation zone in the early stages of the experiments (see for examples K-H waves in Fig 5.5-b in Exp. 1 at t'=40 s and in Fig 5.5-d in Exp. 4 at t'=20 s). The jet flows out of the curtain along with the buoyancy effect were the main cause of these waves. The dip was continuously covered (disappeared) and reappeared depending on the longitudinal seiches' trough and crest. When

the dip was disappearing, however, a noticeable mixing wedge was created. Other waves were born near the dip area as well. Holmboe waves were also noticed in the middle of the reservoir (see these waves in Fig 5.5-a in Exp. 1 at t'=250 s and in Fig 5.5-c in Exp. 4 at t'=170 s). Observation showed that the maximum waves' height of K-H waves were about 4-5 cm whereas the length of Holmboe and other irregular waves noticed in the middle of the reservoir were diverse and ranged between 2-18 cm with a lengthen trend close to the intake zone. However, the waves were generally moving from the middle part of the reservoir towards its opposite ends. In the intake zone, however, the super-critical nature of the flow had washed out any local mixing spot and entrained it into the momentum stream.

Series of the interface positions, as was shown in Fig 5.3 where obtained and a wave characteristics plot can be generated by converting the measured interfacial height into light intensities as could be seen in Fig 5.6 for Exp. 1. For clarity, the plot is divided into four periods (each one is about 230 s). The propagation of the waves can be traced by following the wave patterns. Fig 5.6 showed that the origin of the positive and negative wave characteristics moved with time from the curtain area towards the middle of the reservoir by about 50 cm (about 1/3 of the reservoir length).

Fig 5.6 showed a 'pulse' of about 25 s period that was generated in the transient period of the experiment (see the arrow in Fig 5.6). Since waves were only active on the curtain side in this early time of the experiment and as the withdrawal was merely from the upper layer in this pulse period, it was suspected that this pulse was due to the recirculation frequency itself at that period. This was roughly verified by estimating the perimeter of the recirculation at that period which was around 75 cm while the average 'rotation' speed in the recirculation zone was estimated to about 3 cm/s and thus the time to complete one circle was about (75/3=25 s). While the recirculation zone grew as withdrawal was also changing however, this frequency might change/merge with other flow frequencies.

Wave celerity for different periods was obtained by tracing the wave characteristics as shown in dashed lines (left direction) and dash-dot lines (right direction) in Fig 5.6. The lines

represent the wave propagation with time while the slopes of these lines represent the wave celerity. As shown in the figure, the celerities ranged between 1.6 to 2.2 and 0.8 to 1.2 cm/s for left and right propagation, respectively (i.e. c's values in the left direction was almost double their values in the right direction; notice that the higher the line slope in the figure, the lower celerity represented). These values are in fact lower than the interfacial long wave celerity calculated using ($c=\sqrt{g' h_1 h_2/H}$) which ranged between c=3.3-3.9 cm/s depending on the change of h_1 and h_2 during the experiment. This difference was because the observed waves were the shear-generated interfacial instabilities. Wave length at a certain time could also be found from Fig 5.6. At t=350 s, for example, the average wave's length for the 'left-propagation' and the 'right-propagation' waves was about 6 cm, and 12 cm, respectively. It could be notice generally from the figure that the left-propagating waves were one-half in length of the right-propagating ones whereas their celerities were vice versa.

The dips' movement with time was sought by searching for the minimum level points of the interface along x axis for the experiments 1 to 4. It was interesting to find that all trajectories of the wave's origin almost coincide on one general parabolic curve started close to the curtain and moved with time towards the middle of the reservoir. This trajectory could be traced in Fig 5.6 for Exp. 1. The first part of this trajectory, however, was found approximately a linear line as shown in dotted line in Fig 5.6. Fig 5.6 showed that the dip's location has moved about 55 cm up to t=590 s (from x=145 to x=88 cm). For the remaining time, the dip continued to move until it passed the middle of the reservoir.

Time series of the interface positions at several locations along the length of the reservoir were obtained and analyzed. Fig 5.7 shows the time series at 5 locations and their spectra (using Fast Fourier Transform 'FFT') for Exp. 1. At sections x=112.5 cm and x=131.25 cm from the intake wall, the interface seemed to be disturbed in the transient period (early part of withdrawal, as observed previously in Fig 5.6), causing its general rising to be dipped for long period (about 75 s) at x=131.25 cm. This 'dip' seemed to transmit to the section x=112.5 cm (with a lag time $\approx$100 s) (see Fig 5.7).

Fig 5.7 showed that the most dominant waves' energy was related to low frequency waves. The dominant frequency in Fig 5.7 was about f=0.011 Hz (i.e. its wave period is T=1/f ≈90 s). This frequency appears to be very close to the first mode reservoir-scale internal seiches (f=0.012 Hz) in the reservoir length-direction which was calculated from the equation:

$$T_{nm} = \frac{1}{c}\left[\left(\frac{n}{L}\right)^2 + \left(\frac{m}{B}\right)^2\right]^{-1/2} \qquad \text{..... (2)}$$

where L, and B are length and width of the reservoir, respectively; and n and m are the modes of the oscillation (=0, 0.5, 1, 1.5, etc) in the length and width directions, respectively; and c is the two-layers interfacial long wave celerity given by ($c=\sqrt{g' h_1 h_2/H}$). It should be noticed that the difference between h_1 and h_2 was maximum most of the experimental time in Exps. 1, 2, and 3; and thus the calculated c was about 3.3 cm/s whereas in Exp. 4 this difference was minimum and c was about 3.9 cm/s. Therefore, the calculated first mode longitudinal internal seiches for Exps. 1, 2, and 3 was about f=0.012 Hz (T≈86 s) whereas it was about f=0.013 Hz (T≈77 s) for Exp. 4. This first mode frequency, however, is not expected to appear in the middle of the reservoir (x=75 cm) in Fig 5.7 where the node is located. The reason for this discrepancy is not clear. However, this discrepancy did not appear in Exps. 2, 3, and 4 (not shown). The second dominant frequency in Fig 5.7 is 0.04 Hz (T=25 s). For comparison, Eq. 2 gives f=0.037 Hz for (n=0.5, m=0.5) and f=0.042 for (n=1, m=0.5). Notice that this frequency was highly effective at x=112.5 cm and it might also be related to the disturbance observed previously in Fig 5.6 which was suggested to be the recirculation's frequency in the early period. Other possibility, however, is that this frequency is related to the interfacial disturbance as will be discussed later.

5.5. Velocity Analyses

Mean Velocity Field

Velocity vectors were averaged at certain time intervals over 1.5 second (=15 images).

This short time averaging is needed due to the relative fast change of the flow. Typical velocity vectors were presented in Fig 5.8 at t'=30 s for Exp. 4 in the intake area where the position of the density interface was overplotted. Fig 5.8 showed how the interface inclined towards the intake wall (seiches) at that time interval. It also showed the velocity direction where it was downstream and upstream direction in the lower and upper layer, respectively.

Horizontal velocity profiles u for Exp. 4 were plotted at several time intervals as shown in Fig 5.9. Two general characteristics could be observed in Fig 5.9: first, no significant u changes were noticed in the upper layer after about t'=2 min (recall that the fastest rate of the upper layer erosion has occurred up to t'=2 min) and little changes were noticed after t'=3 min in the lower layer; second, the continuous creating and demolishing eddies close to the interface in the lower layer has caused secondary dips at the interface's 'tail' of these eddies which in turn caused local mixing (the primary interface's disturbances "dips" are close to the curtain).

Fig 5.9 showed that at t'=0 min (when Q_o starts), the interface was declining towards the intake and thus u accelerated a bit in the lower layer towards the intake while its sign has changed in the upper layer (to balance the flow). The depth-average horizontal velocity u_d was almost uniform in the lower layer with minor increase towards the intake (u_d was about 0.67 cm/s with minor differences along x-sections) even up to a relatively close distance to the intake (up to about x=20 cm) where the effect of 3-D flow could then be observed (see Fig 5.9 at t'=0 min). This important result could imply that when the interface does not bounce and the diameter of the intake is relatively small, the effect of the 3-D flow is limited to a small distance, and thus the withdrawal from the lower layer will not be affected by the intake level as long as its location is beneath h_c from the interface. This result explained why the literature didn't differentiate (in defining h_c) between the depths of the intake b whether they are in the bottom of the wall or they are at a certain height when the reservoir length is long enough.

Some interchange mechanism between the jet and the interface was observed later on in Fig 5.9. For example at t'=1 min, the interface returned horizontally and thus the flow

reversed in the upper layer and in the jet flow creating a large circulation (see Fig 5.9 at t'=1 min). At t'=2 min, as the interface inclined towards the intake wall its depth (at the curtain area) the recirculation zone causing the later to elongate horizontally reaching almost two-third reservoir's length (while was shortened vertically). The jet, however, hit the interface between x=60 and 70 cm where two clear outcomes were observed: first, active interfacial waves were created at the area; and second, a reflected downward 'current' was created downstream (at about x=30 to 60 cm) (see Fig 5.4 at t'=2 min). At t'=3 min, the large interface declination/inclination has relatively calmed down (see Fig 5.9 at t'=3 min). Little changes were noticed towards the end of the experiment.

u profiles of Exp. 4, on the other hand, were compared to the potential solution of Shammaa *et al.* (2005) at x=3d at three interval times t'=3, 6, and 9 min in Fig 5.10. It was interesting to find out that u profiles were in good agreement with the potential solution in most of the time intervals (profiles at several other time intervals showed similar agreement with slight increase in u_{max} value at t'=2 min). The small deviation a little below the interface at t'=9 min, however, is due to the effect of the currents reflected from the interface explained in Fig 5.9 before. This general similarity result can be explained with refer to the relative steadiness of the interface (about 2 cm rising along the whole experiment). Thus the flow in the vicinity of the intake was somehow similar to the flow from a homogeneous confined layer with another imaginary 'solid-roof' at the interface. Profiles for x-section beyond x=3d showed no similarity due to the high effect of the reflected currents illustrated before (not shown).

Instantaneous Velocities

Exp. 1

Instantaneous horizontal 'u' and vertical 'v' velocities was studied in Exp. 1 at several grid points spaced about 6.5 cm horizontally and 5.0 cm vertically in the curtain area and 7.5

cm horizontally and 6.0 cm vertically in the intake area. u at three horizontal pairs of points each at the same z-height (z=38, 18, and 8 cm) at two x-locations (x=118 and x=137.5 cm) was plotted in Fig 5.11-a, b, and c. These pairs of points were chosen such that the first pair (at z=38 cm) was located in the upper layer almost all the time of the experiment, the second pair (at z=18 cm) was initially in the upper layer then, by time passing, became in the lower layer exposed in between to the interface effects, and the third pair (at z=8 cm) was in the lower layer the whole time of the experiment. t_o, t_c, and the time that the average interface level passed the points (t_{int}) were added to the figure as well. One more pair of points located in the intake area at x=30 and x=50 cm at z=32 cm was also plotted in Fig 5.11-d. Another 6 points located in the curtain area on a horizontal line at z=33 cm were chosen to plot v in Fig 5.12.

Due to the recirculation effect, at any z-height, u and v in the curtain area were found to be less 'wavy' and more stable as x-location increased (approached the curtain). This can be better noticed in Fig 5.11-b and Fig 5.12. Also, fluctuations in u were generally higher in the lower layer than in the upper layer while it was moderate in the middle height as can be seen in Fig 5.11-c, -a, and -b, respectively. Owing to the interfacial waves effect, however, fluctuations in the middle height points were considerably increased after t_c as can be seen in Fig 5.11-b.

Fluctuations in u and v in the intake area, on the other hand, were generally decreased away from the intake due to the intake effect; however they became more 'wavy' as they approach the recirculation zone. Fig 5.11-d, for example showed that the average u fluctuations between x=35 and x=50 cm was dropped about 25% (from 2.0 into 1.5 cm) (see Fig 5.11-d and notice also the more wavy pattern at x=50 cm). Beyond t_{int}, however, u and v were clearly increased and their fluctuations have increased as well (see Fig 5.11-d). As the major flow disturbances in the lower layer moves with time from the jet zone towards the intake zone, a general increase in fluctuations with time in the intake zone could also be noticed (not shown).

Around t_{int}, considerable change in v in the curtain area was noticed as can be seen, for example, in Fig 5.12 where (under the effect of the interfacial waves) a series of waves in v created around t_{int} around x=92 cm at z=33 cm has moved to the right as time passing with an average speed 0.5 cm/s and wave period T=18 s (see the arrows in Fig 5.11). The average right-going speed of the interfacial waves in the same period was about 1.0 cm/s (taken from Fig 5.6). Thus the interfacial waves have transmitted the disturbance created in v (due to interfacial arrival) with a speed equal to half of their own speed. Less effect on u, however, was found when t_{int} was reached in the curtain area. In the intake area, on the other hand, the phenomenon of v's disturbance transmission wasn't noticed.

Spectra of u and v in Exp. 1 at the grid points where the instantaneous velocities have been studied were plotted in Fig 5.13. For the curtain area, as a considerable change happened in u and v around t_c, time series used in Fig 5.13-a and b was taken from t_c till the end of the experiment.

For u spectra, Fig 5.13-a showed two important points: first, is that the wave energy was one order of magnitude larger in the lower heights than that in the upper heights; thus the wave energy was decreasing with z; and second, that a frequency f=0.011 Hz (i.e. its wave period is T=1/f ≈90 s) was found dominant in all u spectra which is close to the first mode in the reservoir's length-direction internal seiches found before (f≈0.012 Hz; T≈86 s). This result denoted that the internal seiches have a significant effect on u. However, Fig 5.13-a showed that this f was the only significant frequency in the far upper layer (z=38 cm). This f became less dominant in the middle heights (z=18). In the lower heights (z=8 cm), other frequencies appeared (along with this f as well). This was reasonable as it was expected that the frequencies of the circulation in the recirculation zone in the lower heights (z=8 cm) would dominate. However, Fig 5.13-a at z=8 cm didn't show an isolated frequency that could denote to the circulation frequency. One reason might be related to the turbulence frequencies imbedded in the spectra.

In v spectra, no common frequency was clearly isolated except at the middle heights (see

Fig 5.13-b and c at z=18 cm in the curtain area and at z=14 cm in the intake area) where the dominant frequency was about f=0.011 Hz (T=90 s) (internal seiches). Another recognizable two wave periods (T=25 and T=18 s) were noticed at z=14 cm in the intake area (see Fig 5.13-c). As the effect of the recirculation, at this height and location, was reasonably weak, these wave periods were believed to be related to the interfacial shear waves as well as the turbulence.

Since the upper height in the curtain area was far away from the direct effects of the lower layer recirculation, the interfacial seiches, and the intake flow, it was believed that v spectrum at z=38 cm has presented mainly the combination effect of the turbulence and the shear wave frequencies (see Fig 5.13-b at z=38 cm). The figure showed that this combination was between f=0.04 and f=0.07 Hz (T=15-25 s) with two recognized common peaks at T=20 and T=14 s. It was interesting to notice that this range of T was close to those found in the middle heights (z=14 cm) in the intake area as shown previously. It could thus be concluded that the combination wave periods of the turbulence and the shear waves were between T=14 and T=25 s. The frequent birth and demolish of the shear waves observed in the videotaped flow, however, showed that the shear wave periods were probably more close to the upper limit of this rang (T=25 s) and thus the turbulence period was closer to the lower range (T=14 s). Another conclusion could be that the vertical velocities are more affected by interfacial shear waves than by internal seiches. Furthermore, instantaneous v at z=33 cm presented in Fig 5.12 has shown a dominant frequency of 0.04 Hz (T=25 s) between t_c and t_{int} (see Fig 5.12). Based on the previous discussion of wave period range (T=14-25 s), It was suspected that this wave period was only related to the shear waves.

In the lower heights (z=8 cm), on the other hand, v's spectra has showed that the internal seiches frequency only appeared in the intake area, however without a clear dominance; instead, several frequencies has appeared at these heights (see Fig 5.13-b and c at z=8 cm). The diversity of these frequencies was due to a combination of several sources: the eddies', the interfacial waves', the internal seiches', and the turbulence's frequencies as well as some

other sources like the initial valve's opening impact (since these points were close to the inlet).

Exp. 4

Similar to Exp. 1, instantaneous u and v was studied in Exp. 4 at several grid points spaced about 10.5 cm horizontally and vertically in the intake area. u and v at three horizontal pairs of points each at the same z-height: one was in the upper layer (z=32.3 cm), the other was around the interface (z=21.7 cm), and the third was in the lower layer (z=11.1 cm) at two x-locations (x=30.5 and x=62.5 cm) was plotted in Fig 5.14-a, b, and c.

Fig 5.14 showed that the fluctuations in u and v decreased away from the intake in both upper and lower layers and at the interface (see the difference in the fluctuations thickness at x= 30.5 and at x=62.5 cm in Fig 5.14). This is reasonable due to the effect of the high fluctuations at the intake. Also, contrary to Exp. 1, Fig 5.14 showed that the fluctuations values do not increase with time. This was due to the overall steadiness in the position of the interface in Exp. 4 while it was changing with time in Exp. 1.

A long wave period T=80 s could be noticed in Fig 5.14-a at x=62.5 cm while the magnitude of this wave was decreasing (damping) with time. As this wave period was close to the first mode longitudinal seiches (T=77 s; calculated using Equ. 1 for y_1=21 and y_2=20 cm), this implied that the upper layer was only affected by the longitudinal seiches. A "harmonic" change could also be observed in u in the upper layer with a lapse time of about Δt=15 s (see u changes between x=30.5 and x=62.5 cm in Fig 5.14-a). This time delay gives an average speed of data transfer between the two x-sections 2.0 cm/s. Notice that this speed is almost half of the calculated interfacial long wave celerity (c=3.9 cm/s). This deduced that the interfacial waves have transmitted the disturbance created in u with a speed equal to half of their own speed. It is noticeable that this result was similar to that found in Exp. 1 in Fig 5.12 for v disturbance. However, it is evident that the disturbance transmission was related to the interfacial long wave celerity for u changes whereas it was related to the (short) shear

waves for v changes. The harmonic changes in u almost disappeared at the interface and in the lower layer due to the interfacial waves as well as the 'indirect' jet effect in the lower layer (see Fig 5.14-b and c for u changes).

v changes, on the other hand, were more "regular" and showed a general sign of symmetry around an average value ($\approx$zero) in the upper layer as u was harmonic (see Fig 5.14-a for v changes). Less regular and more wavy signs at the interface and in the lower layer especially far from the intake (x=62.5 cm) could be observed (see Fig 5.14-b and c for v changes).

Spectra of u and v in Exp. 4 at several grid points were plotted in Fig 5.15. Similar to Exp. 1, Fig 5.15 showed that both u's and v's wave energy has increased one order of magnitude from the upper to the lower layer (see Fig 5.15). In consistence with Fig 5.14-a for u changes, one dominant frequency (f=0.0125 Hz, T=80 s) could be observed in u in the upper layer (see Fig 5.15-a for u spectra). Same dominant f was found in the lower layer whereas no dominant f was found at the interface, however, with a tendency towards low frequencies which implies higher order oscillation modes (see Fig 5.15-b and c for u spectra). Except at the interface, the domination of the internal seiches on u spectra was similar to that found in Exp.1.

v spectra, on the other hand, showed some domination for the first seiches mode (T=80 s) (see v spectra in Fig 5.15-a, b and c). Higher frequencies were also observed at the interface (T ranged between 14 and 25 s) with a common period T=14 s. This range of wave's period was similar to that found in the middle heights in the curtain area and in the upper heights in the intake area in Exp. 1 (refers to Fig 5.14-b and c). It can be noticed that all these three 'heights' were under intense shear waves for a long time in the experiments. This was another evident that this wave's period range was mostly related to shear waves and turbulence as well.

5.6. Summary and Conclusions

The effect and characters of the waves activity on the withdrawal of a confined two-layer stratified reservoir using a temperature control curtain was investigated through laboratory experiments. The flow condition examined has wide applications in selective withdrawal from reservoirs for the purpose of fish habitat, cooling ponds, solar ponds, etc. This (LIF-PIV) study is the second of two-part study where the first one has concerned the withdrawal quality when the intake is located higher than the critical withdrawal height h_c.

Wave activities were found to prevail in the whole experiments. The nature and characteristics of these waves have been explored. Active K-H waves were observed along the interface in the curtain area. Longitudinal seiches, on the other hand, were observed to deepen or cover these waves. Holmboe waves were also observed in the middle part of the reservoir. Other 'irregular' interfacial waves were also observed along the experiments.

The effect of waves on the withdrawal quality was also studied. While this effect was little when the outlet level was a bit far from the inlet level and thus the average interface was always rising, a significant wave's effect on the overall withdrawal was found when the average interface position was close to both inlet and outlet most of the time of the withdrawal. This effect represented through two mechanisms: the K-H waves in the curtain area has caused some mixing that was partially transported towards the intake; and the seiches which caused the interface in the intake area to oscillate up and down resulting, in the down mode, in withdrawing from the upper layer. Thus, the interface has risen above the theoretical h_c. This was a new contribution to the selective withdrawal theory.

Study of the instantaneous u and v has revealed their close relation to the interfacial waves. It was found generally that the disturbance in u has transmitted along a horizontal line in a half speed of the interfacial long wave celerity whereas it was transmitted for v changes in a half of the (short) shear waves speed.

Spectra of u and v have shown that the frequency of the first mode reservoir's length-direction internal seiches was generally dominant in u whereas it was less dominant in v.

Also, both u's and v's wave energy has increased one order of magnitude from the upper to the lower layer. Spectra of u and v in areas exposed to intense shear waves for a long time in the experiments have revealed that the combination of wave periods of the turbulence and shear waves were between T=14 and T=25 s. However, the present study could not arrive at a firm isolation of these periods due to the fast and transient changes of the flow.

Table 5.1. List of experiments

L=150 cm, g'=1.5 cm/s^2, H=41.2 cm, a=2 cm, B=50cm, Q_0=35 l/m			
	Initial conditions		
Exp. #	h_1 *cm*	h_2 *cm*	b *cm*
1	31	10	30
2	21	20	30
3	21	20	20
4	21	20	10

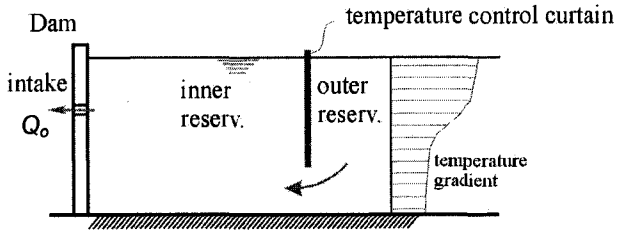

Fig 5. 1 Schematics of selective withdrawal using a temperature control curtain.

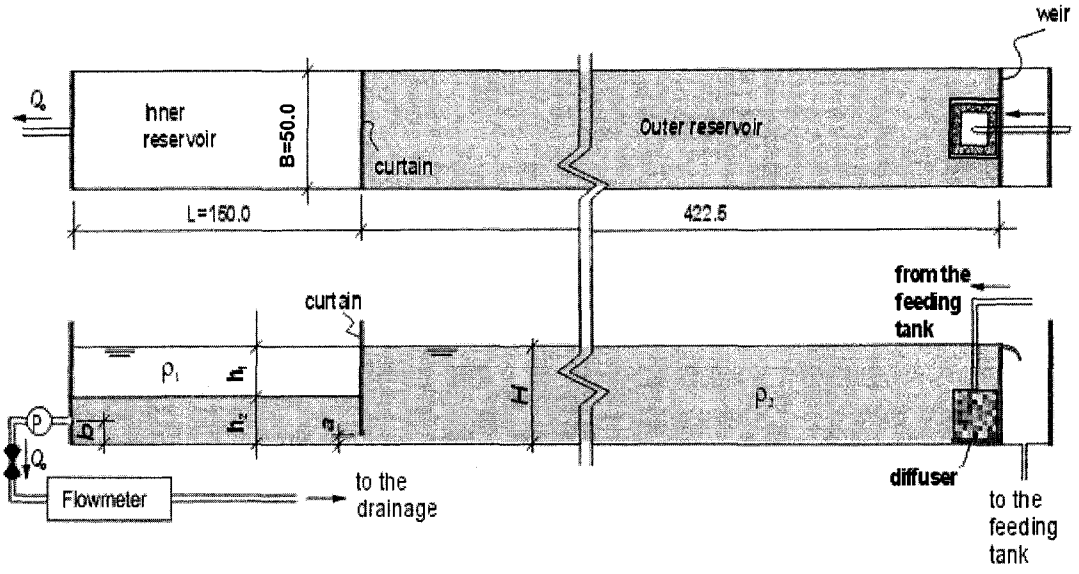

Fig 5. 2 Schematic of experimental setup (Dimensions are in centimeters).

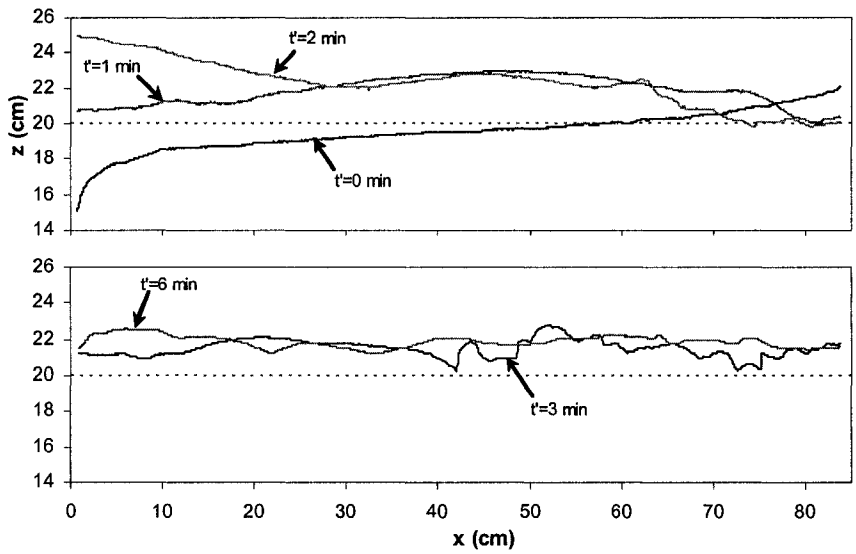

Fig 5. 3 Sequences of interface evolution of Exp. 4 in the intake part of the reservoir: ($t'=t-t_o$). Dash-line is the initial interface height and the intake is at z=10 cm.

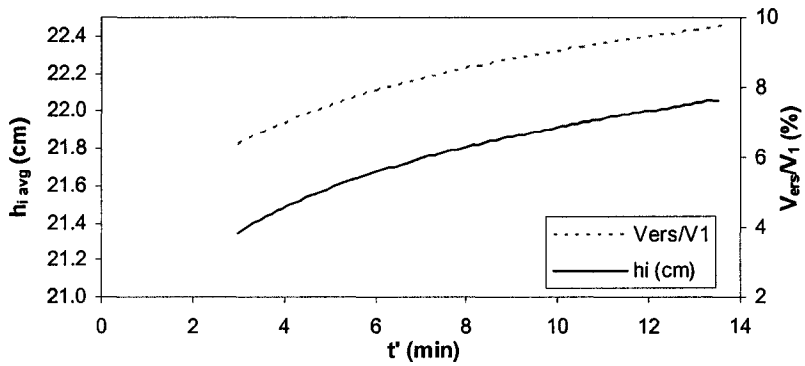

Fig 5. 4 Variation of the average interface height and the upper layer volume erosion with time in Exp. 4.

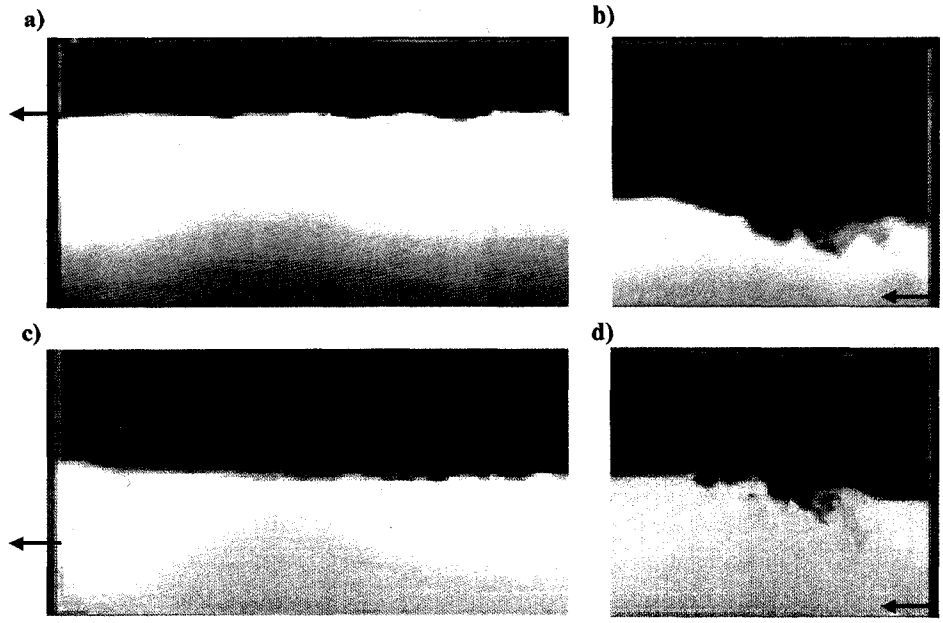

Fig 5. 5 Images showing waves developed in Exp. 1: a) at t'= 250 s and b) at t'=40 s; and in Exp. 4: c) at t'=170 s and d) at t'=20 s. (arrows show the inflow and the outflow).

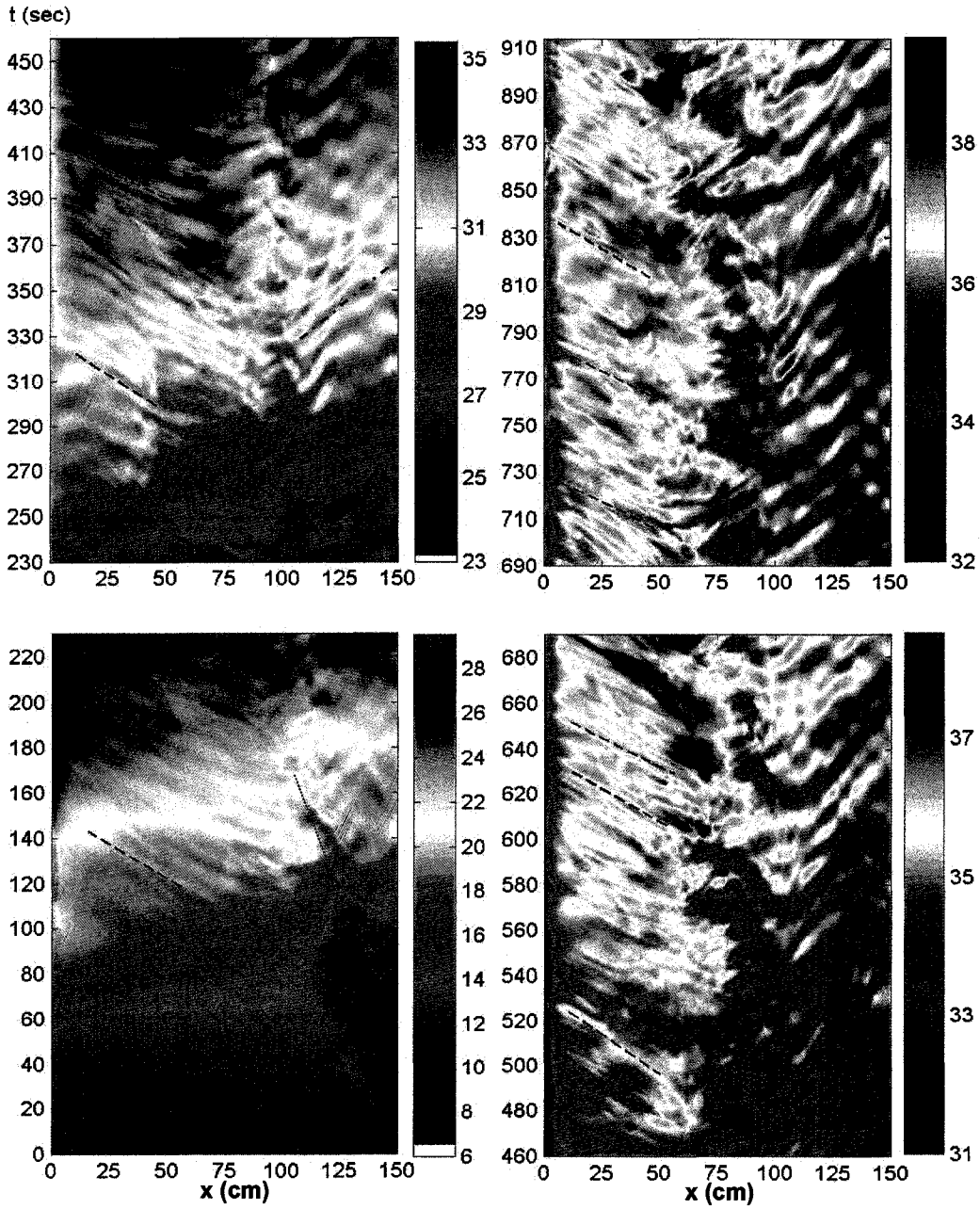

Fig 5. 6 Wave characteristic plot for Exp. 1. The colors represent the depths above the bed. The arrow shows a 'pulse' ($T \approx 25$ sec) in the early period of the experiment. Notice the right and left waves' propagation. Dotted line denoted the dip growth in the early stage of the experiment.

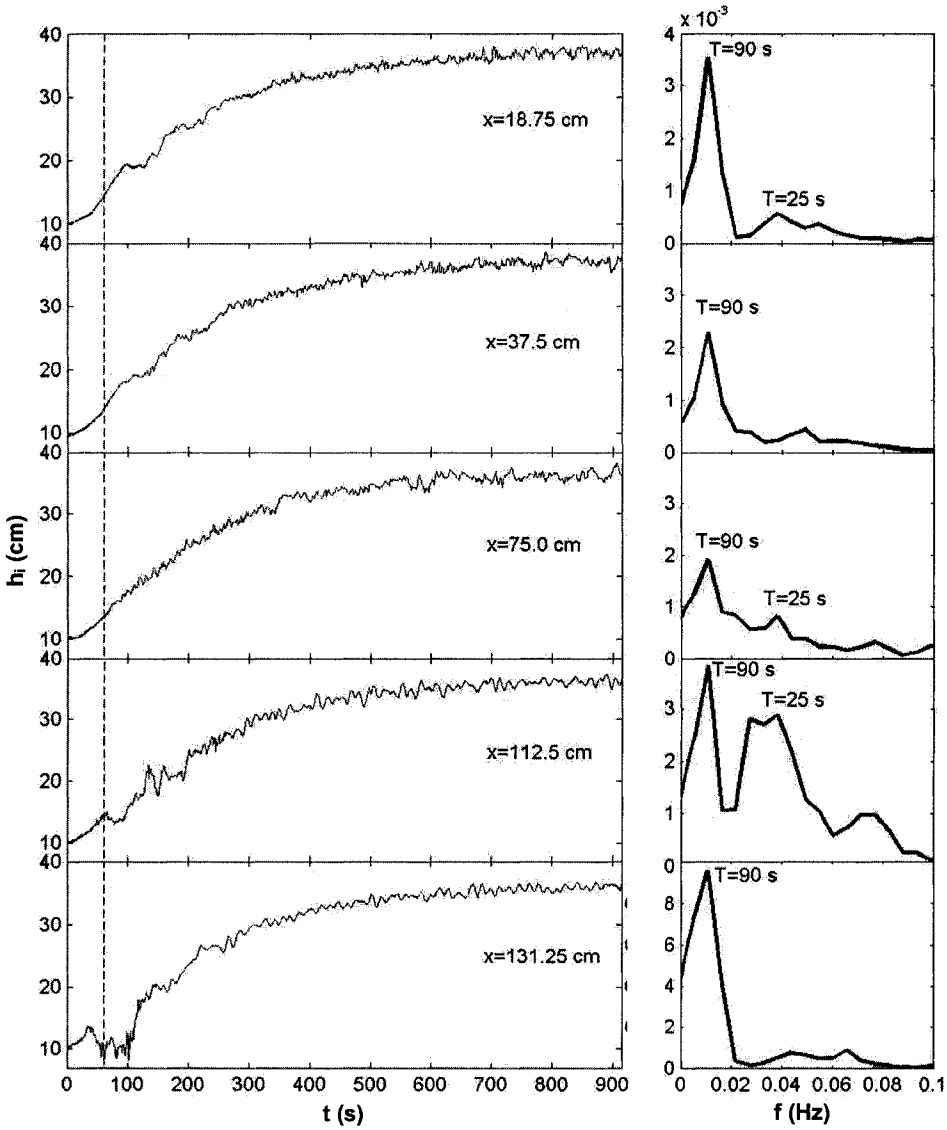

Fig 5. 7 Variation of interface position with time and its spectrum at different locations (Exp. 1)

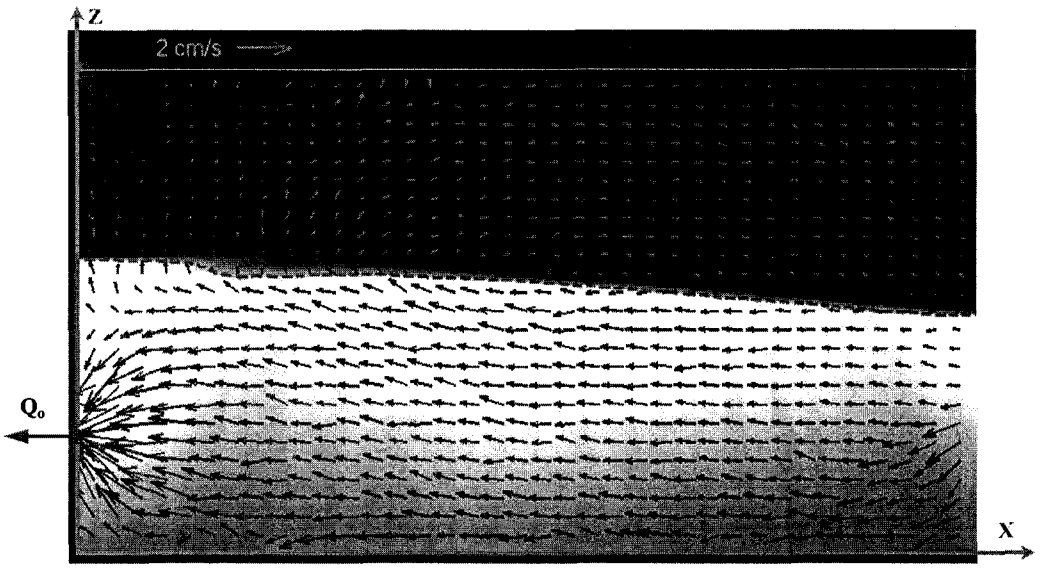

Fig 5. 8 Image and velocity vectors in Exp. 4 at t'=30 s at the intake side. Interface position was shown in dash line.

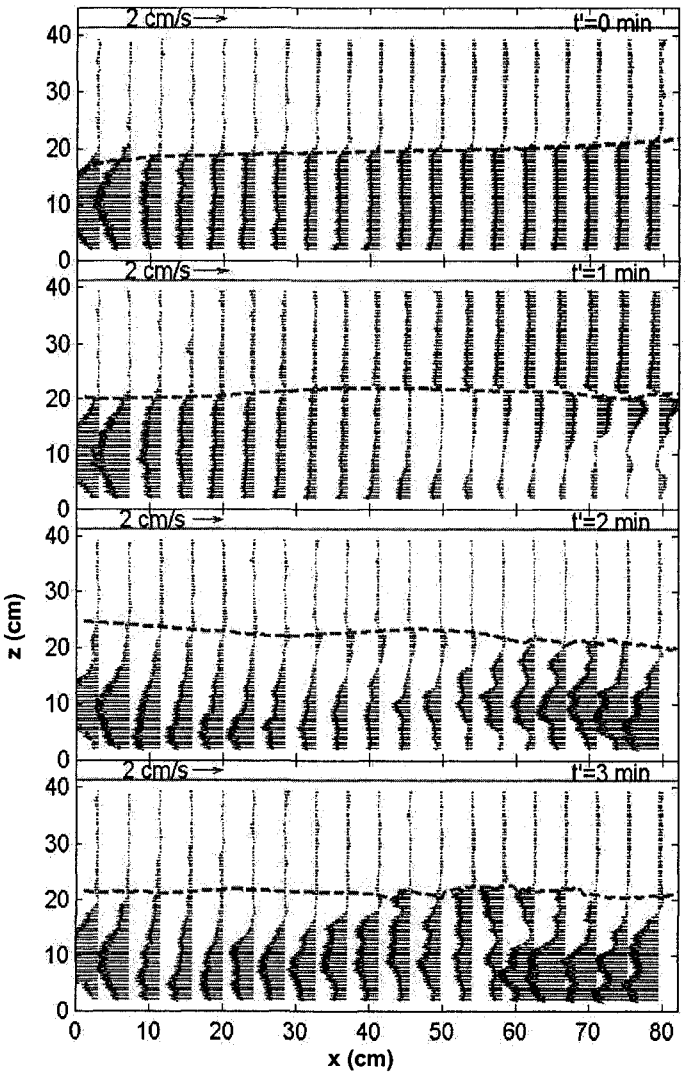

Fig 5. 9 Horizontal velocity profiles in the intake area in Exp. 4. Interface was shown in dash line.

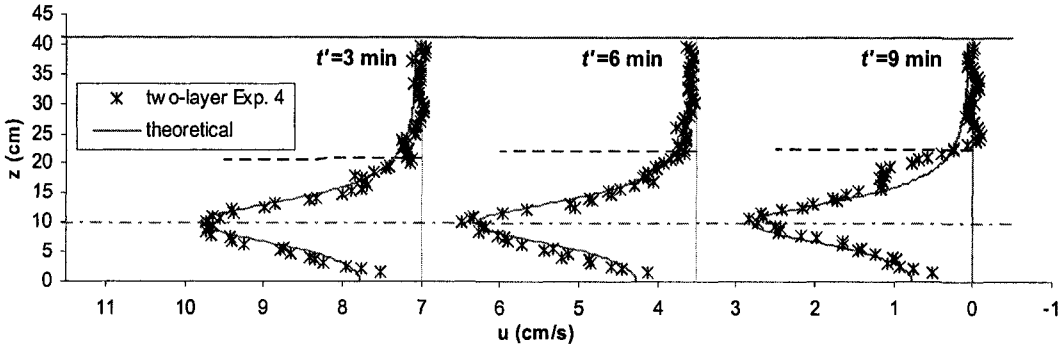

Fig 5. 10 Comparison of experimental u in Exp. 4 to the potential solution for homogeneous flows of Shammaa *et al.* (2005) at $x=3d$ upstream of round intake. Interface at a certain time intervals was shown in dash line. Intake level was shown in dash-dot line.

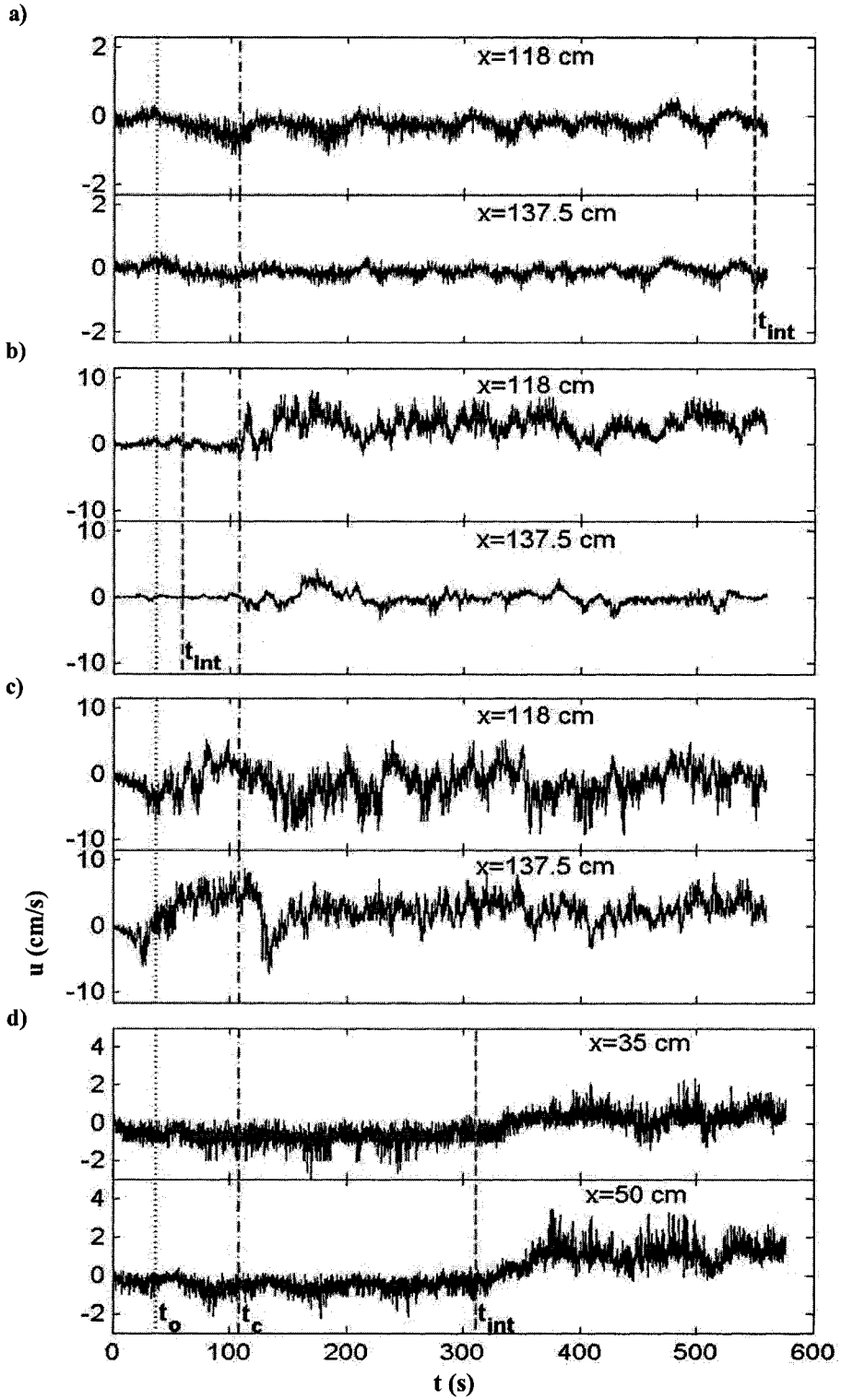

Fig 5. 11 Instantaneous horizontal velocity u in Exp. 1 at: a) z=38 cm, b) z=18 cm, and c) z=8 cm in the curtain area, and d) z=32 cm in the intake area.

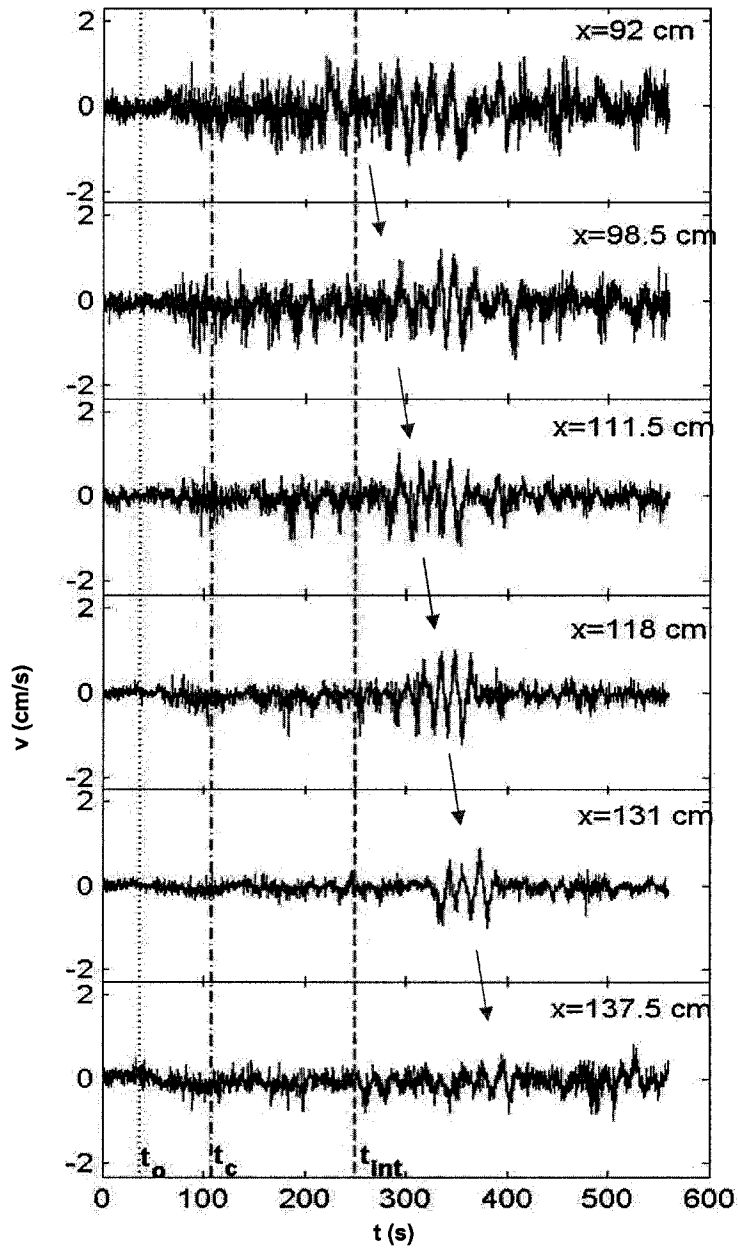

Fig 5. 12 Instantaneous vertical velocity v in Exp. 1 at z=33 cm. the arrows show a series of waves created around t_{int} and moved to the right as time passing.

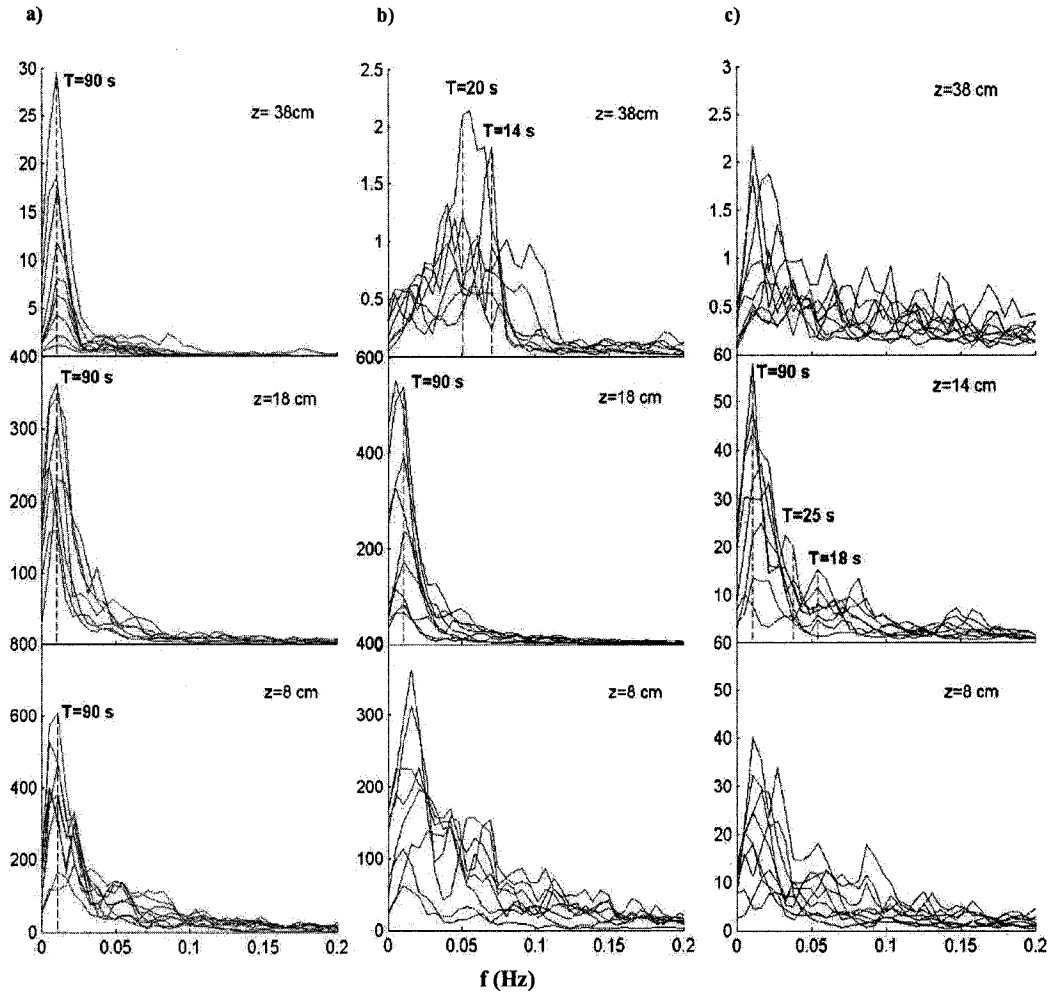

Fig 5. 13 Spectra of Exp. 1.: a) *u* in the curtain side, b)and c) *v* in the curtain side and in the intake side, respectively.

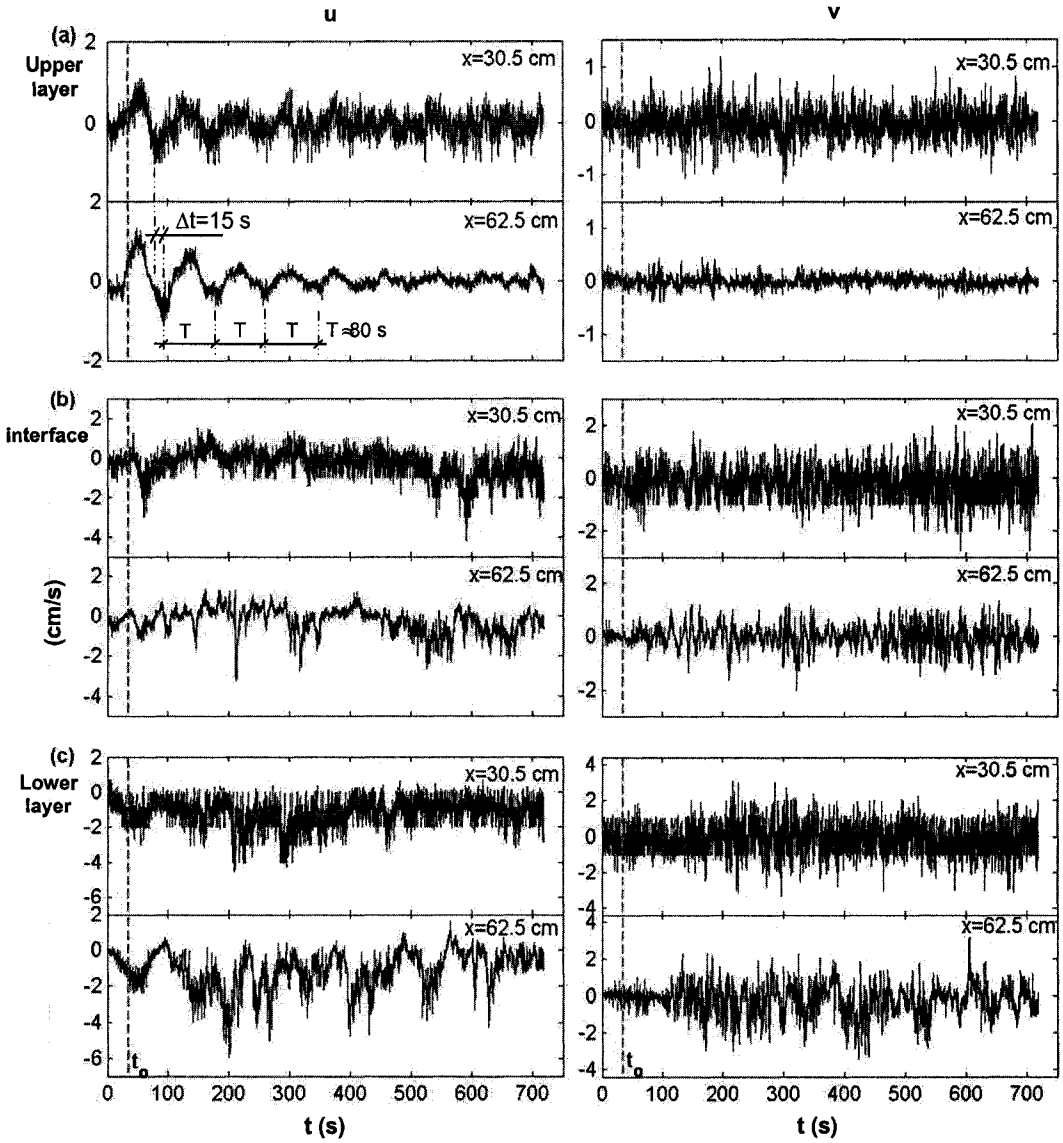

Fig 5. 14 Instantaneous horizontal u and vertical v velocity in Exp. 4 at: a) z=32.3 cm (upper layer), b) z=21.7 cm (interface), and c) z=11.1 cm (lower layer).

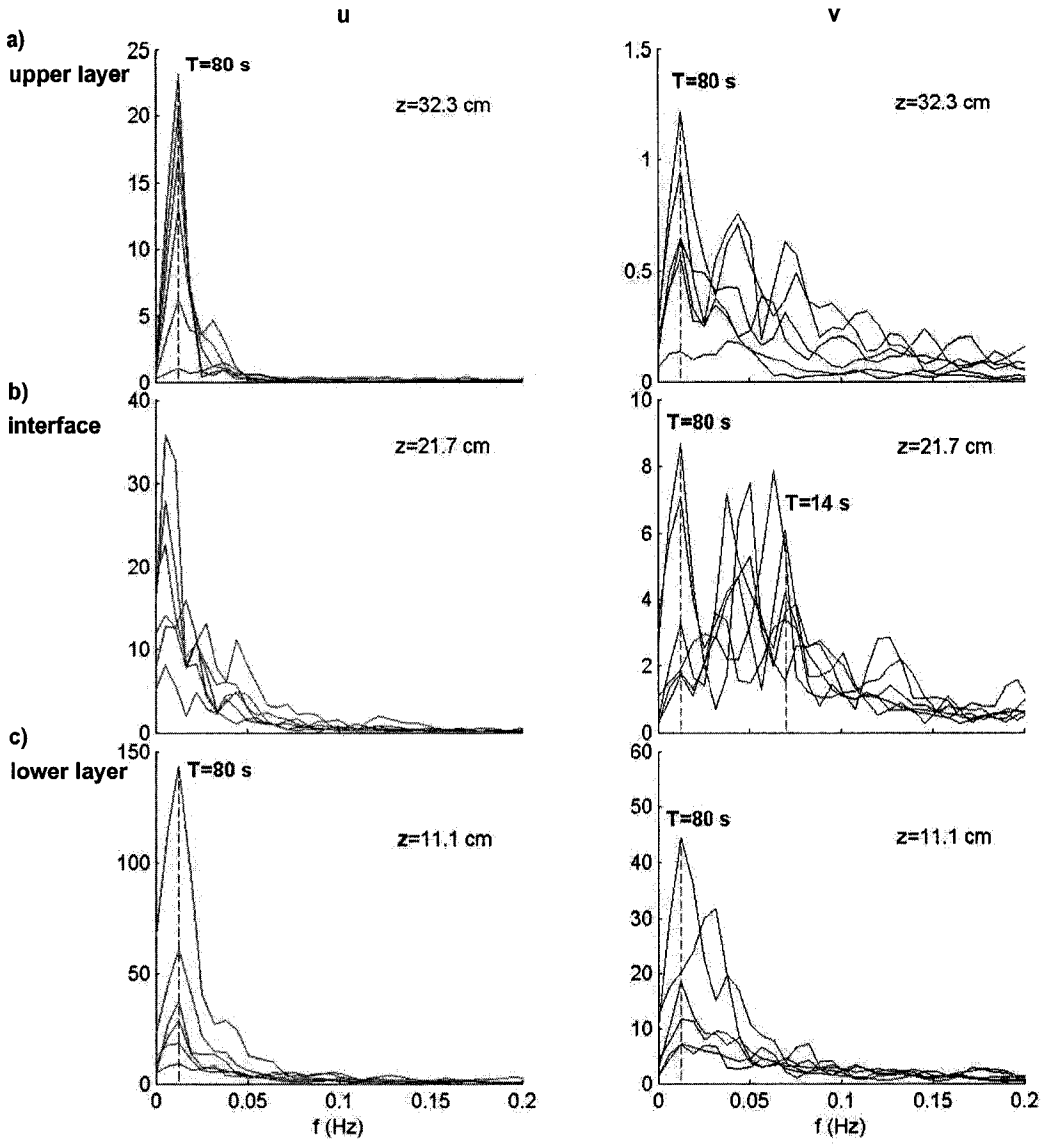

Fig 5. 15 Spectra of u and v in Exp. 4. at the intake side at: a) z=32.3 cm (upper layer), b) z=21.7 cm (interface), and c) z=11.1 cm (lower layer).

References

Anohin, V.V., Imberger, J., Romero, J.R., and Ivey, G.N, 2006. "Effect of Long Internal Waves on the Quality of Water Withdrawn from a Stratified Reservoir", *J. Hydr. Engrg.*, 132(11), 1134-1145.

Bureau of Reclamation, 1997. http://www.doi.gov/pfm/acct97/bor.html.

Craya, A., 1949. "Theoretical research on the flow of nonhomogeneous fluids", *La Houille Blanche,* 4, 44–55.

Drori, U., Dubovsky, V., and Ziskind, G., 2005. "Experimental verification of induced ventilation", *J. Environ. Engrg.*, 131(5), 820–826.

Farrow, D.E., and Hocking, G.C., 2006. "A numerical model for withdrawal from a two-layer fluid", *J. Fluid Mech.,* 549, 141–157.

Fernando, H., 1991. "Turbulent mixing in stratified fluids", *Ann. Rev. of Fluid Mechanic*, 23, 455-493.

Fischer, H.B., List, E.J., Koh, R.C.Y., Imberger, J., and Brooks, N.H., 1979. *Mixing in inland and coastal waters*, Academic, Boston.

Goldstein, S., 1931. "On the stability of superimposed streams of fluids of different densities", *Proc. Roy. Soc. Lond. A,* 132, 524-548.

Heiselberg, P., Svidt, K., and Neilson, P.V., 2001. "Characteristics of airflow from open windows", *Building and Environment*, 36, 859-869.

Horn, D. A., Imberger, J., and Ivey, G.N., 2001. "The degeneration of large-scale interfacial gravity waves in lakes", *J. Fluid Mech.*, 434, 181–207.

Imberger, J., and Hamblin, P.F., 1982. "Dynamics of lakes, reservoirs and cooling ponds", *Ann. Rev. of Fluid Mech.* 14, 153–187.

Imberger, J., and Patterson, J.C., 1990. "Physical limnology", *Applied mechanics*, Vol. 27, T. Wu, ed., Academic, Boston, 303–475.

Kataoka, T., Tsutahara M., and Mizutani S., 2001. "Selective withdrawal through a line sink of non-rotating and rotating stratified fluid in a reservoir of finite depth", *Eur. J. Mech. B-*

Fluids, 20, 167–186.

Kuznik, F., Rusaouen, G., and Hohota, R., 2006. "Experimental and numerical study of a mechanically ventilated enclosure with thermal effects", *Energy and Buildings*, 38, 931-938.

McGrath, J.L., Fernando, J.S., and Hunt, J.C.R., 1997. "Turbulence, waves, and mixing at shear-free density interfaces. Part. 2 Laboratory experiments", *J. Fluid Mech.*, 347, 235-261.

Monismith, S.G., 1985. "Wind-forced motions in stratified lakes and their effect on mixed layer shear", *Limnology Oceanography*, 30, 771–783.

Saggio, A., and Imberger, J., 1998. "Internal wave weather in a stratified lake", *Limnology Oceanography*, 43, 1780–1795.

Shammaa, Y., Zhu, D.Z., and Rajaratnam N., 2005. "Flow upstream of orifices and sluice gates", *J. Hydr. Engrg.*, 131(2), 127-133.

Stashchuk, N., Vlasenko, V., and Hutter, K., 2005. "Numerical modeling of disintegration of basin-scale internal waves in a tank filled with stratified water", *Nonlinear Processes in Geophysics*, 12, 955–964.

Stevens, C., 1999. "Internal waves in small reservoir", *J. Geophysical Res.*, 104, 15 777–15 788.

Stevens, C., and Lawrence, G.A., 1997. "Estimation of wind-forced internal seiche amplitudes in lakes and reservoirs, with data from British Columbia, Canada", *Aquat. Sci.*, 59, 115–134.

Taylor, G.I., 1931. "Effect of variation in density on the stability of superimposed streams", *Proc. Roy. Soc. Lond. A*, 132, 499-523.

Tory, C.D., and Koseff, J.R, 2005. "The generation and qualitative visualization of breaking internal waves", *Experiments in Fluids,* 38, 549-562.

Vermeyen, T.B., 2000. "Application of flexible curtains to control mixing and enable selective withdrawal in reservoirs", *Proceeding of the 5th Intl. Symposium on Stratified Flows*, 457-462.

Vermeyen, T.B., 2001. "Lake Natoma temperature curtains pilot project", *The Water Forum, Sacramento, CA, Tech. rep.,* 24p.

Wood, I.R., 2001. "Extensions to the theory of selective withdrawal", *J. Fluid Mech.,* 448, 315-333.

Chapter 6

Experiments on Horizontal Plane Buoyant Jets in a Shallow Enclosure

6.1. Introduction

Density-induced flow phenomena may result from fluids of different temperature, different suspended sediment or dissolved solid concentration, different salinities, or different gases (Turner, 1986). Examples include sewage discharges into riverine or brackish estuarine waters, thermal effluents from power stations, ocean dumping of sludge, cooling tower, ventilations, and deep sea vents. In all these examples the density flow are studied as buoyant jets and plumes where the flows characterized by a near field zone (close to the source) and far field zone (away from the source). Another two zones might appear if a lighter buoyant flow reached the surface of a denser ambient: impingement zone and a horizontal flow zone.

Buoyant jets have been studied extensively both theoretically and experimentally in deep domains (see most recently: Jirka, 2006). However, many industrial and environmental effluent discharges can be categorized as buoyant jets in shallow depths (Kuang and Lee, 2006). Heat disposal, for instance, may be injected in relatively shallow water. This occurs because the near-shore areas adjacent to power-plant sites are often shallow and because the large quantities of heated water discharged usually require discharge sources of large dimension (Harleman and Stolzenbach, 1972).

Buoyant jets discharging into enclosures of water domain are probably rare engineering cases. However, a recent reservoir's retrofitting solution for selective withdrawal proposed by Vermeyen (2000) is an example of such a flow. The solution includes a curtain that creates an enclosed reservoir within a reservoir. Sound understanding, therefore, that the hydraulics and mixing characteristics of such flows in water domains is needed.

A major interest usually accompanied buoyant jets studies is their dilution with respect to

both time and space. This problem is more than adequately resolved for deep ambient (Ulasir and Wright, 2003). More work however, is still going on in finite depths as the bounding surface serves to re-direct the impinging buoyant jet horizontally causing additional mixing (Wright *et al.*, 1991; Roberts *et al.*, 1997). The rate of dilution, on the other hand, is considered "environmental" depending whether the mixing is desirable or not. In sewage, for example, the quick dilution is desirable (Koh and Brooks, 1975). In contrast, in fires, the slower smoke mixing will be safer Cheung *et al.* (2006). In stilling basins, it is also important to minimize the mixing so that small particles will not be provoked to suspend (Roland *et al.*, 2003).

In enclosures, buoyant-jet flows are more complicated than in unconfined domains and affected by several factors including: the impact of the inflow velocity (jet), mixing and entrainment at the interface, and interfacial wave characteristics and their effect on the withdrawal as well as the domain geometry. The flow will also be transient. Consequently, the dilution wouldn't be determined locally and a general reservoir-size will be searched instead. The problem, on the other hand, comprises several parameters like the reservoir's shape and dimensions, the size and type of the inlet and the outlet, and the reservoir operation (discharges). Therefore, to study such a flow, simplified conditions should be compromised.

This chapter presents the results of an experimental study on wall plane buoyant jets released horizontally in a confined reservoir "enclosure" with a round outlet. The density difference was the only variable to change in the experiments. Our interest here is to examine the mean flow evolution in the reservoir as well as the withdrawal quality (dilution with time). The effect of the internal wave in the flow evolution was also investigated. The study also provides a detailed mean velocity field which is essential for validating future numerical modeling of such flows. The characters and spectra of the instantaneous velocity were also examined. Some characteristics of the jet trajectory were also enlightened and compared to the available literatures.

6.2. Literature Review

It appears that the fundamental work of plane buoyant jets in shallow depths is probably related to Jirka and Harleman (1979) who studied these jets in a limited channel depth and demonstrated that the flow may be either stable (strongly buoyant) or unstable (weakly buoyant) with flow circulation and re-entrainment into the jet. They stated that stable situation usually involves an internal hydraulic jump associated with a roller. Thus they introduced the terminology of "flow instability" to denote the dilution initiated by a direct interaction of the jump with a confining boundary. They also demonstrated that the near field stability depends only on the jet discharge densimetric Froude number and the relative depth, and is not affected by downstream control. This result has been reconfirmed by Lee and Jirka (1981) and Wright *et al.* (1991). However, the subsequent experimental study of Andreopoulos *et al.* (1986) who carried out experiments in a relatively short channel L=2.2 m (and $L/H \approx 3$) has found that the presence of a strong downstream control resulted in a flooded jump. Rajaratnam and Subramanyan (1985) have considered plane buoyant surface jets and demonstrated that if the internal jump depth increases, due to some downstream effect, the two layer structure in the jet vicinity is destroyed and a flooded jump occurs; and hence the flooded jump is a transition from the stable to unstable situation. Recently however, Kuang and Lee (2001, 2006) have shown numerically that this downstream control effect is valid for all buoyant discharges as long as L/H<6.

It is interesting on the other hand, that the experiments of Baddour and Abbink (1983) on buoyant plane underflows (wall jet) in shallow and short channel have showed the same type of flow situation as did Jirka and Harleman (1979) when there is no down-stream control. Rajaratnam and Subramanyan (1986) have also studied the behaviour of the plane turbulent denser wall jets and provided diagrams for predicting their growth rates. Roland *et al.* (2003) have studied experimentally the horizontal buoyant jets flow into a denser sludge in final settling tanks. They showed that the filter effect of the fluidized flow regime is mainly dependent on the jet velocity and on the sludge depth such that: the higher the jet velocity and

the lower the sludge depth (bottom layer), the more suspended solids particles reach the clear water zone (upper layer).

When a denser jet released at the bottom of a less density ambient, the leading edge of the jet will flow as a gravity current. A comprehensive review of density currents entering stratified or un-stratified lakes and reservoirs was reviewed and evaluated by Alavian *et al.* (1992). More broad review of the gravity current was also presented by Simpson (1997). Similar gravity current could be observed when a lighter fluid enter a denser domain as could be seen in underground coal mines, where the stratified methane layer attached to the ceiling of the mineshaft moves along the tunnel with a constant speed (Benjamine, 1968). Chen (2000) has reviewed the progress of research on smoke propagation in tunnels and developed a gravity current approach to predict its behavior.

Buoyant flows into enclosures have received a little attention in civil engineering literature. Our previous two-layer selective withdrawal study using curtain technique, however, is an example of such studies (refer to chapter 4). In ventilation, however, the air-jet diffused into a ventilated enclosure has received a substantial consideration recently (see for example: Etheridge and Sandberg (1996), Yu and Hoff (2002), Yu *et al.* (2003) and Yu (2005, 2006)). Yu (2005) and Yu (2006) derived a theoretical equation describing the trajectory of horizontally diffused plane air wall jet in a non-isothermal ceiling slot-ventilated enclosure. To better understand the influence of gap sizes on the smoke spread, Cheung *et al.* (2006), have performed a numerical study on different door gap configurations affecting the smoke progress in an enclosure fire.

6.3. Experimental Procedures

Experiments were conducted in the same set up described in Chapter 4. However, with an initial difference that is the two water bodies in the inner reservoir and outer one were separated before the beginning of the experiment using a sliding gate as could be seen in Fig 6.1. The rectangular tank has a 6.0 m long, 0.5 m wide, and 0.5 m high as shown in Fig 6.1. The barrier (curtain) opening a=2cm which gives a vena contracta depth b_o=0.6a=1.2 cm (Rajaratnam and Subramanaya, 1967). The inner reservoir was filled with salt water and the outer one with fresh water in three experiments (Exps. 1, 2, and 3, and called "plume-jet" experiments). Whereas, opposite scenario has been applied for one "jet-plume" experiment (Exp. 4). Rhodamine 6G dye was always used in the outer reservoir. In all experiments, the outlet height was fixed to 30 cm above the bed. The discharge used was Q_o=600 cm^3/s (36 l/m). Three different g' were used for the plume-jet experiments: g'≈1.5, 3.0, and 0.15 cm/s^2 for Exps. 1, 2, and 3, which gives initial densimetric Froude numbers (at the vena contracta) F_o= 7.5, 5.5, and 23, respectively. For the jet-plume experiment g'=1.5 cm/s^2. The total water depth was H=41.2 cm in all experiments. As demonstrated in Chapter 4, the size of the barrier opening a=2 cm was merely chosen to create a turbulent jet where calculated Reynolds number gives Re=1200. Table 6.1 summarizes the condition of the experiments. All other experimental details and measurement techniques were basically the same as described in Chapter 4.

In order to detect the interface in the LIF images, on the other hand, a threshold grey scale (I) was used to determine the end of the mixing depth at a certain time (i.e. certain image). However, to account for the mixing change in the reservoir, I in the mixing zones was also necessary. An accurate I requires long complicated calibration procedures (see e.g. Cowen *et al.* (2001) and Law and Wang (2000)) that are not in the scope of this study. Rather, a simplified pre-experiment calibration was done as follows.

The inner reservoir was filled with a mixture of salt water (with "intended" g'=1.5 cm/s^2), particles, and dye up to a certain depth (from 5 to 41.2 cm with about 2.5 cm increase each

time). For each depth, LIF images was recorded for about 20 sec (200 images) and then averaged to get one representative image. The profiles of gray scale values I at several x-distances were plotted for each representative image. As the mixed fluid was homogeneous, the gray scale values should be constant along the profile. Therefore, the deviations of each profile from the vertical line corresponding to the maximum grey scale value (I_{max}) were considered as the correction values. For different filling depths, these profiles have found to have a general linear deviation with depth starting shortly below surface water with an average declination of 2-4 gray scale units each 1 cm depth. This deviation (appeared to be mainly due to laser light "attenuation") summarized the total correction needed for a certain profile. Thus, a reversed inclination has to be compensated in the experiments.

An example of this I profiles was shown in Fig 6.2 at three x-sections (x=50, 75 and 100 cm) for three initial filling H=25, 35 and 41.2 cm. General linear attenuation could be observed in Fig 6.2 for different x-sections and H with a slope of about 2.5-4 gray scale unit/cm. It could be notice however, that the I_{max} (which are supposed to be at the water surface) were not constant for the whole profiles. For example, I_{max} was about 252 at x=50cm for H=35 cm whereas it was about 180 and 215 at x=100 cm for H=41.2, and H=25 cm, respectively. This was due to several reasons: the fact that the Laser was relatively far from the water surface (to cover large areas) and therefore its rays were not distributed evenly along the water surface of the reservoir; the laser has a fringe error so that some areas enlightens more than the others; and the laser light intensity had some fluctuations along the time. However, I_{max} were not important in the experiments and rather, the decrement of these values along the depth was the important issue. Notice however, that I correction should not be applied to the non-dyed layer. Notice also that the images were digitized at 8-bit grey-scale resolution and thus the maximum possible I was 255.

As this calibration considered only a homogeneous "colored" layer and doesn't account for an existence of a lower "mixed" density (lower light intensity) below the high density fluid (as will be seen in Exps. 1, 2, and 3), the calibration slope was considered half of that

found above (i.e. 1-2 gray scale unit/cm). For generality, a calibration value of 1.5 gray scale unit/cm was adopted in these experiments. For Exp. 4 however, as the denser "dyed" fluid was in the bottom of the reservoir, vertical line at the maximum gray-scale value was enough to represent the bottom "dense" layer at any x-section. The depth of the above mixing layer however, was found relatively small and the gray scale correction was in fact not important and thus it was ignored in this specific experiment.

It should also be mentioned that the dye concentration was kept in the experiments below 0.1 μg/l (100 ppb) in order to guarantee the linear response of the luminescence-concentration relation (McGrath *et al.*, 1997; Ferrier *et al.*, 1993). Ferrier *et al.* (1993) stated that the linear response of Rhodamine 6G is up to 50 μg/l, however for a constant laser power. On the other hand, since the molecular diffusivities of salt and Rhodamine 6G are approximately the same (McGrath *et al.*, 1997), the changes of the salt concentration (density) could be monitored by tracking the concentration of Rhodamine 6G.

For the PIV measurements, on the other hand, two runs were conducted one with the barrier 'curtain' area in focus and the other with the outlet area in focus. A slight time adjustment between the two runs was therefore needed and a consequence discontinuity has thus resulted when the measurements overlapped at a certain x-section in the middle of the reservoir. Velocity measurements were only obtained for Exp. 1 and 4. As pre-cautioned in Chapter 4, measurements of about 1-2 cm strips around the reservoir's edges (walls, bed, and water surface) were not possible. Also, measurements close to the jet mouth were not accurate (Refer to Appendix A).

6.4. Experimental Results

Observations

Withdrawal discharge was slowly increased in the experiments (in a period t_o) from zero to the steady discharge Q_o. To reduce the disturbances created by initial transient effects, this increase in the discharge was controlled to take a minimum of about 40 s. Observations showed that this period is somehow enough for the flow field to be established everywhere in the reservoir. After that, the discharge remains at Q_o for about 15 min in all experiments. As the replenishing fluid to the inner reservoir was different in density, the interface position changed significantly as well as different front-flow behavior was observed during the experiments. Observations of plume-jets experiments (Exp. 1, 2, and 3) will be shown first followed by the jet-plume experiment (Exp. 4).

Plume-jets

Time series of the flow evolution in Exp. 1 was shown in Fig 6.3 while two selective images from Exps. 2 and 3 were shown in Fig 6.4-a and 4-b, respectively. Fig 6.3 showed that, driven by the high momentum at the jet opening, the flow advanced horizontally for a short distance (~7 cm) where it then, affected by the buoyancy, turned vertically behind the barrier wall until it reached the water surface. The thickness of this upward buoyant jet seemed constant later on till about t=6 min. A surface buoyant current could then be observed up to the middle of the reservoir where afterwards its leading-edge has thinned and sharpened as it goes towards the intake where it reached it around t=80 s (see Fig 6.3-a at t=80 s). An internal hydraulic jump could be observed as well in Fig 6.3-a. This jump was similar in principle to that observed by previous studies in longer channel lengths (e.g. Jirka and Harleman (1979), Rajaratnam and Subramanyan (1985), and Baddour and Abbink (1983)). However, this "stability" observation was quickly broken here after a short time.

The buoyant flow has then thickened close to the intake wall as could be seen in Fig 6.3-b at t=111 s. This was probably due to the 3-D flow around the outlet as well as the effect of the seiches. The interface was then observed to move backwards until it reached the barrier by t=183 s as could be seen in Fig 6.3-c. Meanwhile, the upper layer was thickening and somehow a "flooded jump" similar to that described in Rajaratnam and Subramanyan (1985) and Andreopoulos *et al.* (1986) has been observed and the previous stability has then broken. Notice that it took about 183-111=82 s for the interface to move from the reservoir's one end to the other. Around t=360 s (6 min), however, the jet trajectory started to expand horizontally. At t=510 (8.5 min), for example, the jet has passed about 30 cm before it turned upward as could be seen in Fig 6.3-d. Even at this time of the experiment, Fig 6.3-d showed also that there was still about 2 cm layer of heavier fluid at the bottom.

Kelvin-Helmholtz (K-H) waves were observed sliding upstream along the interface in the early stages of the experiments as a cause of the high shear created while the surface buoyant flow was advancing horizontally. The direction of billow roll-up was consistent with the sense of the wave-induced shear, leading to counter-clockwise billow roll-up in wave crests, for a right-to-left traveling wave (see Fig 6.3-a). The waves caused a significant mixing which resulted in, at least, one intermediate stratum (see the intermediate layer in Fig 6.3-a and b especially in the first half of the reservoir). Eventually, the intermediate layer prevailed most of the reservoir length within the first 3 minutes of the experiment (see Fig 6.3-c at t=183 s). Observations showed that K-H waves were then mainly constrained to the edges of the vertical flow behind the barrier. However, due to the reduction of the buoyancy effect (due to mixing) in comparison to momentum one in the later stages, these waves became rare and less effective. Holmboe waves were also observed at the interface between the middle "mixing" layer and the lower original heavy layer (see Fig 6.3-c). They were generally carried on the longitudinal waves and thus moving in accordance to their movements. Starting from about minute 8 (t=480 s), however, the bottom interface seemed sharp and didn't show a trace of interfacial waves as could be seen in Fig 6.3-d at t=510 s. Other 'irregular' interfacial waves

were also observed especially along the vertical buoyant flow behind the barrier. Internal seiches were also observed along the experiment. The characters of these waves will be discussed later.

Flow in Exp. 2 has generally behaved similar to that in Exp. 1 however the phenomenon of jet expansion observed from about t=360 s (6 min) in Exp. 1 has never been observed even after t=840 s (14 min) in Exp. 2. Also, the average thickness of the vertical buoyant flow in Exp. 3 was about 5 cm (see Fig 6.4-a at t=234 s) while it was about 10 cm in Exp. 1.

In Exp. 3, a large circulation was observed from the early stage of the experiment which caused a huge mixing behind the barrier (see Fig 6.4-b at t=61 s). The figure was also showed that the jet expanded in a slope 20%, same as that of a classical wall jet (Rajaratnam, 1976). The returning flow was around x=75 cm as could be seen in Fig 6.4-b. In comparison to the case g'=0 (homogeneous flow) this returning was around x=50 cm (i.e. about 100 cm from the barrier).

Jet trajectories in the initial stage (up to about t=3 min) in Exp. 1 (F_o=7.5) and Exp. 3 (F_o=23) before it turned backwards were plotted in Fig 6.5. The jet trajectory was taken from the LIF images approximately at the center thickness of the "dyed" inflow. This approximation was reasonable in Exp. 1 as the jet thickness was relatively thin (maximum 2 cm). In Exp. 3, the trajectory was drawn beyond the "linear" jet expanding. Trajectory in Exp. 2 was very short to be drawn before it turned towards to wall. The experimental results of Anwar (1969) for round jets for F_o=8 and Cederwall (1968) for F_o=20 in unconfined depths and the corresponding numerical results of Law *et al.* (2003) were also added to Fig 6.5. Fig 6.5 showed that for F_o=7.5 the jet trajectory was closer to the wall than the experimental results of Anwar (1969) and the corresponding numerical of Law *et al.* (2003). The localized pressure in the confined zone between the "plane" jet and the barrier was reduced due to the entrainment demand which caused the jet to quickly attach to the wall. This localized decrease in pressure is called "Coanda effect" (Coanda, 1936). Apparently, Coanda effect didn't appear in the round jets experiments of Anwar (1969) as the corresponding zone was

not confined. In Exp. 3 however, the jet trajectory was expanded horizontally more than that of Cederwall (1968) and Law *et al.* (2003) (see Fig 6.5). The reason for that is not clear. However, it also appears to be related to Coanda effect below the front of the plane wall buoyant-jet.

The horizontal expansion Δx of the jet before it turned upward beyond t=360 s (6 min) in Exp. 1 was plotted with time in Fig 6.6. The figure has showed that this expansion drew a quadratic curve according to the equation (for convenient coefficients, t was used in min):

$$\Delta x = -0.6397\ t^2 + 17.558\ t - 76.655 \qquad r^2 = 0.9989 \quad \ldots\ldots (1)$$

As the jet expansion was due to mixing increment in the reservoir, this quadratic relation implemented that the overall mixing beyond t=6 min was almost steady and was proportional to t^2. To verify this conclusion, the change of the relative withdrawal of the dense inflow Q_2/Q_o (will be explained later) was also added to Fig 6.6 where this change has also drawn a quadratic curve.

Jet-Plume

A time series of the flow evolution in Exp. 4 were shown in Fig 6.7. The denser flow advanced as a gravity current (see Fig 6.7-a at t=40 s) until it reached the intake around t=65 s. The interface has then retuned back and reached the barrier around t=140 s (with elapsed time 140-65=75s). Shortly after the returning flow hit the barrier, the interface was deeply dipped above the jet close to the barrier as could be seen in Fig 6.7-b at t=155 s. The combined effect of the jet entrainment as well as the seiches (trough mode) has probably caused this dip. A cusp-like curve (similar to the 'critical withdrawal curve' known in a two-layer withdrawal) was noticed close to the intake while the interface was rising as could also be seen in Fig 6.7-c, and d. This curve was fluctuating, however, up and down according to the internal seiches modes (peak and trough) as could be seen in Fig 6.7-c for peak mode at t=257 s. In the late experiment stage, the mixing process decreased significantly and, except at the top utmost, the flow in the reservoir was similar in sense to that of a two-layer

withdrawal as could be seen in Fig 6.7-e at t=585 s. A thin top mixing layer, however, could still be observed in the figure. Generally, Fig 6.7 showed similar behavior to Exp. 1 (but with reversed depth); however, differences were also noticed like the cusp-like curve observed at the intake vicinity and the interface dipping close to the jet as well as a general slower interface rising.

Wave activities were generally similar (but more intensive) to those observed in two-layer withdrawal experiments (refer to Chapter 4) where the main effect of these waves (mainly K-H) was concentrated in the jet zone (see Fig 6.7-a and b). These waves caused a considerable mixing as could be seen in the jet zone in Fig 6.7-c.

Mixing and Withdrawal Quality

Studying Figs 6.3 and 6.4 have shown that the mixing expansion in Exp.1 has covered about 75% of H by t=183 s ($\approx$3 min) as could be seen in Fig 6.3-c whereas it only covered about 60% of H by t=234 s ($\approx$4 min) in Exp.3 as could be seen in Fig 6.4-a. Also, almost homogeneous intermediate mixing layer was observed in Exp. 1 in the middle of the experiment as could be seen at t=550 s in Fig 6.3-d whereas almost two distinguish layer "stable flow" could be observed in Exp.2 at earlier time as could be seen in Fig 6.4-a at t=234 s. In plume-jet experiments (Exps. 1 to 3), on the other hand, the general mixing speed was inversely proportional to g' (i.e. proportional to F_o). This was evident in Exp. 3 where the original dense water almost disappeared all over the reservoir by t=284 s (less than 5 min) (not shown). It appeared that the jet expansion was the main reason of this result as it allowed more mixing with the surrounding water. In comparison to a homogenous flow case (g'=0) this time was about 150 s (2.5 min). It was concluded, thus, that if both Q_o and H/b_o were fixed, the downstream effect in enclosures becomes less important as g' increases (F_o decreases) and the case approaches to the "stable" one observed in previous buoyant jet studies (e.g. Jirka and Harleman (1979), Rajaratnam and Subramanyan (1985) and Andreopoulos *et al.* (1986)).

The critical withdrawal depth h_c from two-layer withdrawal at the outlet agrees with the previous result as this depth decreases when g' increases according to the equation $h_c=(Q_o^2/(6.5*g'))^{1/5}$ (Craya, 1949). Using this equation, the calculated critical depth was about 13, 8.2, and 7.1 cm for Exp. 2, 1, and 3, respectively. It could also be noticed that using an equation of h_c in a linear stratification (as will be seen later for Exp. 1) would give the same trend in h_c. Thus, when h_c increases, the mixing layer will be more quickly washed out through the outlet and more likely a "stable" flow will be prevailed longer time.

Quantitatively, on the other hand, the mixing phenomena in Exp .1 (plume-jet) and Exp. 4 (jet-plume) were investigated by following the mean interface as well as the withdrawal change with time. The interface pointing to the end of the mixing layer at several time intervals in both experiments was detected using a threshold gray-scale value I ranged between 45 to 55 (depending on the light intensity changes with time and in a manner consistent with the free eye sight). The interface away from the intake (about 17 cm) and away from the high activity waves close to the barrier (about 45 cm) was then averaged to get the mean interface position $h_{i\ avg}$. $h_{i\ avg}$ was measured from the bed for Exp. 4 and form the water surface in Exp. 1. The change of $h_{i\ avg}/H$ with time was depicted in Fig 6.8 for both Exps. 1 and 4. For the sake of comparison, the corresponding interface change for a two-layer withdrawal with same hydraulic conditions to those in Exps. 1 and 4 except that its initial lower layer depth ($h_{i\ avg}$=10 cm) was close to the initial gravity current depth in Exp. 4 was also added to Fig 6.8 (refer to Chapter 4 as well).

Fig 6.8 showed that $h_{i\ avg}/H$ increased quickly in the initial stage of all experiments, however with faster rate's order: Exp.1, Exp. 4, and then two-layer, respectively. Whereas, this increment slowed down in the later stages with almost equal rate for all experiments (say beyond t=200 s; see Fig 6.8). This trend represented the rate of overall mixing process in the enclosure. As the initial conditions were almost similar in all experiments, the faster rate of mixing in the plume-jet experiment was probably related to the relatively higher jet entrainment in Exp. 1 as it had to flow horizontally then vertically and to the shear waves'

effect which was more spatially spread and longer timely active along the experiment course. Whereas, these waves were mainly concentrated in the barrier area and in the early stages in both Exp. 4 (jet-plume) and two-layer experiment (refer to Chapter 4). The internal waves occurred in Exp. 4, were more intensive than that occurred in two-layer experiment due to the initial "damping" cover (10 cm) in the later case. Internal seiches were also observed to significantly increase the mixing in the early stages of Exp. 4 as it drove the flow back to the inflow (jet) zone as was observed in Fig 6.7-b. Thus, the interface rising was faster in Exp. 4 than that in the two-layer case. The internal seiches, however, were believed to have the same mixing rule in both Exp. 1 and 4. Another finding in Fig 6.8 is that the interface in both Exp. 1 and 4 exceeded the "end" critical withdrawal level defined by the two-layer withdrawal concept (see Fig 6.8). In Exp. 4, this exceeding was due to the mixed layer sustained above the lower layer even late in the experiment; whereas in Exp. 1, this was due to the continuous (but gradually slowing down) effect of the jet entrainment.

The overall withdrawal quality was studied based on the light intensity distribution in the images along the time. Gray scale profiles at several x-sections (in the same distance used for the interface detection; i.e. between x=17 and x=105 cm) where plotted and were then corrected according to the calibration result explained before (refer to "experimental procedure"). Examples of these corrected profiles at x=75 cm for both Exps. 1 and 4 at several time intervals were shown in Fig 6.9. For the sake of comparison, all profiles in Fig 6.9 were plotted to have the same I_{max} and I_{min}. I_{max} and I_{min} were indicating to the density of original lighter and denser fluids, respectively in Exp. 1 whereas they pointed out to the opposite indications in Exp. 4. Also, I at any height was representing a density that is in linear correlation between I_{max} and I_{min} (refer to experimental procedures).

Fig 6.9 showed the large expansion depth of mixing layer in Exp. 1 in comparison to that in Exp. 4 in all times of the experiments. As also observed in other x-locations, Fig 6.9 showed linear-like density stratification between the upper lighter and the lower denser layers in Exp. 1. This reflected that the mixing was more spread and homogeneous in Exp. 1 than

locally concentrated in Exp. 4. In other words, the flow was more "stable" in Exp. 4.

Assuming that the gray scale profile at the plane of study (symmetric plane) represent the whole width of the reservoir and neglecting the changes close to the intake, the integrated area constrained between the profile's I_{max} vertical line, I_{min} vertical line, and the water surface at a certain time interval has represented the total upper fluid "volume" (with a thickness of 1 pixel). This area was calculated at several x-sections (minimum of three x-sections: x=50, 75, 100 cm) and then averaged and converted into m^3 to represent the upper fluid volume at a certain time interval. The change of the volume V_1 of the fluid existed originally in the reservoir in both Exp. 1 and Exp. 4 with time was plotted in Fig 6.10. V_1 was found to draw a power curve in both experiments. The figure also showed that V_1 decreased more quickly in Exp. 4 than that in Exp. 1. This was reasonable as the depth of the withdrawal (b=30 cm) was closer to water surface. For example, V_1 was about 0.04 m^3 and 0.09 m^3 at t=720 s in Exp. 1 and Exp. 4, respectively (see Fig 6.10).

The withdrawal from the fluid originally existed in the reservoir Q_1 was obtained from the change of V_1 with time. The change of Q_1/Q_o with time for both experiments was added to Fig 6.10. Fig 6.10 showed that Q_1 started to decrease around t=110 s and t=155 s in Exp. 1 and Exp. 4, respectively. According to selective withdrawal concept, these times are the critical withdrawal times t_{cr} where the flow before t_{cr} is only from one layer (sub-critical) whereas after t_{cr} the flow is from two layers (supercritical). Even though the inflow fluid has reached the outlet earlier than those t_{cr} in both experiments (80 s in Exp. 1 and 65 s in Exp. 4), however the interface was quickly returned back towards the barrier as observed previously which caused t_{cr} to be delayed. In Exp. 1 however, this process was a bit faster as the inflow fluid (in the upper most of the reservoir) was closer to the withdrawal level and thus this delay time was shorter (~30 s in Exp. 1 and ~90 s in Exp. 4).

Adopting the time scale t_w presented in Chapter 4 where t_w is the time of emptying a withdrawal layer defined between two lines, $2h_c$ apart, above and below the intake level, the change of Q_2/Q_o (where Q_2 is the withdrawal from the inflow fluid $=Q_o-Q_1$) in the

supercritical period (t-t_{cr}) was plotted in Fig 6.11. The corresponding change in the two-layer experiment (refer to Chapter 4) was also added to the Fig 6.11. Fig 6.11 showed that Q_2/Q_o was largely coincident in Exps. 1 and 4 in the initial period (up to about 0.68 t_w) and gradually (but slowly) separated afterwards with higher values in Exp. 4 than in Exp. 1. It was interesting to notice that Q_2/Q_o was increased much quicker in Exp. 1 and 4 than that in the two-layer withdrawal case up to about 0.68 t_w (see Fig 6.11). The increment was decreased afterwards gradually up to about 2-2.2 t_w where both curves of Exp. 1 and 4 intersected the two-layer's one. This probably reflects the effective rule of the internal waves as well as the initial starting effects in Exp. 1 and Exp. 4 than that in two-layer case. Beyond 2-2.2 t_w, Fig 6.11 showed that the withdrawal from the inflow fluid in the two-layer's case became larger than the other two cases. All curves, were still slowly continuing their rising when the experiments stopped.

It was noticeable that the time (0.68 t_w) found above to be a "mark" time was also the same found in Chapter 4 for the time the average interface of two-layer needed to reach the intake level (where Q_1=Q_2=0.5Q_o, see Fig 6.11 and also refer to Chapter 4). In comparison however, the withdrawal from the inflow fluid was Q_2=0.67Q_o at this time for both Exp.1 and 4 (see the small-dash lines in Fig 6.11). On the other hand, since Q_2/Q_o asymptotically approaches 1.0, a long time is required to reach 100% of Q_2/Q_o. Adopting the criteria represented in Chapter 4 of Q_2/Q_o = 97% as the time needed for the complete withdrawal from the inflow fluid, the corresponding time found in Chapter 4 for the two-layer case was about 4 t_w whereas it was found here about 5 t_w and 6.5 t_w for Exp. 4 and 1, respectively. The delay differences were probably related to the mixing layer remained at the bottom/top of the withdrawal layer in Exp. 1 and 4, respectively.

Finally, the change of Q_2/Q_o beyond t=360 s in Exp. 1 was drawing a quadratic curve with t as plotted in Fig 6.6 before (see Fig 6.6). This result confirmed what was previously suggested that the overall mixing beyond t=6 min was almost steady and was proportional to t^2 which in turns explained the steady expansion of the jet ($\alpha\ t^2$) beyond this time as was

shown in Fig 6.6 (refer to Fig 6.6).

Flow Velocity Field

Velocity vectors were found to change significantly along the experiment. Velocity vectors were averaged at certain time intervals over 2 seconds (=30 images at the curtain area and 20 images at the intake area). This short time averaging was needed due to the relative fast change of the flow conditions. We will discuss the velocity field in Exp. 1 (plume jet) followed by Exp. 4 (jet-plume).

Plume-jet (Exp. 1)

Fig 6.12 presented the velocity vectors in Exp. 1 at several t' ($t'=t-t_o$). At t'=30 s Fig 6.12-a showed the velocity vectors accompanied the surface current flow. A relatively large circulation was created in the lower front part of this current (see Fig 6.12-a at t'=30). A large circulation "flooded internal jump" was quickly developed around t'=120 s as could be seen in Fig 6.12-b. In comparison to Fig 6.3-c, we could see how this circulation was responsible for the intermediate mixing layer seen in Fig 6.3-c. Due to the backflow driven by the internal seiches, Fig 6.12-b has also shown significant velocity disturbance in the reservoir especially in the surface current zone where the velocity vectors have scattered at several locations.

After the bottom interface has joined that of the vertical buoyant jet, the large circulation above the interface became more regular and extended almost over the whole length as could be seen in Fig 6.12-c at t'=240 s. The vertical buoyant jet, however, was still existed which meant that its density difference with its neighbors was still high. The average interface $h_{i\,avg}$ dropping rate was considerably decreased by this time and the effect of sechies decreased by time as well. Eventually, (around t'=360 s) a strong recirculation zone started to develop between the jet deflection edge and the barrier while an opposite (weaker) counter clockwise circulation was developing in the rest of the reservoir length as could be seen in Fig 6.12-d at t'=720 s. Since the recirculation behind the barrier was expected to produce very little mixing

(refer to similar situation in Kuang and Lee (2006) and Lee and Jirka (1981)), the counter clockwise recirculation was the main reason for the remaining mixing process in the experiment.

It could be noticed that due to small water depth, the typical zone of established flow (ZEF) in the jet had very short length before the zone of surface impingement (ZSI) developed. Studying vertical velocity v profiles in both previous zones have shown non-typical and non-similar velocity profiles in both zones. Kuang *et al.* (2001) however, has reported non-similarity profiles in ZSI but not in ZEF. Their experiments however were for non-buoyant jet and for H/a=130. On the other hand, the dilution along the surface current was calculated at x=100 cm from the equation Q/Q_o where it was about 3.0 and 3.7 at t'=30 and 60 s, respectively. This calculation however, was not possible in later times as the reversed velocities were developed (see for example Fig 6.12-b at t'=120 s).

The values of maximum vertical velocity v_{max} along the jet path normalized by U_o (U_o=10 cm/s; the average u at the vena contracta) were plotted against z-height normalized by H in Fig 6.13 for three time intervals (t'=30, 180, and 360 s). Fig 6.13 showed that the data of each time interval has fitted a quadratic curves (with r^2=0.96-0.97). The curves showed that the peak of v_{max} was close to the middle of the water depth at t'=30 s and t'= 180 s whereas it dropped down considerably around t'=360 s (see v_{max} peaks in Fig 6.13). The increment of v_{max} up to about the middle of the reservoir's height before t'=360 s was understandable as the major momentum was horizontal at the jet opening and it took a certain vertical distance to change into almost complete vertical buoyant jet. The decay of v_{max} beyond the middle of the height, on the other hand, was proportional to $z^{1/2}$ as could be seen in Fig 6.13.

The average leading-edge advancement speed and depth of the horizontal surface buoyant current in Exp. 1 (refer to Fig 6.12-a) was about 2.1 cm/s and 18 cm, respectively, which gave a Froude number F=0.4. This value is in the range of those found in literature which is around 0.5 (see e.g. Turner (1973) and Simpson (1997)). Horizontal velocity profiles u in the surface current however, contrary to free buoyant jet flow characteristics, did not show a sign of

similarity (see Fig 6.12 at several t'). Similar result was found by Jirka and Harleman (1979) for plane buoyant jet in a confined depth. The maximum u_{max}/U_o found in the horizontal surface current was about 0.6 up to about t'=180 s where it was then decreased to about 0.46 around t'=360 s.

Velocity profiles in the outlet's vicinity, on the other hand, were different than that of potential ones most of the experimental time. This was due to the circulations observed previously. However, when the effect of these circulations was relatively far from the intake, u profiles were in a good agreement with potential ones up to about $3d$ (outlet diameter) (see for example u profiles at t'=30 s in Fig 6.12-a).

Jet-plume (Exp. 4)

Fig 6.14 presented velocity vectors of Exp. 4 at several t'. While the heavier fluid was advancing on the bed as a gravity current, an opposite upstream flow was created in the upper lighter fluid as could be seen in Fig 6.14 at t'=30 s. Due to the inter-effect of the buoyancy and the high momentum, a relatively large circulation in the middle of the reservoir with several other small eddies were developed along the interface at this time which caused the interface to be significantly disturbed as could be seen in Fig 6.14 at t'=30 s. With the heavier fluid withdrawal increased, flow below the interface was considerably scattered and several intense (mainly clockwise) internal circulations with a major one along the jet-extension (hydraulic jump) were created as could be seen in Fig 6.14 at t'=120 s. Meanwhile, velocity direction has flipped above the interface and a general downstream flow was developed. This flipping mechanism is interesting as it points to a new flow establishment in the reservoir. The hydraulic jump however, was quickly covered "flooded" as could be seen in Fig 6.14 at t'=240 s while the overall interface tended to be horizontal. Also, a counter clockwise circulation was developed behind the barrier causing a remarkable mixing (see Fig 6.14 at t'=240 s, and see also the mixing in the same zone in Fig 6.7-c). In the late time stages after the average interface height exceeded the intake level, the major withdrawal become from the

fluid below the interface. Consequently, few velocity changes were observed where it was mainly in recirculation's enlargement as could be seen in Fig 6.14 at t'=720 s.

The average leading-edge advancement speed and depth of the heavier buoyant current (refer to Fig 6.14 at t'=30 s) was about 2.1 cm/s and 11 cm, respectively. These values gave F=0.5 which is in consistent with the literature as was found previously in the surface current in Exp. 1. Velocity profiles in the jet forward flow, on the other hand, didn't show a similarity pattern as could be seen in Fig 6.15 where u profiles at t'=180 s and t'=360 s were plotted. This was mainly due to circulation effect. Similar result was found in the two-layer study in Chapter 4. However, no specific line for the jet slope (where $u \approx 0$) could be determined in Exp. 4 as could be seen in Fig 6.15 at t'=180 s and t'=360 s for example.

In the intake vicinity, u profiles at three x-sections (6 cm apart) were also plotted in Fig 6.15. Potential solution adopted from Shammaa *et al.* (2005) was also overplotted on Fig 6.15. General agreement between the potential solution and the measurements were found for x<6cm (~3d) (see for example u profile at x=5.8 cm at t'=180 s and t'=360 s in Fig 6.15). This was a result of momentum domination over the buoyancy at this distance. Beyond x=3d, Fig 6.15 showed that the flow has deviated significantly from potential flow mainly due to jet expansion as well as buoyancy effects. This result was in general consistence with that found for withdrawal from two-layer stratification (refer to Chapter 4). u_{max} of the measurement however, was generally higher than that calculated through potential solution. Fig 6.15 showed, for example, that experimental to potential u_{max} ratio at x=5.8 cm was about 1.2. Also, u_{max} at t'=360 s at the intake level was about 2.0 times the potential one at x=11.8 cm (~6d) (see u profile at x=11.8 cm in Fig 6.15 at t'=360 s).

Instantaneous Velocities

As the waves had the major effect on the overall flow pattern and mixing process in all experiments, an attempt to study these waves' characters was done through studying the instantaneous velocities characteristics. Instantaneous horizontal u and vertical v velocities was studied in Exp. 1 and Exp. 4 at several grid points spaced about 20-24 cm horizontally and 13-14 cm vertically. Due to extensive velocity changes close to the barrier, the study has shown scattered trends and ambiguous results. Velocities, on the other hand, in the second part of the reservoir (outlet part) have shown several clear results in both Exp. 1 and Exp. 4.

u and v at two horizontal pairs of points each at the same z-height (z=23.5, and 10.5 cm) at two x-locations (x=45 and x=69 cm) was plotted in Fig 6.16 for Exp. 1 where t_o was added to the figure. Fig 6.16 showed that fluctuations magnitude in both u and v was decreasing away from the intake wall in both middle and lower heights (compare fluctuating magnitude of u and v between x=45 and x=69 cm at each horizontal pair points in Fig 6.16-a to d). This was probably due to the intake effect. Velocity changes however, were smoother in the lower levels than in the middle levels and in v than in u (compare for example v in Fig 6.16-d to u in Fig 6.16-b at the same x-locations). However, the magnitude of fluctuations was generally steady and didn't change with time. Fig 6.16 also showed that there was a general exchange response between velocities on horizontal basis and not on vertical basis. In other words, u and v pattern could be seen to be similar along x-locations and not along z-locations (compare for example u at x=45 cm in Fig 6.16-a to both u at x=69 cm in Fig 6.16-b and u at x=45 cm in Fig 6.16-a). This horizontal conveyance is a clear indication of the overall horizontal wave's effect in the reservoir.

An interesting short wave's time delay Δt=10 s was observed in u between x=45 and x=69 cm at both heights z=23.5 cm and 10.5 cm. Δt was positive (from x=45 into x=69 cm) when u direction was positive (i.e. u was upstream) and vice versa: Δt was negative when u direction was negative (i.e. u was downstream) (see the time delays Δt in u in Fig 6.16-a and b and see

also the direction of u at certain times in Fig 6.12 at the four points used in Fig 6.16). As an attempt to find the reason of this time period, the buoyancy frequency N was calculated based on the stratification of the intermediate mixing layer observed before to be approximately linear along the experiment. N was thus calculated from the equation $N^2 = -g\partial\rho / \rho\partial z$ where $\partial\rho/\partial z$ is the slope of the density stratification, ρ is the reference density and g is the gravity acceleration. For different density slopes along the experiment, the equation gave N=0.13-0.25 Hz with an average of N=0.2 Hz and thus an average wave period $T=1/N$=5 s. We could notice that Δt was double of this wave period and, therefore, N could be a factor of this time delay. On the other hand, with respect to the two x-locations used in Fig 6.16, this Δt gave a data transfer speed of about (69-45)/10=2.4 cm/s. Fig 6.16-b, has also shown a long wave period $T\approx$200 s in u. The reason of this wave's period is not clear however. v on the other hand, didn't show a clear waves' period or response time as could be seen in Fig 6.16-c and d. However, while longer periodic waves could be noticed in u, shorter ones in v could be noticed in Fig 6.16.

Spectra of u and v in Exp. 1 at nine grid points located at x=21, 45, and 69 cm and at z=10.5, 23.5 and 36.2 cm were plotted in Fig 6.17. Fig 6.17 showed that the most dominant wave energy was related to low frequency waves. General dominant frequency f=0.012 Hz (i.e. its wave period is $T=1/f\approx$85 s) was found to prevail in the upper (z=36.2 cm) and middle (z=23.5 cm) levels in u and in the middle and lower levels in v as could be seen in Fig 6.17-a and b. This wave period is close to the first mode two-layer internal seiches in the reservoir length-direction which was calculated from the equation:

$$T_{NM} = \frac{1}{c}\left[\left(\frac{n}{L}\right)^2 + \left(\frac{m}{B}\right)^2\right]^{-1/2} \qquad \text{..... (2)}$$

where L, and B are length and width of the reservoir, respectively; and n and m are the modes of the oscillation (=0, 0.5, 1, 1.5, etc) in the length and width directions, respectively; and c is the two-layers interfacial long wave celerity given by ($c=\sqrt{g' h_1 h_2/H}$) where h_1 and h_2

is the upper and lower layer depths, respectively. Two notes should be considered however: first, is that h_1 and h_2 in c in Eq. 2 are for homogeneous upper and lower layers which will be assumed correct in our experiments; and second, is that different values of h_1 and h_2 (for the same H) gives different range of T for the same oscillation mode. Therefore, two reasonable values of h_1 and h_2 will be used: h_1=31 and h_2=10 cm (which gives T=90 s), and h_1=21 and h_2=20 cm (which gives T=75 s). Therefore, the range of the first longitudinal mode was T=75-90 s and thus we could notice that the wave period found in the upper and middle z-levels was located in this range. This result reflected the strong effect of the internal seiches on both u and v.

This wave period however, has disappeared in v in the upper levels and instead shorter wave periods were found with a dominant one T=33 s (see Fig 6.17-b at z=36.2 cm). Since this level was the main domain of the buoyant surface current before it was withdrawn, it was suspected that these wave periods were related to the shear waves created at the interface between the surface current and the 'original/mixing' fluid beneath. This also could explain the other wave periods found in the same height in u as could be seen in Fig 6.17-a at z=36.2 cm. Another conclusion could be that the vertical velocities are more affected by interfacial shear waves than by internal seiches. Other reason of these wave periods however might be related to the turbulence frequencies imbedded in the spectra. u in the lower levels (z=10 cm), on the other hand, has shown very long wave period (T=200 s) as could be seen in Fig 6.17-a at z=10.5 cm (refer also to the wave period found in Fig 6.16-b). Other frequencies appeared mainly in v in the upper level might be due to a combination of several sources: the internal seiches', the interfacial shear waves', the large circulations', and the turbulence's frequencies as well as some other sources like the initial valve's opening impact.

Spectra of u and v in Exp. 4, on the other hand, at nine grid points located at x=10, 30, and 50 cm and at z=10.5, 24 and 37.2 cm were plotted in Fig 6.18. u spectra in Fig 6.18-a has showed a range of dominant wave periods T=78, 73, and 90 s in the upper, middle, and lower levels, respectively. These wave periods were in the same range of the first longitudinal

internal waves mode discussed before. It was noticeable however that T was largest in the lower levels. This was probably because the first longitudinal internal seiches has been developed while the gravity current was advancing (which was about 11 cm height; i.e. h_2=11 cm in Eq. 2). Thus the "initial" seiches dominated long time in the experiment. Almost no shorter wave period, on the other hand, could be detected in u spectra at higher levels (z=37.2 cm). This was because the buoyant flow didn't reach this level most of the experimental time (thus no shear waves expected). Other wave periods found in the middle levels (z=24 cm) however, were probably due to fluctuations responded to intake flow effects as well as other 'short' shear waves. v spectra, on the other hand, didn't show a specific dominant wave period for all levels. While the first longitudinal seiches mode has appeared in the upper levels (see v spectra at z=37.2 cm in Fig 6.18-b), its energy was insignificant to be considered. A dominant wave period T=45 s, on the other hand, was found in the lower levels (z=10.5 cm). As this level (and for x-location <=50 cm) was most of the experimental time away from the interfacial fluctuations (and shear waves), a second longitudinal internal wave's mode (calculated from Eq. 2) was probably the reason of this wave period.

6.5. Summary and Conclusions

Flow induced by a horizontal plane buoyant jet discharged in an enclosure (L/H=3.6) with round outlet was investigated experimentally using different initial densimetric Froude number (F_o=5.5, 7.5, and 23). Lighter inflow density "plume-jet" and denser inflow density "jet-plume" was examined. The major goal was to study the overall mixing progress in the experiments as well as the withdrawal quality. The rule of the internal waves was investigated as well. The results of the study are of interest in many civil and environmental engineering applications such as selective withdrawal from reservoirs, brackish estuarine waters, thermal effluents, ocean damping of sludge, fires and ventilations.

Quick changes and relatively short transient times were found to be the main characteristics in such a flow in an enclosure. Hence, experiments showed a short period of

internal hydraulic jump followed quickly (within about 60-100 s) with a flooded jump. Internal seiches have found to play a considerable rule in this regard such that the transient time was much related to the wave period of the first mode two-layer internal seiches in the reservoir's length-direction. It was also concluded that the downstream effect in enclosures becomes less important as F_o decreases where the flow would become more stable.

The study of jet trajectory revealed that for high F_o (F_o=23) the jet expanded longer than that reported in literature for round jets in deeply unlimited extents. Also, for lower F_o (F_o=7.5) the jet expansion was closer to the wall than the experimental and numerical results found in literature for a round jet. The reason of this expansion in both cases was suggested to be related to Coanda effect.

Mixing process was generally found to changed according to the initial g', the location, and the time. The main factor of this process was the shear and internal waves. The resulted rising or declining of the average interface $h_{i\ avg}$ in both jet-plume and plume-jet cases however, was found quicker than that in a two-layer withdrawal case. Also $h_{i\ avg}$ in the end of the experiments has exceeded the "end" critical withdrawal level defined by the two-layer withdrawal concept. This was due to the mixing layer prevailed late in the experiments. The overall mixing in the plume-jet experiment after the flow well established in the reservoir, on the other hand, was found to decay as t^2 and correspondingly the jet trajectory was expanded horizontally as t^2.

Adopting the time scale t_w presented in Chapter 4 where t_w is the time of emptying a withdrawal layer defined between two lines, $2h_c$ apart, above and below the intake level, the rate of the withdrawal from the inflow fluid in the supercritical period in the jet-plume and plume-jet experiments was found to precede that of a two-layer case up to about 0.68 t_w. Beyond $0.68t_w$ however, the difference between the rates decreased until about $2t_w$ where the rate in the two-layer case becomes larger till the end of withdrawal. It was interesting to notice that the time (0.68 t_w) was also the time $h_{i\ avg}$ needed to reach the intake level in a two-layer case where Q_1=Q_2=0.5Q_o. Correspondingly, the withdrawal from the inflow was

Q_2=0.67Q_o at this time for both jet-plume and plume-jet cases. The time needed for the complete withdrawal from the inflow fluid however, was about $5t_w$ and $6.5t_w$ for jet-plume and plume-jet experiments, respectively, whereas it was $4t_w$ for two-layer case. These results are believed to help in reservoir managements.

Mean velocity studies along the jet path of the plume-jet experiment with F_o=7.5 have shown that the peak of the maximum vertical velocity v_{max} was close to the middle of the water depth in the initial stages of the experiment and the decay of v_{max} beyond the middle of the height was proportional to $z^{1/2}$.

General long periodic waves were noticed in the instantaneous u and short ones in v. Also, a general exchange response between velocities on horizontal lines were noticed such that u and v pattern could be seen to be similar along x-locations and not along z-locations. Moreover, in the plume-jet case, a time delay Δt=10s was found in u when moving horizontally from one point to another. It was suspected that this time delay was related to the buoyant wave period ($1/N$=5 s) accompanied with the 'mostly' linear shape of the intermediate mixing layer along the experiment.

Spectra of u and v in the downstream part of the reservoir (outlet part) have revealed that u and v were both affected by the internal seiches with stronger effect on u. The range of this first longitudinal mode was T=75-90 s. Shear waves that prevailed at high depths in the plume-jet experiment were suspected to have a period of T=33 s. A second longitudinal internal wave's mode (T=45 s) was believed to prevail away from the interfacial fluctuations.

Table 6.1. List of experiments

L=150 cm, H=41.2 cm, B=50 cm, a=2 cm (b_o=1.2 cm), b=30 cm, Q_0=36 l/m				
Exp. #	*Description*	*g' (cm/s²)*	F_o	R_e
1		1.50	7.5	1200
2	Plume-Jet	3.00	5.5	1200
3		0.15	23.0	1200
4	Jet-Plume	1.50	7.5	1200

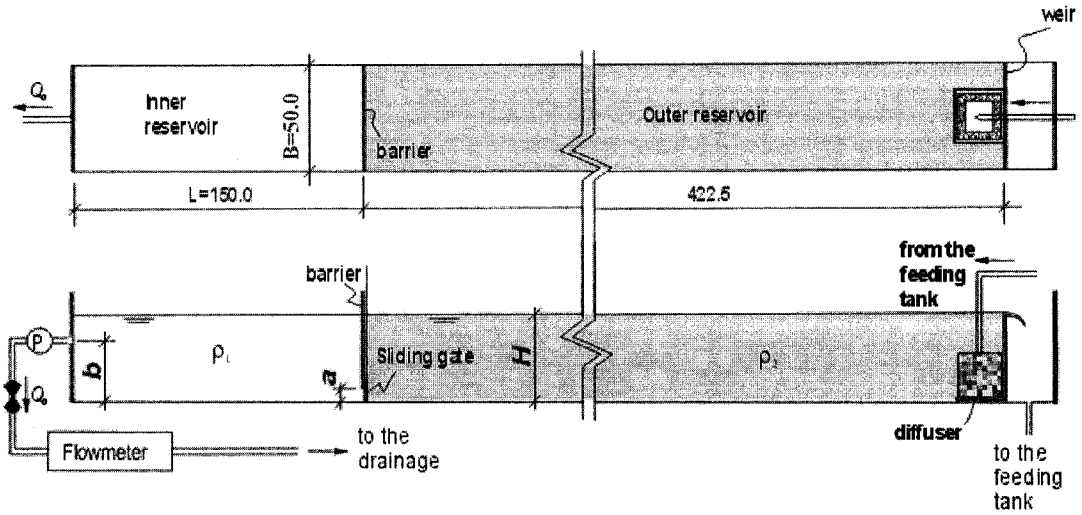

Fig 6. 1 Schematic of experimental setup (Dimensions are in centimeters).

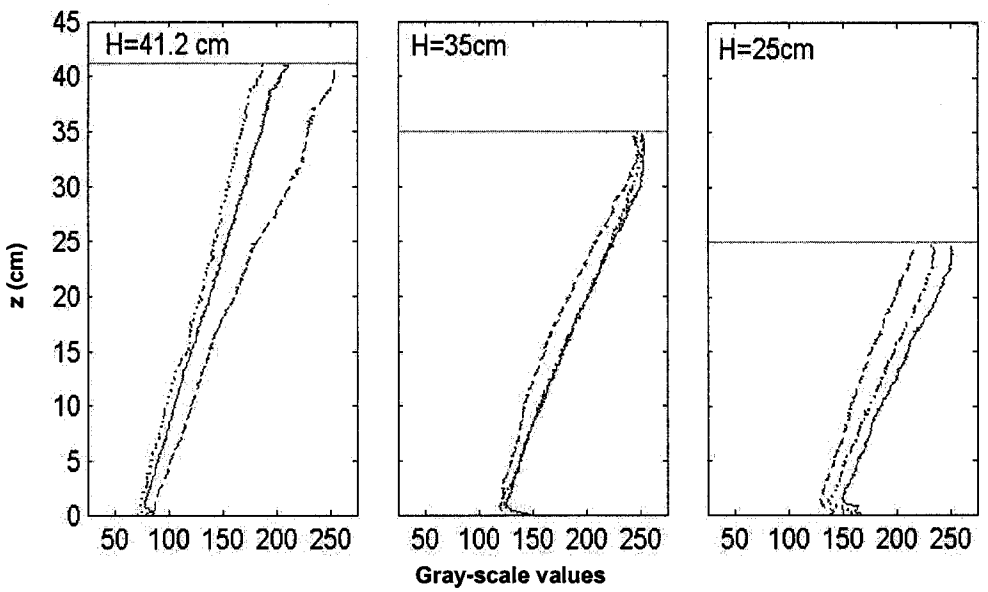

Fig 6. 2 Gray scale values for different initial homogeneous-filling depth H at several x-sections: x=50 cm (solid lines), x=75 cm (dash lines), x=100 cm (dot lines).

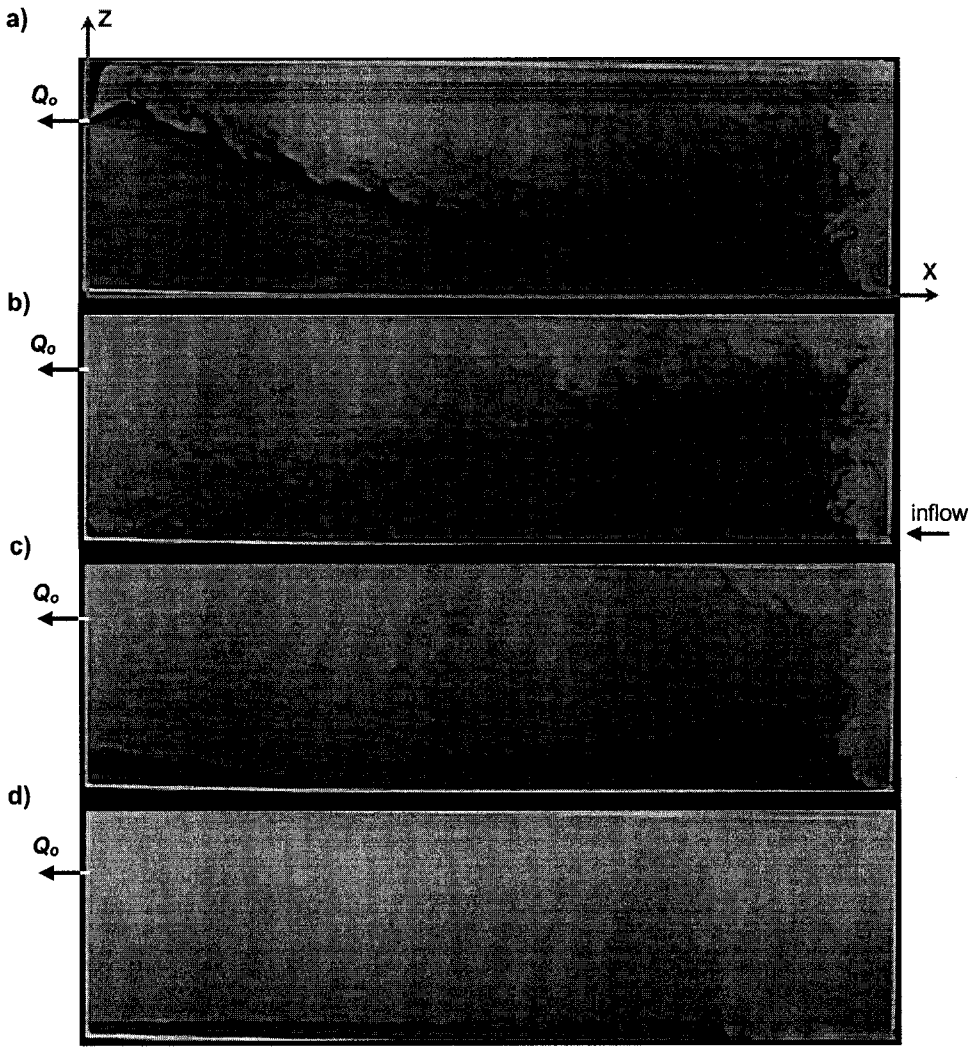

Fig 6. 3 Evolution of flow in Exp. 1 (plume-jet; g'=1.5 cm/s^2) at: a) t=80 s, b) t=111 s, c) t=183 s, and d) t=510 s.

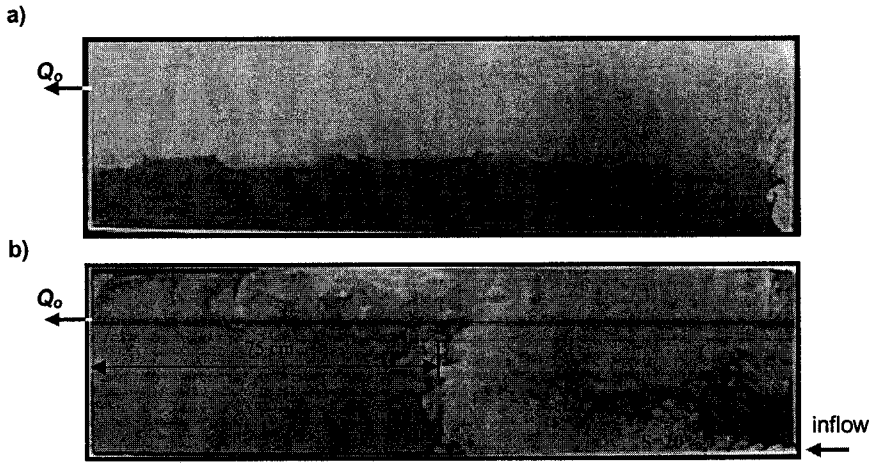

Fig 6. 4 Images of Exps. 2 and 3: a) at t=234 s in Exp. 2, and b) at t= 61 s in Exp.3.

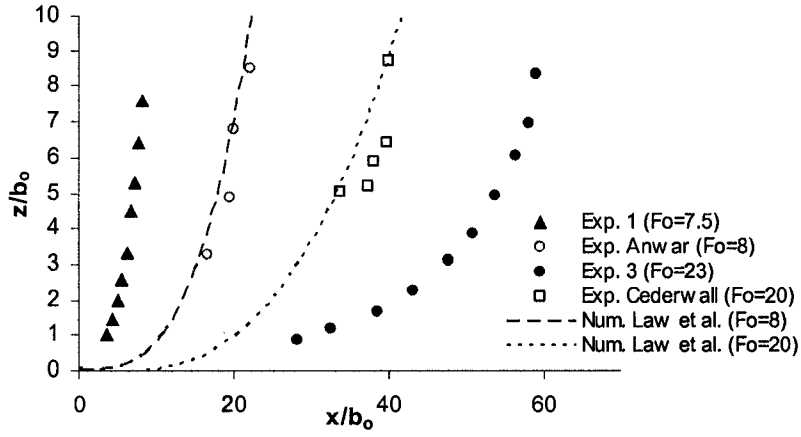

Fig 6. 5 Trajectory of horizontal buoyant jets

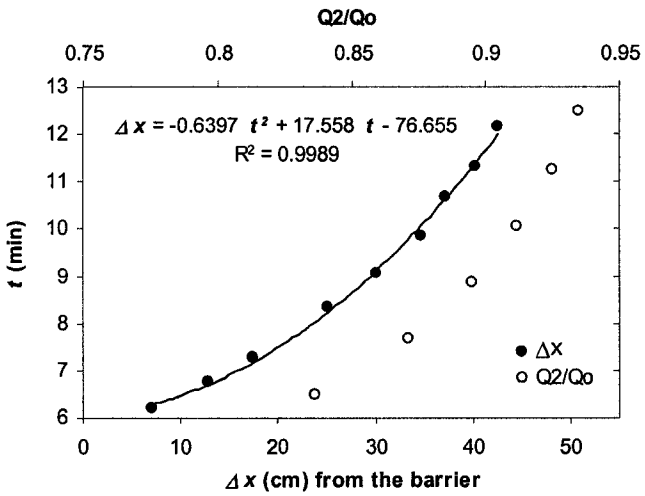

Fig 6. 6 Horizontal expansion of the buoyant jet in Exp.1 and the change of Q_2/Q_o beyond t=6 min.

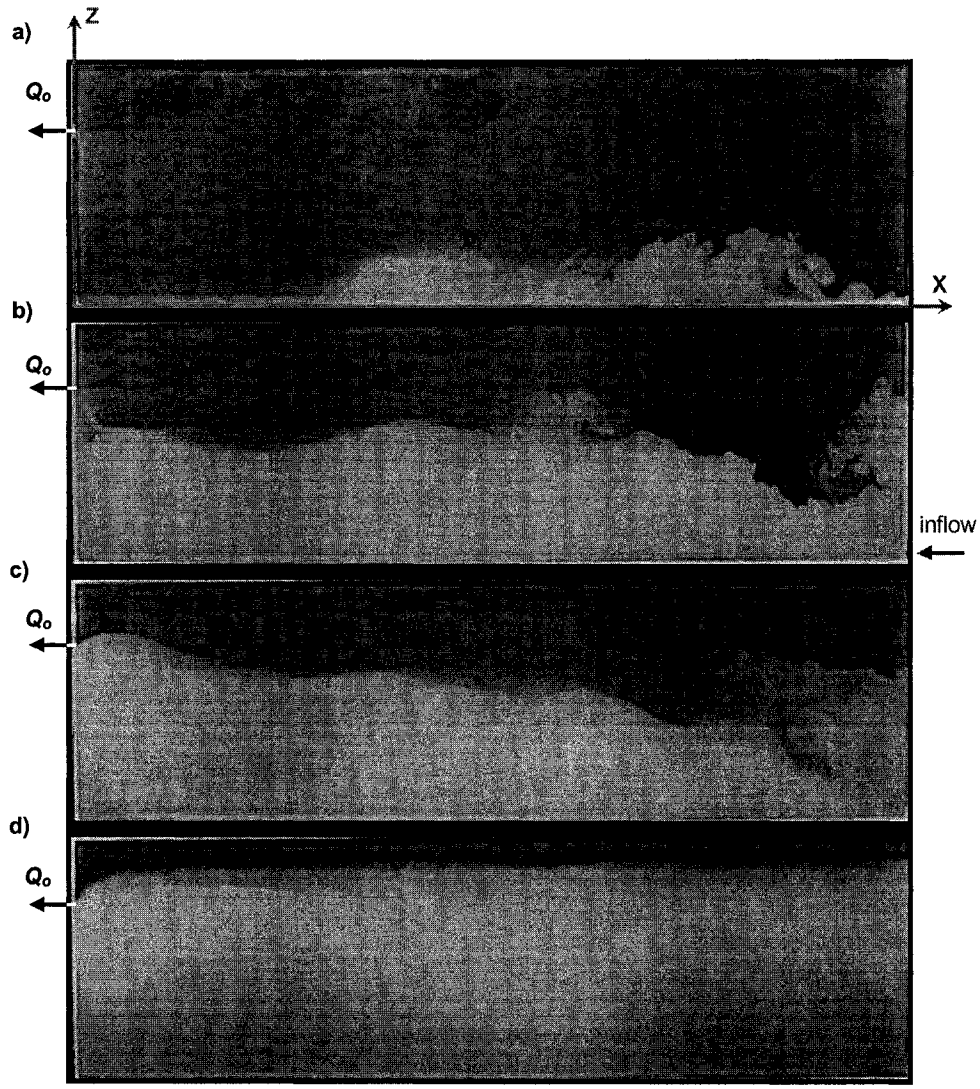

Fig 6. 7 Evolution of flow in Exp. 4 (jet-plume, g'=1.5 cm/s^2) at: a) t=40 s, b) t=155 s, c) t=207 s, and d) t=585 s.

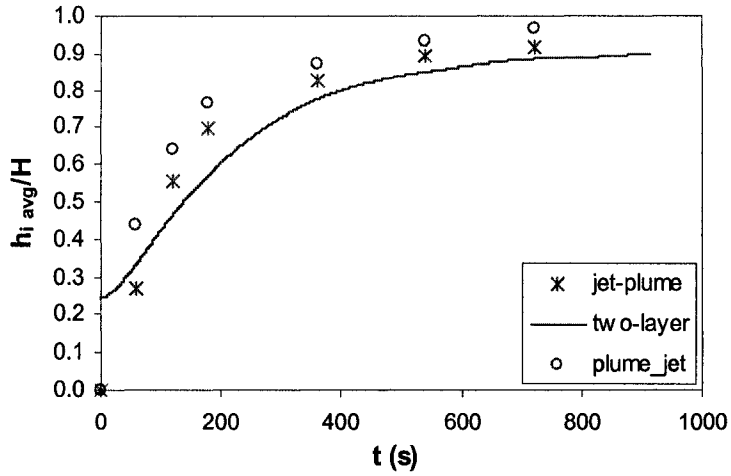

Fig 6. 8 Changes of average interface with time in Exp. 1 (Plume-Jet), Exp. 4 (Jet-Plume), and in a two-layer experiment with initial $h_{i\,avg}$=10 cm above the bed.

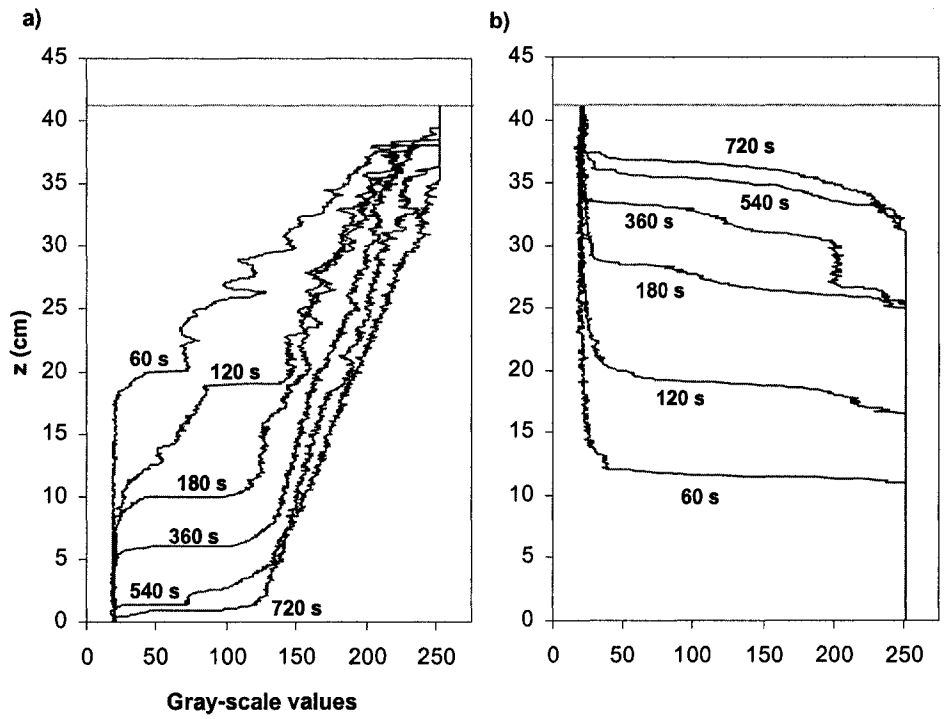

Fig 6. 9 Gray scale values at x=75 cm in: a) Exp. 1, and b) Exp. 4.

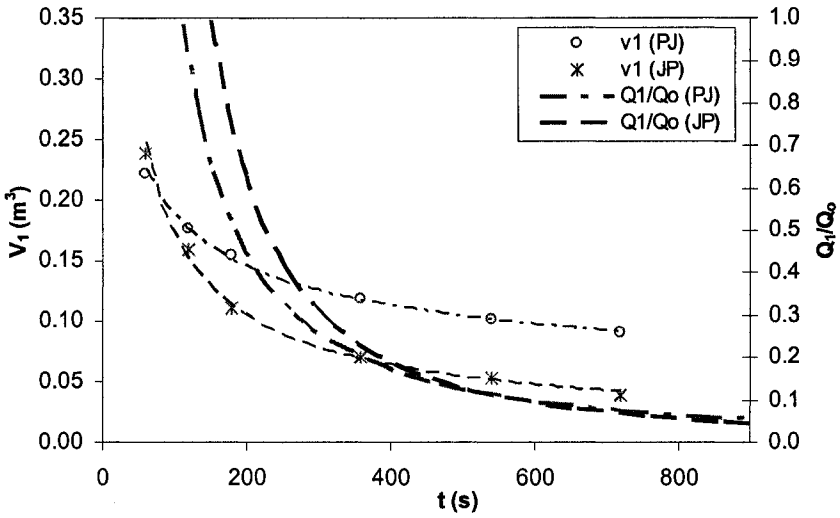

Fig 6. 10 Change of the original layer volume V_1 and Q_1/Q_o with time in Exp. 1and Exp. 4.

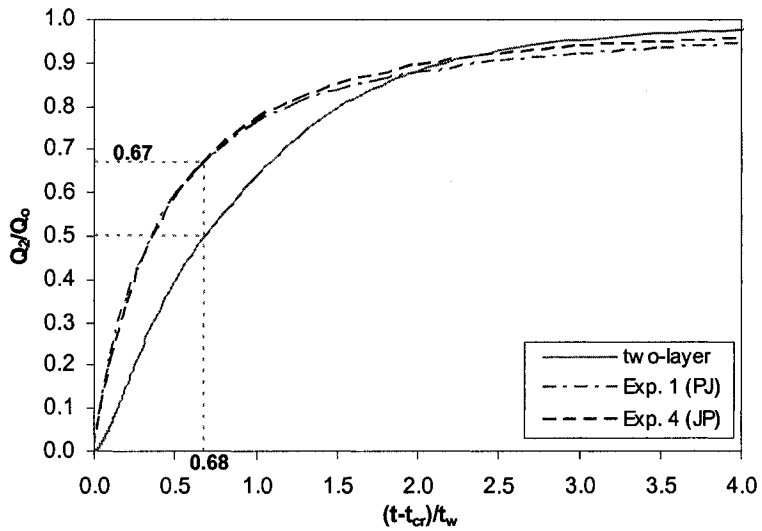

Fig 6. 11 Change of Q_2/Q_o with time in Exp. 1, Exp. 4, and two-layer withdrawal in the super-critical flow period with $(t-t_{cr})/t_w$.

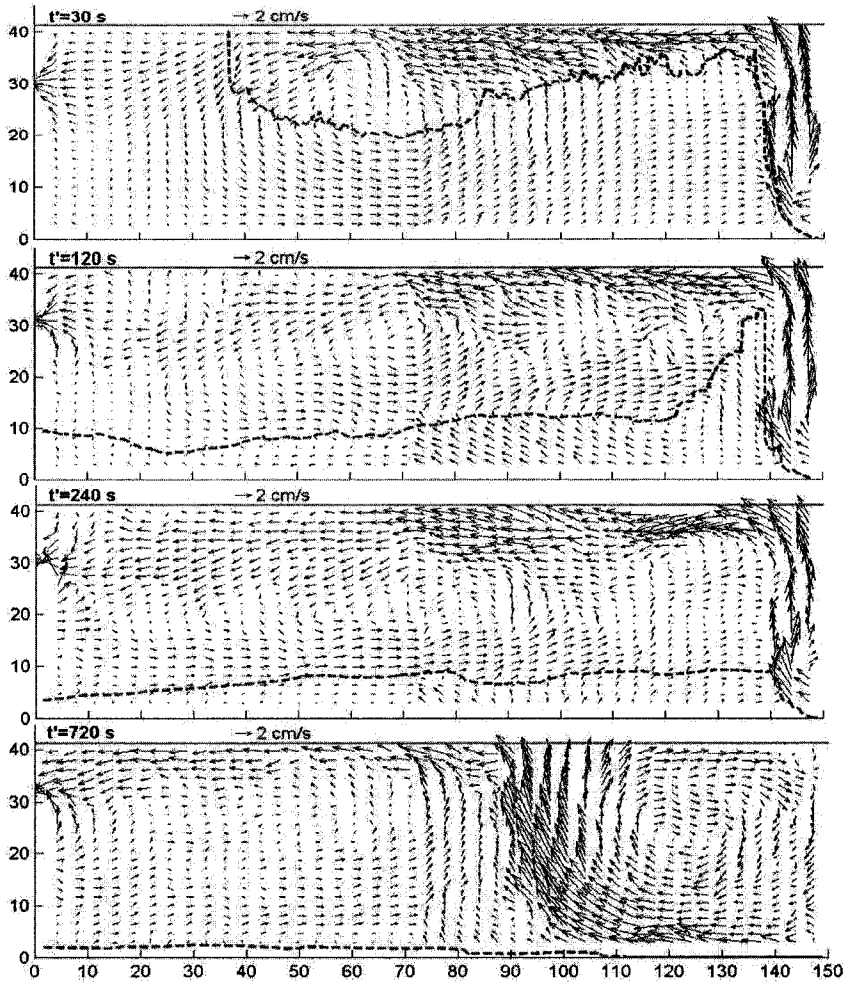

Fig 6. 12 Velocity vectors in Exp. 1 at different t' ($t'=t-t_o$). Interface was shown in dash line.

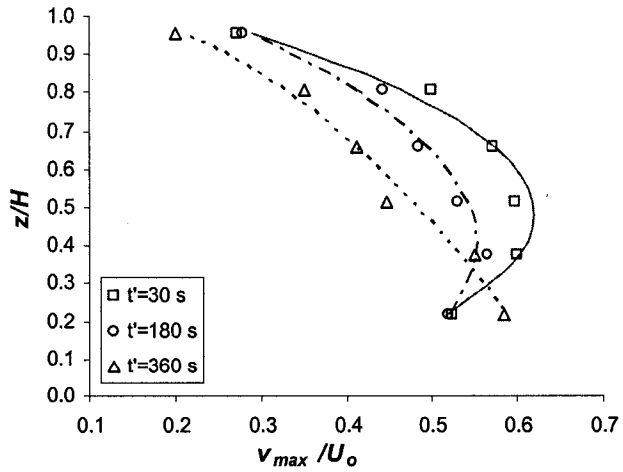

Fig 6. 13 Variation of v_{max} close to the barrier in Exp. 1 with depth. Quadratic curves have fitted each data series.

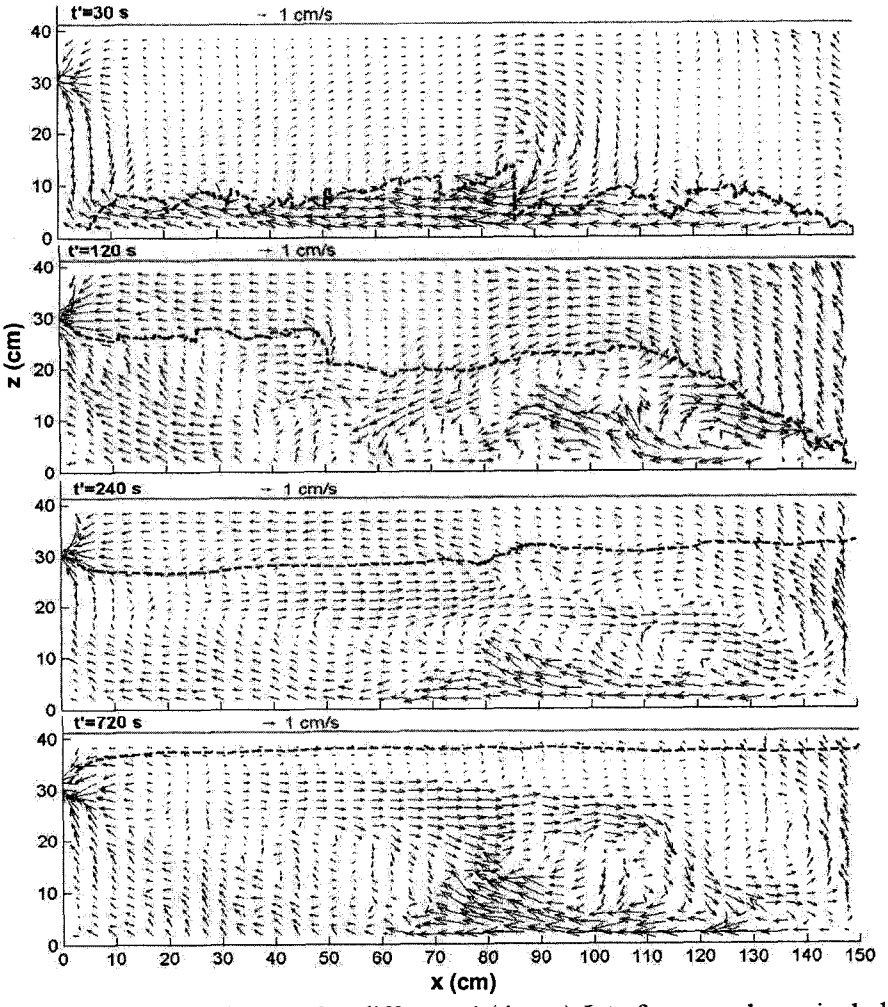

Fig 6. 14 Velocity vectors in Exp. 4 at different t' ($t'=t-t_o$). Interface was shown in dash line.

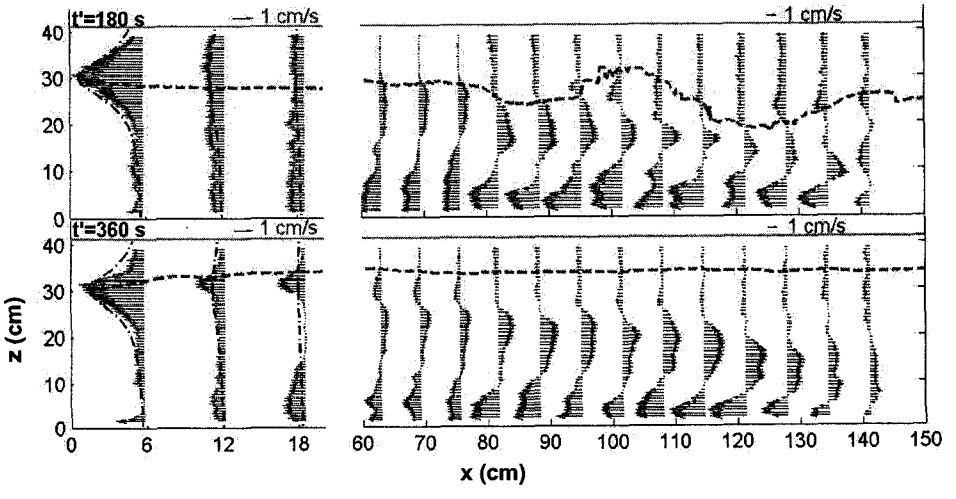

Fig 6. 15 u profiles in Exp. 4 at t'=180 s and t'=360 s. Potential solution for homogenous flow of Shammaa *et al.* (2005) upstream of round intake was added in dash-dot line. Interface was shown in dash line.

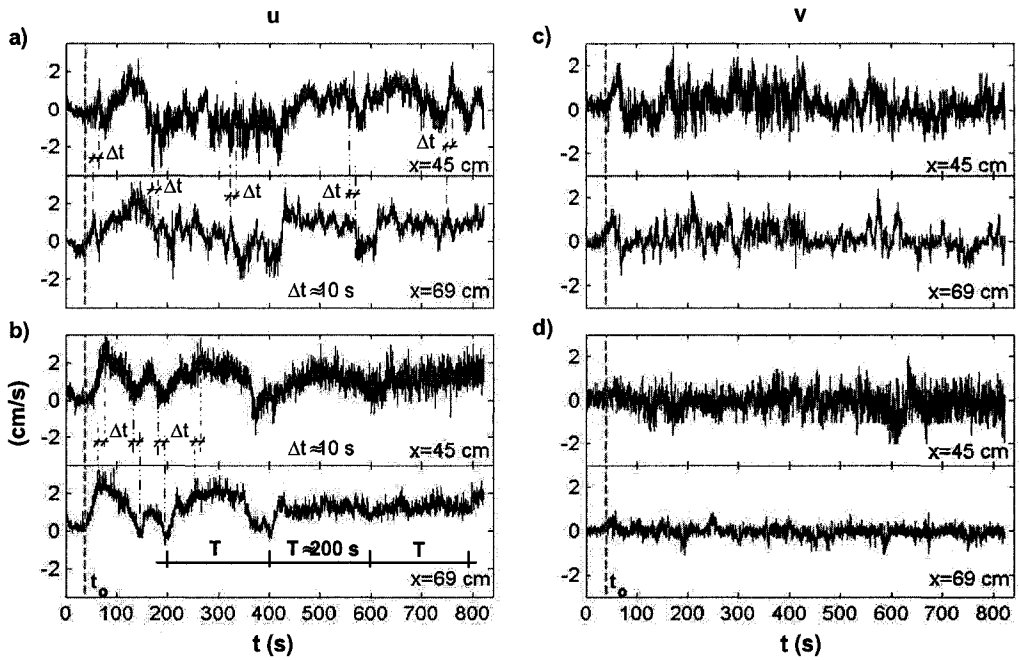

Fig 6. 16 Instantaneous u and v in Exp. 1 at: (a and c) z=23.5 cm, and (b and d) z=10.5 cm. A positive Δt delay was shown using dash-dot lines and a negative Δt delay was shown using dash-two dots line.

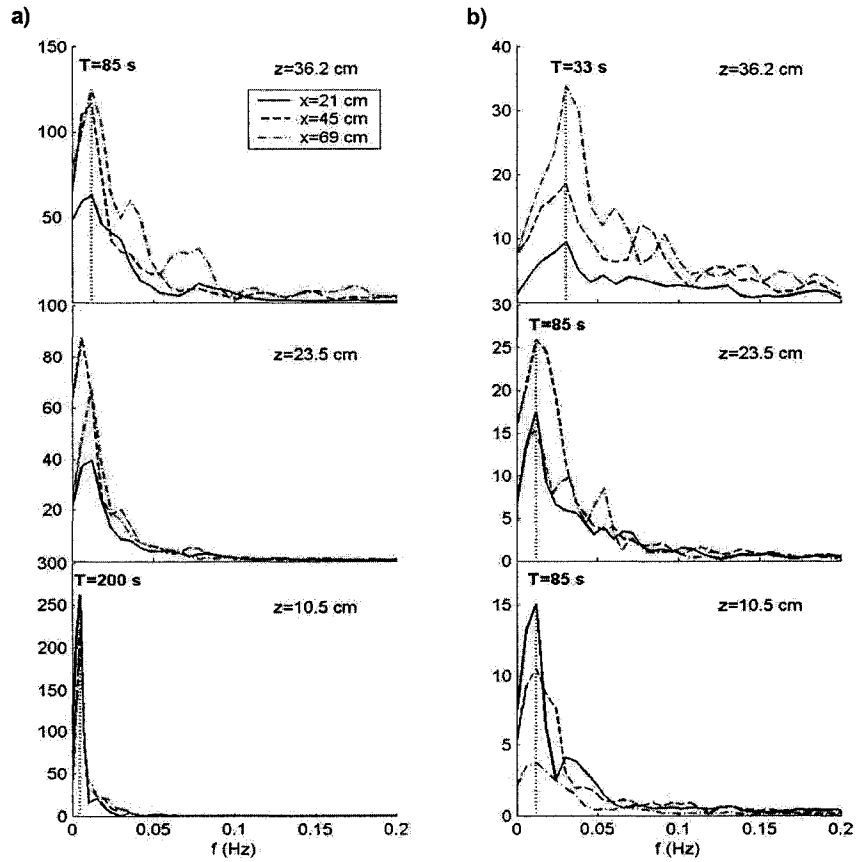

Fig 6. 17 Velocity spectra of Exp. 1 at several grid points: a) u and b) v.

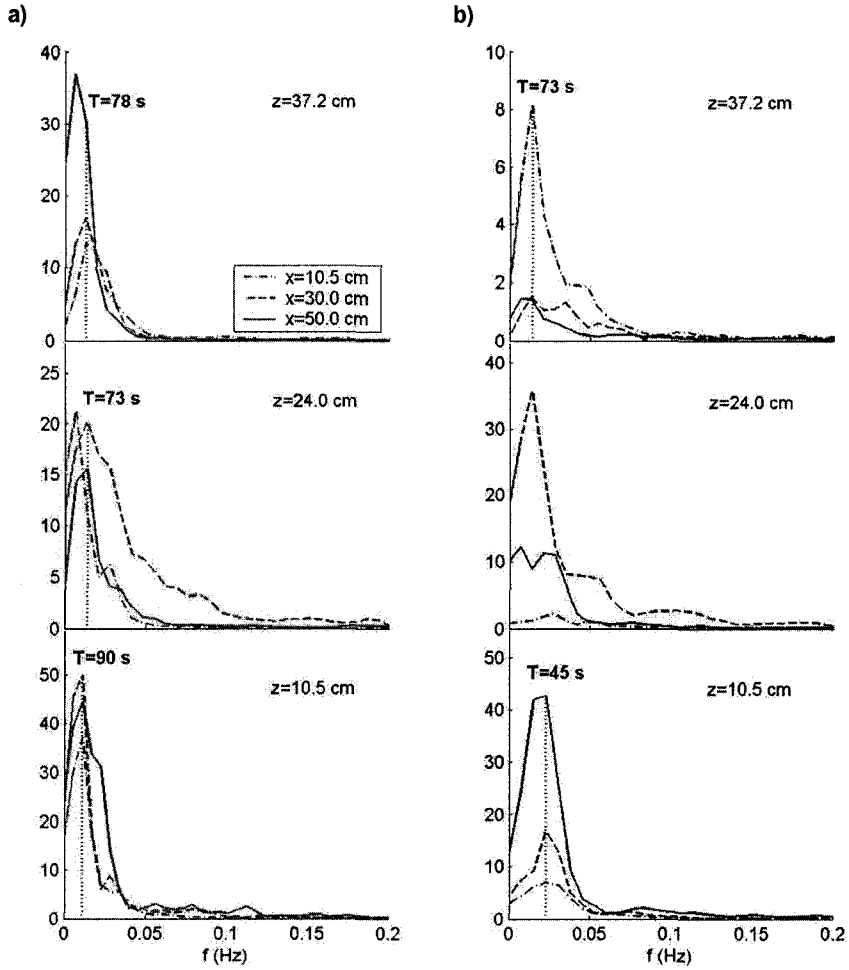

Fig 6. 18 Spectra of Exp. 4 at several grid points: a) *u* and b) *v*.

References

Alavian, V., Jirka, G.H., Denton, R.A., Johnson, M.C., and Stefan, H.G., 1992. "Density currents entering lakes and reservoirs", *J. Hydr. Engrg.,* 118, 1464-14-89

Andreopoulos, J., Praturi, A., and Rodi, W., 1986. "Experiments on vertical plane buoyant jets in shallow water", *J. Fluid Mech.*, 168, 305–336.

Anwar, H.O., 1969. "Behavior of a buoyant jet in a calm fluid", *Proc. Am. Soc. Civ. Eng.,* 95(4), 1289-1303.

Baddour, R.E., and Abbink, H., 1983. "Turbulent underflow in a short channel of limited depth", *J. Hydr. Engrg., ASCE*, 109, 722-740.

Benjamine, T.B., 1968. "Gravity currents and related phenomena", *J Fluid Mech.*, 31, 209-248.

Cederwall, K., 1968. "Hydraulics of marine waste water disposal", *Hydraul. Div. Rep. No. 42*, Chalmers Institute of Technology, Sweden.

Chen, F., 2000. "Smoke propagation in road tunnels", *Appl. Mech. Rev.,* 53, 207-218.

Cheung, S.C.P., Lo, S.M., Yeoh, G.H., and Yuen, R.K.K., 2006. "The influence of gaps of fire-resisting doors on the smoke spread in a building fire", *Fire Safety J.*, 41, 539-546.

Coanda, H., 1936. "Device for deflecting a stream of elastic fluid projected into an elastic fluid", *US Patent* No 2,052,869.

Cowen, E.A., Chang, K.-A., and Liao, Q., 2001. "A single–camera coupled PTV-LIF technique", *Experiments in Fluids*, 31, 63-73.

Craya, A., 1949. "Theoretical research on the flow of nonhomogeneous fluids", *La Houille Blanche,* 4, 44–55.

Etheridge, D., and Sandberg, M., 1996. *Building Ventilation: Theory and Measurement,* John Wiley & Sons Ltd., West Sussex, England.

Ferrier, A.J., Funk, D.R., and Roberts, P.J.W., 1993. "Application of optical techniques to the study of plumes in stratified fluids", *Dynamics of Atmospheres and Oceans*, 20, 155-183.

Harleman, D.R.F., and Stolzenbach, K.D., 1972. "Fluid mechanics of heat disposal from

power generation", *Ann. Rev. Fluid Mech.*, 4, 7-32.

Jirka, G.H., 2006. "Integral model for turbulent buoyant jets in unbounded stratified flows part 2: plane jet dynamics resulting from multiport diffuser jets", *Environ. Fluid Mech.*, 6, 43–100.

Jirka, G.H., and Harleman, D.R.F., 1979. "Stability and mixing of a vertical plane buoyant jet in confined depth", *J. Fluid Mech.*, 94, 275–304.

Koh, R.C.Y., and Brooks, N.H., 1975. "Fluid mechanics of waste water disposal in the ocean", *Ann. Rev. Fluid Mech.*, 7, 187-211.

Kuang, C.P. and Lee, J.H.W., 2001. "Effect of downstream control on the stability and mixing of a vertical plane buoyant jet", *J. Hydraul. Res.*, 39, 375–391.

Kuang, C.P. and Lee, J.H.W., 2006. "Stability and mixing of a vertical axisymmetric buoyant jet in shallow water", *Environ. Fluid Mech.*, 6, 153–180.

Kuang, J., Hsu, C.T., and Qiu, H., 2001. "experiments on vertical turbulent plane jets in water of finite depth", *J. Eng. Mech.*, 127, 18-26.

Law, A.W.-K., and Wang, H., 2000. "Measurement of mixing processes with combined digital particle image velocimetry and planar laser induced fluorescence" *Experimental Thermal and Fluid Science,* 22, 213-229.

Law, A.W.-K., Wang, H., and Herlina, 2003. "Combined particle image velocimetry/planer laser induced fluorescence for integral modeling of buoyant jets", *J. Eng. Mech.*, 129(10), 1189-1196.

Lee, J.H.W., and Jirka, G.H., 1981. "Vertical round buoyant jet in shallow water", *J. Hydraul. Div., Proc. ASCE*, 107(HY12), 1651–1675.

McGrath, J.L., Fernando, H.J.S., and Hunt, J.C.R., 1997. "Turbulence, waves and mixing at shear-free density interfaces, Part 2. laboratory experiments", *J Fluid Mech.*, 347, 235-261.

Rajaratnam, N., 1976. *Turbulent Jets*, Elsevier, Amsterdam, the Netherlands.

Rajaratnam, N., and Subramanya, K., 1967. "Flow immediately below submerged sluice

gate", *J. Hydraul. Div., HY4*, 93, 57-77.

Rajaratnam, N., and Subramanyan, S., 1985. "Plane turbulent buoyant surface jets and jumps", *J. Hydraul. Res.*, 23, 131-146.

Rajaratnam, N., and Subramanya, S., 1986. "Plane denser wall jets and jumps", *J. Hydraul. Res.*, 24(4), 281-296.

Roberts, P.J.W., Adrian, F. and Daviero, G., 1997. "Mixing in inclined dense jets", *J. Hydr. Engrg.*, 123, 693–699.

Roland, H., and Volkart, P., 2003. "Buoyant jets in horizontal-flow final settling tanks", *Swiss Federal Institute of Technology Zurich*, http://www.vaw.ethz.ch/research/2_phase/waste_water_hydr/wb_influence_inflow_jet, 9p.

Simpson, J.E., 1997. *Gravity current, Second Edition,* Cambridge University Press.

Turner, J.S., 1986. "Turbulent entrainment: The development of the entrainment assumption, and its application to geophysical flows", *J. Fluid Mech.*, 173, 431-439.

Turner, J.S., 1973. *Buoyancy effects in Fluids*, p76-90.

Ulasir, M. and Wright, S.J., 2003. "Influence of downstream control and limited depth on flow hydrodynamics of impinging buoyant jets", *Environ. Fluid Mech.*, 3, 85–107.

Vermeyen, T.B., 2000. "Application of flexible curtains to control mixing and enable selective withdrawal in reservoirs", *Proceeding of the 5th Intl. Symposium on Stratified Flows*, 457-462.

Wright, S.J., Roberts, P.J.W., Zhongmin, Y. and Bradley, N.E., 1991. "Surface dilution of round submerged buoyant jets", *J. Hydraul. Res.*, 29, 67–89.

Yu, H., 2005. "Trajectory of a horizontally diffused plane wall jet in a non-isothermal ceiling slot-ventilated enclosure", *Biosystems Engineering*, 91(1), 99–109.

Yu, H., 2006. "A modified estimation of a plane wall jet trajectory horizontally diffused from a ceiling slot in non-isothermal ventilated enclosures", *Biosystems Engineering*, 95 (2), 255–269.

Yu, H., and Hoff, S.J., 2002. "Criteria for ceiling slot-ventilated agricultural enclosures: non-

isothermal", *Transactions of the ASAE*, 45 (1), 201–214.

Yu, H., Liao, C.M., and Liang, H.M., 2003. "Scale model study of airflow performance in a ceiling slot-ventilated enclosure: isothermal condition", *Building and Environment*, 38, 1271–1279.

Chapter 7

Conclusions

This thesis investigated experimentally the hydraulic performance of a curtain as a temperature control device (TCD) in selective withdrawal from reservoirs. The use of this technique is fairly new and needs to be explored. Three scenarios were assumed: no stratification, two-layer stratification, and lighter or denser buoyant inflow. The study presented a comprehensive understanding of the flow behavior when this TCD is used.

The reservoirs' intake flow was first generally investigated using a proposed potential solution. The velocity field upstream of a finite-size orifice and sluice gates was thus presented. It was found that the iso-velocity surfaces draw semi-ellipsoidals close to the orifice; while they become hemispheres away from the orifice. The shape and size of the orifice/sluice gate were found to be of no effect on the flow behavior beyond a certain distance. For orifices of different geometries, this distance did not exceed *2*-3 times of $\sqrt{A}$, where A is the area of the opening.

A set of particle image velocimetry (PIV) and laser induced fluorescent (LIF) experiments were then conducted to examine the flow behavior when a temperature curtain is used in a reservoir. Plane wall-jet inflow and round intake outflow were used in the experiments. The first case studied has dealt with a homogeneous density inflow and outflow. This case assumed there is no stratification (fluid is a homogenous). Three general flow regimes were identified: jet zone with strong recirculation, outlet zone with a special 3-D flow shape, and separation zone. A special flow characteristics however were distinguished when $b \approx H/2$ (b is the intake height and H is the total water height). For instance, jets spreading as well as its entrainment rate were found to exceed those of a classical wall jet and reach their maximal when $b \approx H/2$. An interesting 3-D flow with secondary circulation zone was found upstream the outlet where the flow was rounded spatially around a 'globe' before it went through the outlet. The dimensions of the globe were increased with b and with the perpendicular distance

between the main velocity causing the secondary circulation and the intake. Radial velocity v_r in the vicinity of the outlet in the plane $z=b$ were found to fit ellipses with their long axes along x-axis. Instantaneous velocity and turbulence characteristics were also examined.

The second case investigated was the selective withdrawal from two-layer stratification. Different intake levels and stratifications heights were considered. Flow evolution was found to pass through two time-stages: one sub-critical and one super-critical. Three flow zones were distinguished in this case: the recirculation zone in the lower layer, the intake, and the middle "separation" zones. The curtain existence has caused a recirculation zone to be created with strong shear waves traveling along the interface which in turns caused a considerable mixing. In spite of this mixing however, it was found that the critical withdrawal compares well with the theory for the semi-infinite reservoirs and the withdrawal process was well described using a withdrawal time scale t_w. The trajectory of the maximum horizontal velocity in the separation zone was found to draw a quadratic curve. Potential flow theory was found to predict the flow upstream the intake up to about $3d$ (intake diameter). Interfacial waves were observed to propagate in both left and right directions throughout the experiments.

The effect of interfacial waves on withdrawal quality was further investigated by conducting an experiment with initial interface height above the theoretical critical withdrawal height (h_c). It was found that relative positions of the inlet level, the intake level, and the initial interfacial level play a significant role in selective withdrawal. If these positions for example create intensive interfacial waves, the interface will continue to rise above h_c. This was found to happen through two mechanisms: the K-H waves in the inflow area caused some mixing that was partially transported towards the intake and then released; and the interfacial waves and basin-scale oscillation (i.e. seiches) in the intake area was resulting a withdrawal from the upper layer. The mechanisms however, were damping slowly with time as the main withdrawn layer (lower layer) thickened.

Waves characteristics were also investigated for several withdrawal cases and revealed that the energy of the most dominant waves was related to the first mode of the internal

seiches. In the jet inflow zone, the recirculation period was dominant and was isolated to be around 25 s in the initial stage of the flow. Internal seiches were found to have a significant effect on the horizontal instantaneous velocity u whereas the instantaneous vertical velocity v was more affected by interfacial shear waves. For example, the disturbance in u has propagated with half speed of the interfacial long wave celerity. Whereas the disturbance in v has propagated with half speed of the 'short' shear waves speed. The major interface's disturbance was found to move with time from the jet zone towards the middle of the reservoir (it moved about 1/3 of the reservoir length). Spectra analyses of u and v showed that the periods of the turbulence and shear waves were T=14-25 s with lower range related to the turbulence while upper range related to the shear waves.

The third case investigated was for lighter or denser buoyant inflows. Three different initial inflow Froude numbers were used (F_o=5.5, 7.5 and 23). With respect to the ambient fluid in the reservoir, one lighter density (plume-jet) and one denser density (jet-plume) inflow with F_o=7.5 were studied in details. Generally, the stable and unstable flows observed in previous studies in relatively long extents were found here to be transient and only appeared for very short periods and the longer stability periods were accompanied with the lower F_o values. The transient time was much related to the period of the first mode of longitudinal internal seiches. Due to Coanda effect, jet trajectory was found to shrink towards the wall more than that reported for a round jet for relatively low F_o=7.5.

Internal seiches as well as shear waves considerably accelerated the mixing process in the reservoir with more dominant effect in the plume-jet case. The consequence mixing and withdrawal quality therefore, have showed a considerable difference from that in a two-layer selective withdrawal with similar density conditions. Using a withdrawal time scale t_w, the rate of the withdrawal from the inflow fluid (Q_2) in the supercritical period in the jet-plume and plume-jet experiments was found to considerably precede that of a two-layer case up to about 0.68 t_w. At this time it was found that Q_2=0.67Q_o at both buoyant jet experiments whereas it was Q_2=0.5Q_o for the two-layer case. Also, the time needed for the complete

withdrawal from the inflow fluid was about $5t_w$ and $6.5t_w$ for jet-plume and plume-jet experiments, respectively, whereas it was $4t_w$ for two-layer case. Detailed mean and instantaneous velocities were also provided. Velocity spectra have showed the dominant effect of the internal seiches on velocities (with at least two periodic modes).

The overall knowledge provided in this study is practical in a sense. It helps the design and management decisions when control of water quality in lakes and reservoirs is needed. It is also of useful interest for many other applications. Examples could be but not limited to: ventilations from confined spaces, the influence of gap sizes on the smoke progress in an enclosure fire, sewage discharges into riverine or brackish estuarine waters, and industrial discharges.

As a leading study in using the curtain technique, the experiments were focused on the general flow behavior in the reservoir as well as the overall withdrawal. Many aspects are still in need to be improved and investigated however, whether they are related to the experimental set up, the flow measurements, or to the flow conditions.

Even though a considerable attention was paid in the experimental set up, however several short comings are still need to be improved in a future work. For example, the transient time of rising the discharge up to the designed one needs to be controlled and monitored. The simultaneous work of the valves, pumps, as well as cameras should be automated. The flow in the vicinity of both the jet opening and the intake needs higher frequency recording as well as higher frequency camera's exposure (it also appears that a pulsed laser would be more beneficial to be used for such an area as it usually allows for detecting higher velocities than that allowed by a continuous laser). Smaller reservoir's width is preferable as the water thickness between the laser plane and the wall becomes smaller. More experimental time would also be preferable for some flow conditions. This can be probably achieved by enlarging the volume of the feeding tank.

The detailed flow at the interfaces and in the jet expansion area close to the bed needs more exploration. This can only be done through local and much smaller view experiments. A

smaller view will reduce the laser sheet width at the plane of study, especially close to bed and thus it cause less illumination reflections. For interface study, a special LIF calibration is required. Measurements of the withdrawal water density (either continuous or sampling at specific times) would also be useful to verify and modify the overall LIF results. Study of the flow in a non-symmetric plane and in the third dimension would be beneficial as well.

Finally, other flow conditions should be explored. Examples could be: different discharges, different reservoir lengths, the other two curtain flow scenarios: flow over the curtain and from both above and below the curtain, different curtain opening size, different densities between the upper and the lower layer, different reservoir geometries (mainly the bed slope effect), and different total water depth.

The diversity of these conditions and requirements can not be considered simultaneously and simplifications are essential. Numerical simulation might be a good solution as well. However, it should be done carefully as the preliminary work in this regard (done by the author and other colleges using CFD) showed: ambiguous results, long time requirements (several weeks for one run with the available computer speeds), and verifications from experimental data are not available yet.

Appendix A

Experimental Setup and Error Analysis

A.1. Instrumentation and Methods

A series of experiments were conducted in a rectangular tank at T-blench Hydraulics Laboratory, University of Alberta, Edmonton, Canada. Fig. A.1 is a schematic of the experimental setup and instrumentation. The tank is 6.0 m long, 0.5 m wide, and 0.5 m depth. The tank walls are made of Plexiglass placed in steel frames. An intake of 3/4 inch (1.9 cm) diameter is positioned on one end panel of the tank. The intake is connected to a centrifugal pump which withdraws water at a set discharge (Q_o). The outflow is measured using a digital magnetic flowmeter. Another 1.2cm-thickness Plexiglass panel is used as a curtain and placed 1.5 m from the intake with a 2-cm opening at the bottom permitting under-withdrawal. The water level in the reservoir is controlled by a weir at the far end of the main reservoir. The compensated water is fed from a feeding tank using a submersible pump. A diffuser is used to dissipate the momentum of the feed water, and the overflow water returns back to the feeding tank.

The total number of experimental runs was 30. Table A.1 lists the general conditions of the experiments. The table classified the experiments according to the case studied: homogeneous, two-layer, and plume-jet and jet-plume cases. For each run, the focus part of the run was indicated whether it's the whole length, the curtain part, or the intake part of the inner reservoir. The technique used, the dimensions of the field of view, the withdrawal level, the plane of study, and the dye used for each run were depicted in Table A.1 as well. Other specific detailed conditions related to each case studied will be presented in the later chapters.

In all the experiments, the total water depth H=41.2 cm, the length of the inner reservoir L=150 cm, the discharge Q_o=583 cm^3/s (35 l/min), and the curtain opening a=2 cm. This size was chosen solely to create a turbulent jet under the curtain. The calculated Reynolds number

at the vena contracta depth (b_o=0.6a=1.2 cm, Rajaratnam and Subramanaya 1967) gives R_e=1178. According to Rajaratnam and Flint-Petersen (1989) this value creates turbulent wall jet with a small length of laminar region at the beginning.

Both the tank and the feeding tank were first filled with fresh water in all the experiments. Sodium chloride salt (*NaCl*), Rhodamine 6G dye, and/or tracer particles (silver-coated spherical glass particles with mean diameter of 15 μm and specific gravity of 1.65, Potters Industries) were then added to both the tank and the feeding tank depending on the flow case study. The salt was added such that to create the desired g' of each experiment. The main g' used in this research was g'=1.5 cm/s^2. This value was chosen to represent a typical temperature difference between epilimnion and hypolymnion in reservoirs in summer (in the range of 10 °C). For Homogenous case, only Rhodamine 6G dye was added as a background for later visualization while only tracer particles were added for PIV studies. For two-layer case, the salt, the dye, and the particles were all added to both the tank and the feeding tank. For plume-jet and jet-plume cases, only particles were added. For all these cases, the water was then circulated between the main and the feeding tanks so that to ensure complete mixing.

For the two-layer stratification, the initial stratification in the inner reservoir (between the curtain and the intake panel) was created by adding fresh water into the surface layer using a diffuser, which floated on the top of the 'coloured' salty layer. Considerable attentions were given while creating this layer so that a very thin interface would be created. Tracer particles were added slowly into the diffuser while the upper layer was created. For the plume-jet and jet-plume cases, on the other hand, a gate was used to separate the inner reservoir from the outer one. Salt and particles were then added and homogeneously mixed in the inner reservoir while dye and particles were added and homogeneously mixed in the outer reservoir and feeding tank for the plume-jet case. For the jet-plume case, only particles were added and mixed in the inner reservoir while salt, particles, and dye were all added and mixed in the outer reservoir and feeding tank.

Before an experiment was started, both fresh and salt waters were left enough time until the temperature difference was within 1 °C. Water was then pumped from the feeding tank to the main tank using a submersible pump (with gradual discharge increase) for about 10 minutes where the over-weir flow return back to the feeding tank in a recycling pattern. This process was to make sure that the initial motions caused by pumping water to the main reservoir were sufficiently damped. For the plume-jet and jet-plume cases, the gate separating the inner reservoir from the outer one was then slowly pulled out. Leaving the submersible pump working, the withdrawal pump was then started and its discharge was increased slowly until it reached the intended steady discharge. The volume of the feeding tank allows the steady discharge flow to continue for about 12-15 minutes (when the water in the feeding tank runs out).

A laser sheet was produced through a 5W argon-ion laser operating at 488 nm (Stabilite 2017, Spectra-Physics Lasers). A fibre optical cable (OZ Optics Ltd.) transmitted the light to a top-located lens produced a thin laser sheet at the center plane of the channel where measurements were made. The lens location was varied from about 60 to 150 cm above the water surface depending on the field of view intended and thus the laser sheet was ranged between 2 and 5 mm thickness. A Sony Hi-8 video camera was used to capture the images of the whole inner reservoir (150 cm length) and was located about 200 cm from the reservoir wall. Video recording from this camera was then digitized into individual greyscale images (640 x 480 pixels) at a rate of 5 frames per second. The resolution of the video images was thus about 0.23 cm/pixel.

Two high resolution 16-bit JAI-Pulnix CCD cameras (1392 x 1040 pixels) were used to simultaneously capture the PIV and LIF images (with resolution 0.05 cm/pixel). Rhodamine 6G dye has excitation and emission wavelength peaks in water at ≈ 526 and 550 nm, respectively (Bindhu et al., 1999). A band-pass filter with a rejection range of 525 - 800 nm was used with the PIV camera to filter out the dye and a high-pass filter with a cutoff at 520 nm was used with the LIF camera to filter out the particles. Both cameras were connected to a

PC computer which had an image acquisition software and a frame grabber; both of which allowed capturing and streaming the PIV images onto a scsi drive at a rate of 30 Hz and subsequent export of individual image frames in an 8-bit tagged image file format (TIFF) for further analysis.

Interface Detection and LIF Calibration

The density interface position in the two-layer case was detected using an algorithm based on the differing gray scale values of the upper and lower layers. To account for the mixing depth, pixels above the base interface, z_b, having gray scale values less than that of the lower layer were integrated and an equivalent excess level, z_e, was estimated as follows:

$$z_e = (\sum_{z_b}^{z_f} I \cdot dz)/\bar{I} \quad \text{..... (1)}$$

Where z_f is the level of the free surface, I is the gray scale value of any pixel, dz is the vertical discretization (one pixel), and $\bar{I}$ is the depth averaged gray scale value between the channel bed and z_b at any location. The true interface, z_t, is then predicted as:

$$z_t = z_b + z_e \quad \text{..... (2)}$$

Where no interfacial thickness occurred, the interface was sharp and both z_t and z_b coincided.

In order to detect the interface in the in the plume-jet and jet-plume cases, on the other hand, a threshold grey scale value I was used to determine the end of the mixing depth at a certain time (i.e. certain image). However, to account for the mixing change in the reservoir, I in the mixing zones was also necessary. A simplified pre-experiment calibration was done as follows. The inner reservoir was filled with a mixture of salt water (with "intended" g'=1.5 cm/s^2), particles, and dye up to a certain depth varied from 5 to 41.2 cm with about 2.5 cm increase each time. For each depth, LIF images was recorded for about 20 sec (200 images) and then averaged to get one representative image. The profiles of gray scale values I at several x-distances from the intake wall were plotted for each representative image. As the

mixed fluid was homogeneous, the deviations of each profile from the vertical line corresponding to the maximum grey scale value (I_{max}) were considered as the correction values. For different filling depths, these profiles have found to have a general linear deviation with depth starting shortly below surface water with an average declination of 2-4 grey scale value *(I)* for each 1 cm depth. This deviation (appeared to be mainly "attenuation") summarized the total correction needed for a certain profile. Thus, a reversed inclination has to be compensated in the experiments.

An example of this I profiles was shown in Fig. A.2 at three x-sections (x=50, 75 and 100 cm) for three initial filling H=25, 35 and 41.2 cm. General linear attenuation could be observed in Fig. A.2 for different x-sections and H with a slope of about 2.5-4 *I*/cm. It could be notice however, that the I_{max} (which are supposed to be at the water surface) were not constant for the whole profiles. For example, I_{max} was about 252 at x=50cm for H=35 cm whereas it was about 180 and 215 at x=100 cm for H=41.2, and H=25 cm, respectively. This was due to several reasons: the fact that the laser was relatively far from the water surface (to cover large areas) and therefore its rays were not distributed evenly along the water surface of the reservoir; the laser used in these experiments has a fringe error so that some areas enlightens more than the others; and the laser light intensity had some fluctuations along the time. However, I_{max} were not important in the experiments and rather the decrement of these values along the depth was the important issue. Notice however, that the I correction should not be applied to the non-dyed layer. Notice also that the images were digitized at 8-bit grey-scale resolution and thus the maximum possible I was 255.

As this calibration considered only a homogeneous "coloured" layer and doesn't account for an existence of a lower "mixed" density (lower light intensity) below the high density fluid (as will be seen in the plume-jet experiments in Chapter 7), the calibration slope was considered half of that found above (i.e. 1-2 *I*/cm). For generality, a calibration value of 1.5 *I*/cm was adopted in these experiments. For the jet-plume experiment however, as the denser "dyed" fluid was in the bottom of the reservoir, vertical line at the maximum gray-scale value

was enough to represent the bottom "dense" layer at any x-section. The depth of the above mixing layer however, was found relatively small and the gray scale correction was in fact not important and thus it was ignored in this specific experiment.

In order to guarantee the linear response of the luminescence-concentration relation, the dye concentration was kept below 0.1 μg/l (100 ppb) in the whole experiments (McGrath et al., 1997; Ferrier et al., 1993). Ferrier et al. (1993) stated that the linear response of Rhodamine 6G is up to 50 μg/l, however for a constant laser power. On the other hand, since the molecular diffusivities of salt and Rhodamine 6G are approximately the same (McGrath et al., 1997), the changes of the salt concentration (density) could be monitored by tracking the concentration of Rhodamine.

Velocity Measurements

Using the PIV images, velocity measurements were taken at different field of views as shown in Table A.1. The velocity fields were computed using an iterative multi-grid cross-correlation PIV algorithm (Scarano and Riethmuller, 1999). The algorithm makes use of a translation of the interrogation areas (windows) instead of the classical fixed interrogation areas. Such a displacement is predicted and corrected by means of an iterative procedure. In addition, while iterating, the method allows a refinement of the size of the interrogation areas. Using this algorithm with 3 iterations, the final search and interrogation windows in the curtain area, were 16 and 8 pixels, respectively, with a grid velocity measurement each 8 pixels. The sampling frequency used for this area was 10 Hz. For intake area, 4 iterations have been used and the final search and interrogation windows were 8 and 4 pixels, respectively, with a grid velocity measurement each 4 pixel. The sampling frequency used for this area was 15 Hz. A 50% window overlap was used in both curtain and intake areas.

Velocity measurements close to both reservoir's sides (curtain and intake walls) and bed were not possible. This was due to a combination of several reasons: the high illumination reflection concentrated at the edges and the bed of the flume, the 'dead' distance at the right

and bottom edges of the view that the software considers when it processes the PIV images, the high velocity value under the curtain and at the intake which exceeds the possible grapping by the maximum sampling rate and search window of the software used (also, the amount of laser energy incident upon a particle decreases as the flow velocity increases, which places an upper bound on the flow velocity (Prasad, 2000)), and the relatively large field of view required in these runs (the camera bends the images at their edges). Thus about 2-2.5 cm distances from the sides and the bed were in lack of measurements. Also, the measurements close to the jet mouth (within about 10 cm) were not accurate. Measurements close to the water surface (within 1 cm) were not accurate as well. All measurements were taken at the vertical symmetric plane of the inner reservoir.

A.2. Error Analysis

The recorded flowmeter measurements showed that the fluctuation in Q_o was around ±2%. The density of the fresh and salt water was determined using the CRC handbook for sodium chloride solution (Lide, 1998). The procedure needed the water temperature and the weight concentration of the salt. The weighing scale allowed a precision of 0.1 g while the amount of added salt was more than 3.0 kg in all experiments. Also, the water temperature was measured to 0.1°C using a high precision digital thermometer (Fisher Scientific). With these parameters, the error estimates for g' was less than 1%.

Errors in detecting the interface position were estimated to about 1-2 pixels (2-4 mm) for the whole inner reservoir view (Sony camera). As the interface depth was ranging from 10-37 cm in different experiments, this error was therefore corresponding to about (0.4/37 to 0.4/10) =1-4%. For curtain and intake areas (Pulnix cameras), the error in detecting the interface was about 2-3 pixels (1-1.5 mm) which corresponded to about 1% or less in the different experiments.

For PIV measurments, there are two main contributors to the uncertainties; the experimental conditions (which include image quality, flow field characteristics and seed

particle properties) and the accuracy of the computing algorithm (Cowen and Monismith 1997). The experimental conditions were designed to minimize the uncertainty in the PIV measurements. These conditions were: the dynamic range which was 8 bits, i.e., gray scale ranged from 0 for black pixels to 255 for white pixels and the average background grayscale value was 30; time difference between paired PIV images ranged from 100 milliseconds at the curtain area to 67 milliseconds at the intake area. The particle used, on the other hand, had a settling speed of about 0.01 mm/s. As the total time of an experiment was less than 16 min, the maximum settelement of a certain particle was about 9 mm. In comparison to the vertical dimentions of the reservoir, this settlement is negligible (~2% error).

Velocity is usually calculated using the displacement of particles obtained by a correlation technique, either by auto-correlation of a doubly (or multiply) exposed single particle image or by cross correlation between two successive single-exposure images. In general, the correlation methods were found to be very accurate for nearly uniform flows. However, the accuracy is drastically reduced in the presence of high velocity gradients, which are found, for example, in turbulent flows, in boundary layers or in the cores of concentrated vortices (Meunier and Leweke, 2003). On the other hand, there are bias errors that occur when the estimated location of the cross-correlation peak is shifted towards the nearest integer value and this is referred to peak locking (Fincham and Spedding, 1997). Generally, in any type of image velocimetry technique where sub-pixel determination of the correlation peak is attempted, peak locking occurs. Pixel locking can affect the velocity calculation greatly in experiments (Feng et al., 2007).

Fincham and Delerce (2000) developed a method to calculate the peak locking error (i.e., the percentage of vectors affected by peak locking error) based on the histogram of the computed velocity vectors. We used thier scheme to calculate the peak locking errors and found that from 10% to 18% of the vectors were affected by peak locking. Siddiqui *et al.* (2001) and Fincham and Spedding (1997) reported that typically 15 % of velocity vectors are

affected by peak locking when using a sub-pixel fit cross correlation DPIV algorithm. Therefore, peak locking errors of 10% to18% are acceptable.

An algorithm adapted from Siddiqui et al. (2001) was used to identify spurious vectors and then correct them. The algorithm uses the local median value of eight or fewer neighboring velocity vectors depending on the location of the given vector. Vectors are identified as spurious based on two criteria. First if the magnitude of the raw vector was less than 0.75 or larger than 1.25 times the local median value. Second if the angular difference between the raw vector and the local median value is larger than 15 degrees. We found that on average less than 5% of the velocity vectors were spurious.

Cowen and Monismith (1997) reported that the total error in the PIV measurements is the sum of the errors due to particle diameter, particle density, out of plane motion, gradient, dynamic range, peak locking and the Adaptive Gaussian Window AGW interpolation. We used the results of Cowen and Monismith (1997) to estimate the error in our PIV data since they used a similar cross correlation algorithm and the same AGW interpolator in their analysis. We estimated the maximum percentage errors in the instantaneous velocity measurements to be about 4%. This error is comparable to those found in literature. For example Siddiqui *et al.* (2001) reported errors of about 7% and Pierson (1997) reported errors of 6% in the instantaneous velocity measurements. Moreover, the error in time-averaged velocities is expected to be smaller due to the averaging. Therefore we can conclude that the errors associated with our PIV measurements are within the acceptable range.

Table A.1 List of Experiments

Run #	Case studied	Focus part of the reservoir	Tech. used	Approximate field of view*	Withdrawal level*	Plane of study**	Dye used
1		Whole reservoir	LIF	150 x 41	30	X-Z	Rhd. 6G & WT
2		Curtain	PIV	80 x 41	30	X-Z	-
3		Intake	PIV	80 x 41	30	X-Z	-
4		Curtain	PIV	80 x 50	30	X-Y (z=30)*	-
5		Intake	PIV	80 x 50	30	X-Y (z=30)*	-
6		Curtain	PIV	80 x 50	30	X-Y (z=15)*	-
7	Homogeneous Flow	Intake	PIV	80 x 50	30	X-Y (z=15)*	-
8		Curtain	PIV	50 x 50	30	Y-Z (x=10)*	-
9		Intake	PIV	50 x 50	30	Y-Z (x=20)*	-
10		Curtain	PIV	80 x 41	20	X-Z	-
11		Intake	PIV	80 x 41	20	X-Z	-
12		Curtain	PIV	80 x 41	10	X-Z	-
13		Intake	PIV	80 x 41	10	X-Z	-
14		Curtain	PIV	80 x 41	2	X-Z	-
15		Intake	PIV	80 x 41	2	X-Z	-
1		Whole reservoir	LIF	150 x 41	30	X-Z	Rhd. 6G
2		Whole reservoir	LIF	150 x 41	30	X-Z	Rhd. 6G
3	Two-Layer	Whole reservoir	LIF	150 x 41	20	X-Z	Rhd. 6G
4	Flow	Whole reservoir	LIF	150 x 41	10	X-Z	Rhd. 6G
5	(g'=1.5 cm/s^2)	Intake	LIF+PIV	65 x 50	30	X-Z	Rhd. 6G
6		Curtain	LIF+PIV	65 x 50	30	X-Z	Rhd. 6G
7		Intake	LIF+PIV	70 x 50	20	X-Z	Rhd. 6G
1	Plume-Jet (g'=1.5 cm/s^2)	Whole reservoir	LIF	150 x 41	30	X-Z	Rhd. 6G
2	Plume-Jet (g'=3.0 cm/s^2)	Whole reservoir	LIF	150 x 41	30	X-Z	Rhd. 6G
3	Plume-Jet (g'=0.15 cm/s^2)	Whole reservoir	LIF	150 x 41	30	X-Z	Rhd. 6G
4	Jet-Plume (g'=1.5 cm/s^2)	Whole reservoir	LIF	150 x 41	30	X-Z	Rhd. 6G
5	Plume-Jet	Curtain	LIF+PIV	80 x 41	30	X-Z	Rhd. 6G
6	(g'=1.5 cm/s^2)	Intake	LIF+PIV	80 x 41	30	X-Z	Rhd. 6G
7	Jet-Plume	Curtain	LIF+PIV	80 x 41	30	X-Z	Rhd. 6G
8	(g'=1.5 cm/s^2)	Intake	LIF+PIV	80 x 41	30	X-Z	Rhd. 6G

* All dimensions are in cm ** All X-Z planes are in the middle of the width

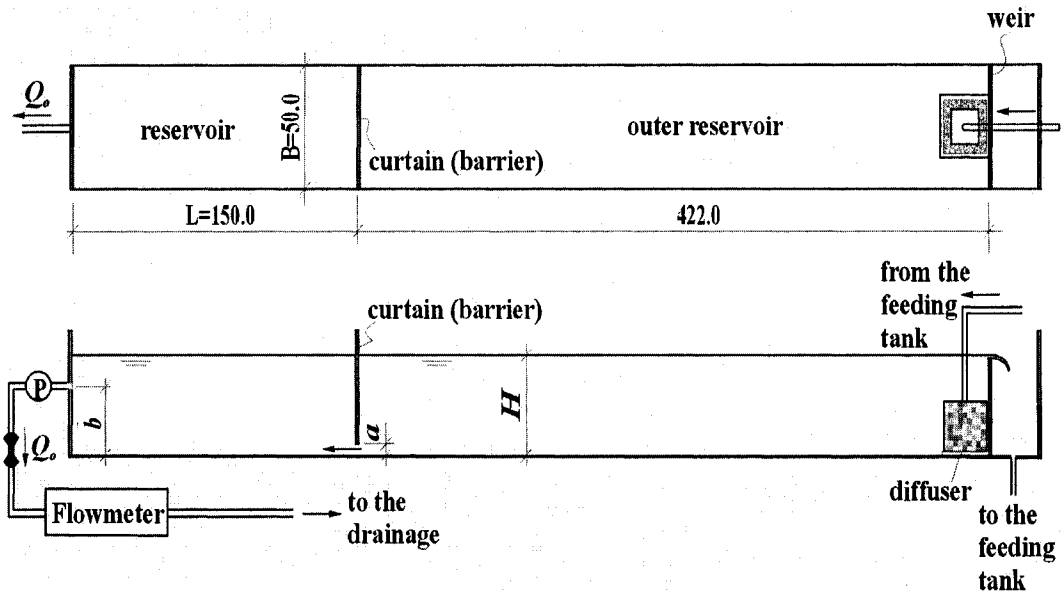

Fig A.1. Schematic of experimental setup. All dimensions are in centimeters. (not to scale).

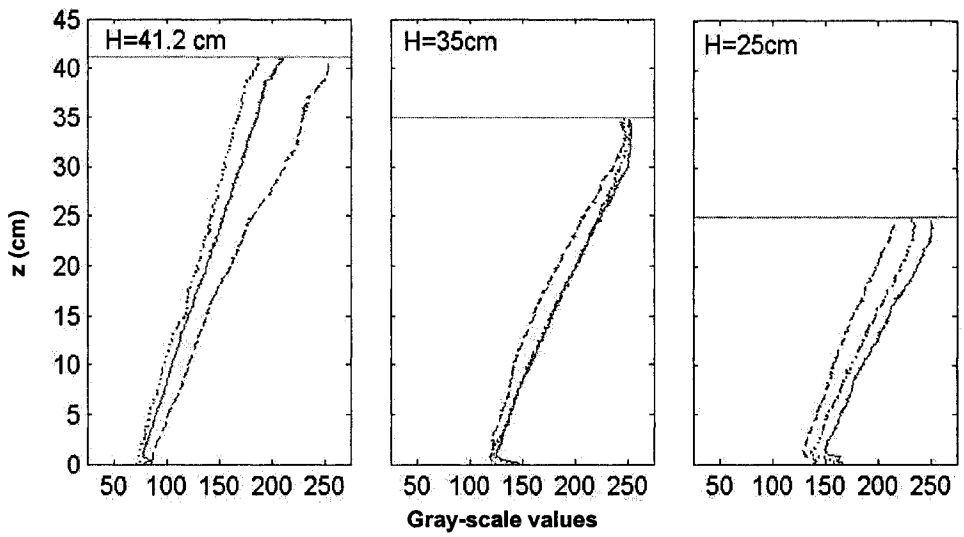

Fig A.2. Gray scale values I for different initial homogeneous-filling depth H at several x-sections: x=50 cm (solid lines), x=75 cm (dash lines), x=100 cm (dot lines). x is measured from the intake wall.

References

Bindhu, C.V., Harilal, S.S., Nampoori, V.P.N. and Vallabhan, C.P.G., 1999. "Solvent effect on absolute fluorescence quantum yield of Rhodamine 6G determined using transparent thermal lens technique", *Modern Physics Letters B*, 13 (16), 563-576.

Cowen, E.A., and Monismith, S.G., 1997. "A hybrid digital particle tracking velocimetry technique", *Exp. in Fluids,* 22, 199-211.

Feng, Y., Goree, J., and Liu, B., 2007. "Accurate particle position measurement from images", *Review of Scientific Instruments*, 78 (5): Art. No. 053704.

Ferrier, A.J., Funk, D.R., and Roberts, P.J.W., 1993. "Application of optical techniques to the study of plumes in stratified fluids", *Dynamics of Atmospheres and Oceans*, 20, 155-183.

Fincham, A., and Delerce, G., 2000. "Advanced optimization of correlation imaging velocimetry algorithms", *Exps. Fluids* [Suppl] 29, S13–S22.

Fincham, A., and Spedding, G.R., 1997. "Low cost, high resolution DPIV for measurement of turbulent fluid", *Exps. Fluids*, 23, 449–462.

Lide, D.R., 1998. *CRC handbook of chemistry and physics*, 79th Ed., CRC, Boca Raton, Fla.

McGrath, J.L., Fernando, H.J.S., and Hunt, J.C.R., 1997. "Turbulence, waves and mixing at shear-free density interfaces, Part 2. laboratory experiments", *J Fluid Mech.,* 347, 235-261.

Meunier, P., and Leweke, T., 2003. "Analysis and treatment of errors due to high velocity gradients in particle image velocimetry", *Exps. Fluids*, 35, 408–421.

Peirson, W.L., 1997. "Measurements of surface velocities and shear at a wavy air–water interface using particle image velocimetry", *Exps. Fluids*, 23, 427–437.

Prasad, A.K., 2000. "Particle image velocimetry", *Current Science*, 79(1), 51-60.

Rajaratnam, N., and Flint-Petersen, L., 1989. "Low Reynolds number circular turbulent jets", *Proc. Instn Civ. Engrs, Part 2*, 87, 299-305.

Rajaratnam, N., and Subramanya, K., 1967. "Flow immediately below submerged sluice gate," *J. Hydr. Div.,* HY4, 93, 57-77.

Scarano, F. and Riethmuller, M.L., 1999. "Iterative multigrid approach in PIV image processing with discrete window offset", *Experiments in Fluids,* 26, 513-523.

Siddiqui, M.H.K., Loewen, M.R., Richardson, C., Asher, W.E., and Jessup, A.T., 2001. "Simultaneous particle image velocimetry and infrared imagery of microscale breaking waves", *Phys. Fluids,* 13, 1891–1903.

Appendix B

Experimental Documentation

The experimental data and analysis of this study was stored on four hard drives with total storage of 900 GB. For the clarity and applicability purposes, some of the data that only its average values where in concern was deleted after its averages was calculated and saved. Repeatable files that calculate the same parameters and quantities were deleted as well. Many images were also deleted after they were processed and their results were obtained and saved. Thus, the final version of the data and analysis were stored on one external hard drive with total storage of 300 GB. Experimental films recorded using Sony Hi-8 video camera, on the other hand, were downloaded to a PC computer and then were burned on CD's and DVD's.

Each experiment has an Excel file named "Experiment-info" that includes all or some of the following descriptions (see Table B.1): name, date, focus area, average steady discharge, withdrawal level, capturing frequency (for LIF and for PIV), edges of the images (water surface, bed, and wall: in pixels), interrogation and search window sizes used in PIV calculations, and image numbers related to a specific time concern (t_o, t_s, t'=1min, t'=2min, etc).

The content of the final hard drive is divided into three main folders named: 'Homogeneous', 'Two-layer', and 'Plume-&-jet'. The first is referring to the homogeneous flow discussed in Chapter 4, the second is referring to the two-layer flow discussed in Chapters 5 and 6, and the third is referring to the Plume-jet and Jet-plume flows discussed in Chapter 7. The skeleton of the main folders of the experiments is illustrated in Chart 1.

The 'Homogeneous' folder has four sub-divided folders: 'Profiles', 'Cross-sections', 'Horizontal-sections', and 'Results-&-analysis'. The first three sub-folders referred to the plane of studies. The 'Profile' folder is divided into four sub-folders in accordance to the four withdrawal levels studied; thus they named: '30cm', '20cm', '10cm', and '2cm'. For each

level case, two sub-folders are used: 'intake' and 'curtain' referring to the area of focus. In each one of these folders, two main types of files are used: image files recorded by Pulnix Camera (*tif* extension) and displacement and instantaneous velocities calculated (*piv* extension). Other files that can be found in these folders are either Matlab's codes or results or excel files related to certain calculations. Similarly, 'Horizontal-sections' folder is also divided into two sub-folders: '30cm' and '15cm' referring to the level of the horizontal sections. These subfolders are re-divided in a similar manner to those in the 'Profile' folder.

The 'Two-layer' folder has two sub-folders 'Sony' and 'Pulnix' referring to the data collected by either one of those cameras. In the 'Sony' folder, four sub-folders have represented the four experiments discussed in Chapters 5 and 6: 'E1', 'E2', 'E3', and 'E4'. In the 'Pulnix' folder, two subfolders have represented the two experiments studied using PIV and LIF techniques simultaneously: 'E1' and 'E4'. 'E1' is divided into two sub-folders: 'intake' and 'curtain'. Each one of these two folders is divided into three sub-folders: 'LIF', 'PIV', and 'Results' where each name represents the content of the folder. The folder 'E4' contains only the intake area's data and results and thus it is directly divided into three sub-folders: 'LIF', 'PIV', and 'Results'. All 'Results' folders mentioned contain several sub-folders related to the time period in concern: 'min-1', 'min-2', 'min-3', etc; where min-1, for instance, represents the first minute after the steady discharge Q_o is reached. Each one of these (final) sub-folders contains Matlab and Excel files. A special folder named 'Instantaneous-velocities' could also be found under the 'Results' folders.

The 'Plume-&-jet' folder is divided into three sub-folders: 'P-J' to represent the Plume-jet, 'J-P' to represent the Jet-plume, and 'Calibration' where a calibration images and procedures are saved. Both 'P-J' and 'J-P' folders are divided into three sub-folders: 'curtain', 'intake', and 'whole-section'. Both 'curtain' and 'intake' folders are divided into three sub-folders: 'PIV', 'LIF', and 'Results'. All 'Results' folders as well as the 'whole-section' folder contain several sub-folders related to the time period in concern: 'min-1', 'min-2', 'min-3', etc; where these minutes represent the time lab after the steady discharge Q_o is reached. A

special folder named 'Instantaneous-velocities' could also be found under the 'Results' folders.

Table B.1. An example of 'Experimental-info" for a two-layer case in the curtain area.

Two_layer Dec_22_2005	Curtain Area	Q_{avg} = 36.2 l/min

PIV (10 f/s) Boundaries

	limit	edges
up	ws = 25	
bottom	884	899
left	1	
right	curtain = 1248	1300

scale:1 cm = 20.85 | (884-25)/41.2

LIF (10 f/s) Boundaries

	cut	limit	edges
wtr. Surf.		~28	
bottom		742	783
left		1	
right		curtain = 1201	1216

(742-27)/41.2 scale:1 cm = 17.3301 pxls

		time PIV min:sec	PIV img#	LIF min:sec	LIF img#
Exp. Start	t_o	0:22	205	0:21	208
Q_o start	t_s	1:01	579	1:01	586
Exp. End	t_E	17:33	10101	17:33	10125

Note:actual frequency was about 9.6 fps

PIV		LIF					
410	420	415					
		t_s	t_E	t_s	t_E	$t_E - t_s$	$t_E - t_s$
		579	10101	586	10125	9522	9539
		t	$t - t_s$	$t - t_s$	t	$t - t_s$ (sec)	min
580	590	585	6	6	592	1	0.0
675	685	680	101	101	687	10	0.168
875	885	880	301	302	888	30	0.5
1175	1185	1180	601	602	1188	60	1.0
1775	1785	1780	1201	1203	1789	120	2.0
2375	2385	2380	1801	1804	2390	180	3.0
2975	2985	2980	2401	2405	2991	240	4.0
3575	3585	3580	3001	3006	3592	300	5.0
4175	4185	4180	3601	3607	4193	360	6.0
6575	6585	6580	6001	6012	6598	600	10.0
9575	9585	9580	9001	9017	9603.07	900.1	15.0

Heurisko

interogation	search win.	grid space	
32	64	32	8
		3 iterations	

Note: Interogation win. = question win.

final grid spa	8
ngrid-x	160
ngrid-y	112

t_{cr} ~108 s

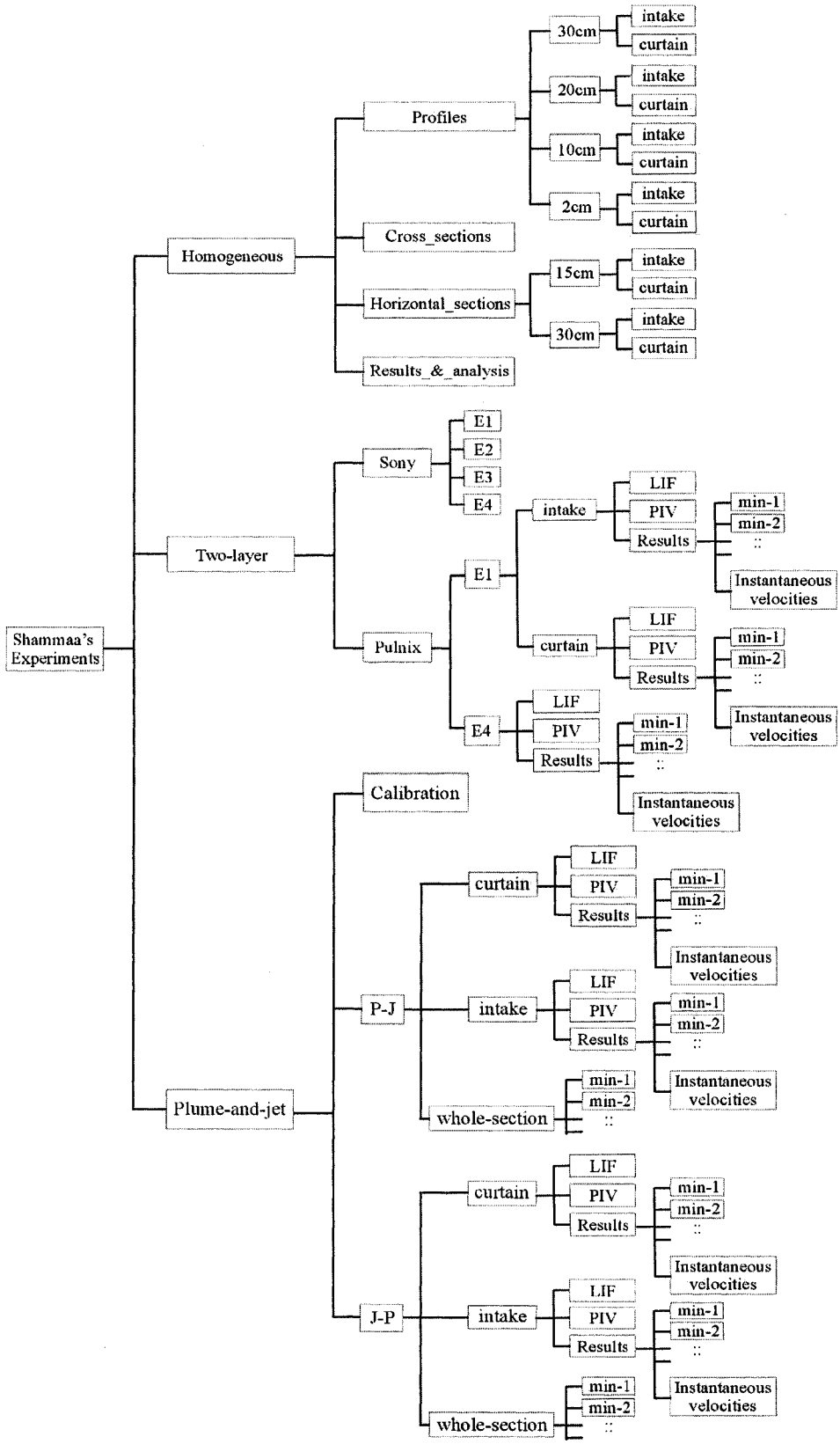

Chart B.1. Skeleton of the experimental folders.